ADVANCED FRACTURE MECHANICS MODELLING OF GLACIAL CALVING

A thesis submitted to Imperial College London for the degree of Doctor of Philosophy

by
Theo Clayton
MEng

Department of Civil and Environmental Engineering,
Imperial College of Science, Technology and Medicine
London SW7 2AZ, United Kingdom

Abstract

Sea level rise primarily occurs from glacial mass loss from ice sheets, through iceberg calving and meltwater production. However, iceberg calving from meltwater driven hydrofracture remains poorly understood.

A stress-based phase field simulation is proposed to model surface and basal crevasse propagation in ice sheets and ice shelves. The model incorporates: a constitutive description of nonlinear viscous ice rheology; a phase field formulation capturing complex fracture patterns; and a poro-damage approach representing crevasse meltwater pressures. Crevasse depth predictions are compared to analytical solutions with good agreement for appropriate idealisations.

The influence of firn material properties on longitudinal stress and crevasse depth are explored. Novel analytical solutions for longitudinal stress are derived considering depth-dependent density and Young's modulus, used subsequently in fracture mechanics studies to determine the contribution of firn to crevasse growth compared to homogeneous ice. The largest crevasse depth reductions were for shallow crevasses in thin glaciers, with Young's modulus being more influential. However, for near-terminus crevasses in ice shelves, firn density increased penetration depth, with differences observed in ice shelves up to a kilometre in thickness.

A phase field model based on the Mohr-Coulomb failure criteria is proposed for subaerial cliff calving, where failure stresses are decomposed into maximum shear stress and pressure components. Free slip glaciers are prone to mode I failures away from the terminus, whereas glaciers frozen to the bedrock are vulnerable to full thickness cliff failure beyond a critical thickness. This is dependent on cohesion, and damage initiation sites depend on internal friction. For tidewater glaciers, iceberg detachment occurs above a critical glacier free-board, with ice slumping above the oceanwater height. Stability envelope diagrams are produced based on critical conditions for cliff failure from multiple simulations. The under-

standing of crevasse behaviour in glaciers alongside the required conditions for iceberg calving are thereby enhanced.

Acknowledgements

I would like to express my gratitude to all those who have provided encouragement and support throughout my PhD. Firstly, I would like to thank my supervisors Professor Emilio Martínez-Pañeda, Professor Ravindra Duddu, Dr Tim Hageman and Professor Ahmer Wadee for providing the opportunity to develop my research skills and for their guidance and insight that has helped shaped the thesis into its final form.

In addition, I would like to thank my parents, my sister Sophie and my brother Oliver and all other family members and friends for providing me with love, support and encouragement throughout these past few years.

Declaration

The research presented in this thesis was carried out in the Materials Section of the Department of Civil and Environmental Engineering at Imperial College London. I hereby declare that this thesis and the work within is my own. Any published research from others has been acknowledged in the text and references are given in the list of sources.

Signature: Theo Clayton

Date: 22nd June 2025

Contents

Abstract **i**

Acknowledgements **iii**

1 Introduction **1**

1.1 Ice Sheets and Glaciers 1

1.2 Motivation and Objectives 5

1.3 Publications 6

1.4 Thesis Outline 7

2 Review of Current Methods for Assessing Crevasse Depths **9**

2.1 Analytical and Empirical Methods 11

2.1.1 Nye Stress Method 11

2.1.2 Linear Elastic Fracture Mechanics 12

2.1.3 Observational and Field Based Methods 14

2.2 Numerical Modelling 16

2.2.1 Continuum Damage Mechanics Methods 16

2.2.2 Cohesive Zone Modelling 17

2.2.3 Phase Field Method 18

2.2.4 Summary 19

3 Theory **20**

3.1 Phase Field Theory 20

3.1.1 Energy Based Approach for Brittle Elastic Solids 21

3.1.2 Phase Field Formulation - Stress Based Approach 27

3.2 Nonlinear viscous Rheology 31

3.3 Poro-Damage Mechanics 34

3.4 Numerical Implementation in COMSOL Multiphysics 36

4 Crevasse Propagation in Glaciers & Ice Shelves **41**

4.1 Geometry and Boundary Conditions 42

4.2 Stress state within a grounded glacier 44

4.3 Propagation of isolated surface crevasses in grounded glaciers . . . 48

4.3.1 Isolated surface crevasses-linear elastic rheology 49

4.3.2 Isolated surface crevasses – nonlinear viscous rheology . . . 54

4.3.3 Sensitivity analysis of model parameters 57

4.4 Densely spaced surface crevasses in grounded glaciers 61

4.5 Propagation of crevasses in floating ice shelves 64

4.5.1 Isolated surface crevasses 65

4.5.2 Basal and surface crevasse interactions 68

4.6 Initiation of damage from arbitrary sites – Helheim Glacier case study 72

4.7 Three dimensional case studies 75

4.8 Water filled crevasses close to ice sheet terminus 78

4.9 Concluding Remarks 80

5 Firn Layer Material Properties 83

5.1 Analytical solutions for the longitudinal stress 85

5.1.1 Depth-Dependent Density 88

5.1.2 Depth-Dependent Young's Modulus 91

5.1.3 Depth-Dependent Density and Young's Modulus 93

5.1.4 Limitations of analytical LEFM models 96

5.2 Results for grounded glaciers 97

5.2.1 Influence of Depth-Dependent Density 98

5.2.2 Influence of Depth-Dependent Young's Modulus 103

5.2.3 Influence of Depth-Dependent Young's Modulus and Density 105

5.2.4 Influence of Depth-Dependent Poisson Ratio 106

5.3 Results for floating ice shelves 108

5.4 Nonlinear Viscous Incompressible Rheology 114

5.5 Discussion 119

5.6 Concluding Remarks 121

6 Subaerial Ice Cliff Calving **123**

6.1 Shear Stress Based Crack Driving Force 127

6.2 Boundary Conditions 131

6.3 Land Terminating Glaciers 134

6.3.1 Stress Distributions 134

6.3.2 Cliff Failure: Influence of Basal Boundary Condition . . . 136

6.3.3 Cliff Failure: Influence of Internal Friction 139

6.3.4 Cliff Failure: Influence of Shear Strength 143

6.4 Ocean Terminating Glaciers 144

6.4.1 Inclusion of Buttressing Stresses 150

6.5 Discussion 151

6.5.1 Implications for fracture modelling 153

6.5.2 Stability criteria for large scale ice sheet models 155

6.6 Concluding Remarks 156

7 Conclusions **158**

7.1 Future Work 160

References **161**

A Single Edge Notched Specimen **187**

A.1 Uniaxial Tension Test 188

A.2 Remote Shear Test 192

B Longitudinal Stress Derivations **196**

C Linear Elastic Fracture Mechanics for a Grounded Glacier **201**

D Linear Elastic Fracture Mechanics for a Floating Ice Shelf **204**

E Shallow Ice/Shelf Approximations **208**

List of Tables

4.1 Material properties assumed presently (unless otherwise stated). The values are chosen to characterise the behaviour of glacial ice, with the final column denoting the relevant reference. 42

5.1 Normalised crevasse depths for a dry ($h_s/d_s = 0.0$) isolated surface crevasse within a floating ice shelf close to the front (x = 4750 m), calculated using the LEFM method. 110

5.2 Normalised crevasse depths for an isolated surface crevasse with a meltwater depth ratio of $h_s/d_s = 0.75$ within a floating ice shelf close to the front ($x = 4750$ m), calculated using the LEFM method. 110

6.1 Characteristic material properties for glacial ice assumed in this work (unless otherwise stated). 132

A.1 Characteristic material properties for steel assumed to model the square cracked plate in tension, taken from [1]. 189

D.1 Coefficients of normalised longitudinal stress in Eq. (D.6) for a floating ice shelf at horizontal position ($x = 4750$ m). 207

List of Figures

1.1 Illustration of a grounded ice sheet and a floating ice shelf, containing both surface and basal crevasses, and with calving events occurring at the terminus. 3

3.1 (a) Schematic diagram showing a sharp crack. (b) Schematic diagram showing a diffusive phase field crack over length scale ℓ_c. . . 23

3.2 Non-dimensionalized graph showing the distribution in phase field parameter ϕ with distance away from the sharp crack. 23

3.3 Uniaxial stress-strain response, as predicted by the stress-based phase field model adopted, showcasing the role of the post peak parameter ζ 31

3.4 Schematic diagram of a viscoelastic Maxwell model 32

3.5 Schematic diagram of a meltwater filled crevasse in glacial ice, illustrating the intact phase ($\phi = 0$), fully cracked phase ($\phi = 1$) and transition phase ($0 < \phi < 1$). 36

4.1 Crevasse growth in a grounded glacier: (a) diagram showing the boundary conditions of a grounded glacier containing a single surface crevasse, and (b) finite element mesh employed, with the mesh refined along the expected crevasse propagation path. 44

4.2 Contours of the longitudinal stress σ_{xx}, vertical stress σ_{zz}, in-plane shear stress σ_{xz} and crack diving force state function D_{d} for a pristine grounded glacier. 47

4.3 Crevasse growth in a grounded glacier. Normalised crevasse depth predictions (d_{s}/H) for a single isolated crevasse in a linear elastic ice sheet. 51

4.4 Phase field damage contour plots showing growth of a single isolated crevasse in a grounded glacier. 52

4.5 Crevasse growth in a grounded glacier. Normalised crevasse depth predictions for a single isolated crevasse in a grounded glacier, assuming a nonlinear viscous rheology. 56

4.6 Normalised surface crevasse depth (d_{s}/H)versus time predictions for a dry isolated crevasse with an oceanwater ratio of $h_{\mathrm{w}} = 0.5H$. Parametric studies varying critical fracture stress σ_{c}, crack driving force threshold F^{th}, post peak slope parameter ζ, phase field length scale ℓ_{c}, number of solver iterations N and refined mesh size h_{c}. . 60

4.7 Multiple crevasse growth in a grounded marine-terminating glacier. Diagram shows the boundary conditions of a grounded glacier with a field of densely spaced crevasses (spaced 50 m apart from each other). 61

4.8 Phase field damage contour plots showing growth of densely spaced field of surface crevasses in a grounded glacier. 62

4.9 Multiple crevasse growth in a grounded glacier. Normalised crevasse depth versus meltwater depth ratio predictions as a function of the oceanwater height. Comparisons between the present phase field model and analytical predictions from Nye's zero stress model [2], for a linear elastic ice sheet. 63

4.10 Schematic diagram showing the applied boundary conditions of a floating ice shelf containing an isolated surface crevasse 65

4.11 Distribution of longitudinal stress σ_{xx} versus depth at different horizontal positions in a floating ice shelf. 66

4.12 Growth of a surface crevasse in a floating ice shelf. Analytical (LEFM-based) and computational phase field predictions of stabilised crevasse depths (d_s/H) as a function of the meltwater depth ratio (h_s/d_s). The results are provided at horizontal locations $x = 2500$ m and $x = 4950$ m. 67

4.13 Growth of surface and basal crevasses in a floating ice shelf. Phase field damage contours after reaching the arrest of the crevasses, considering four selected values for the horizontal separation (S) between the basal and surface crevasse. For the surface crevasse, the meltwater depth ratio equals $h_s/d_s = 0.8$. 69

4.14 Growth of surface and basal crevasses in a floating ice shelf. The basal and surface crevasses are separated by a horizontal distance S. (a) Predictions of crevasse depth versus time for surface and basal crevasses with varying horizontal spacing S; and (b) evolution of the combined basal and surface crevasse depth versus time for selected choices of the horizontal spacing S. 71

4.15 Nucleation and growth of crevasses in the Helheim glacier. Initial geometry, as taken from observational data in Nick *et al.* [3]. . . . 72

4.16 Nucleation and growth of crevasses in the Helheim glacier. Distribution of the nucleation variable $D_{\mathrm{d}}\varepsilon^{c}$, with red colour contours denoting the areas where the nucleation threshold has been exceeded. 74

4.17 Phase field damage evolution of the Helheim glacier assuming a nonlinear viscous rheology. 74

4.18 Crevasse interactions in 3D marine-terminating ice sheets. Diagram showing the boundary conditions and geometry of the three dimensional boundary value problem. 75

4.19 Phase field contour plots showing the evolution of two dry edge surface crevasses in a 3D ice sheet. 77

4.20 Phase field contour plots of a fully saturated isolated crevasse close to the terminus of a near floatation glacier ($h_{\mathrm{w}} = 0.9H$). 79

5.1 Profile of depth-dependent mechanical properties for ice density and Young's modulus. Data extracted from ice core specimens from the Ronne ice shelf by [4] are displayed as markers. Homogeneous properties are displayed with the dotted lines. 86

5.2 Far field longitudinal stress σ_{xx} throughout the depth of a land terminating glacier ($h_{\mathrm{w}} = 0$), showing the effects of (a) variations in density, (b) variations in Young's modulus, and (c) variations in both density and Young's modulus. 99

5.3 Normalised crevasse depth predictions versus oceanwater height ratio for a single isolated dry crevasse in a linear elastic ice sheet, considering homogeneous and depth-dependent mechanical properties. 100

5.4 Normalised crevasse depth predictions versus meltwater depth ratio for a single isolated crevasse in a linear elastic ice sheet, considering homogeneous and depth-dependent mechanical properties, for an oceanwater height $h_w = 0.5H$. 101

5.5 Normalised crevasse depth predictions versus oceanwater height ratio for a single isolated dry crevasse in a linear elastic ice sheet, considering homogeneous and depth-dependent Poisson Ratio. . . 107

5.6 Normalised crevasse depth predictions versus meltwater depth ratio for an isolated surface crevasse in a floating ice shelf close to the front $x = 4750$ m. 111

5.7 Far field longitudinal stress σ_{xx} throughout the depth of a land terminating glacier ($h_w = 0$), showing the effects of depth-dependent density $\rho(z)$; considering linear elastic compressibility ($\nu = 0.35$), linear elastic incompressibility ($\nu \approx 0.5$) and a nonlinear viscous rheology. 115

5.8 Normalised crevasse depth predictions versus oceanwater height ratio for a single isolated dry crevasse in a grounded glacier, considering compressible ($\nu = 0.35$) and incompressible ($\nu \approx 0.5$) ice homogeneous and depth-dependent mechanical properties. 116

5.9 Normalised crevasse depth predictions versus meltwater depth ratio for a single isolated surface crevasse located in the far field region ($x = 2500$ m) considering a linear elastic (LE) and nonlinear viscous (NLV) rheology for (a) the far field region ($x = 2500$ m) and (b) close to the front ($x = 4750$ m). 118

6.1 Diagram showing yield surfaces for the principal stress criterion (blue surface) and Mohr-Coulomb failure criterion for internal friction $\mu = 0.0$ (red surface), $\mu = 0.3$ (green surface), $\mu = 0.8$ (black surface). Shaded regions indicate combinations of stress σ_{xx} and σ_{zz} where the material does not undergo yielding (i.e. $D_{\mathrm{d}} = 0$). . 129

6.2 Graph showing the 2D yield surface for internal friction values $\mu = 0.3$ and $\mu = 0.8$ for applied shear stress τ versus normal stress P. If the stress regime is beneath the yield line, then the material will not fail. 131

6.3 Schematic diagram showing boundary conditions for a grounded glacier subject to the following basal conditions (a) free slip, (b) basal sliding and (c) frozen base. 133

6.4 Steady state creep stress states showing maximum shear stress and first principal stress for a grounded glacier of height $H = 200$ m undergoing free slip (a) and (c) and no slip (b) and (d). 135

6.5 Phase field damage evolution over time for a land terminating grounded glacier undergoing free slip at the base with internal friction $\mu = 0.8$ and cohesion $\tau_{\mathrm{c}} = 1$ MPa at time (a) $t = 15$s, (b) $t = 50$ s, (c) $t = 75$ s and (d) $t = 200$ s. 139

6.6 Phase field damage evolution over time for a land terminating grounded glacier subject to a frozen base with internal friction $\mu = 0.8$ and cohesion $\tau_{\mathrm{c}} = 1$ MPa at time (a) $t = 15$ s, (b) $t = 60$ s, (c) $t = 150$ s and (d) $t = 250$ s. 140

6.7 Graph showing damage accumulation area normalised with respect to in-plane glacier area ($H \times L$) versus time for a land terminating graph of height $H = 200$ m for different basal boundary conditions. 141

6.8 Phase field damage evolution over time for a land terminating grounded glacier subject to a frozen base with internal friction $\mu = 0.0$ and cohesion $\tau_c = 1$ MPa at time (a) $t = 17$ s, (b) $t = 35$ s, (c) $t = 70$ s and (d) $t = 93$ s. 142

6.9 Graph showing minimum glacier thickness required to trigger cliff failure versus cohesion τ_c. 144

6.10 Phase field damage evolution over time for a grounded glacier subject to a frozen base, of height $H = 800$ m and oceanwater height of $h_w = 585$ m with internal friction $\mu = 0.8$ and cohesion $\tau_c = 0.5$ MPa at time (a) $t = 5$ s, (b) $t = 40$ s, (c) $t = 100$ s and (d) $t = 250$ s. 146

6.11 Combination of glacier thickness and oceanwater height required for stable ice cliffs to exist (shaded regions), floatation to occur (upper-left triangular region), or cliff slumping to trigger (bottom right triangle). Observational data from Alaska, Svalbard and West Greenland Glaciers from Pelto et al [5] and MCoRDS radar data for various Greenland outlet glaciers from Ma et al [6]. 148

A.1 (a) Schematic diagram of the cracked plate in tension (dimensions in mm) (b) finite element mesh used for the analysis 189

A.2 Evolution of the phase field parameter for the uniaxial tension test, from (a) an intact specimen to (c) an intermediate crack and (e) to a fully fractured specimen for the strain energy density approach. Phase field plots for the principal stress based approach are shown in (b), (d) and (f) respectively. 190

A.3 Uniaxial force versus applied displacement at the base of the single notched edge plate for the phase field strain energy based scheme and principal stress based scheme. 192

A.4 (a) Schematic diagram of the cracked plate undergoing shear (dimensions in mm) (b) finite element mesh used for the analysis . . 193

A.5 Evolution of the phase field parameter for the shear test, from (a) an intact specimen to (c) an intermediate crack and (e) to a fully fractured specimen for the strain energy density approach. Phase field plots for the principal stress based approach are shown in (b), (d) and (f) respectively. 194

A.6 Force versus applied displacement graph for the remote shear test considering the phase field strain energy based scheme and principal stress based scheme. 195

B.1 Plot of the lithostatic, hydrostatic and combined stress states with depth for a grounded ice sheet 200

Chapter 1

Introduction

1.1 Ice Sheets and Glaciers

Ice sheets are large masses of grounded glacial ice, that inundate the surrounding landscape, which cover an area greater than 50,000 km^2. Today, ice sheets are confined to polar regions (Greenland and Antarctica), but during the Pleistocene era, ice sheets covered large parts of Northern America and Europe [7]. Ice sheets are one of the largest stores of fresh water on the planet, containing approximately 70% of the Earth's fresh water [8]. The majority of which is located in Antarctica, which consists of the Eastern and Western Antarctic ice sheets, containing approximately 30 million km^3 of ice, by contrast the Greenland ice sheet contains 2.85 million km^3 of ice [9].

Ice sheets become thinner toward their margins, and if these thinner regions are located in marine settings with sufficient oceanwater height, they will form floating extensions known as ice shelves. Ice shelves play an important role in maintaining glacial stability by providing resistive buttressing forces to down-

slope flow and reduce the flux of grounded ice into the ocean.

Buttressing occurs as a result of shearing at confined lateral margins and local regions where ice becomes grounded due to ice rises or rumples. The degree of buttressing is quantified by considering the stress regime at the grounding line, through the use of data assimilation and ice flow modelling and comparing this to the hydrostatic ocean pressure exerted on the ice if the shelf is removed [10]. If these are equal then the ice shelf is considered unbuttressed. Studies have been conducted to determine the influence of ice shelf thinning on the flux of ice over the grounding line [11].

A recent study by Lai et al, which mapped surface fractures in satellite imagery and compared this with theoretical predictions of water filled fracture propagations suggests that approximately 60% $\pm$ 10% of Antarctic ice shelves provide significant buttressing and are vulnerable to calving [12], including large regions of the Ross and Ronne ice shelves. However, this conclusion has been debated, with the relationship between damage from ice sheet modelling and damage identified from remote sensing remaining unclear [13].

An illustration of a grounded ice sheet, transitioning to a crevassed floating ice shelf is shown in Figure 1.1.

As a result, ice sheets play a pivotal role in maintaining a stable global environment through two processes. Firstly, ice sheets reflect large amounts of solar radiation away from the Earth's surface due to the high albedo properties of glacial ice, leading to reduced surface temperatures. Secondly, the storage of freshwater as ice assists in the process of maintaining global oceanwater levels [14]. Thus, ensuring the stability of ice sheets is of great importance to maintaining a stable global climate.

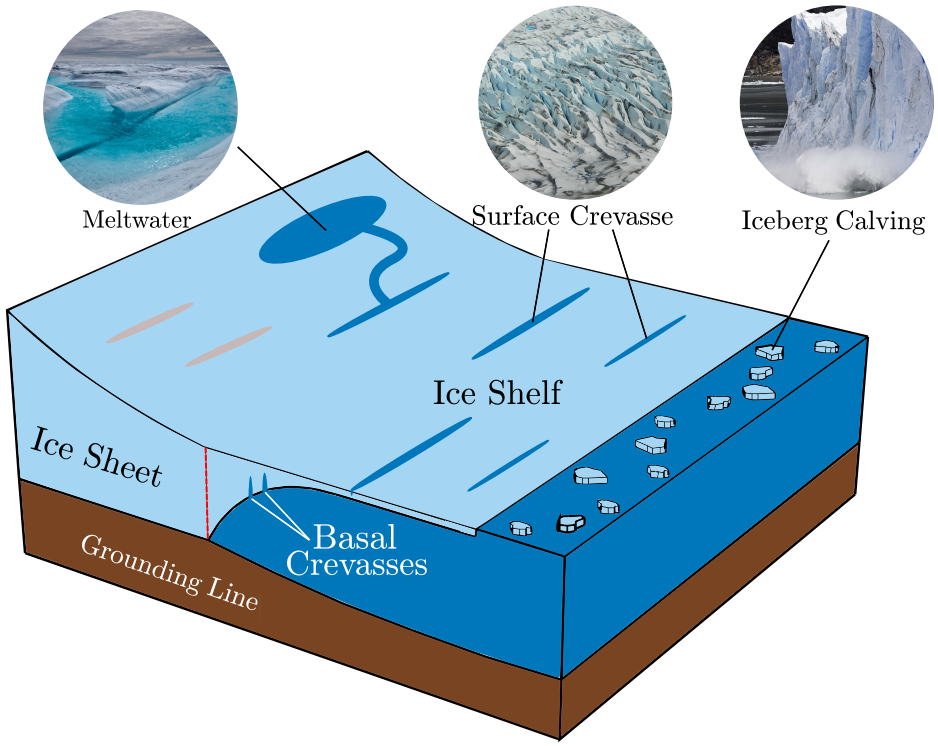

Figure 1.1: Illustration of a grounded ice sheet and a floating ice shelf, containing both surface and basal crevasses, and with calving events occurring at the terminus.

Ice sheets are in a state of constant flux and originate at high altitudes, where surface temperatures are low and mass is accumulated due to snowfall [15]. Over time, the snowfall compacts into denser glacial ice, which deforms due to its self-weight and flows down-slope towards warmer regions, where net ablation occurs, primarily due to iceberg calving events and surface and basal melt. The combination of accumulation and ablation volumes leads to the glacial mass balance. These two processes should be in equilibrium with each other, meaning that there is no net change in glacial volume.

The effect of atmospheric warming on the stability of ice shelves has been well documented. This was first postulated by Mercer in 1978 [16] who linked increases in greenhouse gas emissions to deglaciation of Antarctica. Elevated surface temperatures leads to a greater production of surface meltwater, which can accelerate the rate of iceberg calving events and in extreme cases may lead to complete ice

shelf disintegration. The frequency of these events has grown in recent decades, beginning with the disintegration of Larsen A (1995) [17] and Larsen B (2002) [18] ice shelves, and more recently, significant surface melting and iceberg calving on Larsen C (2017) [19], Pine Island and Thwaites (2018–2020) [20], and Conger (2022) ice shelves [21].

The stability of floating ice shelves are also vulnerable at the ice-ocean barrier. Increasing ocean temperatures lead to increased eddy currents at the lower ice shelf boundary, particularly in regions of Western Antarctica [22]. These eddy currents transfer heat from the ocean to the ice shelf, leading to localised basal melting [23] and thinning of the ice shelf section [24]. This in turn, affects the stress state within the ice shelf and therefore the fracture pattern. Whilst ice mass losses from ice shelves do not directly contribute to sea level rise, ice shelf removal results in loss of resistive buttressing forces and leads to accelerated flow of grounded ice into the ocean [25].

Deposition of grounded glacial ice into the ocean is the leading contributor to sea level rise [26], having recently exceeded expansion of oceanwater due to warming [8]. Sea level rise has direct implications within this Century on low-lying coastal regions through flooding, increased extreme environmental events, degradation of farmland and loss of habitat, among others. It is estimated by the IPCC that approximately 10% of the global population (680 million people) live within these low-lying regions [27]. This highlights the importance of maintaining ice sheet stability, the direct role ice sheets have on controlling global climates and the need for modelling and monitoring fracture propagation in ice sheets and ice shelves.

1.2 Motivation and Objectives

The goal of this work is to predict the stability of ice cliffs and crevasses in ice sheets undergoing hydro-fracture. To achieve this, the following objectives are considered:

The first objective of the current work is to predict the propagation of surface and basal crevasses in free slip grounded glaciers and floating ice shelves, subject to meltwater driven hydrofracture and to determine the conditions required to promote full thickness crevasse propagation. This is achieved by developing a numerical framework for the phase field fracture model, coupled with poro--damage mechanics methods to model meltwater in crevasses and a nonlinear viscous rheology to capture time dependent glacial flow. In this model, crevasse propagation is driven by tensile states of the principal stresses, to capture the tension-compression asymmetric behaviour of ice. Several benchmark examples are considered, and results are compared to analytical solutions such as linear elastic fracture mechanics and Nye zero stress methods.

The second objective is to determine the influence of firn mechanical properties, including the density and Young's modulus, on longitudinal stress and surface crevasse propagation, using borehole data from the Ronne ice shelf. Glacial ice forms from the accumulation of snowfall at the upper surface and undergoes compaction under the overburden pressure, thus mechanical properties vary with depth. The majority of crevasse propagation studies consider the material properties of ice to be homogeneous, taken at fully consolidated strata, leading to an overestimation of mechanical properties in the upper surface. Derivations for the longitudinal stress are presented, considering depth-dependent mechanical properties. Linear elastic fracture mechanics studies are subsequently conducted to determine the stabilised crevasse penetration depth with the results being

compared to predictions for fully consolidated homogeneous glacial ice.

The third objective is to determine the critical conditions required for glaciers to undergo subaerial cliff calving. Damage propagation is driven by a stress based Mohr-Coulomb failure criterion, where the failure surface is dependent on the internal friction coefficient and cohesive strength. A variety of factors are considered in the analysis, including ice thickness, oceanwater height and basal boundary conditions. The stability criteria produced from these phase field simulations are compared to predictions from discrete element methods and empirical calving laws, based on the height above buoyancy. In addition, observational data in the form of stable ice thicknesses and oceanwater heights are considered, taken from tidewater outlet glaciers in Greenland and Alaska.

1.3 Publications

The work conducted during the present doctoral study has resulted in the production of three published journal papers. This has aided the formation of the structure of the thesis, discussed in Section 1.4. The following journal papers have been produced by the candidate:

- T. Clayton, R. Duddu, M. Siegert, E. Martínez-Pañeda, A stress-based poro-damage phase field model for hydrofracturing of creeping glaciers and ice shelves, Engineering Fracture Mechanics 272 (2022) 108693.
- T. Clayton, R. Duddu, T. Hageman, E. Martinez-Pañeda, The influence of firn layer material properties on surface crevasse propagation in glaciers and ice shelves, The Cryosphere 18 (2024).
- T. Clayton, R. Duddu, T. Hageman, E. Martinez-Pañeda, Modeling ice

cliff stability using a new Mohr-Coulomb-based phase field fracture model, Journal of Glaciology (2025). [Accepted]

1.4 Thesis Outline

The present thesis comprises six further chapters. Chapter 2 presents a review of existing analytical and numerical fracture mechanics methods in the literature.

In Chapter 3, the key theoretical components to the numerical model are presented, including the phase field model for fracture, nonlinear viscous creep deformation and poro-damage mechanics concepts. In addition, the coupled system of governing equations are outlined and the numerical implementation into the finite element system COMSOL Multiphysics is presented.

In Chapter 4, the numerical results for several benchmark case studies using phase field fracture are presented, considering both isolated and densely spaced crevasses in idealised grounded glaciers and floating ice shelves. The results are verified with analytical methods such as linear elastic fracture mechaincs (LEFM) and the Nye zero stress method.

The inclusion of firn material properties is explored in Chapter 5; analytical solutions for the far field longitudinal stress are derived, responsible for driving mode I crevasse propagation, considering the effects of depth-dependent density and depth-dependent Young's Modulus. Fracture propagation studies are then conducted using these analytical solutions and compared to the homogeneous case, for isolated surface crevasses in grounded glaciers and floating ice shelves.

In Chapter 6, a Mohr-Coulomb failure criterion is implemented into the phase field method to study the collapse of tall ice cliffs, leading to iceberg calving

events. Numerical simulations are conducted to determine the critical conditions required to cause subaerial ice cliff failure, including basal boundary condition, cohesive strength, internal friction coefficient, ice thickness and oceanwater height. The results presented are compared to semi-empirical calving laws and simulations from discrete element methods in the literature. Stability diagrams are produced based on ice thickness and oceanwater height, with observational data overlapping well within the stability envelope.

The main conclusions drawn are summarised in Chapter 7 along with recommendations for future research work.

Chapter 2

Review of Current Methods for Assessing Crevasse Depths

Glacial ice is a polycrystalline material formed through the accumulation and compaction of snow under gravitational force. Ice may exhibit several crystal structures, depending on its thermal-mechanical history. The mechanical behaviour of ice is dependent on numerous factors, including strain rate, temperature, density and grain size [28]. In tension, ice behaves as a ductile material for low strain rates. However, for intermediate and high strain rates, ice behaves in a brittle manner. In compression, ice behaves as a ductile material for low and moderate strain rates, but for higher strain rates ice exhibits brittle behaviour. An increase in strength is observed as ice temperature decreases, with the effect being more prominent under compression, compared to tension. Ice density is also influential on strength, with a higher strength being observed as the density increases [29]. Finally, the tensile strength of ice is significantly lower than the compressive strength, indicating that crevasse nucleation and growth is likely to occur as a result of tensile stress states.

Basal and surface crevasses are predominantly mode I tensile fractures found in both Greenland and Antarctica that propagate vertically and tend towards a stabilised depth [30]. The extent of these fractures range from tens of metres [31], to full thickness propagation, leading to iceberg calving events. The latter may lead to rapid drainage of supraglacial lakes [32] that enhances basal sliding by altering subaerial hydrology and causes glacial mass losses into the ocean [33, 34, 35]. Crevasse propagation is driven by the state of the longitudinal tensile stresses, normal to the fracture surface in ice sheets, as a result of self-gravitational loading. Fracture propagation can be further aided by the accumulation of meltwater within surface crevasses, the supply and storage of which can be attributed to supraglacial lakes and firn aquifers [36]. This can trigger a process known as hydrofracture, wherein the meltwater in the crevasse exerts additional opening stress on the crevasse walls [37]. If the volume of meltwater is sufficiently large, hydrofracture can cause full thickness crevasse propagation and lead to large scale iceberg calving events in ice shelves and glaciers [38]. It is therefore important to develop models to capture the propagation of crevasses accurately and to predict the likelihood of potential iceberg calving events, leading to glacial mass loss.

In this present chapter, an overview is presented of both analytical, observational and numerical models used previously, to model crevasse propagation and their advantages and limitations.

2.1 Analytical and Empirical Methods

2.1.1 Nye Stress Method

The assessment of crevasse penetration depths was first considered in 1957 by Nye [39] who derived an equation for dry surface crevasse depths, based on the balance of stresses. Tensile stresses within the ice aim to open and propagate the crevasse by mode I fracture. However these are offset by the lithostatic compressive stresses in the ice due to the self weight which increase with depth. Nye assumed that ice has no tensile strength and predicted that the crevasse will stabilise at a depth at which the tensile stress is balanced by the lithostatic compressive stress, deriving Eq. (2.1):

$$d = \frac{2}{\rho_{\mathrm{i}} g} \left(\frac{\dot{\varepsilon}_{xx}}{A} \right)^{\frac{1}{n}} . \tag{2.1}$$

However, this assessment does not account for the hydraulic pressure inside water filled crevasses. The presence of meltwater causes the crevasse to open, leading to deeper crevasse propagation and is thus treated as an additional tensile stress. The Nye zero stress model was later adapted by Benn et al [40] to include the effects of surface meltwater in Eq. (2.2):

$$d = \frac{2}{\rho_{\mathrm{i}} g} \left[\left(\frac{\dot{\varepsilon}_{xx}}{A} \right)^{\frac{1}{n}} + (\rho_{\mathrm{w}} g d_{\mathrm{w}}) \right] , \tag{2.2}$$

where d is the depth of crevasse, ρ_{i} is the density of ice, g is gravitational acceleration, A and n are flow law parameters, $\dot{\varepsilon}_{xx}$ is the longitudinal surface strain rate, ρ_{w} is the density of meltwater and d_{w} is the depth of water in the crevasse.

The Nye zero stress method is advantageous as it a simple method that has been widely implemented into ice sheet models [41, 42]. However it is a primitive for-

mulation as it does not consider the effect of local stress concentrations (stress singularity) near the crack tip. This is acceptable for closely spaced crevasses because multiple cracks exhibit a "shielding" effect on local stress concentrations. However, for isolated crevasses, the Nye zero stress method leads to an underestimation in crevasse depths.

2.1.2 Linear Elastic Fracture Mechanics

To address the limitations of the Nye zero stress method, researchers began to consider individual crevasses by assuming crevasses as sharp discontinuities and accounting for the stress singularity at the tip. The first work was conducted by Weertman [43, 44], who considered dislocation based methods. Weertman calculated the crack opening displacement and stated that the crevasse would stabilise at a depth at which the crack displacement becomes negative (i.e. the crack no longer opens). However, these methods assume an infinite ice thickness and are therefore only valid for shallow crevasses with respect to the ice thickness.

Linear elastic fracture mechanics (LEFM) based methods are founded on the works of Irwin [45], who considered stresses in the proximity of the crack tip to be infinite and diminish towards the remote stress with distance r from the crack tip at a rate of $1/\sqrt{r}$. LEFM assumes that the crack is sufficiently small in comparison to the specimen geometry, while also being greater than the transition flaw size, to allow for the material to fail by crack growth instead of material yielding. Moreover, LEFM assumes that the material undergoes local yielding and plastic deformation around the crack tip, an area known as the fracture process zone [46, 47]. The stress singularity around the crack tip can be characterised by introducing the stress intensity factor and is proportional to the remote normal stress and square root of the crack length.

LEFM was first proposed to model water filled crevasses by Smith [48], assuming an infinite ice thickness. This was later developed by van der Veen [49, 50], to account for the glacier geometry using weight functions, to calculate surface and basal crevasse propagation in glaciers. Van der Veen individually evaluated the mode I stress intensity factors K_I for the tensile normal stress, lithostatic compressive stress and tensile stress due to water pressure and superimposed them to determine the net stress intensity factor K_I^{net}. The stress intensity factors are integrated over the depth due to the stress state varying with depth [49]. In order for cracks to propagate at an unstable rate, the net stress intensity factor must be greater than a threshold value, known as the fracture toughness K_c. A generalised equation for a mode I stress intensity factor is shown in Eq. (2.3):

$$K_{\mathrm{I}} = \beta\sigma\sqrt{\pi a}\,, \tag{2.3}$$

where β is a dimensionless factor based on crack geometry and loading (for shallow surface cracks $\beta = 1.12$), σ is the remote normal stress applied and a is the crack length.

An alternative approach for quantifying the stress singularity is the J-Integral analysis by Rice [51]. This evaluates the strain energy release rate around the crack tip through a path independent line integral using a finite element analysis ; J-integral based fracture mechanics operates in a similar manner to K based LEFM methods, with crack growth ceasing below a critical value J_{IC}. Furthermore, the J-integral can be directly related to the stress intensity factor and is advantageous since it alleviates the need for weight functions required for traditional K based approaches.

LEFM is advantageous since it allows for isolated crevasses to be evaluated. In addition, LEFM has provided better predictions than the Nye zero stress method,

when comparing to field observations of crevasses in the Breidamerkurjökull glacier in Iceland, despite crevasse depth measurements being 'difficult, dangerous and time-consuming' [52]. The LEFM approach has also been combined with full--Stokes models to study surface and basal crevasse propagation in the Thwaites glacier, with results agreeing well with NASA's radar penetration depths [53]. In addition, LEFM has been used to map the vulnerability of Antarctic ice shelf crevasses subject to meltwater driven hydrofracture, with projections agreeing well with existing fractures being mapped by neural networks [12]. The LEFM approach has been successfully combined with boundary element methods, capturing the interactions between basal and surface crevasses and providing estimates for stability [54] and evolution of crevasse shape [55].

However, these methods have their limitations, most notably the assumption that ice behaves as a linear elastic compressible material, with crevasses propagating in a rapid and brittle manner. LEFM methods also assume weight functions to calculate the net stress intensity factor that are dependent on highly idealised specimen geometries and boundary conditions. Moreover, LEFM methods also require a pre-existing crack to determine propagation and cannot determine crevasse nucleation. Crack geometries are assumed as sharp discontinuities, hence complex fracture patterns such as bifurcation and crack coalescence are both difficult to capture.

2.1.3 Observational and Field Based Methods

Satellite imagery and field observations have been used to map the evolution of ice sheet flow, production of meltwater, grounding line positions and the propagation of crevasses and rifts. Satellites such as Sentinel-1 and TerraSAR-X emit microwave radiation and imagery is produced based on the reflected electromag-

netic waves. Synthetic Aperture Radar (SAR) can identify both open crevasses and crevasses covered in snow layers of thickness up to 10 m [56]. With satellite imagery taken at regular time intervals, SAR allows for the tracking of rifts prior to ice shelf collapse. An example of this was the study conducted by Glasser and Scambos [57], who tracked the accumulation of meltwater ponds in the northern and central parts of the Larsen B ice shelf due to frequent warm summers prior to ice shelf collapse [58, 59]. Rignot and others used satellite radar interferometry data to determine ice sheet velocities, surface strain rates and bed elevations for Antarctica with a resolution of 300 m [60]; allowing for validations with ice sheet models. Ground penetrating radar has also been used to detect both surface and basal crevasses [61, 62].

Observational methods are advantageous since they can map large areas of Greenland and Antarctica at high resolutions and provide insights into previous iceberg calving events. Whilst the use of observational methods are beyond the scope of the present work, it is important to acknowledge their use in mapping crevasse growth in ice sheets and ice shelves.

2.2 Numerical Modelling

2.2.1 Continuum Damage Mechanics Methods

In recent years, numerical methods have been developed to address the limitations of the above analytical models, most notably continuum damage mechanics (CDM) methods. CDM methods describe the distribution of microvoids and microcracks by introducing a scalar damage variable D that ranges from $D = 0$ in the intact domain to $D = 1$ to the fully damaged state. Thus, cracks are described as diffuse damage regions as opposed to sharp interfaces. The true Cauchy stress can be mapped to the effective stress by a factor of $(1 - D)$ and the evolution law for damage is driven by the Hayhurst stress invariant, which is coupled with the momentum balance and solved in a finite element solver.

Karr and Choi [63] were the first to propose a simple isotropic continuum damage mechanics model for polycrystalline ice and compared the results to experimental testing for uniaxial and multiaxial stress states [64]. Pralong and Funk [65, 66] developed a local creep damage model within incompressible Stokes flow to simulate crevasse propagation, with numerical results agreeing well with field predictions. This work was further extended by Duddu et al who presented a non-local CDM model that captured the effects of temperature dependency, in a Lagrangian [67, 68] and Updated Lagrangian [69] finite element framework respectively.

Non-local methods incorporate Gaussian or Green weighting functions into the nonlocal damage rate, which introduce a non-local length scale. The local damage rate $\dot{D}^{loc}$ is expanded as a Taylor series and the partial differential equation related to the implicit gradient formation is found by taking the Laplacian and subtracting from the Taylor series, such that $\dot{D} - \frac{1}{2}\ell_c \nabla^2 \dot{D} = \dot{D}^{loc}$ [70].

Non-local methods can be either gradient based or integral based and the introduction of a fracture length scale alleviates any mesh sensitivity or bias associated with local methods. CDM methods have also been coupled with poro-damage mechanics methods to capture meltwater driven hydrofracture, allowing for meltwater to follow the evolution of the damaged zone [71, 72].

CDM is advantageous since it can capture the nucleation and propagation of crevasses from arbitrary sites, and alleviates the requirement of pre-existing cracks or complicated crack tracking algorithms to be implemented. In addition, CDM is appropriate for a wide range of glacier geometries and basal boundary conditions, negating the need for specific weight functions to be applied. CDM methods can also be combined with nonlinear viscous creep deformation, thus failure is modelled as a time dependent gradual process.

However, CDM methods also have their limitations; firstly, they rely on empirical parameters that may not be well calibrated with existing observations. In addition, damage mechanics methods coupled with full Stokes equations may be computationally expensive when modelling crevasses in real ice sheets and ice shelves. To address these limitations, CDM has recently been coupled with shallow shelf approximations and material point methods to reduce the computational burden [73, 74, 75].

2.2.2 Cohesive Zone Modelling

In contrast to the continuum damage mechanics approach, cohesive zone models assume cracks to be a sharp, zero-thickness fracture. Cohesive zone models were first proposed by Dugdale and Barenblatt [76, 77] which consider a bounded stress around the crack tip. Fracture behaviour is based on a traction-separation law,

with interface elements being inserted dynamically or *a priori* ahead of the crack tip along the fracture path. Cohesive zone models have the ability to capture mixed mode fracture propagation by considering tractions normal or tangential to the interface elements. The relative separation displacement between the two nodes of the interface element is measured, and typically, an elastic force displacement response is observed prior to damage. The maximum traction that may be sustained by the interface elements is equal to the cohesive strength, which is achieved at a critical displacement value. Once the displacement exceeds the critical value, damage initiates and the material enters a softening regime, which may follow a bilinear [78], exponential [79], or polynomial [80] distribution.

Originally used to model concrete and popularised by the delamination and debonding of composite structures [81, 82, 78]; cohesive zone modelling has been used to model the process of pressure driven, hydrostatic hydraulic fracture of crevasses in ice sheets and ice shelves, coupled with nonlinear viscous ice rheologies [83]. Recently, cohesive zone modelling in ice has been extended to consider the effects of pressure driven flow and thermal processes, to study drainage of supraglacial lakes, resulting in the change in subglacial hydrology and basal friction [84].

2.2.3 Phase Field Method

The final numerical method considered in the literature is the phase field fracture method. Phase field methods are particularly advantageous, since they are based on thermodynamic principles, can capture complex, mixed-mode fracture such as bifurcation and coalescence and are independent of geometry specific weight functions. Because this method is used to simulate the propagation of crevasses in this dissertation, the formulation is described in detail in Chapter 3.

2.2.4 Summary

To summarise, the assessment of surface and basal crevasse depths has been conducted using a variety of analytical, observational and numerical methods. Surface crevasses were first studied using the Nye Zero stress method, which considers the simple criterion that a crack will cease to propagate when the tensile stress within a glacier is sufficiently balanced by the lithostatic compressive stress. This criterion is simple to implement into ice sheet models, however is only valid for densely spaced crevasses, since it ignores local stress concentrations. LEFM methods have subsequently been adopted to capture the propagation of isolated surface crevasses by considering stress intensity factors around a sharp discontinuity. However, these require appropriate weighting functions for specific geometry and boundary conditions to accurately capture crevasse growth. In recent years, numerical modelling approaches such as CDM methods and CZM have been utilised to model crack growth in glaciers. These emerging methods are popular, since they can be coupled with other multiphysics - including non-linear viscous flow and meltwater driven hydrofracture, alleviate the need for pre-existing cracks and can capture complex fracture geometries. However, these methods come at a high computational cost and rely on empirical parameters that require calibration.

Chapter 3

Theory

3.1 Phase Field Theory

The phase field method is an emerging computational framework, that applies thermodynamic principles to a fracture mechanics scenario. The method is advantageous since it can capture a wide range of advanced fracture behaviours, including crack bifurcation, coalescence of multiple cracks and initiation from arbitrary sites. Phase field modelling was initially based on brittle fracture in elastic media by Bourdin et al [85], Francfort & Marigo [86] and Miehe [87], but the mathematical formulation can also be adapted to incorporate and solve for various multi-physics problems. Recent applications include ductile and brittle fracture [88, 89], functionally graded materials [90], composites [91, 92, 93], shape memory alloys [94, 95], rock fracture and poroelastic media [96, 97, 98, 99], hydrogen embrittlement [100, 101], corrosion damage [102, 103, 104], fatigue damage [105, 106], battery degradation [107, 108, 109] and dynamic fracture [110]. However, the phase field method is a novel approach to ice shelf fracture.

In this current chapter, the derivation of the phase field formulation for fracture is presented. Section 3.1.1 presents the original formulation, considering the energy based approach for a brittle elastic solid and Section 3.1.2 considers the adaptation for a stress based crack driving force D_{d}. A discussion of nonlinear viscous rheology is found in Section 3.2, while Section 3.3 presents the poro-damage mechanics approach to model meltwater driven hydrofracture. Finally, the governing equations and numerical implementation for finite element computation is presented in Section 3.4.

3.1.1 Energy Based Approach for Brittle Elastic Solids

The phase field method originates as an approximation of Griffith's energy balance, developed in the 1920s, which is regarded as one of the founding equations of fracture mechanics [111]. An arbitrary domain $\Omega \subset \mathbb{R}^n$ is first considered, in $n \in [1, 3]$ dimensions, with a volume V. A sharp crack surface Γ of surface area A within the domain is also considered, represented schematically in Figure 3.1a.

Griffith applied the first law of thermodynamics to cracks in elastic brittle solids, stating that the total potential energy Π within the system must remain constant. For an isothermal solid, the total potential energy is composed of the internal potential strain energy Ψ_{s} (a function of the strain tensor $\boldsymbol{\varepsilon}$) and the fracture energy Ψ_{f}. Griffith states that there must be sufficient strain energy stored in the solid as a result of loading, to overcome the work required to produce new fracture surfaces. Thus for a crack to propagate there must be a net decrease in internal strain energy within the system. The energy balance is illustrated thus:

$$\frac{d\Pi}{dA} = \frac{d\Psi_{\mathrm{s}}}{dA} + \frac{d\Psi_{\mathrm{f}}}{dA} = 0 \tag{3.1}$$

where the work done from external forces is excluded. This was later adapted by Francfort and Marigo who considered a variational approach to minimize the global energy of the system [86, 112], allowing for a mapping of the evolving crack surface Γ through time and space. This indicates that the critical condition for fracture to occur is when there is no net change in total potential energy [113], thus:

$$\Pi = \int_{\Omega} \Psi(\boldsymbol{\varepsilon}) \mathrm{d}V + \int_{\Gamma} G_{\mathrm{c}} \mathrm{d}\Gamma \tag{3.2}$$

where $G_{\mathrm{c}} = d\Psi_{\mathrm{f}}/dA$ is the critical energy release rate, which is a measure of a material's resistance to fracture. However, for complex crack geometries, the crack face Γ is unknown, meaning that the surface fracture energy integral cannot be evaluated.

This difficulty is overcome by introducing the phase field paradigm which includes an auxiliary parameter ϕ (known as the phase field parameter) that converts the discrete discontinuous crack into a smeared, implicit damage zone - represented by the schematic diagram in Figure 3.1b. Thus, the phase field parameter ϕ is a measure of the extent of damage within the material; ranging from $\phi = 0$ in undamaged regions to $\phi = 1$ in the fully fractured domain. The crack surface integral in Eq. (3.2) is converted into a volume integral by introducing a crack surface density functional, which allows the problem to be computationally tractable.

$$\int_{\Gamma} G_{\mathrm{c}} \mathrm{d}\Gamma = \int_{\Omega} G_{\mathrm{c}} \gamma \left(\phi, \nabla\phi\right) \mathrm{d}V \tag{3.3}$$

The crack surface density functional is a function of the phase field parameter ϕ and a length scale parameter ℓ_{c}. The form of which is inspired by the Ambrosio and Tortorelli approximation [114] of the Mumford-Shah potential [115], which is a popular functional used in image segmentation. The phase field method produces a diffusive damage region where, the width of variation in phase field parameter is governed by the length scale parameter. As the length scale para-

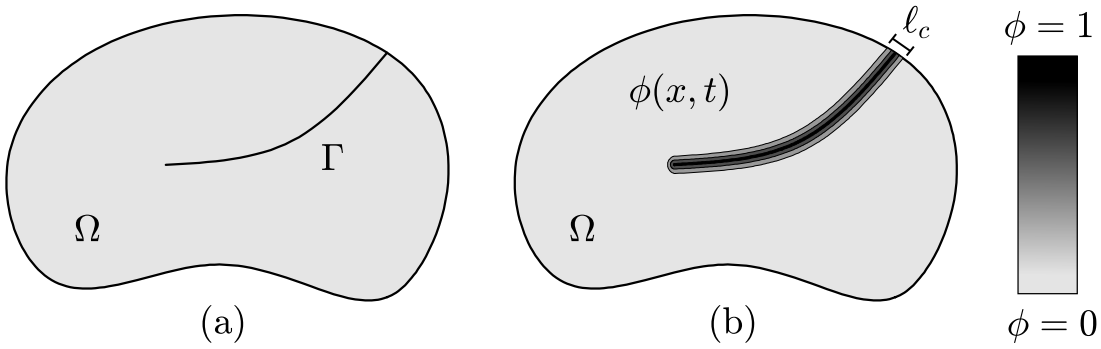

Figure 3.1: (a) Schematic diagram showing a sharp crack. (b) Schematic diagram showing a diffusive phase field crack over length scale ℓ_c.

meter $\ell_c \to 0$ the crack tends towards a sharp discontinuity and approaches the Griffith criteria (as shown in Figure 3.2), which has been demonstrated through Γ-convergence studies [116, 117]. The presence of the non-local length scale parameter ℓ_c also eliminates mesh dependency and directional mesh bias on the fracture zone if the mesh size is approximately six times smaller than the length scale parameter in the fracture zone ahead of the crack tip [118]. The variation in phase field parameter ϕ with distance away from the sharp discontinuity x is represented by an exponential equation suggested by Miehe et al [87] in Eq. (3.4).

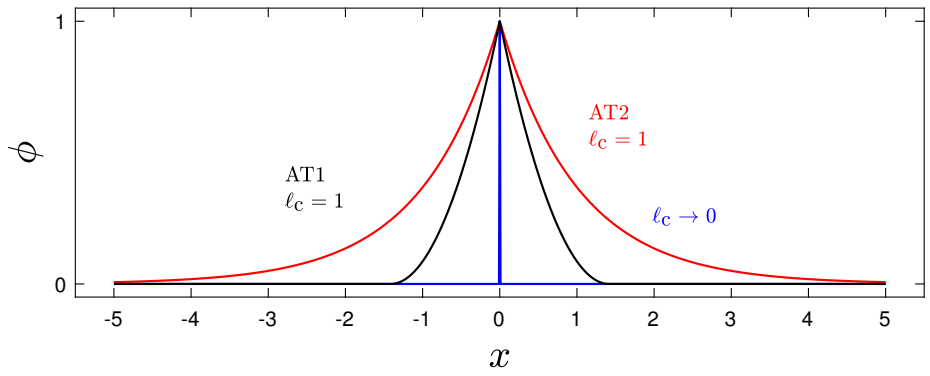

Figure 3.2: Non-dimensionalized graph showing the distribution in phase field parameter ϕ with distance away from the sharp crack for both AT1 and AT2 formulations. As $\ell_c \to 0$ the distribution tends towards the sharp crack (blue curve), whereas the diffusive crack shows an exponential distribution (red curve).

$$\phi(x) = e^{-|x|/\ell_c} \,. \tag{3.4}$$

This approximation gives a solution to a second order differential equation, used to formulate the crack surface density functional, in the form:

$$\phi(x) - \ell_c^2 \Delta\phi(x) = 0 \,, \tag{3.5}$$

where Δ is the Laplacian operator. Integrating a Galerkin - type weak form of Eq. (3.5) gives a functional $I(\phi)$, which is related to the crack surface functional by $I(\phi) = \ell_c \gamma\left(\phi, \nabla\phi\right)$.

$$I(\phi) = \frac{1}{2} \int_\Omega (\phi^2 + \ell_c^2 \left|\left|\nabla\phi\right|\right|^2) \, \mathrm{d}V \tag{3.6}$$

The crack density functional is thus derived as:

$$\gamma\left(\phi, \nabla\phi\right) = \frac{I(\phi)}{\ell_c} = \frac{1}{2\ell_c} \int_\Omega (\phi^2 + \ell_c^2 \left|\left|\nabla\phi\right|\right|^2) \, \mathrm{d}V \tag{3.7}$$

The phase field model presented above is the commonly adopted second order crack surface density functional proposed by Bourdin et al [85] and Miehe et al [87]. Here, the phase field parameter enters the crack surface density functional as a quadratic term ϕ^2 and is often referred to as the AT2 model [119]. Fourth order models have also been debated by Borden et al [88] who suggested a fourth order functional, solved through isogeometric analysis, providing greater accuracy and improved convergence rates. However, these require C^1 continuity and come at a higher computational cost.

The displacement field $\mathbf{u}$ is introduced to measure the material response to the applied loads. This is used to define the strain tensor and subsequently the strain energy density Ψ. For the current analysis, the small strain approximation

is assumed and isothermal conditions are considered. The strain tensor $\boldsymbol{\varepsilon}$ reads:

$$\boldsymbol{\varepsilon} = \frac{1}{2}\left(\nabla \mathbf{u}^{\mathrm{T}} + \nabla \mathbf{u}\right) , \tag{3.8}$$

The elastic strain energy density $\Psi(\boldsymbol{\varepsilon})_{\mathrm{e}}$ is a representation of the elastic strain energy stored within the undamaged solid and is equivalent to the area under the stress-strain response curve. For an isotropic material this is formulated thus:

$$\Psi_{\mathrm{e}}^{\pm}(\boldsymbol{\varepsilon}) = \frac{1}{2}\lambda \left\langle \mathrm{tr}\left(\boldsymbol{\varepsilon}_{\mathrm{e}}\right)\right\rangle_{\pm}^{2} + G\mathrm{tr}\left(\boldsymbol{\varepsilon}_{\mathrm{e}}^{\pm\ 2}\right) = \boldsymbol{\sigma} : \boldsymbol{\varepsilon}_{\mathrm{e}} \tag{3.9}$$

$$\lambda = \frac{E\nu}{(1+\nu)(1-2\nu)} \tag{3.10}$$

$$G = \frac{E}{2(1+\nu)} \tag{3.11}$$

where λ and G are Lamé parameters that can be written as a function of the Young's Modulus E and Poisson's ratio ν while $\mathrm{tr}\left(\boldsymbol{\varepsilon}_{\mathrm{e}}\right)$ is the trace of the elastic strain tensor.

As the solid undergoes failure, new fracture surfaces are created and dependent on the stress state, the material loses its ability to store strain energy. Crack surfaces in regions of tensile stress will not be in contact with each other and therefore loads may not be transmitted through the damaged material. Whereas crack surfaces in compressive stress are in contact, allowing for stresses to be transmitted through the crack surface, a phenomenon known as crack closure. To accommodate this, the strain energy density can be decomposed either through a spectral tension-compression split proposed by Miehe et al [87] to prevent cracking under compression, or a volumetric-deviatoric split where fracture is driven by the deviatoric component and positive volumetric component proposed by Amor et al [120]. The strain energy density split for the spectral split approach is noted by the $\pm$ symbol in Eq. (3.9), where $\boldsymbol{\varepsilon}_{\mathrm{e}}^{+}$ and $\boldsymbol{\varepsilon}_{\mathrm{e}}^{-}$ are the positive and negative

components of the elastic strain tensor respectively and $\langle x \rangle_{\pm} = (x \pm |x|)/2$.

In order to accommodate for the loss of material resistance around the crack zone under tensile stresses, a phase field degradation function $g(\phi)$ should be applied to the positive component of the elastic strain energy density, thus

$$\Psi\left(\boldsymbol{\varepsilon}\right)_{\mathrm{e}} = g(\phi)\Psi\left(\boldsymbol{\varepsilon}\right)_{\mathrm{e}}^{+} + \Psi\left(\boldsymbol{\varepsilon}\right)_{\mathrm{e}}^{-} \,. \tag{3.12}$$

The degradation function considers the constraints $g(0) = 1$, $g(1) = 0$ and $g'(1) = 0$, which are the limits for the intact and fully fractured states, and the derivative ensures that convergence occurs to a finite value. The phase field degradation function takes the form:

$$g(\phi) = (1 - \phi)^2 \,. \tag{3.13}$$

An additional small positive parameter k is added into Eq. (3.13) to prevent ill conditioning in the fully broken state. This is chosen as small as possible such that the algebraic conditioning number of the applied numerical discretization method remains well-posed for partly broken systems [87]. Finally, a local history field H_{d} is implemented by stating that the crack driving force is equal to the maximum value from previous time increments, to ensure that fracture is irreversible (i.e. the crack cannot heal):

$$H_{\mathrm{d}} = \max\left(\Psi^{+}\right) \,. \tag{3.14}$$

The weak form of the balance equation for phase field in brittle elastic solids is thus:

$$\begin{aligned} \delta\Pi = &\int_{\Omega} d(\phi)\frac{\partial\Psi^{+}}{\partial\varepsilon}\delta\varepsilon \,\mathrm{d}V + \int_{\Omega}\frac{G_{\mathrm{c}}}{\ell_{\mathrm{c}}}\left(\phi\delta\phi + \ell_{\mathrm{c}}^{2}\nabla\phi\nabla\delta\phi\right)\,\mathrm{d}V \\ &- \int_{\Omega} 2(1-\phi)\delta\phi\Psi^{+}\,\mathrm{d}V - \int_{\Omega} b\;\delta u\,\mathrm{d}V - \int_{S} t\;\delta u\,\mathrm{d}S = 0 \end{aligned} \tag{3.15}$$

The external work done by the applied body forces b or surface tractions t are

incorporated into the total potential energy ODE. Since the internal energy is produced to sustain the external loads, the external work is subtracted from the internal energy.

3.1.2 Phase Field Formulation - Stress Based Approach

The derivation of the phase field model shown in Section 3.1.1 is based on thermodynamic arguments, stating that the total potential energy is balanced between stored elastic strain energy and released fracture energy. Within the current section, a more modular and geometric approach to phase field fracture is explored, allowing for the derivation of alternative crack driving forces including a purely stress based phase field fracture formulation. This is inspired by the work of Miehe et al [121].

Here, the strong form of the phase field evolution law is considered by taking the variational derivative of the total potential energy with respect to the phase field variable ϕ, presented thus:

$$2\left(1-\phi\right)H_{\mathrm{d}} - \left(\phi - \ell_{\mathrm{c}}^{2}\Delta\phi\right) = \eta\frac{\delta\phi}{\delta t}. \tag{3.16}$$

For rate-dependent problems, this is composed of three terms: the first being the crack driving force term, responsible for damage growth; the second term being the geometric resistance of the surrounding material and the final term representing a rate-dependency, governed by an artificial phase field viscosity η. It is noted that the viscosity term is not founded from the variational derivative, instead it is a parameter added for numerical stability reasons. For rate-independent problems $\eta = 0$.

For convenience, the crack driving force D_{d} for the strain energy density based

approach is $D_{\mathrm{d}} = \left(\Psi^{+}\ell_{\mathrm{c}}\right)/G_{\mathrm{c}}$ and is thus dependent on critical energy release rate and phase field length scale. Miehe [121] suggested the introduction of a critical strain energy ψ_{c}, in order to avoid damage at low occurring stress levels. The fracture energy ψ_{f} is therefore adapted to include this critical value $\psi_{\mathrm{c}} = 3G_{\mathrm{c}}/16\ell_{\mathrm{c}}$:

$$\psi_{\mathrm{f}}\left(\phi,\, \nabla\phi\right) = 2\psi_{\mathrm{c}}\left(\phi + \frac{\ell_{\mathrm{c}}^{2}}{2}\left|\left|\nabla\phi\right|\right|^{2}\right) . \tag{3.17}$$

Unlike conventional fracture models, the phase field parameter in the crack surface functional is introduced as a linear term, resulting in a natural damage threshold, preserving elastic properties in uncracked regions. This approach is also present in the AT1 phase field model [122]. The threshold effect can be observed in the black curve in Figure 3.2, in regions away from the crack, $\phi = 0$ for the AT1 model, whereas for the AT2 model ϕ only tends toward zero. The introduction of the critical fracture energy density results in the following total potential energy:

$$\left(1-\phi\right)^{2}\left(\psi^{+}(\boldsymbol{\varepsilon}) - \psi_{\mathrm{c}}\right) + \psi_{\mathrm{c}} + 2\psi_{\mathrm{c}}\left(\phi + \frac{\ell_{\mathrm{c}}^{2}}{2}\left|\left|\nabla\phi\right|\right|^{2}\right) . \tag{3.18}$$

Taking the variational derivative with respect to the phase field parameter gives the appropriate phase field evolution law:

$$2\left(1-\phi\right)\left\langle\psi^{+}(\boldsymbol{\varepsilon}) - \psi_{\mathrm{c}}\right\rangle = 2\psi_{\mathrm{c}}\left(\phi - \ell_{\mathrm{c}}^{2}\nabla^{2}\phi\right) \quad . \tag{3.19}$$

Manipulating Eq. (3.19) provides the crack driving force, with the inclusion of the critical strain energy density.

$$D_{\mathrm{d}} = \left\langle\frac{\psi^{+}(\boldsymbol{\varepsilon})}{\psi_{\mathrm{c}}} - 1\right\rangle . \tag{3.20}$$

This threshold based approach can be adapted to consider a stress based criterion for brittle fracture. Here, the critical fracture energy density is defined, based on

the relation of Young's modulus E and critical fracture stress σ_{c}:

$$\psi_{\mathrm{c}} = \frac{\sigma_{\mathrm{c}}^2}{2E}\,, \tag{3.21}$$

while the fracturing strain energy is defined as follows:

$$\psi^{+}(\boldsymbol{\sigma}) = \frac{1}{2E}\sum_{a=1}^{3}\langle\tilde{\sigma}_{\mathrm{a}}\rangle^2\,. \tag{3.22}$$

Substituting Eq. (3.21) and Eq. (3.22) into Eq. (3.20) provides a purely stress based crack driving force for an isotropic medium, thus:

$$D_{\mathrm{d}} = \zeta\left\langle\sum_{\mathrm{a}=1}^{3}\left(\frac{\langle\tilde{\sigma}_{\mathrm{a}}\rangle}{\sigma_{\mathrm{c}}}\right)^2 - 1\right\rangle \tag{3.23}$$

Here, the principal stress $\tilde{\sigma}_{\mathrm{a}}$ in each of the three principal directions a, is compared to the material strength σ_{c}. This crack driving force function is sufficient for fractures resulting from the decohesion of surfaces perpendicular to the maximum principal stress. This also provides a quadratically increasing stress threshold for stresses above the failure surface. The inclusion of the Macaulay brackets is also noted in Eq. (3.23), since this allows for fractures to propagate as a result of tensile principal stresses only, capturing tensile-compressive asymmetric behaviour required to model glacial crevasses. In addition, it is also noted that the driving force presented in Eq. (3.23) is independent of phase field length scale ℓ_{c}. This is advantageous for solving large scale problems such as iceberg calving, because the finite element mesh has to be sufficiently refined to resolve ℓ_{c}, typically requiring element sizes six times smaller [118]. In addition, a non-dimensional multiplication parameter ζ is included into the stress based crack driving force, which influences the stress-strain response curve in the post-critical region. The effect of this is explored by considering the evolution of the phase field balance equation and crack driving force. Eq. (3.16) can therefore be arranged to find

the phase field parameter in a one-dimensional setting (i.e. $\nabla\phi = 0$):

$$\phi = \frac{2D_\mathrm{d}}{1 + 2D_\mathrm{d}}\,. \tag{3.24}$$

The damaged uniaxial stress can therefore be calculated through the following relation:

$$\sigma = (1-\phi)^2\,\sigma_0 = \left(1 - \frac{2D_\mathrm{d}}{1 + 2D_\mathrm{d}}\right)^2 E\varepsilon \tag{3.25}$$

where ε is the uniaxial strain. The uniaxial stress-strain response is plotted in Figure 3.3 for different values of post peak slope parameter ζ. Both uniaxial stress and strain are normalised with respect to the critical values at which brittle failure occurs. A linear elastic response is observed for stresses beneath the critical fracture stress σ_c, for all values of ζ, with the rate of increase in stress being independent of ζ. However, the post critical regime is sensitive to ζ, as larger values of ζ result in a less dissipative damage process. For glacial crevasse simulations, a value of $\zeta = 1$ is used, although the influence of ζ on stabilised crevasse depth is investigated in a sensitivity analysis in Section 4.3.3.

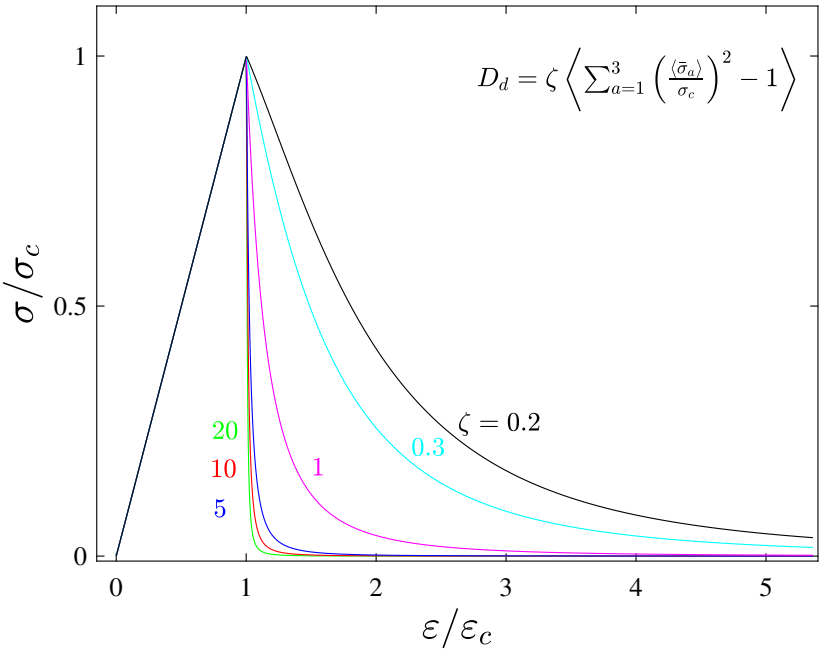

Figure 3.3: Uniaxial stress-strain response, as predicted by the stress-based phase field model adopted, showcasing the role of the post peak parameter ζ on the material's post failure behaviour.

3.2 Nonlinear viscous Rheology

The current presentation of phase field fracture has assumed a material undergoing linear elastic deformation. However, over long timescales ice sheet and ice shelf motion has been known to deform through nonlinear incompressible viscous creep flow, since glacial ice is a polycrystalline material undergoing a state of constant stress and operating close to its melting point.

Several constitutive viscoelastic models have been suggested to combine the instantaneous, recoverable elastic deformation with time dependent, permanent viscous deformation. The components of which can be visualised through a series of elastic springs and viscous dashpots elements; with different combinations representing different types of time dependent deformation. A common approach for modelling steady state creep is the use of a viscoelastic Maxwell model. Here,

the elastic spring and viscous dashpot are arranged in series, shown in Figure 3.4: The Maxwell model results in the strain field being additively decomposed into

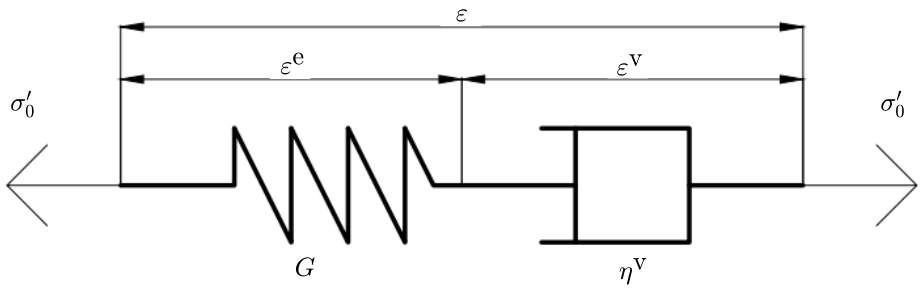

Figure 3.4: Schematic diagram of a viscoelastic Maxwell model.

elastic and viscous parts, whilst the elastic and viscous stresses are equal:

$$\boldsymbol{\varepsilon} = \boldsymbol{\varepsilon}^{\mathrm{e}} + \boldsymbol{\varepsilon}^{\mathrm{v}}\,, \tag{3.26}$$

thus, a Maxwell material held at a constant stress will result in a constant strain rate and a linear time-dependent deformation response, suitable for capturing steady state creep deformation.

The viscous contribution can be modelled through the process of creep. Creep deformation is a well documented process within glaciers and was first studied by Glen in 1955 [123], who proposed a steady state creep law based on the Bingham-Norton/Maxwell model, by which the viscous strain rates are given as

$$\dot{\boldsymbol{\varepsilon}}^{\mathrm{v}} = A\,(\sigma_{\mathrm{eq}})^{n-1}\,\boldsymbol{\sigma}_0'\,. \tag{3.27}$$

Here, A is the creep coefficient, $\boldsymbol{\sigma}_0' = \boldsymbol{\sigma}_0 - \mathrm{tr}(\boldsymbol{\sigma}_0)\boldsymbol{I}/3$ is the undamaged deviatoric stress tensor, n is the creep exponent, and σ_{eq} is an equivalent stress measure defined as $\sigma_{\mathrm{eq}} = \sqrt{\frac{1}{2}\boldsymbol{\sigma}_0' : \boldsymbol{\sigma}_0'}$. The creep coefficient A and the creep exponent n are typically calibrated with experimental or field data, with the former exhibiting

the following Arrhenius dependency with temperature:

$$A = A_0 \exp\left[\frac{Q}{R}\left(\frac{1}{T} - \frac{1}{T_0}\right)\right] . \tag{3.28}$$

Where T is the absolute temperature, Q is the activation energy, R is the universal gas constant, and A_0 is the creep coefficient at a reference temperature T_0.

The timescale at which the mechanical response transitions from linear elastic compressible to nonlinear viscous behaviour is measured by the relaxation time t_{Maxwell} of the Maxwell model, first proposed by Jellinek and Brill [124]. This is given by the ratio of ice viscosity η^{v} to elastic modulus E, where:

$$\eta^{\text{v}} = \frac{1}{2A{\sigma_{\text{eq}}}^{n-1}} , \tag{3.29}$$

$$t_{\text{Maxwell}} = \frac{2\eta^{\text{v}}\,(1+\nu)}{E} , \tag{3.30}$$

for glacial ice, the Maxwell relaxation time is in the order of $t_{\text{Maxwell}} \approx 10$ h [125]. However, the Maxwell time is highly dependent on deviatoric stress, meaning that the Maxwell relaxation time is greatly reduced in regions of high deviatoric stress, close to the crack tip. This implies that the viscous component may be influential on crevasse growth [84]. In addition, Glen's flow predicts unrealistic values of ice viscosity that approach infinity in regions of low deviatoric stress states, such as at the base of ice divides. In these regions, the linear term (i.e. $n = 1$) is expected to dominate ice behaviour [126]

The viscoelastic Maxwell model, however, neglects the contributions of primary and tertiary creep stages, which exhibit a nonlinear response. This can be captured by introducing a Burger's model which includes a Maxwell element (that controls the elastic and steady state creep response) in series with a Kelvin-Voigt element (that controls the primary creep stage which transitions between elastic

and steady state creep) [127]. However it has been shown that the retardation time of the Kelvin-Voigt element is negligible in comparison to relaxation time of the Maxwell element, and therefore can be neglected here [128].

3.3 Poro-Damage Mechanics

The modelling of meltwater pressure in crevasses is critical for obtaining accurate predictions of penetration depths. Meltwater can accumulate in damaged zones and localised pore structures, leading to additional tensile stresses that can become significant to offset the lithostatic compressive stresses. To capture this, a poro-damage mechanics method is employed, based on Terzaghi's principle of effective stress [129] and Biot's theory of poroelasticity [130]. The effective stress $\tilde{\boldsymbol{\sigma}}$ can therefore be written as:

$$\tilde{\boldsymbol{\sigma}} = \left[(1-\phi)^2 + k\right] \boldsymbol{\sigma}_0 - \left[1 - \left[(1-\phi)^2 + k\right]\right] p_{\mathrm{w}} \alpha \boldsymbol{I} \,, \tag{3.31}$$

Here, the stress is multiplied by the phase field degradation function $g(\phi)$ to remove the load carrying capacity in damaged regions and the water pressure p_{w} is multiplied by $1 - g(\phi)$ to limit the water pressure to solely within the crevasse. Thus the effective stress is an interpolation between the stress and the water pressure, an approach which has been adopted within the literature [131].

A small numerical parameter k is introduced into the degradation function to prevent ill-conditioning in the fully fractured state ($\phi = 1$). In this example, the Biot coefficient α is taken as $\alpha = 1$. It is assumed that the water pressure is hydrostatic and depth dependent. For surface crevasses, p_{w} is defined as:

$$p_{\mathrm{w}} = \rho_{\mathrm{w}} g \left\langle h_{\mathrm{s}} - (z - z_{\mathrm{s}}) \right\rangle \,, \tag{3.32}$$

where ρ_w is the density of freshwater, h_s is meltwater height and z_s is the vertical elevation of the crevasse tip from the bed, illustrated in Figure 3.5. The presence of the Macaulay brackets denotes that there is zero pressure above the meltwater height h_s. When phase field evolution is simulated, the value of z_s is updated on each time increment, defined as the minimum z-coordinate where $\phi = 1$. Consequently, the meltwater pressure extends beyond the initial notch and evolves with the propagating crevasse. For the basal crevasse, it is assumed that the crevasse is fully saturated for depths beneath the oceanwater height h_w. The oceanwater pressure takes the form:

$$p_w = -\rho_s g \langle h_w - z \rangle \tag{3.33}$$

where ρ_s is the oceanwater density. The material density ρ is interpolated based on the damage state, between glacial ice ρ_i and freshwater density ρ_w using the phase field degradation function $g(\phi)$, thus:

$$\rho = \left[(1-\phi)^2 + k\right] \rho_i + \left[1 - \left[(1-\phi)^2 + k\right]\right] \rho_w \,. \tag{3.34}$$

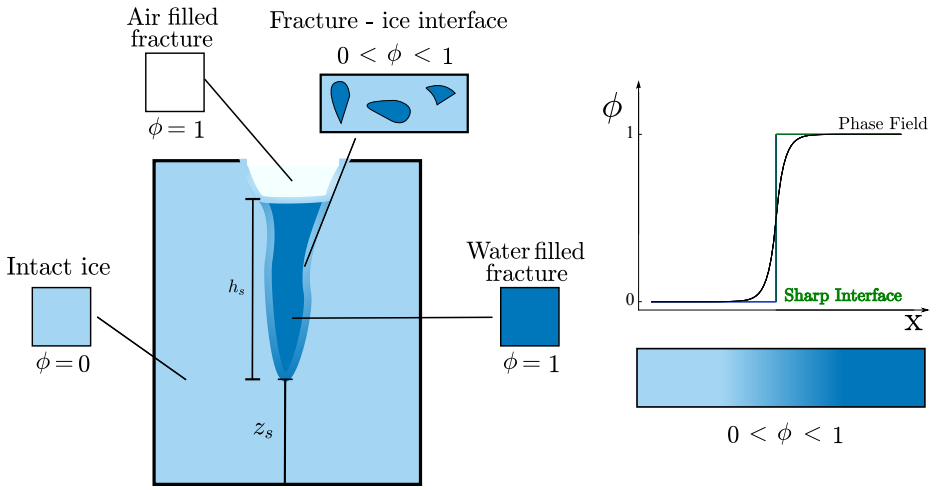

Figure 3.5: Schematic diagram of a meltwater filled crevasse in glacial ice, illustrating the intact phase ($\phi = 0$), fully cracked phase ($\phi = 1$) and transition phase ($0 < \phi < 1$). In the damaged and transition phases, there is a hydrostatic pressure contribution to damage arising from the meltwater. Relevant to the poro-damage part of the model, h_s denotes the meltwater depth, and z_s is the distance between the glacier base and the bottom of the crevasse, with z being the vertical height.

3.4 Numerical Implementation in COMSOL Multiphysics

The phase field method for brittle materials provides a fully coupled system of equations that need to be solved; these being the static equilibrium conditions for degraded stress:

$$\nabla \cdot \left\{ \left[(1-\phi)^2 + k \right] \boldsymbol{C}_0 \left(\boldsymbol{\varepsilon} - \boldsymbol{\varepsilon}^v \right) - \left[1 - \left[(1-\phi)^2 + k \right] \right] p_\mathrm{w} \boldsymbol{I} \right\} + \mathbf{b} = \rho \ddot{\mathbf{u}} \quad \text{in} \quad \Omega \,. \tag{3.35}$$

and the balance equation for the phase field:

$$-2\,(1-\phi) \max_{\tau \in [0,t]} \zeta \left\langle \sum_{a=1}^{3} \left(\frac{\langle \tilde{\sigma}_a \rangle}{\sigma_\mathrm{c}} \right)^2 - 1 \right\rangle + \left(\phi - \ell_\mathrm{c}^2 \nabla^2 \phi \right) = \eta \frac{\delta \phi}{\delta t} \quad \text{in} \quad \Omega \,. \tag{3.36}$$

where $\boldsymbol{C}_0$ is the fourth order elastic stiffness tensor. This generates two sets of dependent field variables, these being the displacement field $\mathbf{u}$ and the cracked phase

field ϕ. Owing to the coupled nature of the problem, a closed form solution does not exist, thus the commercial finite element package COMSOL Multiphysics is used to compute a numerical solution. COMSOL consists of application specific physics modules that can be combined together to solve multiphysics problems. The main modulues utilised within this work are Solid Mechanics, Damage and Creep. Within the Damage module, the phase field parameter ϕ is established and is updated through the phase field evolution law in Eq. (3.36). The crack driving force is also established within the damage module and is defined based on principal tensile stresses, shown in Eq. (3.23). COMSOL also implements a history variable, which stores the maximum value of the crack driving force within previously solved solutions to prevent damage reversibility and is updated after every iteration. The Solid Mechanics module is implemented to solve for the displacements $\boldsymbol{u}$, with the default material response being linear elastic. Sub-modules are also added, including creep, where the non-linear viscous response is defined through a Maxwell model and the meltwater pressure is also defined using a body force, which is updated after every numerical iteration as the crack evolves.

The domain is spatially discretised using a finite element mesh, with the solutions of the dependent variables being approximated at mesh nodes by numerical methods, using the weak forms of the governing equations. Intermediate values are found by interpolating between the nodal values using shape functions thus:

$$\mathbf{u} = \sum_{i=1}^{q} \boldsymbol{N}_i^u \mathbf{u_i}\,, \qquad\qquad \phi = \sum_{i=1}^{q} N_i^\phi \phi_i\,, \tag{3.37}$$

where q is the number of nodes per element, N_i is the shape function at node i, $\mathbf{u_i} = [u_x, u_y]^T$ and ϕ_i are the displacement and phase field variables at node i respectively. The accuracy of the solution is improved by either increasing the number of mesh nodes (reducing the mesh element size) or increasing the order

of the shape function. For a single node in the 2D plane strain case, the shape function matrix is given as:

$$\boldsymbol{N}_i^u = \begin{bmatrix} N_{i,x} & 0 & 0 \\ 0 & N_{i,y} & 0 \\ 0 & 0 & N_{i,z} \end{bmatrix} . \tag{3.38}$$

The gradients of the dependent variables are found using the derivative of the shape functions:

$$\boldsymbol{\varepsilon} = \sum_{i=1}^{q} \boldsymbol{B}_i^u \mathbf{u_i} \,, \qquad\qquad \nabla\phi = \sum_{i=1}^{q} \boldsymbol{B}_i^\phi \phi_i \,, \tag{3.39}$$

$$\boldsymbol{B}_i^u = \begin{bmatrix} \partial N_i/\partial x & 0 & 0 \\ 0 & \partial N_i/\partial y & 0 \\ 0 & 0 & \partial N_i/\partial z \\ \partial N_i/\partial x & \partial N_i/\partial y & 0 \\ \partial N_i/\partial x & 0 & \partial N_i/\partial z \\ 0 & \partial N_i/\partial y & \partial N_i/\partial z \end{bmatrix} , \qquad \boldsymbol{B}_i^\phi = \begin{bmatrix} \partial N_i/\partial x \\ \partial N_i/\partial y \\ \partial N_i/\partial z \end{bmatrix} . \tag{3.40}$$

Substituting these definitions into the weak form of the stress equilibrium equation gives the residual with respect to the displacement field

$$\boldsymbol{r}_i^u = \int_\Omega [(1-\phi)^2 + k](\boldsymbol{B}_i^u)^T \boldsymbol{\sigma_0} \, \mathrm{d}V - \int_\Omega (\boldsymbol{N}_i^u)^T \boldsymbol{b} \, \mathrm{d}V - \int_S (\boldsymbol{N}_i^u)^T \boldsymbol{t} \, \mathrm{d}S \,. \tag{3.41}$$

Similarly, the residual for the phase field with respect to the phase field variable is defined as:

$$\boldsymbol{r}_i^\phi = \int_\Omega \left\{ -2\,(1-\phi)\, N_i^\phi \; H_\mathrm{d} + \left[\phi \; N_i^\phi + \ell_c^2 \left(\boldsymbol{B}_i^\phi \right)^T \nabla\phi \right] \right\} \, \mathrm{d}V \,. \tag{3.42}$$

Where H_{d} is the maximum value of the crack driving force D_{d}. The numerical solutions are obtained for $\boldsymbol{r}_i^u = 0$ and $\boldsymbol{r}_i^\phi = 0$ using an incremental iterative Newton-Raphson scheme, with an implicit backward differential formula (BDF) time-stepping scheme being employed to solve each set of equations, in a Backward Euler fashion.

When solving for the dependent variables, a staggered solver approach is implemented, where the system is decoupled and the dependent variables are solved separately (as opposed to a monolithic approach, where the coupled set of equations are solved simultaneously). Staggered solvers may be either single pass (one iteration) or multi-pass (alternate minimisation) approaches, with the former requiring sufficiently small time increment sizes to maintain equilibrium. Multi-pass staggered solvers alleviate the need for small increments by including multiple iterations within a single time increment. This is a more advantageous approach compared to the monolithic scheme, since convergence is faster, more stable and robust. The solving process is as follows:

1. The initial values of the displacement field $\mathbf{u}_n$ and phase field parameter ϕ_n at time t_n are known.

2. The prescribed loads at time t_{n+1} are calculated and the updated displacement field $\mathbf{u}_{n+1}$ is found by minimising the static stress equilibrium equation using the initial crack phase field ϕ_n: $\boldsymbol{K}_{\boldsymbol{ij}}^{\boldsymbol{uu}}\boldsymbol{u}_{n+1} = \boldsymbol{r}_i^u\left(\phi_n\right)$

3. The updated values of the phase field ϕ_{n+1} are then computed by using the updated displacement field $\mathbf{u}_{n+1}$, by minimising the phase field evolution law: $\boldsymbol{K}_{\boldsymbol{ij}}^{\boldsymbol{\phi\phi}}\phi_{n+1} = \boldsymbol{r}_i^\phi\left(\boldsymbol{u}_{n+1}\right)$

4. The relative errors between the initial and updated variables are then calculated.

5. If the relative errors are greater than the specified tolerance, another numerical iteration is taken.

6. If the relative errors are less than the specified tolerance, or the maximum number of iterations N is reached, the solution is considered to be converged and the time increment is evolved (i.e. $n+1 \rightarrow n$).

Here, $\boldsymbol{K_{ij}^{uu}}$ and $\boldsymbol{K_{ij}^{\phi\phi}}$ are the tangent stiffness matrices, evaluated by taking the derivative of the residual $\boldsymbol{r}_i^u$ and $\boldsymbol{r}_i^\phi$ respectively.

$$\boldsymbol{K_{ij}^{uu}} = \frac{\partial \boldsymbol{r}_i^u}{\partial \boldsymbol{u_j}} = \int_\Omega [(1-\phi)^2 + k](\boldsymbol{B}_i^u)^T \boldsymbol{C}_0 \boldsymbol{B}_j^u \, \mathrm{d}V \,. \tag{3.43}$$

$$\boldsymbol{K_{ij}^{\phi\phi}} = \frac{\partial \boldsymbol{r}_i^\phi}{\partial \phi_j} = \int_\Omega \left\{ [2H_\mathrm{d} + 1] \, N_i^\phi N_j^\phi + \ell_c^2 \left(\boldsymbol{B}_i^\phi\right)^T \left(\boldsymbol{B}_j^\phi\right) \right\} \, \mathrm{d}V \,. \tag{3.44}$$

In order to validate the finite element implementation, a benchmark example of fracture was conducted, considering a thin square plate with a single edge notch, firstly undergoing uniaxial tension, then loaded under remote shear, with the results being presented in Appendix A. The numerical framework presented in this current chapter is also used to conduct the glacier crevasse propagation studies presented in Chapter 4.

Chapter 4

Propagation of Crevasses in Grounded Glaciers and Floating Ice Shelves

In the present chapter, the numerical results for a series of 2D and 3D benchmark case studies are presented for crevasse growth in grounded glaciers and floating ice shelves. Here, damage evolution studies are executed using the phase field fracture model developed in Section 3.1.2 to obtain stabilised crevasse depth results. These are compared to analytical solutions such as linear elastic fracture mechanics (LEFM) and Nye Zero Stress results. This comparison will confirm the accuracy of phase field models, and show when LEFM models are appropriate, or where phase field models are required to predict crevasse formation.[1]

[1]The work reported in this section has been published in Engineering Fracture Mechanics [132]

4.1 Geometry and Boundary Conditions

For 2D examples, a glacier with an idealised rectangular geometry of length $L = 500$ m and thickness $H = 125$ m is considered, illustrated in Figure 4.1a. It is assumed that the out-of-plane dimension is much larger than the glacier length, and so the plane strain assumption can be adopted (i.e. $\varepsilon_{yy} = 0$). Lateral shear is neglected, and for simplicity, the domain is restricted to a flow line near the terminus, with x and z representing the along-flow and vertical coordinates respectively. Damage is initialised by introducing a rectangular notch of depth $d_s = 10$ m and width $b = 2.5$ m. For the current study, a grounded glacier undergoing free slip conditions is assumed, therefore restraining only vertical displacement at the base. The displacement normal to the far left terminus is restrained to prevent free body motion in the horizontal direction, while the upper surface representing the atmosphere-ice interface is defined as a free surface. The material properties assumed presently are reported in Table 4.1 along with the densities of oceanwater and meltwater.

Material parameter	Magnitude	Source
Young's modulus, E [MPa]	9500	[133]
Poisson's ratio, ν [-]	0.35	[133]
Density of glacial ice, ρ_i [kg/m^3]	917	[134]
Density of meltwater, ρ_w [kg/m^3]	1000	[134]
Density of seawater, ρ_s [kg/m^3]	1020	[134]
Fracture toughness, K_{Ic} [MPa$\sqrt{\text{m}}$]	0.10	[135]
Critical fracture stress, σ_c [MPa]	0.1185	[136]
Creep exponent, n [-]	3	[72]
Creep coefficient A [MPa^{-n}s^{-1}]	7.156 $\times 10^{-7}$	[137]
Numerical parameter	**Magnitude**	
Refined mesh size, h_c [m]	0.15	
Damage evolution time increment, t [s]	0.01	
Number of multi-pass iterations, N [-]	3	

Table 4.1: Material properties assumed presently (unless otherwise stated). The values are chosen to characterise the behaviour of glacial ice, with the final column denoting the relevant reference.

Gravitational body forces are applied in the z-direction, and for isotropic, homogeneous glacial ice gives a magnitude of $\rho_{\mathrm{i}}g$. A Neumann-type traction is applied normal to the far right terminus, representing the oceanwater pressure at the ice-ocean interface. This hydrostatic pressure varies linearly with depth and takes the form $\rho_{\mathrm{s}}g\left\langle h_{\mathrm{w}}-z\right\rangle$, with the Macaulay brackets eliminating a pressure above the oceanwater surface. Meltwater pressure is applied as a Neumann-type traction to the initial crevasse walls in the form of $\rho_{\mathrm{w}}g\left\langle h_{\mathrm{s}}-(z-z_{\mathrm{s}})\right\rangle$, where d_{s} is the surface crevasse depth, h_{s} is the meltwater height above the crevasse tip and z_{s} is the elevation of the crevasse tip. As damage propagates beyond the initial specified notch, the meltwater pressure is modelled using poro-damage mechanics as described in Section 3.3 and h_{s} and z_{s} are updated after every numerical iteration to evolve with the fracture propagation. A visual representation of the applied loading and boundary conditions can be found in Figure 4.1a. An estimate of the phase field length scale, which plays a negligible role in this model, can be obtained through the Hillerborg relation [138], which for plane strain reads: $\ell_{\mathrm{c}}=(1-\nu^2)K_{\mathrm{Ic}}^2/\sigma_{\mathrm{c}}^2$. Considering the toughness of glacial ice ($K_{\mathrm{c}}=0.1\mathrm{MPa}\sqrt{\mathrm{m}}$), this gives a magnitude of $\ell_{\mathrm{c}}=0.625$ m, which is the value adopted here (unless otherwise stated). The domain is discretised numerically using a finite element mesh, with elements being refined along the expected crack path. In order to achieve mesh independent results, an element size smaller than 4 times the phase field length scale ℓ_{c} should be selected, giving a refined mesh size of $h_{\mathrm{c}}=0.15$ m. The finite element mesh used for the numerical analysis in Section 4.3 consists of approximately 200,000 quadrilateral quadratic elements and is shown in Figure 4.1b.

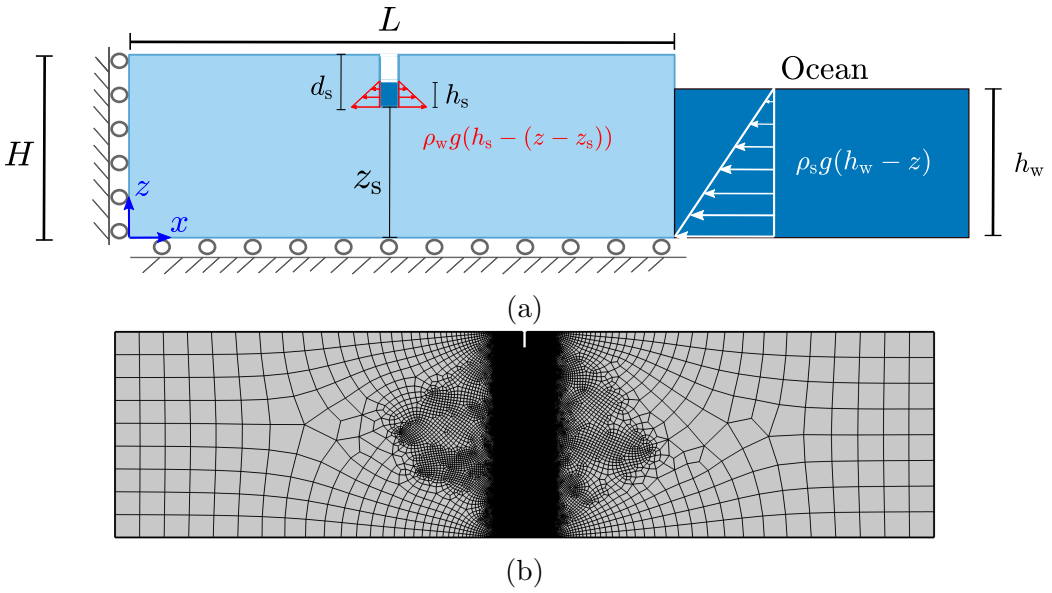

Figure 4.1: Crevasse growth in a grounded glacier: (a) diagram showing the boundary conditions of a grounded glacier containing a single surface crevasse, and (b) finite element mesh employed, with the mesh refined along the expected crevasse propagation path.

4.2 Stress state within a grounded glacier

Prior to introducing damage, the stress states of a pristine grounded glacier are considered without any initial notches, which are land terminating ($h_w = 0$) and ocean terminating ($h_w = 0.5H$). For this instance, ice is assumed to behave as a linear elastic compressible material ($\nu = 0.35$). The important variables considered are the longitudinal (horizontal) stress states σ_{xx} and the phase field crack driving force D_d. Values obtained for these variables from COMSOL Multiphysics are presented in Figure 4.2. It can be observed that there is an edge effect present at the far right terminus for σ_{xx}. However, away from the terminus in the 'far field' region, the longitudinal stress field is invariant with x-coordinate, owing to the idealised geometry. Maximum tensile stresses are present at the uppermost surface of the glacier and become more compressive with depth in a linear fashion, until maximum compressive stresses are achieved at the base. For land terminating glaciers, the distribution of longitudinal stress is symmetric

about the centreline $z = H/2$ (illustrated in Figure 4.2a). The effect of including the oceanwater pressure can be observed by comparing the stress contours in Figure 4.2a and Figure 4.2b. Here, the oceanwater pressure provides a compressive stress that is constant, which offsets the contribution from gravitational loading. This compressive stress is dependent on oceanwater height h_{w} and, if significantly large, can result in the glacier to become buoyant, hence forming a floating ice shelf/tongue. Numerical values of the far field longitudinal stress can be verified with the analytical solution,

$$\sigma_{xx} = \frac{\nu}{1-\nu}\left[\rho_{\mathrm{i}} g\left(z - \frac{H}{2}\right)\right] - \frac{1}{2}\rho_{\mathrm{s}} g \frac{h_w^2}{H} \tag{4.1}$$

where ν is the Poisson's ratio, ρ_{i} is the density of fully consolidated ice, g is the gravitational acceleration, z is the vertical co-ordinate, H is the glacier thickness, ρ_{s} is the density of oceanwater, and h_{w} is the oceanwater height; with good agreement being shown between the two methods. A derivation of the analytical stress for homogeneous glacial ice can be found in Appendix B.

The distribution of vertical stress σ_{zz} for both land and ocean terminating glaciers is shown in Figure 4.2c and Figure 4.2d respectively. As expected, the vertical stress is independent of horizontal position, as well as ocean water height h_{w}. The vertical stress is compressive throughout the entire geometry due to the applied gravitational body force. This varies linearly with depth, and can be modelled:

$$\sigma_{zz} = -\rho_{\mathrm{i}} g\,(H - z) \tag{4.2}$$

The in-plane shear stresses σ_{xz} are also reported in Figure 4.2e and Figure 4.2f. It is observed that the magnitude of in-plane shear stress is comparatively small, with concentrations occurring close to the glacier front.

The phase field crack driving force contours D_{d} are presented in Figure 4.2g and Figure 4.2h, defined by Eq. (3.23). A non-zero distribution of crack driving force is observed in tensile regions only, with the maximum value being achieved at the upper surface and a value of zero achieved in compressive regions. This is owing to tensile principal stresses above the material strength solely contributing to damage (see Eq. (3.23)). The driving force distribution is as expected, since vertical stresses are compressive throughout the entire ice sheet, therefore any damage propagation should be mode I, driven by the longitudinal stress σ_{xx}. This is consistent with linear elastic fracture mechanics (LEFM) predictions.

This is in contrast to various strain energy based approaches [131], where non-zero values of crack driving force are found in compressive regions. This is owing to the vertical strain ε_{zz} being compressive throughout the entire domain, and as a result of the Poisson effect, longitudinal strain ε_{xx} is tensile everywhere. The driving force is dictated by the trace of $\langle\varepsilon\rangle^2$ which is positive throughout the entire domain, leading to a non-zero crack driving force everywhere. It is therefore concluded that the phase field crack driving force based on the principal stress criterion is appropriate for capturing the tension-compression asymmetric behaviour of ice required to model crevasse propagation accurately, driven by tensile longitudinal stress states.

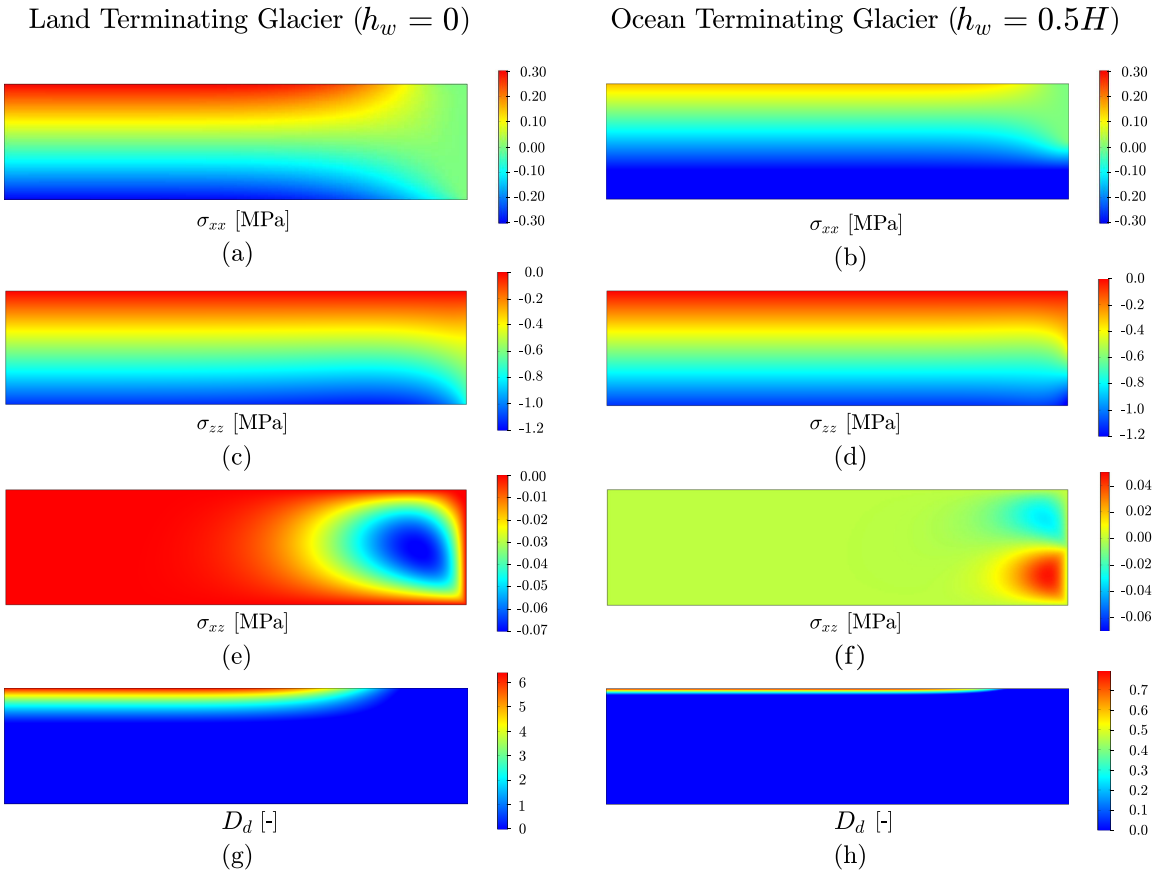

Figure 4.2: Contours of the longitudinal stress σ_{xx}, (a) and (b), vertical stress σ_{zz}, (c) and (d), in-plane shear stress σ_{xz}, (e) and (f) and the crack diving force state function D_{d}, (g) and (h), for a pristine grounded, land terminating glacier ($h_{\mathrm{w}} = 0$) and an ocean terminating glacier ($h_{\mathrm{w}} = 0.5H$).

4.3 Propagation of isolated surface crevasses in grounded glaciers

The propagation of an isolated surface crevasse in a grounded glacier is now considered. Damage is initiated by specifying a rectangular notch of height $d_{\mathrm{s}} = 10$ m and width $b = 2.5$ m at the mid-length of the upper surface. A damage threshold F^{th} is introduced to this idealised scenario, below which $D_{\mathrm{d}} = 0$. This is to assist in localisation of damage nucleation directly beneath the crevasse, facilitating comparisons with LEFM. The value of F^{th} is determined by the maximum value of D_{d} predicted in the pristine (unnotched) glacier simulation. However, it is established in [131] and Section 4.3.3 that the magnitude of damage threshold does not influence the final stabilised crevasse depth.

The finite element analysis is initiated by determining the stress state without the presence of damage. The results from this study are used to initialise a time dependent simulation used to capture damage evolution. Here, the multi-pass staggered solver is used to solve for values of displacement u and phase field parameter ϕ over 100 time increments. For each simulation, the meltwater depth ratio $h_{\mathrm{s}}/d_{\mathrm{s}}$ is kept at a constant value (i.e. the meltwater depth increases proportionally with crevasse depth) to quantify the amount of meltwater within the crevasse. This approach was adopted due to being commonplace within the surrounding literature [131, 72]. The evolving crevasse depth d_{s} is measured at every time increment within COMSOL by calculating the lowest vertical coordinate at which the phase field parameter $\phi = 1$. This allows for z_{s} to be updated and for the meltwater pressure in Eq. (3.33) to evolve with the crack tip and extend into damaged regions. Alternatively, the meltwater height h_{s} could have been held constant, to indicate a fixed head of meltwater pressure within a crack and sensitivity analyses conducted to determine the influence of meltwater height h_{s}

on the stabilised crevasse penetration depth.

A parametric analysis is conducted for selected values of oceanwater height ($h_{\mathrm{w}} = \{0.0H, 0.5H, 0.9H\}$) and meltwater depth ratios ($h_{\mathrm{s}}/d_{\mathrm{s}} = \{0.0, 0.1, 0.2, 0.3, 0.4, 0.5, 0.6, 0.7, 0.8, 0$ to determine the effect on final crevasse depth. The stabilised crevasse depths predicted by the phase field are compared to analytical results obtained from linear elastic fracture mechanics using the 'double edge cracks' formulation, presented in Appendix C. This study is performed for both linear elastic and nonlinear viscous rheologies.

4.3.1 Isolated surface crevasses-linear elastic rheology

A linear elastic compressive rheology for a grounded glacier is initially considered, to validate the model predictions with those obtained using analytical LEFM methods. Phase field predictions of normalised crevasse depth versus time for an oceanwater height of $h_{\mathrm{w}} = 0.5H$ are shown in Figure 4.3a. It can be seen that crevasses propagate rapidly beyond the initial notch and stabilise to a constant depth, with each curve representing a specific meltwater depth ratio. A plot of normalised crevasse depth versus meltwater depth ratio can be found in Figure 4.3b for both LEFM and phase field predictions for oceanwater heights of $h_{\mathrm{w}} = \{0.0H, 0.5H, 0.9H\}$. The normalised crevasse depths predicted by the phase field model are in very good agreement with those predicted by LEFM for all values of meltwater depth ratios and oceanwater height. It can be seen that land terminating glaciers ($h_{\mathrm{w}} = 0.0H$) are susceptible to full thickness fracture propagation, regardless of meltwater depth ratio, due to insufficient compressive stress being provided by the oceanwater at the far terminus. The crevasse depth begins to reduce with the increase in oceanwater height h_{w}. For instance, a dry crevasse with an oceanwater height of $h_{\mathrm{w}} = 0.5H$ propagates to 37.8% of

the glacier thickness. The influence of meltwater depth ratio on stabilised crevasse depth can be observed in intermediate oceanwater heights, where a gradual increase in penetration depth is recorded for meltwater depth ratios less than 0.5. Full thickness penetration is achieved with a meltwater depth ratio of 0.5 or higher.

For the near floatation glacier ($h_{\mathrm{w}} = 0.9H$), the compressive stress is sufficiently large enough to offset the tensile regions in the upper surface, therefore damage does not propagate beyond the initial specified notch, regardless of meltwater depth ratio.

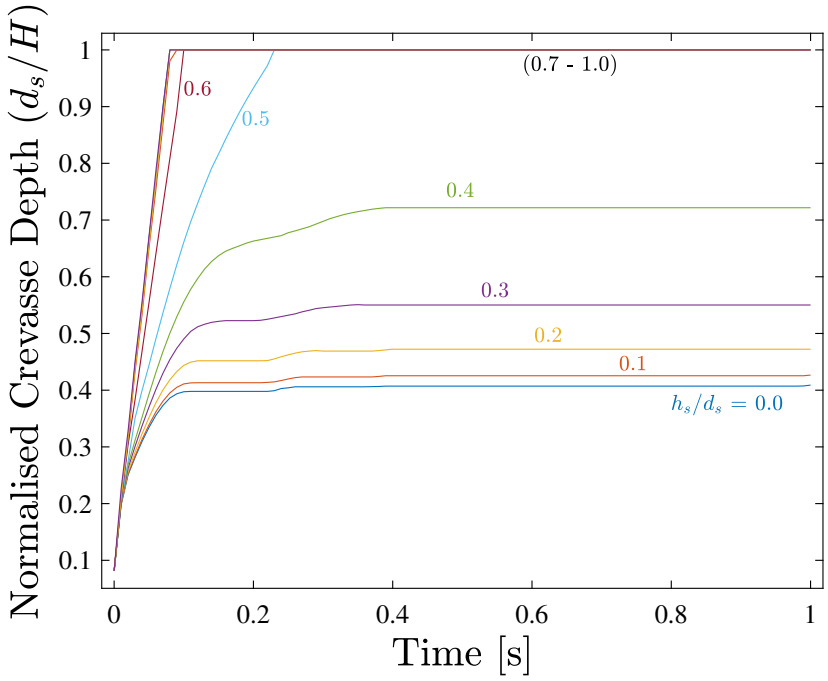

(a)

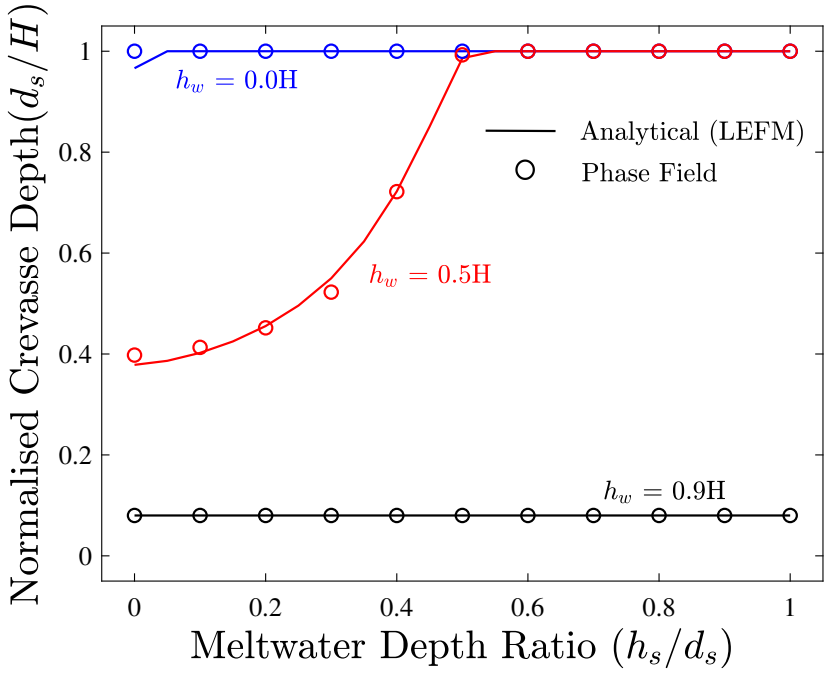

(b)

Figure 4.3: Crevasse growth in a grounded glacier. Normalised crevasse depth predictions (d_s/H) for a single isolated crevasse in a linear elastic ice sheet: (a) phase field predictions of normalised crevasse depth versus time; and (b) phase field and analytical LEFM predictions of normalised crevasse depth versus meltwater depth ratio (h_s/d_s) as a function of the oceanwater height h_w.

The process of crevasse growth is shown in Figure 4.4, through plots of phase field ϕ contours at selected time intervals. Here, blue regions represent intact ice ($\phi = 0$), whilst red regions represent the fully fractured domain ($\phi = 1$). The results correspond to the case of a meltwater depth ratio of $h_s/d_s = 0.2$ and an oceanwater height of $h_w = 0.5H$, but the qualitative behaviour is the same in all cases. A sharp mode I crack propagates vertically downwards, directly below the initial crevasse until it reaches the region where the compressive stresses are sufficiently large to arrest the crack.

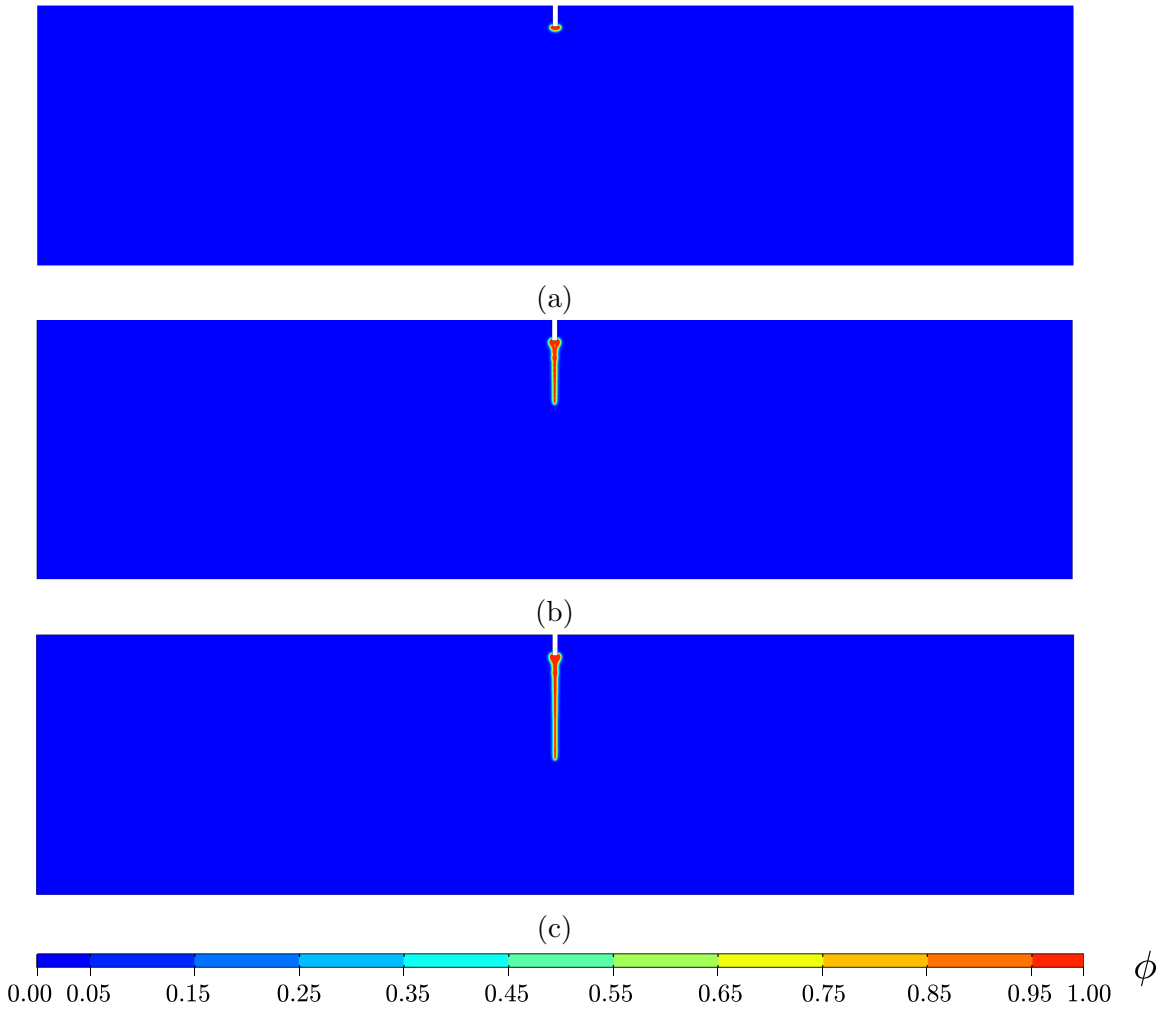

Figure 4.4: Crevasse growth in a grounded glacier. Phase field damage evolution as a function of time: (a) t = 0.00 s, (b) t = 0.02 s, and (c) t = 0.40 s. The results correspond to the case of a meltwater depth ratio of $h_s/d_s = 0.2$ and an oceanwater height of $h_w = 0.5H$, assuming a linear elastic compressible rheology.

The fracture process from the current study may be reconciled with a single

seasonal cycle of melt accumulation, where meltwater will drain into the crevasse from firn aquifers, and the crevasse will grow accordingly to a new stabilised penetration depth. This crack growth may further increase and potentially lead to full thickness crevasse propagation, if the flow of meltwater into the crevasse increases, or is sufficiently large. Alternatively, the crack may undergo crevasse closure during the winter months, when meltwater accumulation rates reduce; depending on the stress state, the location within the ice sheet, the ice flow and ambient temperature. However, it may be possible that crevasses which appear stable after a single seasonal cycle of meltwater, may culminate in full thickness rift propagations after multiple cycles of meltwater seasons (similar to the process of fatigue in metallic materials).

4.3.2 Isolated surface crevasses – nonlinear viscous rheology

The influence of ice rheology on the stabilised crevasse depth is now investigated, by considering nonlinear viscous deformation through Glen's flow law - presented in Section 3.2. Here, a time dependent creep study is conducted, without the presence of phase field damage to develop a steady-state stress profile within the glacier. The results of the creep study are subsequently used to initialise the phase field model and simulate crevasse propagation studies, based on the incompressible viscous stress state. The results of the normalised penetration depth versus time, predicted by the phase field model, for a nonlinear viscous rheology are presented in Figure 4.5a, for an isolated surface crevasse of oceanwater height $h_{\mathrm{w}} = 0.5H$ and varying values of meltwater depth ratio $h_{\mathrm{s}}/d_{\mathrm{s}}$. Similarly to the linear elastic case, damage propagates vertically downwards in a mode I manner, with crevasses growing rapidly and stabilising to a constant depth. The inclusion of meltwater results in a deeper crevasse, with penetration depths becoming progressively larger with meltwater increment. Full thickness propagation is achieved with a minimum meltwater depth ratio $h_{\mathrm{s}}/d_{\mathrm{s}}$ of 0.5. The stabilised crevasse depths are plotted against meltwater depth ratio, and compared with the analytical LEFM solutions in Figure 4.5b. It is observed that neglecting the inclusion of nonlinear viscous deformation results in an underestimation in stabilised crevasse depth, due to stresses becoming more extensional in the upper strata when considering creep contributions. An isolated dry crevasse within a grounded glacier is expected to propagate to 65.6% of the glacier thickness when considering nonlinear viscous deformation, compared to 37.8% of the glacier thickness for a linear elastic rheology. It is also found that the phase field predictions that consider nonlinear viscous deformation (with $\nu = 0.35$) are in close agreement to the LEFM predictions when considering an incompressible stress state ($\nu = 0.5$).

First order estimates obtained from analytical LEFM approaches should consider a Poisson's ratio of $\nu = 0.5$ to avoid under-predicting the impact of meltwater on ice sheet stability. The present findings are consistent with the calculations by Plate et al. [139], where Poisson's ratio was found to have a notable influence on the fracture driving force for elastic ice sheets.

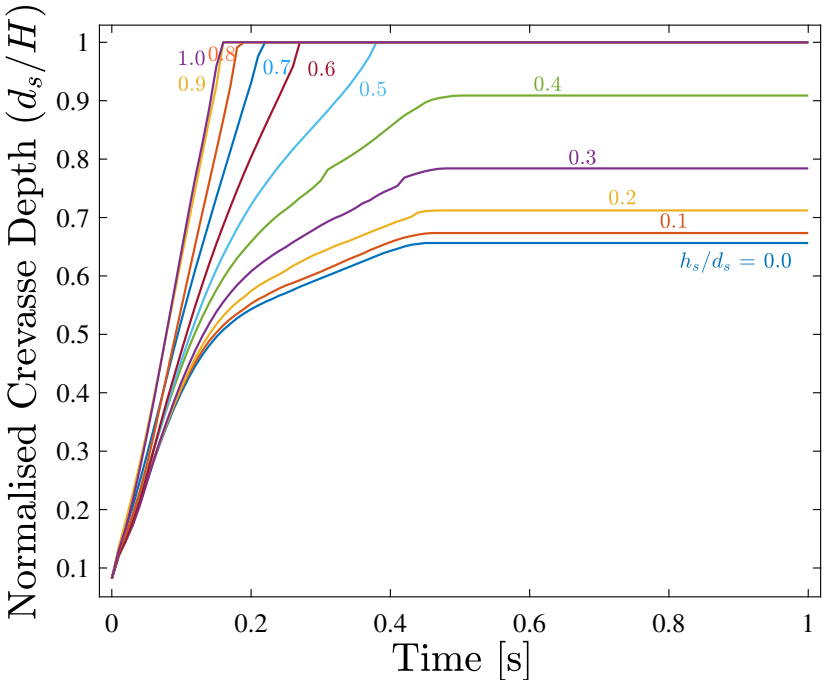

(a)

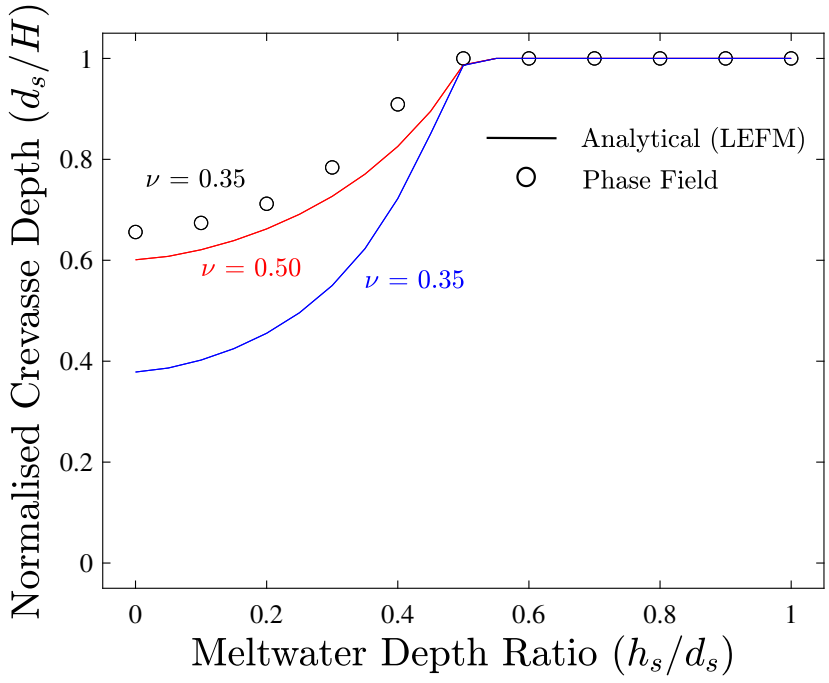

(b)

Figure 4.5: Crevasse growth in a grounded glacier. Normalised crevasse depth predictions for a single isolated crevasse assuming a nonlinear viscous rheology: (a) phase field predictions of normalised crevasse depth (d_s/H) versus time; and (b) phase field and analytical LEFM predictions of normalised crevasse depth versus meltwater depth ratio (h_s/d_s) as a function of the oceanwater height h_w. The LEFM predictions are shown for both compressible ($\nu = 0.35$) and incompressible ($\nu = 0.5$) constitutive behaviour.

4.3.3 Sensitivity analysis of model parameters

In order to test the validity of the produced results, a series of sensitivity analyses on material, numerical and fracture parameters are conducted. The base model considered is a dry isolated surface crevasse, with an oceanwater level of $h_{\mathrm{w}} = 0.5H$ and a linear elastic compressible rheology. Here, the influence of varying critical fracture stress σ_{c}, the crack driving force threshold F^{Th}, phase field post peak slope parameter ζ, number of solver iterations N, mesh size h_{c} and phase field length scale ℓ_{c} are discussed. When considering variations in a particular parameter, all other parameters are kept at constant values, as reported in Table 4.1.

Plots of normalised crevasse depth versus time are presented in Figure 4.6, with each subfigure representing a different sensitivity analysis. The first study considers the effect of the critical fracture stress σ_c, with results reported in Figure 4.6a. The range of values considered for $\sigma_c = \{0.1185 - 0.4740\}$ MPa since this is in accordance with the variation in experimental values of K_{IC} presented in [135, 140, 4], converted using the Hilleborg relation [138]. As expected, an increase in material strength results in a reduction in the stabilised crevasse depth, which is in agreement with LEFM crevasse depths when assuming the equivalent K_{IC} value. For the sharp crack, an increase in strength up to 4 times the original value yields a reduction of 8.48 m in penetration depth.

Variations in the crack driving force threshold F^{Th} are next considered, with results found in Figure 4.6b. Here, minimal variations in stabilised crevasse depth are found when increasing the threshold up to 7 times the original value, with a maximum percentage difference of 2.4% between values of stabilised crevasse depth. Thus the driving force threshold is used to isolate damage to directly beneath the notch only, allowing comparisons with LEFM results.

The results obtained for various values of the post-peak parameter ζ are given in Figure 4.6c. A small influence on crevasse depth is observed, with crevasses propagating deeper for higher values of ζ, as they result in higher values of D_{d} magnitude for the same level of stress. This is also consistent with the sharper drop in the stress-strain curve with increasing value of ζ as shown in Figure 3.3.

The influence of the phase field length scale ℓ_{c} on stabilised penetration depth is explored in Figure 4.6d. It is found that there is negligible influence on the final crevasse depth when increasing the length scale up to 8 times the reference value. An alteration in phase field length scale only yields a change in the width of the smeared damage region. This is advantageous for modelling fracture in glaciers, since large geometry sizes would lead to excessively high numbers of degrees of freedom. By increasing the phase field length scale, large geometry sizes can be accurately modelled without any alterations in crevasse penetration depth, whilst reducing computational cost. This is similar to the effect on the results found by Miehe, where the phase field length scale did not influence the stress-strain relation when conducting a single notch tension test with the stress based phase field approach [121].

The sensitivity to the number of numerical iterations is considered in Figure 4.6e. As stated in Section 3.4, the computational simulation of phase field evolution is conducted using a multi-pass staggered solver approach. Here, it can be seen that the dependent variables are well converged, with solution errors being below the specified relative tolerance, as there is negligible influence in crevasse depth when increasing the maximum number of solver iterations.

The final sensitivity analysis gauges the influence of refined mesh size h_{c} ahead of the projected crack path, with results shown in Figure 4.6f. It is observed

that there is minimal influence on stabilised crack depth when refining the mesh size from approximately 2 to 12.5 times less than the phase field length scale ℓ_c, yielding a percentage difference of 0.34% in crevasse depths and thus concluding that mesh independent results are achieved.

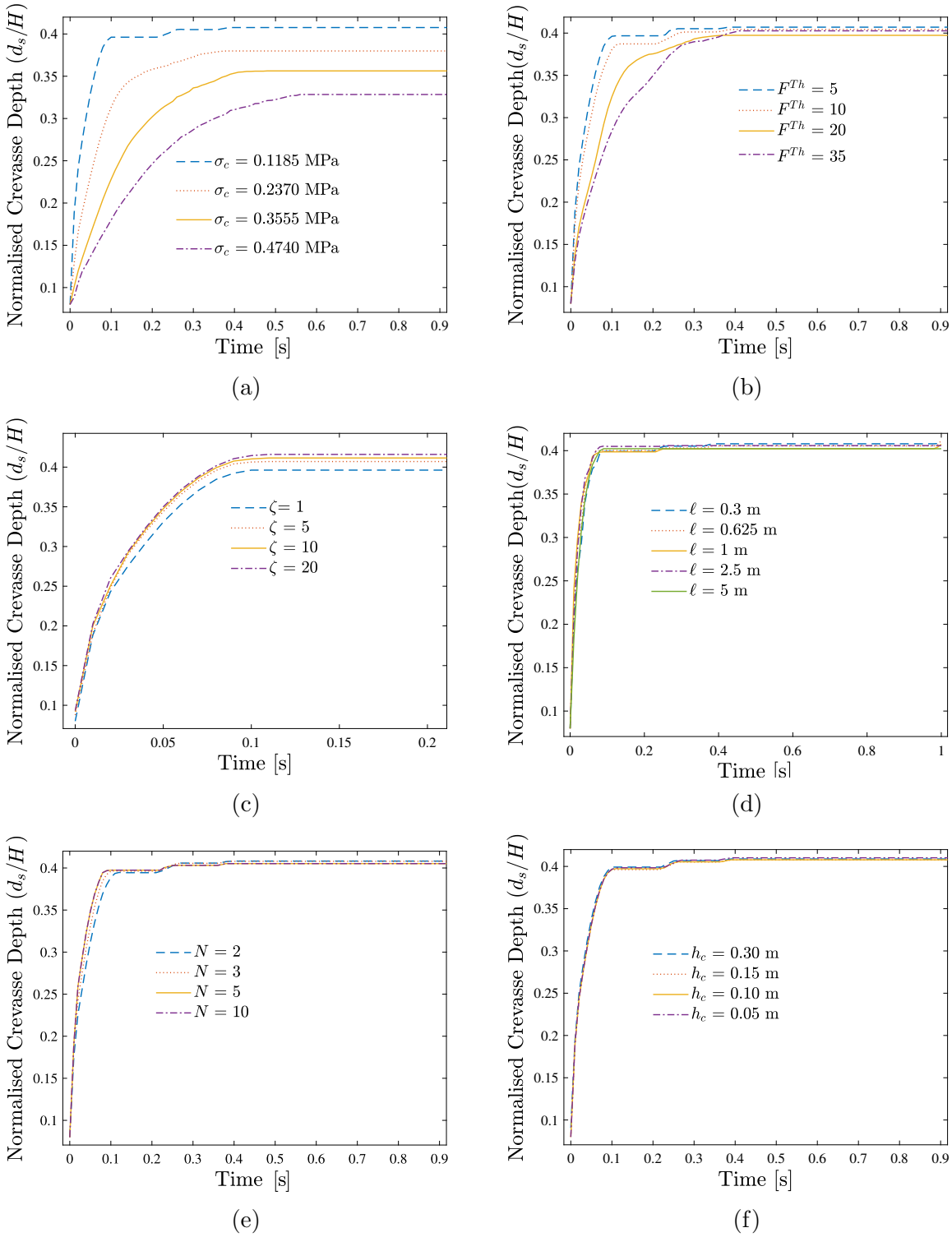

Figure 4.6: Crevasse growth in a grounded glacier. Normalised surface crevasse depth (d_s/H) versus time predictions for a dry isolated crevasse with an ocean-water ratio of $h_w = 0.5H$. Parametric studies varying (a) critical fracture stress σ_c , (b) crack driving force threshold F^{th}, (c) post peak slope parameter ζ, (d) phase field length scale ℓ_c, (e) number of solver iterations N, and (f) refined mesh size h_c.

4.4 Densely spaced surface crevasses in grounded glaciers

The propagation of a uniform field of densely spaced surface crevasses is now explored. The same domain and specimen geometry is employed from the previous study, with the isolated crevasse removed and seven surface crevasses implemented in the far field region, horizontally spaced 50 m apart. The study is conducted to investigate the influence of neighbouring cracks on the penetration depth. It is expected that neighbouring crevasses provide a shielding effect on the stress concentrations around the crack tip, and thus reducing the depth to which they stabilise. Phase field predictions for crevasses that are densely spaced are compared to results obtained from the Nye zero stress method. The results for the Nye zero stress method are calculated by finding the depth at which the net longitudinal stress is equal to zero, considering the contributions of lithostatic stress σ_{zz}, resistive stress R_{xx} and meltwater pressure p_{w}. The Nye depths are illustrated by the purple dashed line in Figure 4.7. The model uses approximately

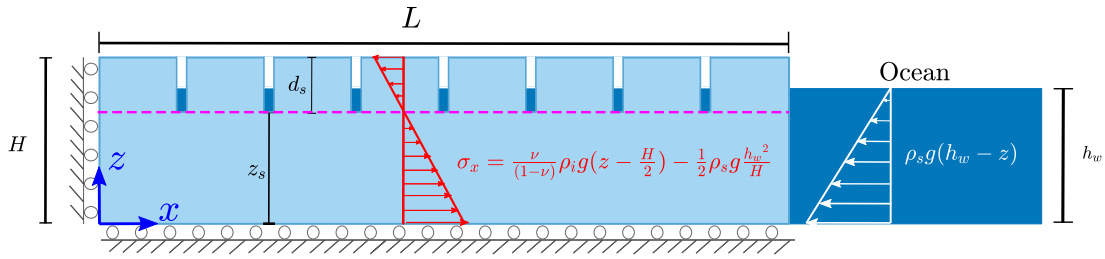

Figure 4.7: Multiple crevasse growth in a grounded marine-terminating glacier. Diagram shows the boundary conditions of a grounded glacier with a field of densely spaced crevasses (spaced 50 m apart from each other).

1.6 million linear triangular elements, with the mesh being refined ahead of each crevasse. Triangular mesh elements are chosen for this particular case study to aid in mesh construction, owing to mesh refinement regions around the crevasses being in close proximity of each other.

Plots of the phase field damage variable can be found in Figure 4.8, for an oceanwater height of $h_{\mathrm{w}} = 0.5H$ and a meltwater depth ratio of $h_{\mathrm{s}}/d_{\mathrm{s}} = 0.1$. Qualitatively, the behaviour resembles that of the single crevasse model — crevasses propagate rapidly and subsequently arrest upon reaching a region of sufficiently compressive stress at the bottom. Each crevasse stabilises to a similar depth, although the outer crevasses penetrate slightly deeper because they experience shielding only from one side. To shed light on the effect of crack shielding, meas-

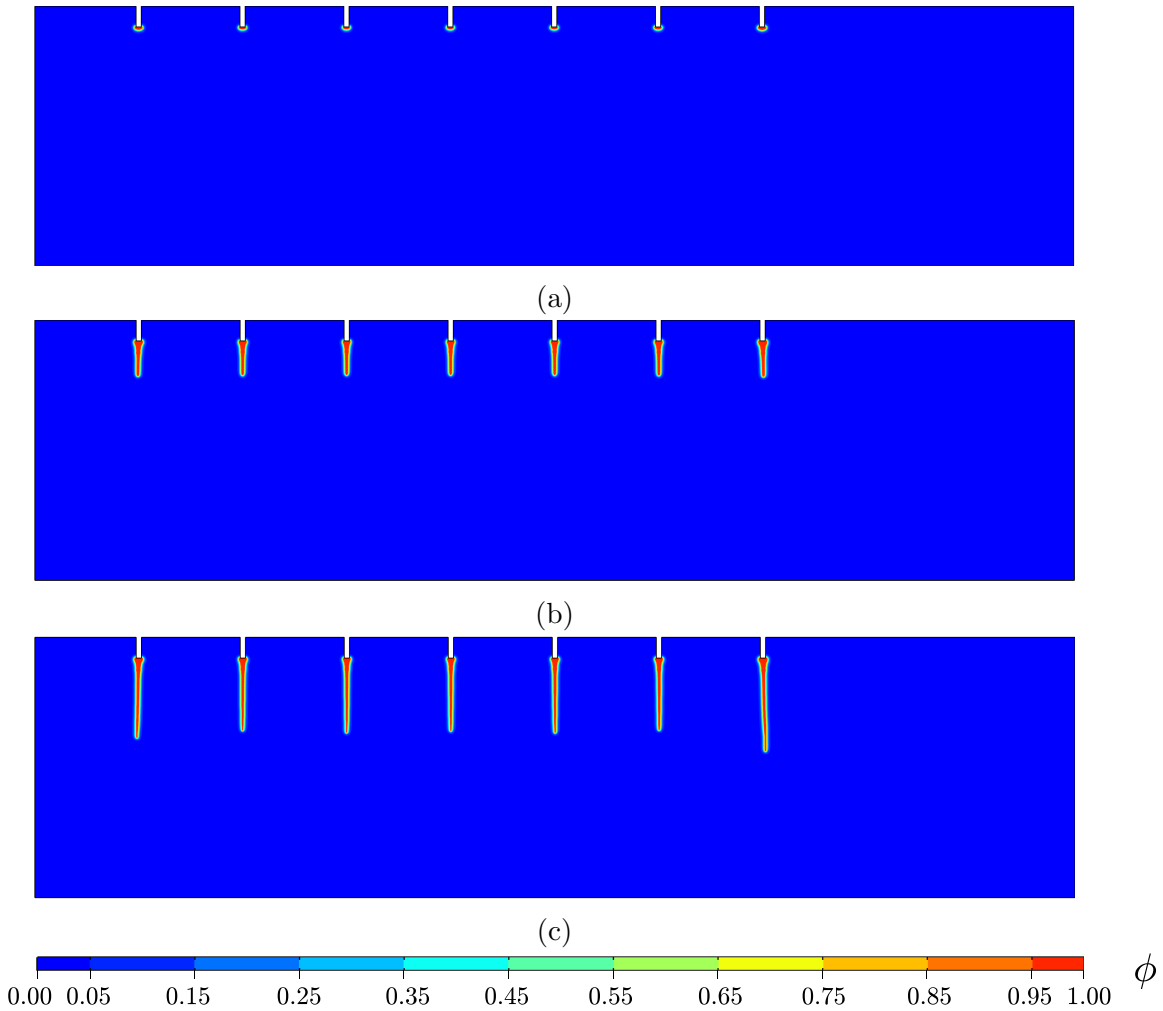

Figure 4.8: Multiple crevasse growth in a grounded glacier. Phase field damage evolution as a function of time: (a) t = 0.00 s, (b) t = 0.01 s, and (c) t = 0.40 s. The results correspond to the case of a meltwater depth ratio of $h_{\mathrm{s}}/d_{\mathrm{s}} = 0.1$ and an oceanwater height of $h_{\mathrm{w}} = 0.5H$, assuming a linear elastic compressible rheology.

urements are taken from the fourth crevasse at mid-length and compare them with

the predictions from the zero stress model; the results are shown in Figure 4.9. The agreement is very good overall; as also observed in the LEFM comparisons,

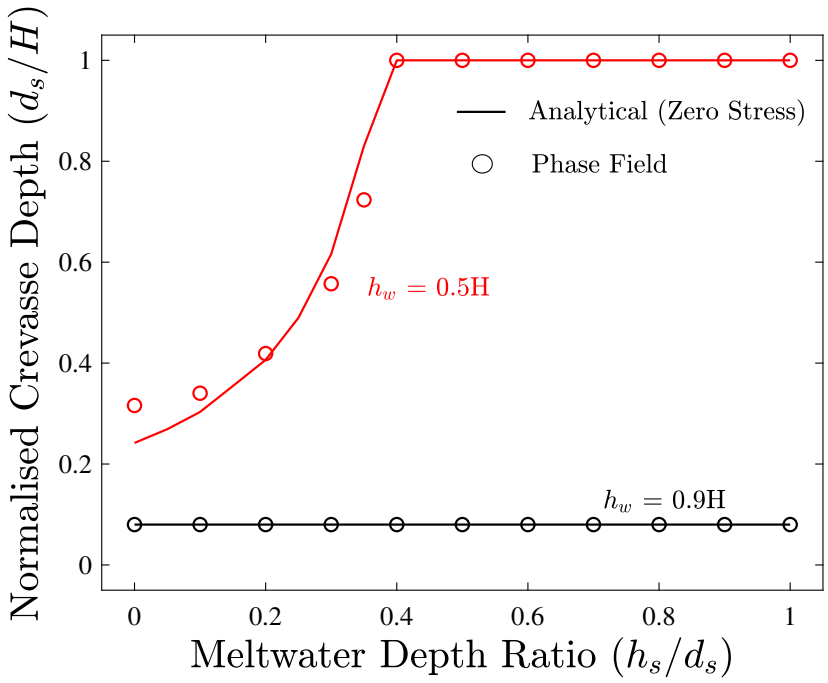

Figure 4.9: Multiple crevasse growth in a grounded glacier. Normalised crevasse depth versus meltwater depth ratio predictions as a function of the oceanwater height. Comparisons between the present phase field model and analytical predictions from Nye's zero stress model [2], for a linear elastic ice sheet.

the model provides a good agreement with analytical predictions, especially when the conditions where these analytical estimates are relevant. For the specific case of oceanwater height of $h_{\mathrm{w}} = 0.5H$, the phase field model predicts a slightly deeper crevasse penetration compared to the zero stress model for smaller values of meltwater depth ratio. For the near floating condition ($h_{\mathrm{w}} = 0.9H$), the oceanwater height is sufficiently large to completely offset the tensile region in the upper surface of the glacier. Thus the longitudinal stress profile is compressive throughout the entire height of the glacier (except near the terminus) and no amount of meltwater in the crevasse can extend it beyond its initial geometry.

4.5 Propagation of crevasses in floating ice shelves

Ice shelves are floating masses of glacial ice, typically several kilometres in length, which form along coastal regions of Antarctica as a result of grounded glaciers flowing into the ocean. The presence of which is dependent on the rate of ablation along the grounding line. If flux is sufficiently large enough to overcome glacial mass loss due to calving events and melting, then the ice sheet undergoes thinning and flow beyond the grounding line to form a floating extension. However, if ablation and calving equal or exceed the ice rate at the grounding line, then the ice sheet remains grounded and terminates at the grounding line.

In this section, a rectangular floating ice shelf of dimensions $H = 125$ m and $L = 5000$ m is modelled under the plane strain assumption. The free slip boundary condition at the base is removed and a Robin/mixed boundary condition is applied normal to the base, to represent the buoyancy pressure at the underside of the ice shelf $p_w = \rho_{\mathrm{s}} g\,(h_w - u_z)$ which is dependent on the vertical displacement u_z. Similar to the grounded glacier case, displacement is restrained at the far left edge to prevent rigid body motion in the horizontal direction. The oceanwater pressure, applied to the far right terminus varies linearly with depth and the oceanwater height h_{w} is found by considering the ratio of ice density ρ_{i} to seawater density ρ_{s} ($h_{\mathrm{w}} = \rho_{\mathrm{i}}/\rho_{\mathrm{s}} \approx 0.9H$). Gravitational body forces are applied to the domain and water pressures in the surface/basal crevasses are modelled using the poro-damage mechanics approach presented in Section 3.3. A schematic diagram of the floating ice shelf is illustrated in Figure 4.10.

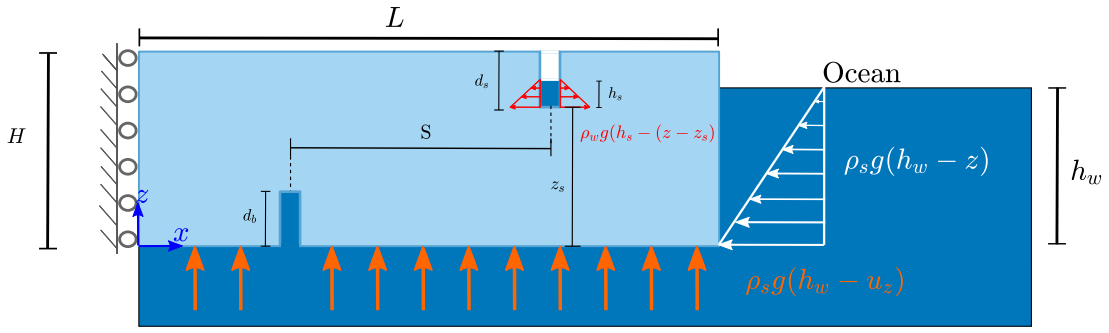

Figure 4.10: Schematic diagram showing the applied boundary conditions of a floating ice shelf containing an isolated surface crevasse

4.5.1 Isolated surface crevasses

Prior to running phase field damage simulations, the stress states within a pristine floating ice shelf at horizontal positions $x = [2500, 4750, 4950]$ m away from the left terminus are first determined, using the finite element model. In Figure 4.11 the longitudinal stress σ_{xx} versus depth is plotted at the aforementioned locations and are compared to the analytical solution for longitudinal stress in Appendix B, determined through the theory of elasticity and the membrane stress assumption. It can be observed that the longitudinal stress profiles away from the ice shelf front ($x = 2500$ m) are in good agreement with the analytical solution found in Eq. (B.21), resulting in a stress profile that is fully compressive throughout the depth. By contrast, at locations close to the ice shelf front ($x = 4750$ m and $x = 4950$ m) the longitudinal stress begins to deviate from the analytical solution, leading to a tensile stress observed in the upper surface, a region which is limited to half of the vertical distance from the upper ice surface to the ocean. This edge effect is a consequence of the applied bending moment from the uplift pressure at the ice shelf base and is in effect over a much larger horizontal distance compared to the grounded glacier case. This distribution assumes ice to behave as an elastic compressive material. Crevasse propagation studies are now presented, which have employed numerical phase field simulations for an isolated surface crevasse, assuming linear elastic compressive behaviour. The damage study is ini-

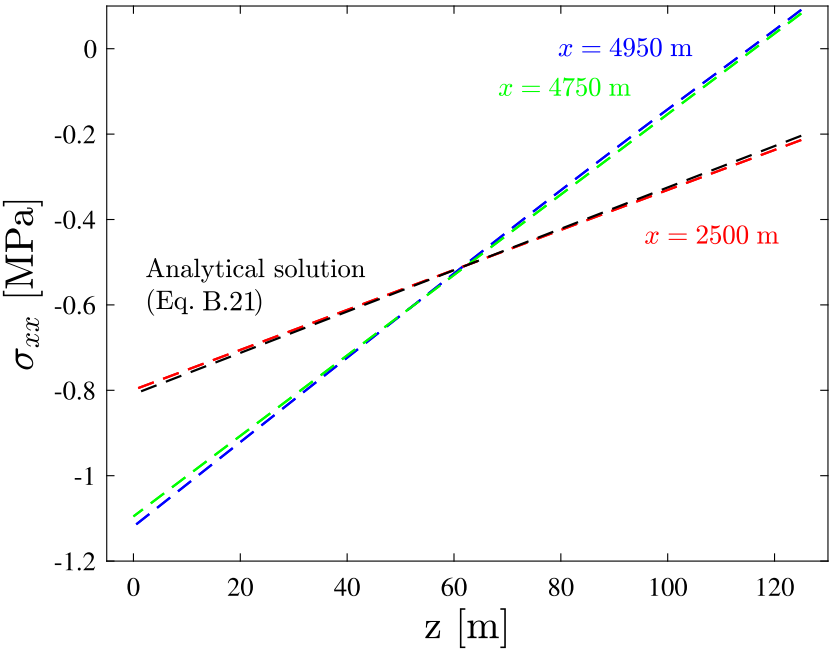

Figure 4.11: Surface crevasse in a floating ice shelf. Distribution of longitudinal stress σ_{xx} versus depth at different horizontal positions; the numerical predictions are compared to the analytical solution, given in Eq. (B.21).

tially conducted for a crevasse within the far field region ($x = 2500$ m) and then close to the ice shelf front ($x = 4950$ m). Similar to the grounded glacier case, damage is initialised by the inclusion of a geometric notch of height $d_s = 10$ m and width $b = 2.5$ m. The results of this study are verified using the analytical LEFM solution. However, the inclusion of the Robin-type boundary condition for the buoyancy pressure invalidates the 'double edge crack' formulation used for the grounded glacier. The most appropriate formulation for the stress intensity factor K_I^{net} for a floating ice shelf was shown to be the single edge crack weighting given by Krug [141] – presented in Appendix D – since this matches stress intensity factors computed numerically by the displacement correlation method [142]. When calculating the analytical results for crevasses close to the front, the longitudinal stress distribution is extracted from the finite element simulation, since the influence from the uplift pressure cannot be captured analytically.

The results for the predicted stabilised crevasse depths are plotted in Figure 4.12 below, normalised with respect to the ice shelf thickness H. Each data point is represented by an individual simulation, where the meltwater depth is held as a constant ratio h_s/d_s. It can be observed that surface crevasses within the far field region will not propagate beyond the initial specified notch (represented by the black curve), regardless of the volume of meltwater present in the crack, this is owing to the longitudinal stress being compressive throughout the entire ice shelf thickness. By contrast, surface crevasses close to the ice shelf front are

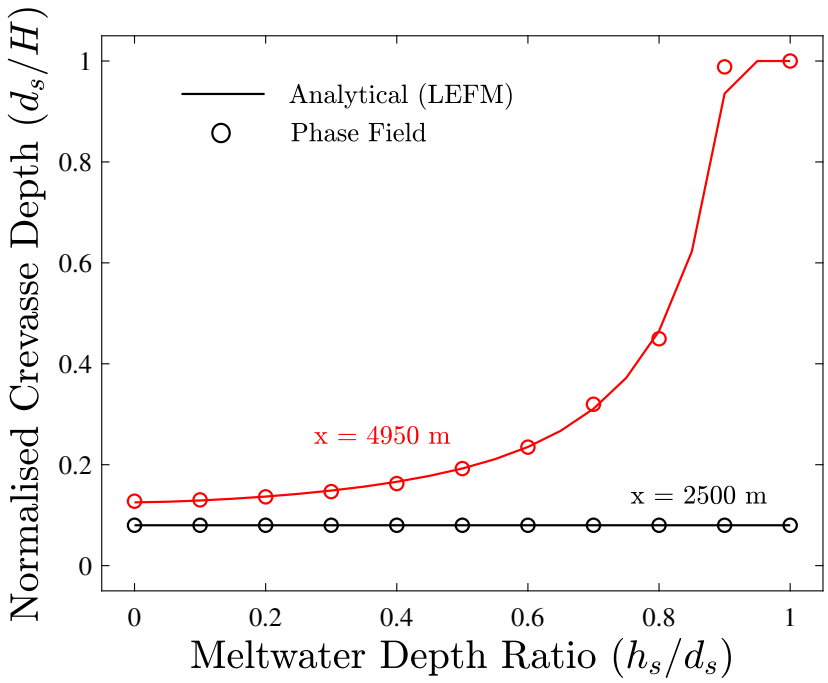

Figure 4.12: Growth of a surface crevasse in a floating ice shelf. Analytical (LEFM-based) and computational phase field predictions of stabilised crevasse depths (d_s/H) as a function of the meltwater depth ratio (h_s/d_s). The results are provided at horizontal locations $x = 2500$ m and $x = 4950$ m.

less stable than those in the far field region (represented by the red curve). For low values of meltwater depth ratio, there is a marginal increase in penetration depth compared to the original geometry. However, as the meltwater depth ratio increases, so does the rate in increase of penetration depth due to the additional tensile stresses overcoming the overburden pressure. Surface crevasses close to

the front can be susceptible to full thickness propagation for meltwater depth ratios greater than $h_s/d_s = 0.9$. The phase field model gives good agreement with results predicted by the LEFM model for floating ice shelves when using the longitudinal stress distribution obtained from the finite element simulation and the weighting function given by Krug [141], presented in Appendix D.

4.5.2 Basal and surface crevasse interactions

An iceberg calving event is the loss of glacial mass close to the front of either a grounded glacier or floating ice shelf, through the propagation of fracture. In floating ice shelves, these events occur when basal and surface crevasses combine to propagate through the full thickness [41]. The phase field method is therefore used to capture the interaction of surface and basal crevasses close to the calving front. A surface crevasse at a horizontal location $x = 4950$ m is introduced, and a meltwater depth ratio of $h_s/d_s = 0.8$ is prescribed. The basal crevasse is assumed to be fully saturated beneath the oceanwater surface and is introduced at a horizontal offset distance S away from the surface crevasse. The horizontal spacing is varied $S = \{0, 5, 10, 15\}$ m between the surface and basal crevasses to determine if they coalesce to form a full depth crevasse. The qualitative results take the form of phase field contour plots and are presented in Figure 4.13. From this, three main observations are made: (1) the surface crevasse depth is insensitive to the position of the basal crevasse, (2) the basal crevasse depth is influenced by the spacing S – with a smaller spacing resulting in a reduced penetration depth – and (3) the basal and surface crevasses do not coalesce regardless of spacing factor. Instead of coalescence, the basal crevasse path is observed to be deflected as it approaches the crack tip of the surface crevasse. This is owing to the mixed mode conditions arising from two mode I cracks in close proximity [143]. The quantitative data is presented as graphs of crevasse growth in Figure 4.14. Plots

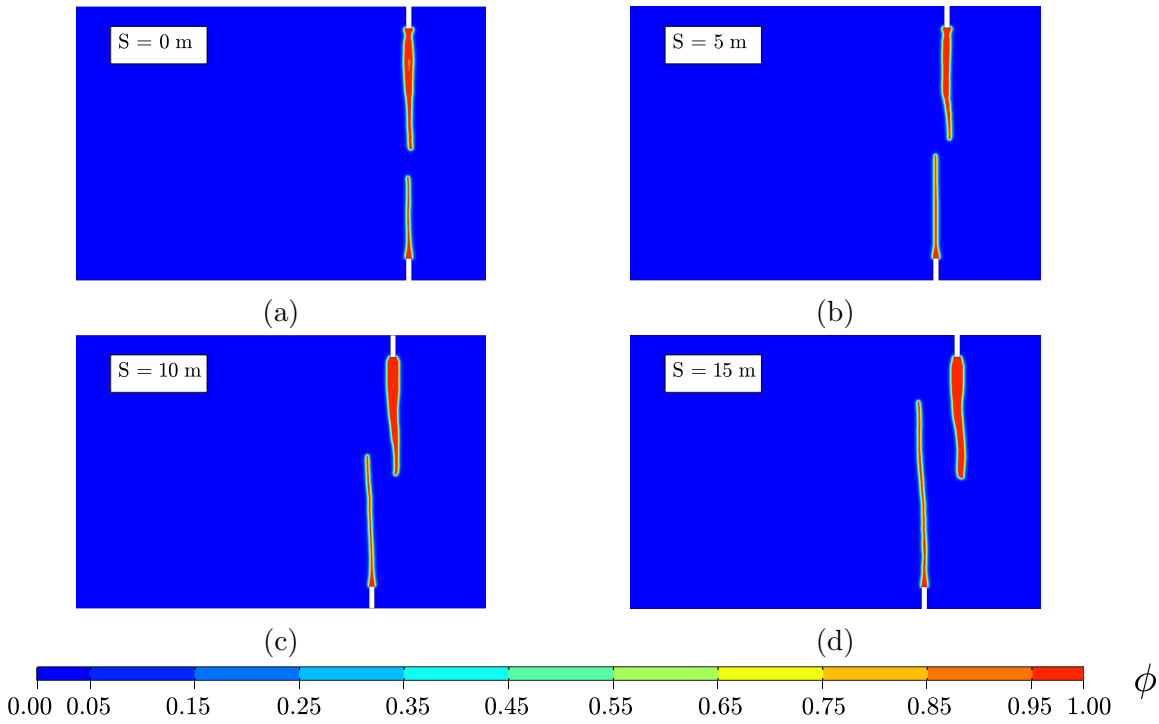

Figure 4.13: Growth of surface and basal crevasses in a floating ice shelf. Phase field damage contours after reaching the arrest of the crevasses, considering four selected values for the horizontal separation (S) between the basal and surface crevasse. For the surface crevasse, the meltwater depth ratio equals $h_s/d_s = 0.8$.

for the individual crevasse predictions are shown in Figure 4.14a, showing the isolated surface crevasse, isolated basal crevasse and basal crevasse for each of the following spacing values S. The surface crevasse data is initially compared to the result in Figure 4.12 (for $h_s/d_s = 0.8$), it can be seen that neither the existence or extent of the surface crevasse is affected by the presence of the basal crevasse, with the normalised depth equal to approximately half the shelf thickness. By contrast, the growth of the basal crevasse is stunted by the proximity of the surface crevasse. As shown in Figure 4.14a, the stabilised basal crevasse depth begins to increase with distance away from the surface crevasse. Basal crevasses located greater than 15 m away from the surface crevasse tend towards the penetration depth of the isolated basal crevasse. For basal crevasses directly beneath the surface crevasse, the crevasse propagates to 37.7% of the ice shelf depth, compared with 80.6% for the isolated basal crevasse. The combined basal

and surface crevasse depth is shown in Figure 4.14b. For large separations, the combined penetration depth exceeds the entire thickness of the ice shelf, but calving is not observed due to diverging crack paths. Calving is also not observed for aligned crevasses as basal crevasse growth is hindered. The ice shelf fracture is therefore found to be independent of ice shelf thickness H, since the stress distribution is unaffected by thickness but the magnitudes are scaled; instead, it is dictated by the combination of horizontal position of surface crevasses and the accumulation of meltwater within them. Furthermore, unless perfectly aligned in close proximity, surface and basal crevasses, their failure criterion may be studied independently.

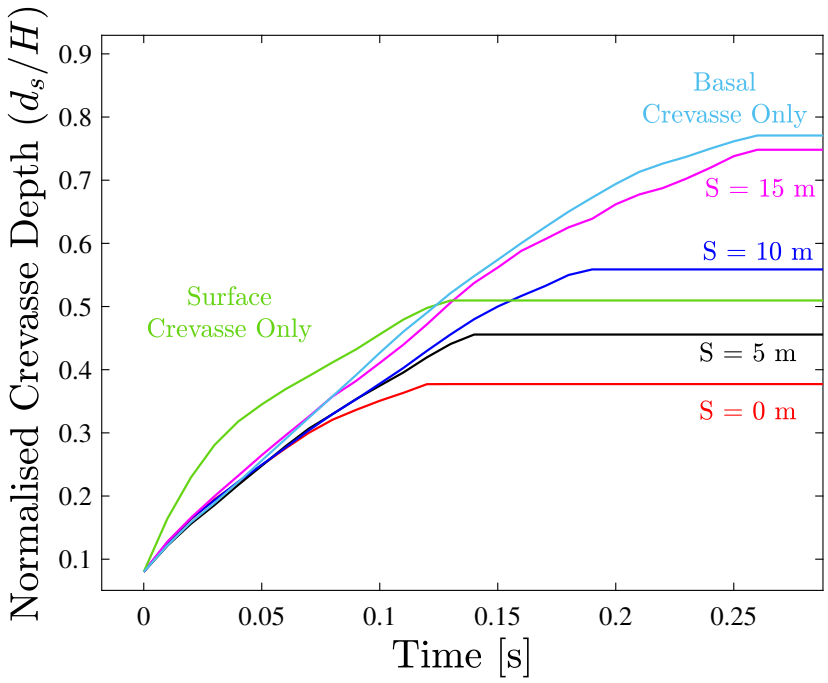

(a)

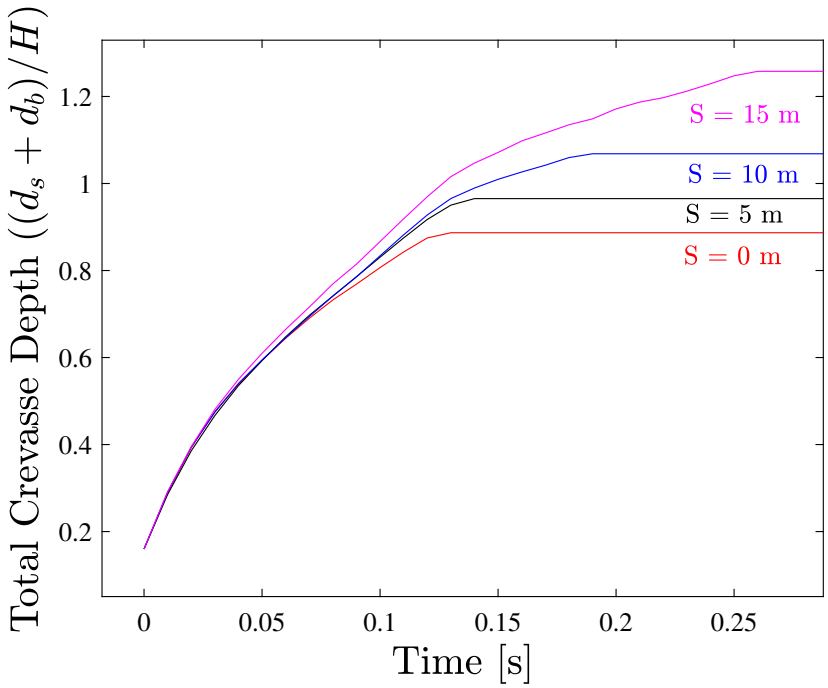

(b)

Figure 4.14: Growth of surface and basal crevasses in a floating ice shelf. The basal and surface crevasses are separated by a horizontal distance S. (a) Predictions of crevasse depth versus time for surface and basal crevasses with varying horizontal spacing S; and (b) evolution of the combined basal and surface crevasse depth versus time for selected choices of the horizontal spacing S.

4.6 Initiation of damage from arbitrary sites – Helheim Glacier case study

In this section, the initiation and propagation of crevasses from arbitrary sites is simulated in the Helheim glacier, one of the largest outlet glaciers in southeast Greenland. The aim is to demonstrate how the creep analysis can be used to determine the nucleation of crevasses, which are then predicted to grow in a coupled deformation-fracture simulation. To generate the glacier geometry, the surface elevation and basal topography data is taken from field observations (see Refs. [3, 136]). A free slip boundary condition is applied normal to the base and the inlet flow velocity is restrained to zero at the left edge. Also, an oceanwater pressure is applied at the glacier terminus and an ocean water height of $h_{\mathrm{w}} = 0.85H$ is assumed. The geometry is discretised using approximately 140,000 triangular quadratic plane strain elements, with the surface geometry being kept constant over time.

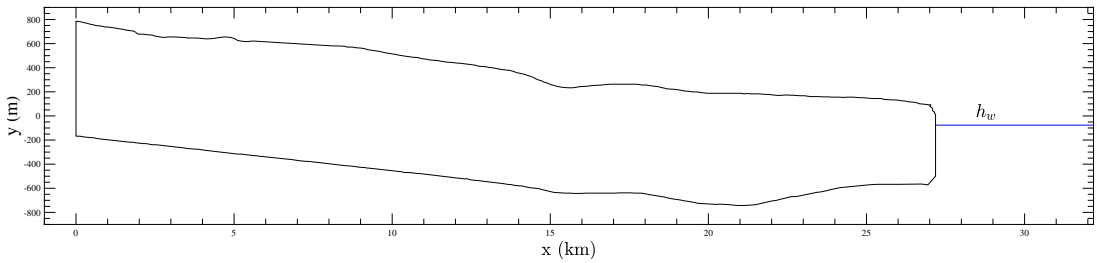

Figure 4.15: Nucleation and growth of crevasses in the Helheim glacier. Initial geometry, as taken from observational data in Nick *et al.* [3].

The first step involves running a time-dependent creep simulation to determine the regions in which damage initiates, with the model assuming that ice behaves as a Maxwell body. A crevasse nucleation criterion is defined by which crevasses are assumed to nucleate in regions where the product of the damage driving force state function D_{d} and the equivalent creep strain $\varepsilon^c = \sqrt{(2/3)\boldsymbol{\varepsilon^c} : \boldsymbol{\varepsilon^c}}$ is above

a certain threshold. This is denoted by red colour contours in Figure 4.16. As it can be observed, this crack nucleation criterion is fulfilled at shallow regions within the upper surface, notably in areas with increased surface gradient and regions close to the calving front. This distribution is supported by the results by Krug *et al.* [136], wherein a similar pattern to initiation sites was reported from a time dependent creep analysis. Ice is then removed from the regions, where the nucleation criterion has been met, to act as initiation points for crevasse growth in the subsequent phase field step.

Damage evolution is subsequently predicted using the phase field model with the updated geometry, assuming nonlinear viscous ice rheology. As shown in Figure 4.17c, it is found that a field of densely spaced surface crevasses can initiate at sites both close to and away from the calving front. However, the depth to which they propagate is shallow in comparison with the glacier geometry (approximately 40 m deep). This is in agreement with the field observations of Mottram and Benn [52], who measured crevasse depths close to the calving front of Breidamerkurjokull in Iceland, finding that crevasses only penetrated tens of metres in depth. At the calving front, it is also observed that damage can propagate to the full depth of the glacier, illustrating the possibility of ice cliff failure and retreat of the grounding line. This case study showcases the ability of the computational framework, developed to combine creep and damage modelling, to predict both the nucleation of crevasses and the subsequent propagation, for realistic geometries and conditions.

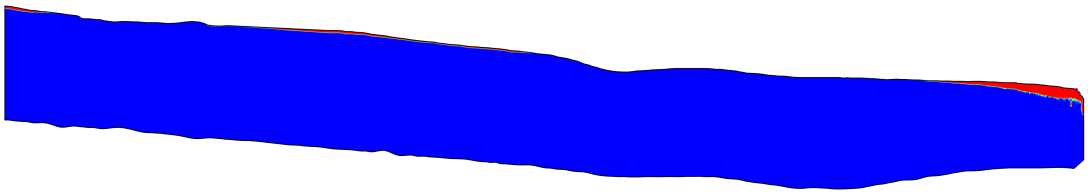

Figure 4.16: Nucleation and growth of crevasses in the Helheim glacier. Distribution of the nucleation variable $D_{\mathrm{d}}\varepsilon^{c}$, with red colour contours denoting the areas where the nucleation threshold has been exceeded.

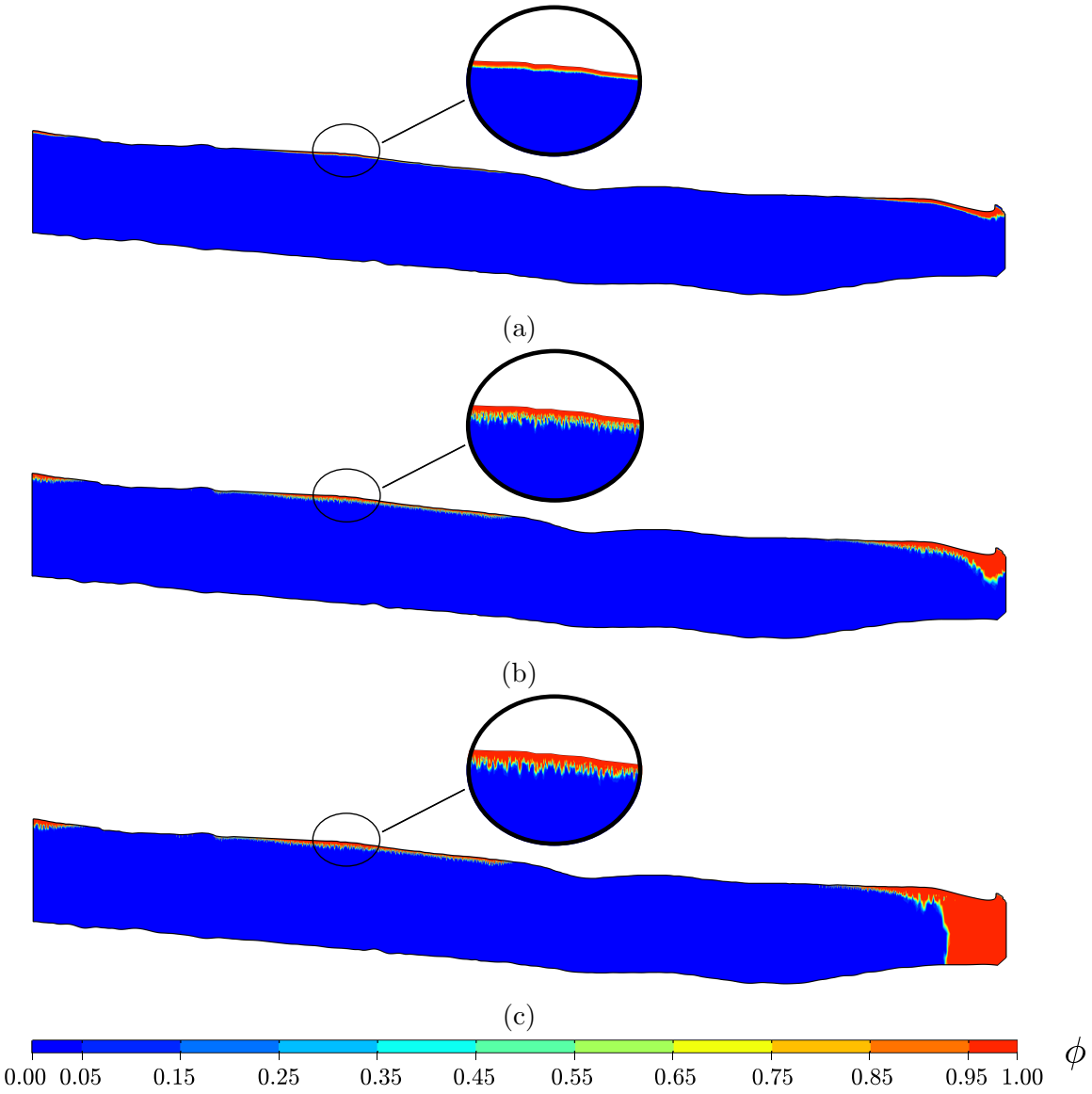

Figure 4.17: Nucleation and growth of crevasses in the Helheim glacier. Phase field damage evolution of the Helheim glacier assuming a nonlinear viscous rheology at times (a) $t = 0$ s, (b) $t = 0.30$ s, and (c) $t = 0.80$ s.

4.7 Three dimensional case studies

Within this section, the ability for the numerical phase field model to capture complex fracture phenomena such as crevasse interaction in three dimensions is demonstrated. Here, an idealised grounded glacier of height $H = 125$ m, length $L = 500$ m and width $W = 750$ m is modelled – schematically represented by Figure 4.18. Two dry edge surface crevasses are considered at either end of the glacier. These are horizontally offset by 25 m either side of the centreline $x = L/2$ and are initialised through cuboid notches of height $d_s = 10$ m, width $b = 2.5$ m and length $l_s = 25$ m. Similar to the 2D plane strain case study, displacement is restrained in the vertical z-direction normal to the base, and restrained in the horizontal x-direction at the far left terminus, normal to y-z plane. Weak margins at the lateral sides are assumed by restraining displacement in the y--direction at both faces of the x-z plane. Gravitational body forces are applied to the entire domain and the oceanwater pressure is applied normal to the far right terminus, with an oceanwater height of $h_{\mathrm{w}} = 0.5H$ being assumed. As

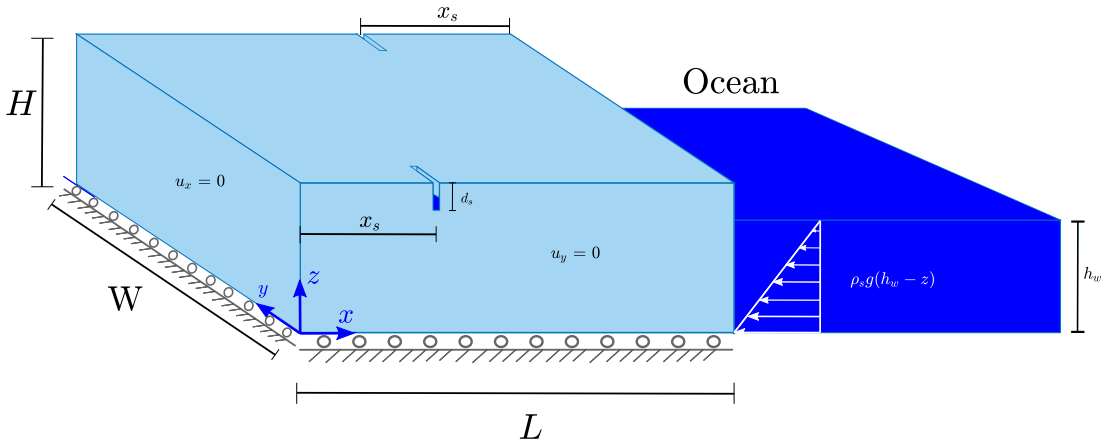

Figure 4.18: Crevasse interactions in 3D marine-terminating ice sheets. Diagram showing the boundary conditions and geometry of the three dimensional boundary value problem.

discussed in Section 3.1.2 and Section 4.3.3, the stress based phase field model is advantageous for studying glacial fracture since the results are insensitive to

values of length scale ℓ_c. Therefore, a value of $\ell_c = 10$ m is prescribed to reduce the computational cost associated with larger geometries in three dimensions. The finite element mesh is composed of linear tetrahedral elements and is refined locally around the expected crack path, with a refined element size of $h_c = 2.5$ m. An element size of 25 m is prescribed elsewhere, resulting in 1.5 million degrees of freedom to be solved for. The results for the study are presented as phase field damage contour plots shown in Figure 4.19. It is observed that initial crevasse propagation occurs vertically downwards (z-direction), directly beneath the notches and stabilises to a depth equivalent to that of the 2D plane strain case. After this, damage propagates inward in the horizontal direction (y-direction) in a mode I manner. As the two crevasses approach each other, the stress field close to the crack tip becomes mixed-mode and the crack paths begin to curve away from each other. Full coalescence is achieved at the centre of the grounded glacier and a hooked shaped damage pattern is achieved. This crack path has been commonly observed in geological faulting, with remote sections of the fault growing as purely tensile fractures, whilst in close proximity to each other the faults grow as mixed mode fractures [144, 145]. This fracture pattern has also been observed in laboratory experiments [143]. The ability of the phase field method to model complex fracture phenomena in areas of surface crevasse coalescence in 3D has therefore been demonstrated, however this comes at a high computational cost.

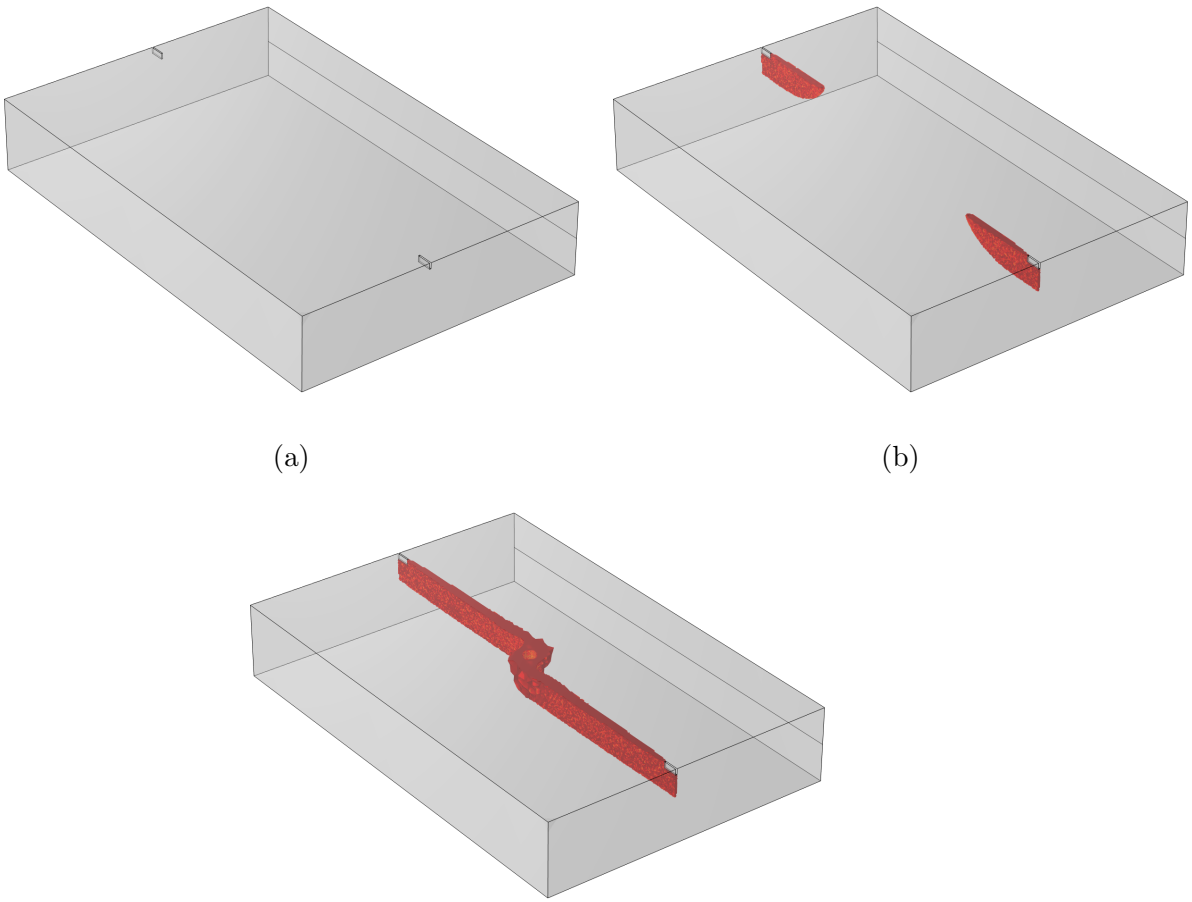

(a) (b)

(c)

Figure 4.19: Crevasse interactions in 3D ice sheets: $\phi = 1$ contours showing the evolution of the two dry surface crevasses at times (a) $t = 0$ s, (b) $t = 0.05$ s, and (c) $t = 0.4$ s.

4.8 Water filled crevasses close to ice sheet terminus

The final numerical example in the current chapter considers the propagation of a water filled isolated crevasse located close to the terminus, in a grounded glacier of dimensions $H = 125$ m and $L = 500$ m. A rectangular notch is inserted into the geometry at a horizontal position of $x = 475$ m of depth $d_{\mathrm{s}} = 10$ m and width $b_{\mathrm{s}} = 2.5$ m. The oceanwater pressure is applied at the far right terminus, considering an oceanwater height of $h_{\mathrm{w}} = 0.9H$ and the crevasse is assumed to be fully saturated with meltwater (i.e. $h_{\mathrm{s}}/d_{\mathrm{s}} = 1.0$). Presently, the aim is to demonstrate the process of iceberg detachment as a result of meltwater driven crevasses in near floatation glaciers. The propagation of damage is qualitatively displayed in Figure 4.20. It can be seen that the crack initially propagates downward, but this begins to curve towards the far right terminus and reaches this position at an approximate elevation of $z = 56$ m. Once this is achieved, the damage zone begins to spread from a sharp crack to a smeared damaged region, until the entire upper right corner of the glacier is fully damaged. It is important to note that for this example, the positioning of the damage initiation zone plays a pivotal role in determining whether damage propagation will occur. As shown in Section 4.3.1, if a fully saturated surface crevasse is initiated in the far field region of a near floatation glacier, no propagation occurs. In addition, this fracture is driven by two key factors: (1) the presence of meltwater in the crevasse results in an increase in tensile stress allowing for damage accumulation – if a dry crevasse is considered in this example, damage will cease to propagate and (2) the concentration of in-plane shear stresses close to the front locally alters the principal stress directions, causing the crack path to be deflected towards the cliff face. This phenomena was not observed for the fully saturated crevasse close to the terminus in a floating

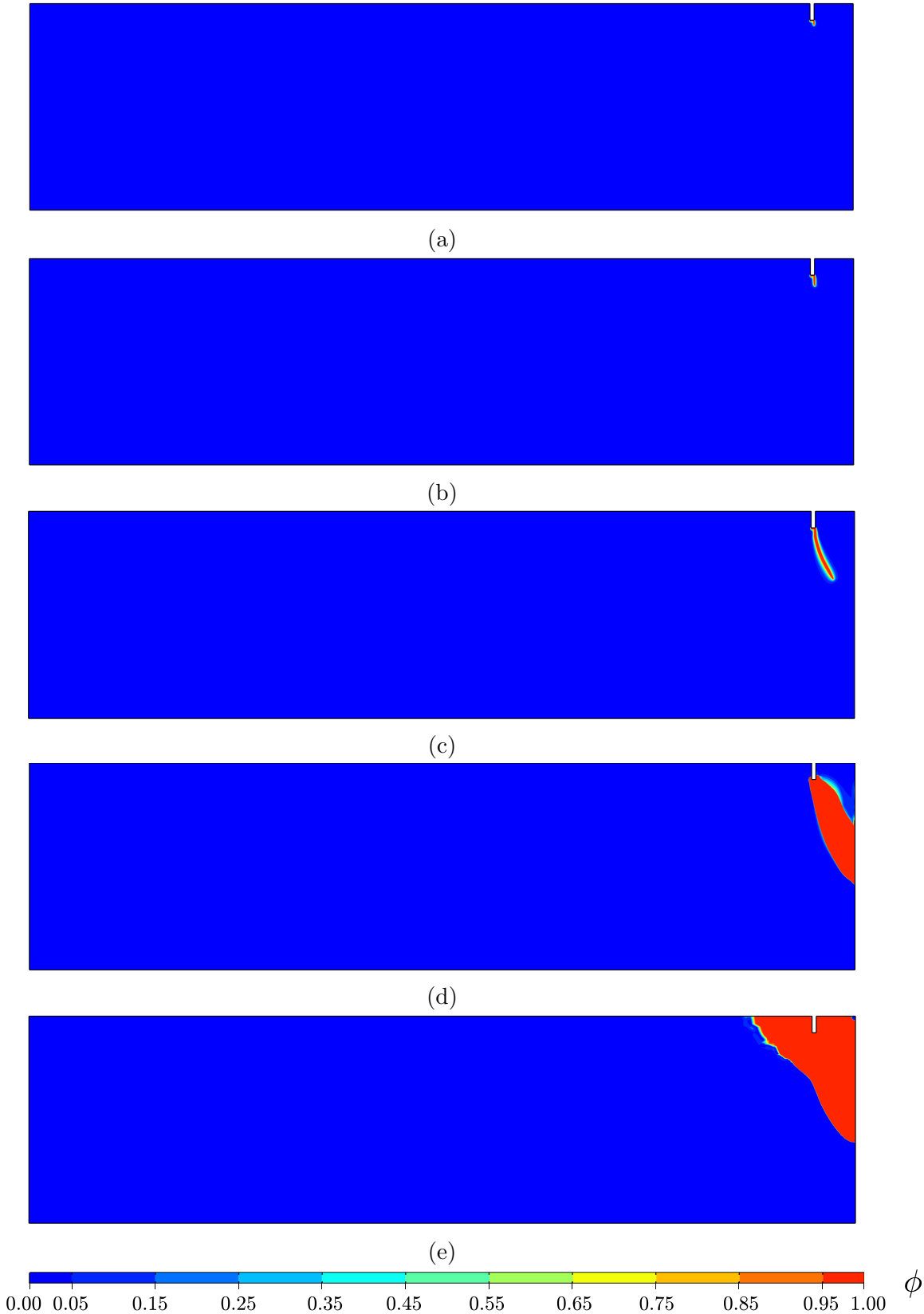

Figure 4.20: Phase field contour plots of a fully saturated isolated crevasse close to the terminus of a near floatation glacier ($h_w = 0.9H$). Contours outputs taken at time increments: (a) $t = 5$ s, (b) $t = 7.5$ s, (c) $t = 11.4$ s, (d) $t = 15$ s and (e) $t = 26$ s

ice shelf, since the full thickness propagation was a purely mode I failure. This study highlights the detrimental effect of meltwater accumulation in these near terminus crevasses, as maximum exposed cliff heights from empirical relations are in the order of 100 m [146, 147, 148] without the presence of meltwater, as opposed to the exposed cliff height of 12.5 m when considering a fully saturated crevasse.

4.9 Concluding Remarks

In the current chapter, the results of several numerical examples in 2D plane strain and 3D have been presented. Phase field fracture simulations have been executed to capture the propagation of water filled basal and surface crevasses in grounded glaciers and floating ice shelves. These results have been compared to analytical solutions from LEFM and the Nye zero stress method, with good agreement being shown between numerical and analytical solutions. The following conclusions can be obtained from the presented work:

- The implementation of a stress-based phase field fracture model accurately captures tension-compression asymmetric behaviour required to model crevasses in grounded glaciers and floating ice shelves, without the need for *ad hoc* fracture driving force decompositions. The stress based approach is also advantageous for large scale simulations due to its insensitivity to change in phase field length scale ℓ_c.

- Phase field predictions provide good agreement with analytical approaches such as LEFM and the Nye zero stress model, when considering the appropriate relevant idealised conditions and weight functions.

- Increasing amounts of meltwater, as a result of climate change, can have a profound effect on stabilised crevasse depth for intermediate oceanwater heights, with iceberg calving being predicted for meltwater depth ratios of 50% or higher.

- The presence of an ocean at the far right terminus provides a compressive stress in the longitudinal direction that is constant with depth and aids the prevention of surface crevasse propagation.

- When accounting for the viscoelastic behaviour of ice using Glen's flow law, the longitudinal stress state tends towards the incompressible distribution. The stress based approach captures this effect when initialising the model with a time dependent creep simulation. Depths of surface crevasses are greater when accounting for this effect.

- Phase field models can capture the effect of neighbouring crevasses providing a shielding effect on the stress concentration in a field of densely spaced crevasses, leading to a reduced crevasse depth that is comparable to the Nye zero stress method.

- The horizontal position of surface crevasses is a determining factor of whether propagation will occur. Surface crevasses in floating ice shelves will only propagate in close proximity to the ice shelf front and for large values of meltwater depth ratios due to the presence of the bending moment resulting from the buoyancy pressure at the base. In addition, a reduction in basal crevasse depth is observed if in the vicinity of a surface crevasse.

- Crevasses are predicted to nucleate in areas with high surface gradients, highlighting the need for an adequate geometrical characterisation of the glacier.

- The large-scale 3D analyses conducted demonstrate the capabilities of the

model of opening new horizons in the modelling of crevasse growth phenomena under the computationally demanding conditions relevant to iceberg calving. Mixed mode failure may be observed when two parallel surface crevasses propagate close to each other in regions of coalescence.

- The presence of surface crevasses, which are fully saturated with meltwater and located close to the front of a near floatation glacier are susceptible to mix-mode failure, leading to iceberg detachment. This can occur at relatively small glacier freeboards, compared to empirical predictions without the presence of meltwater.

Chapter 5

Influence of Firn Layer Material Properties on Surface Crevasse Propagation in Glaciers and Ice Shelves

While the majority of crevasse propagation studies capture a range of mechanical interactions, they assume glacial ice to be a homogeneous material, with values of mechanical properties taken as constants equal to that of fully consolidated ice. In reality, glacial ice forms from the accumulation of snowfall at the upper surface and undergoes compaction as a result of the overburden pressure, the rate of which being dependent on accumulation rates and surrounding temperatures [149]. Moreover, snowflakes are restructured into smaller ice crystals due to wind, which then deform into more stable, compact crystal arrangements [15]; this causes large differences in porosity, density, and strength between these top snow layers, referred to as firn, and deeper glacial ice.

Neglecting firn layers may lead to an overestimation of mechanical properties in the upper strata [4, 150]. This is of particular importance for geological media subject to self-gravitational loading [151], because the driving stresses are dependent on the mechanical properties in such layered or vertically graded materials. The principal hypothesis of this study is that accounting for these depth-dependent material parameters in the LEFM framework would alter the crevasse penetration depths in glaciers and ice shelves.[1]

Within the present chapter, the maximum crevasse depths in idealized glaciers and ice shelves are determined assuming two different material conditions: fully-consolidated homogeneous ice and vertically graded ice, as reported from ice core samples with depth-dependent material properties.

Analytical solutions for the far field longitudinal stress σ_{xx} in grounded glaciers are derived, considering depth-dependent material properties, which primarily drives the vertical propagation of mode I crevasses. A systematic investigation is then conducted to determine the effect of varying each material property in the unconsolidated firn layers through parametric studies as follows: (1) only depth--dependent density in Section 5.1.1; (2) only depth-dependent Young's modulus in Section 5.1.2; and (3) both depth-dependent density and Young's modulus in Section 5.1.3.

Fracture mechanics studies are then conducted for surface crevasses in a grounded glacier using analytical LEFM models and these are verified using this with the stress based phase field model presented in Chapter 3. Through variations in meltwater depth ratios in water filled surface crevasses and oceanwater heights in marine terminating glaciers, the conditions where depth-dependent material properties are influential are explored. In Section 5.3, a similar study is conducted

[1]The work reported in this section is presently under review within the journal, The Cryosphere [152]

for surface crevasses in floating ice shelves, with the limitations of the study being discussed in Section 5.5. Finally, the findings are summarized in Section 5.6 and conclusions are drawn.

5.1 Analytical solutions for the longitudinal stress

The far-field longitudinal stress (based on the long wavelength approximation) within the grounded glacier or ice shelf was derived for the case of steady-state creep with constant (i.e. depth-independent) and homogeneous material properties by Weertman in 1957 [153]. Recently, the longitudinal stress based on linear elastic compressibility was derived by Sun et al. [131] considering plane strain conditions, Hooke's law and the membrane strain equation. The derivation for this is presented in Appendix B. Where positive values of σ_{xx} indicate regions of tensile stress, responsible for crevasse propagation; whereas negative values indicate compressive stress. The analytical solution for stress:

$$\sigma_{xx} = \frac{\nu}{(1-\nu)}\rho_{\mathrm{i}} g \left(z - \frac{1}{2}H \right) - \frac{1}{2}\frac{\rho_{\mathrm{s}} g h_{\mathrm{w}}^2}{H} \tag{5.1}$$

is used to compare between the homogeneous case and depth-dependent material properties. The Poisson ratio ν used within the results represents ice as a linear elastic compressible solid, which is a valid assumption for rapidly developing cracks, such that the full crevassing process occurs on a timescale well below the Maxwell timescale (for ice, on the order of hours to days). If instead the slow development of crevasses is studied, with crevasses slowly penetrating the ice sheet over the span of weeks, using a Poisson ratio of $\nu = 0.5$ allows for the model derived presently to be used to represent an incompressible solid, more closely resembling the stress state within ice at longer timescales.

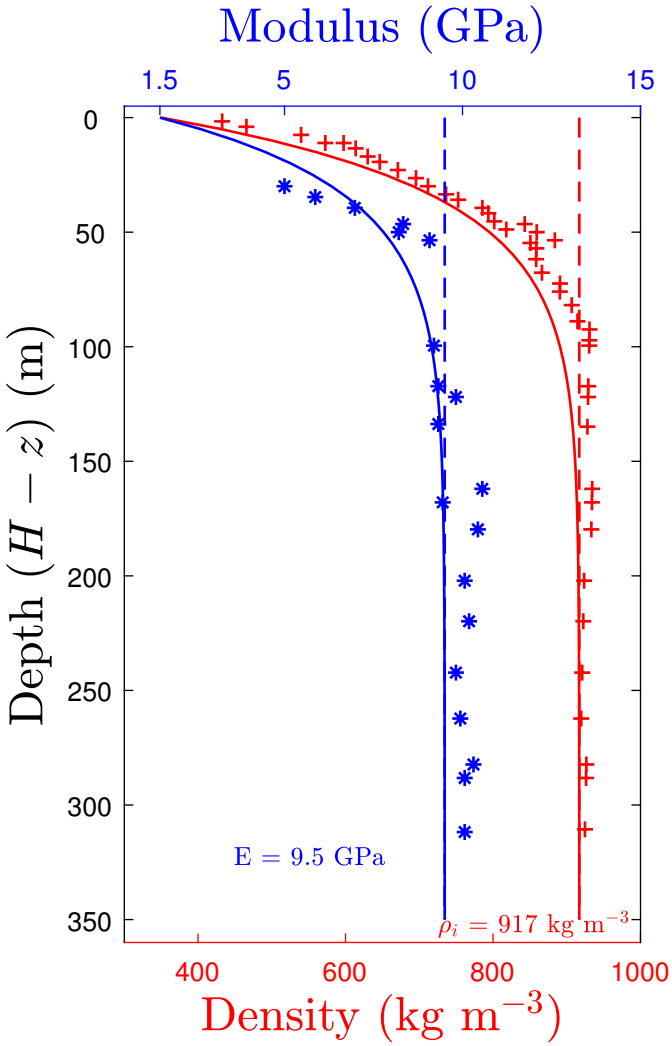

Figure 5.1: Profile of depth-dependent mechanical properties for ice density (red, bottom axis) and Young's modulus (blue, top axis). Data extracted from ice core specimens from the Ronne ice shelf by [4] are displayed as markers. Homogeneous properties are displayed with the dotted lines.

Ice core sample data from the Ronne Ice Shelf, gathered and presented by Rist et al [4] shown in Figure 5.1, indicates large variations in material properties within the firn and meteoric ice layers forming the upper 150 m of the ice core. The ice core data for density can be fitted using the exponential equation [151, 49]:

$$\rho(z) = \rho_{\mathrm{i}} - (\rho_{\mathrm{i}} - \rho_{\mathrm{f}})e^{-(H-z)/D} \tag{5.2}$$

where $\rho_{\mathrm{f}} = 350$ kg/m^3 is the density of upper surface unconsolidated firn layers, H is the height of the glacier, z is the vertical coordinate ($z = 0$ at the base of the glacier, $z = H$ at the surface), and D is a constant taken as 32.5 m [4]. This constant gives an indication of the thickness of the firn layer: at the surface $z = H$, the density of the glacier is equal to that of the unconsolidated firn; at a depth of $D = H - z$ below the surface, the density is between that of firn and ice, at 75% of the density of ice, while at a depth of $H - z = 2.5D$ below the surface the density of the glacier is 95% of the density of consolidated ice.

The ice core sample data for elastic modulus was found through acoustic velocity measurements prior to mechanical testing [4]. Elastic modulus data from Figure 5.1 can be fitted using a similar function as used for the density, including the depth-dependent Young's modulus as:

$$E(z) = E_{\mathrm{i}} - (E_{\mathrm{i}} - E_{\mathrm{f}})\, e^{-(H-z)/D} \tag{5.3}$$

where $E_{\mathrm{i}} = 9.5$ GPa is the Young's modulus for solid ice, $E_{\mathrm{f}} = 1.5$ GPa is the Young's modulus for upper surface unconsolidated firn layers, and $D = 32.5$ m is a tuned constant as above. Here, a single constant D is used to describe both the depth variations in density and Young's modulus. While this is not necessary for the derivation of the analytical solutions, the interpretation of D as a length scale of the firn layer thickness indicates that the Young's modulus

is directly proportional to density and inherently related to porosity, similar to porous metallic foams [154].

In the following subsections, the derivation of the far field longitudinal stress is presented, responsible for driving the propagation of mode I crevasses. Two separate cases are first considered, these being the sole inclusion of depth-dependent density and Young's modulus to isolate their individual contributions to maximum crevasse penetration depth. The final case considers the combined effect of depth-dependent density and Young's modulus, the most realistic scenario.

5.1.1 Depth-Dependent Density

In the current section, the derivation of longitudinal stress σ_{xx} is considered for a depth-dependent density following Eq. (5.2), whilst maintaining a constant Young's modulus through the glacier thickness. The derivative of the lithostatic compressive stress for the density distribution is:

$$\frac{\partial \sigma_{zz}}{\partial z} = -\rho(z)g \tag{5.4}$$

where g is the gravitational acceleration. The depth-dependent density is substituted into Eq. (5.4) and integrated over the depth to obtain the vertical stress σ_{zz}.

$$\sigma_{zz} = -\rho_{\mathrm{i}} g\,(H - z) + (\rho_{\mathrm{i}} - \rho_{\mathrm{f}}) D g\left[1 - e^{-(H-z)/D}\right]. \tag{5.5}$$

The above relation consists of a linear stress contribution from fully consolidated ice ρ_{i} and an exponential term that reduces the lithostatic stress, containing the contributions of firn density ρ_{f}. This solution simplifies to the homogeneous ice case when considering $\rho_{\mathrm{i}} = \rho_{\mathrm{f}}$.

Exploiting the plane strain assumption $\varepsilon_{yy} = 0$, allows for the out-of-plane stress σ_{yy} to be found in terms of longitudinal stress σ_{xx} and lithostatic stress σ_{zz}:

$$\sigma_{yy} = \nu \left(\sigma_{xx} + \sigma_{zz} \right) . \tag{5.6}$$

Assuming small strains and small rotations, the longitudinal strain can then be written in terms of σ_{xx} and σ_{zz} by using Hooke's law and Eq. (5.6):

$$\varepsilon_{xx} = \frac{1}{E} \left[(1 - \nu^2)\sigma_{xx} - \nu(1 + \nu)\sigma_{zz} \right] . \tag{5.7}$$

Following this, the membrane strain assumption is adopted due to the thickness of the glacier being several orders of magnitude smaller than the length. The longitudinal strain is therefore invariant with depth [131]:

$$\frac{\partial \varepsilon_{xx}}{\partial z} = 0 . \tag{5.8}$$

Note that the above condition can be derived using Föppl–von Kármán equations describing the large deflections of thin flat plates [155]. Applying this constraint to Eq. (5.7) allows for the derivative of the horizontal stress to be found:

$$\frac{\partial \sigma_{xx}}{\partial z} = \left(\frac{\nu}{1 - \nu} \right) \frac{\partial \sigma_{zz}}{\partial z} \tag{5.9}$$

leading to a far field longitudinal stress of:

$$\sigma_{xx} = \frac{\nu}{1 - \nu} \sigma_{zz} + R_{xx} \tag{5.10}$$

where R_{xx} is the indefinite integration constant that can be interpreted as the depth-invariant tensile resistive stress. Substituting the lithostatic compressive

stress σ_{zz} from Eq. (5.5) gives:

$$\sigma_{xx} = \frac{\nu}{1-\nu}\left\{-\rho_{\mathrm{i}} g(H-z) + (\rho_{\mathrm{i}} - \rho_{\mathrm{f}}) Dg\left[1 - e^{-(H-z)/D}\right]\right\} + R_{xx} \tag{5.11}$$

It can be observed that the far field longitudinal stress is formed of two components: the first being the contribution of the lithostatic compressive stress, which is always negative and is responsible for crevasse closure, while the resistive tensile stress component R_{xx}, which is typically invariant with depth, is responsible for crevasse propagation. It was suggested in van der Veen [49] that the inclusion of firn density would result in deeper crevasse propagation, because the magnitude of the lithostatic compressive stress would be reduced. However, this analysis does not consider the effect of firn density on the tensile resistive stress. The resistive tensile stress R_{xx} can be evaluated by considering force equilibrium over the entire thickness in the longitudinal direction as:

$$\int_0^H \sigma_{xx}\, \mathrm{d}z + F_{\mathrm{w}} = 0 \tag{5.12}$$

where $F_{\mathrm{w}} = \frac{1}{2}\rho_{\mathrm{s}} g h_{\mathrm{w}}^2$ is the hydrostatic force as a result of the ocean water pressure at the glacier terminus. From this equilibrium between the glaciological longitudinal stress and ocean water pressure at the terminus, the resistive tensile stress is found as:

$$R_{xx} = \left(\frac{\nu}{1-\nu}\right) g\left[\frac{\rho_{\mathrm{i}} H}{2} - (\rho_{\mathrm{i}} - \rho_{\mathrm{f}})\, D + \frac{(\rho_{\mathrm{i}} - \rho_{\mathrm{f}})\, D^2}{H}\left(1 - e^{-H/D}\right)\right] - \rho_{\mathrm{s}} g \frac{h_{\mathrm{w}}^2}{2H}\,. \tag{5.13}$$

It is observed that R_{xx} is invariant with depth and may be compressive or tensile, thus may either contribute or prevent crevasse propagation, depending on the ocean water height h_{w}. Substituting the value of R_{xx} into the far field longitudinal

stress Eq. (5.11) gives the following analytical solution:

$$\begin{aligned}\sigma_{xx} =& \frac{\nu}{1-\nu}\rho_{\mathrm{i}} g\left(z-\frac{1}{2}H\right) - \frac{1}{2}\frac{\rho_{\mathrm{s}} g h_{\mathrm{w}}^2}{H} \\ &+ \frac{\nu}{1-\nu}(\rho_{\mathrm{i}}-\rho_{\mathrm{f}})gD\left(-e^{-(H-z)/D} + \frac{D}{H}(1-e^{-H/D})\right)\end{aligned} \tag{5.14}$$

It is noted that this derivation of far field longitudinal stress simplifies to the homogeneous case in Eq. (4.1) when considering $\rho_{\mathrm{i}} = \rho_{\mathrm{f}}$. The first term in Eq. (5.14) is the lithostatic component for homogeneous ice, stating that crevasses in land terminating glaciers may propagate to half of the the glacier thickness, based on the zero stress model. The second term is the contribution of the oceanwater pressure, which is independent of firn density and is always compressive (negative), reducing the stress driving crevasse propagation. The final term contains the contribution of depth-dependent density, found in both the resistive stress and lithostatic stress components. This is a function of the vertical coordinate z and is found to be negative in upper surface regions, allowing for stabilisation of the firn layers and tends to a positive (tensile) constant in deeper regions of the glacier, thus allowing for the potential of deeper crevasses. Thus the inclusion of depth-dependent density may either encourage or prohibit deeper crevasse propagation, depending on glacier thickness H and oceanwater heights h_{w}, which is a more nuanced description than that proposed by van der Veen [49] who neglected any influence of depth-dependent density on resistive stress R_{xx}.

5.1.2 Depth-Dependent Young's Modulus

The influence of a depth-dependent Young's modulus $E(z)$ on far field longitudinal stress is now considered, whilst maintaining a constant density. The contribution from Young's modulus can be seen in the depth-dependent longitudinal

strain:

$$\varepsilon_{xx} = \frac{1}{E(z)}\left[(1-\nu^2)\sigma_{xx} - \nu(1+\nu)\sigma_{zz}\right] . \tag{5.15}$$

Here, the Young's modulus is modelled using the exponential distribution described in Eq. (5.3). For the depth invariant case, Young's modulus E is simply eliminated when considering the membrane strain assumption in Eq. (5.8), thus the longitudinal stress is independent of Young's modulus magnitude, shown in Eq. (5.1) and Eq. (5.14). However, for the depth-dependent Young's Modulus case, E is not eliminated and the longitudinal strain derivative is expressed below using the quotient rule:

$$\frac{\partial \varepsilon_{xx}}{\partial z} = (1-\nu^2)\frac{E\frac{\partial \sigma_{xx}}{\partial z} - \sigma_{xx}\frac{\partial E}{\partial z}}{E^2} - \nu(1+\nu)\frac{E\frac{\partial \sigma_{zz}}{\partial z} - \sigma_{zz}\frac{\partial E}{\partial z}}{E^2} = 0 . \tag{5.16}$$

This can then be rearranged to obtain the following expression for the horizontal stress derivative:

$$\frac{\partial \sigma_{xx}}{\partial z} = \frac{\nu}{1-\nu}\frac{\partial \sigma_{zz}}{\partial z} - \frac{\nu}{1-\nu}\frac{\sigma_{zz}}{E}\frac{\partial E}{\partial z} + \frac{\sigma_{xx}}{E}\frac{\partial E}{\partial z} . \tag{5.17}$$

This derivation simplifies to the depth invariant case if $\partial E/\partial z = 0$. Solving the above ordinary differential equation yields the following longitudinal stress for constant density:

$$\sigma_{xx} = \left(\frac{\nu}{1-\nu}\right)\rho_{\mathrm{i}} g\left[z - \frac{(E_{\mathrm{i}} - E_{\mathrm{f}})}{E_{\mathrm{i}}} H e^{-(H-z)/D}\right] + C_1\left[E_{\mathrm{i}} e^{(H/D)} - (E_{\mathrm{i}} - E_{\mathrm{f}})\, e^{(z/D)}\right] \tag{5.18}$$

where C_1 is an integration constant that can be determined using force equilibrium in the longitudinal direction, defined by Eq. (5.12), which yields:

$$\begin{aligned} C_1 = & \frac{1}{E_{\mathrm{i}} H e^{H/D} - (E_{\mathrm{i}} - E_{\mathrm{f}})\, D\, (e^{H/D} - 1)} \left\{ \frac{\nu}{1-\nu} \right. \\ & \left. \left[\frac{E_{\mathrm{i}} - E_{\mathrm{f}}}{E_{\mathrm{i}}} D \rho_{\mathrm{i}} g H \left(1 - e^{-H/D}\right) - \frac{\rho_{\mathrm{i}} g H^2}{2} \right] - \frac{\rho_{\mathrm{s}} g h_{\mathrm{w}}^2}{2} \right\} \end{aligned} \tag{5.19}$$

Substituting the above into Eq. (5.18), the longitudinal stress distribution is obtained for the depth-dependent Young's modulus and constant density case as:

$$\sigma_{xx} = \frac{\nu}{1-\nu}\rho_i g\left(z - \frac{1-E^*}{2}H\right) - \frac{1}{2}(1+E^*)\frac{\rho_{\mathrm{s}} g h_{\mathrm{w}}^2}{H}\,, \tag{5.20}$$

$$\text{where } E^* = \frac{(E_{\mathrm{i}} - E_{\mathrm{f}})}{E_{\mathrm{i}}}\frac{(1-e^{-H/D})\frac{D}{H} - e^{-(H-z)/D}}{1-(1-e^{-H/D})\frac{(E_{\mathrm{i}}-E_{\mathrm{f}})D}{E_{\mathrm{i}}H}}\,.$$

As expected, the solution for the depth-dependent Young's Modulus case simplifies to the far field longitudinal stress for the depth invariant case, when $E_{\mathrm{i}} = E_{\mathrm{f}}$ ($E^* = 0$). It is observed that the far field longitudinal stress in Eq. (5.20) resembles the homogeneous case, in that σ_{xx} consists of two terms: one considering contributions from glacier self-weight, and the other considering contributions from oceanwater pressure. This is in contrast to the depth-dependent density case, which provided an additional term accounting for firn density ρ_{f}. Instead, the depth-dependent Young's modulus alters both of the existing terms in the longitudinal stress relation by introducing the term E^*. Including the effects of firn layer's modulus redistributes the contribution of the horizontal ocean water pressure from a constant pressure, to being smaller near the surface ($E^* < 0$) and larger near the base ($E^* > 0$).

5.1.3 Depth-Dependent Density and Young's Modulus

The final stress relationship considered is the inclusion of both a depth-dependent density and a depth-dependent Young's modulus, with distributions being described by Eq. (5.2) and Eq. (5.3) respectively. The same derivation process described in the above sections are followed. Here, the longitudinal stress derivative is considered for the depth-dependent Young's modulus presented in Eq. (5.17)

and the lithostatic compressive stress and derivative for depth-dependent density in Eq. (5.4) and Eq. (5.5) respectively, are substituted. The ordinary differential equation is solved using the MATLAB symbolic toolkit to obtain the following longitudinal stress distribution σ_{xx} below:

$$\begin{aligned}\sigma_{xx} =& \frac{\nu}{1-\nu} g\left(-\rho_{\mathrm{i}}(H-z) + (\rho_{\mathrm{i}}-\rho_{\mathrm{f}})\, D(1-e^{-(H-z)/D})\right) \\ &+ (E_{\mathrm{i}} e^{H/D} - (E_{\mathrm{i}}-E_{\mathrm{f}})\, e^{z/D}) C_2\end{aligned} \tag{5.21}$$

where C_2 is the indefinite integration constant, which can found using force equilibrium thus:

$$\begin{aligned}C_2 =& \frac{1}{E_{\mathrm{i}} H e^{H/D} - (E_{\mathrm{i}}-E_{\mathrm{f}})\, D\,(e^{H/D}-1)} \left\{ \frac{\nu}{1-\nu} \left[\frac{\rho_{\mathrm{i}} g H^2}{2} \right.\right. \\ &\left.\left. -(\rho_{\mathrm{i}}-\rho_{\mathrm{f}}) g H D + (\rho_{\mathrm{i}}-\rho_{\mathrm{f}}) g D^2 (1-e^{-H/D}) \right] - \frac{\rho_{\mathrm{s}} g h_{\mathrm{w}}^2}{2} \right\}\end{aligned} \tag{5.22}$$

Substituting C_2 back into σ_{xx} and rearranging gives the final expression:

$$\begin{aligned}\sigma_{xx} =& \frac{\nu}{1-\nu} \rho_{\mathrm{i}} g \left(z - \frac{1-E^*}{2} H \right) - \frac{1}{2}(1+E^*) \frac{\rho_{\mathrm{s}} g h_{\mathrm{w}}^2}{H} \\ &+ \frac{\nu}{1-\nu} (\rho_{\mathrm{i}}-\rho_{\mathrm{f}}) g D \left\{ \left[1 - e^{-(H-z)/D}\right] + (1+E^*) \left[-1 + \frac{D}{H}(1-e^{-H/D}) \right] \right\}\end{aligned} \tag{5.23}$$

where the Young's modulus ratio E^* defined in Eq. (5.20). It is observed that the first two terms of Eq. (5.23) are identical to the longitudinal stress for depth--dependent Young's modulus, Eq. (5.20). The additional term contains the contribution of firn density. This can be further decomposed into a component independent of Young's modulus and a component multiplied by the Young's modulus ratio. An exponential distribution is observed when plotting the third term in Eq. (5.23), leading to a compressive stress in the upper surface regions, reducing to a small tensile stress close to the base. The above equation reduces to the analytical relation for depth-dependent density in Eq. (5.14), if the Young's

modulus is constant ($E^* = 0$); and to the analytical relation for depth-dependent Young's modulus Eq. (5.20), if the density is constant, $\rho_\mathrm{i} - \rho_\mathrm{f} = 0$.

5.1.4 Limitations of analytical LEFM models

There are a few limitations to be noted, regarding the outcomes of the LEFM models used in this study (refer to the Appendix C and Appendix D). First, the depth variations of the mechanical properties are assumed to be based on borehole samples from ice cores in the Ronne ice shelf; therefore they may not be fully representative of other Antarctic ice shelves or glaciers elsewhere. For example, temperate glaciers that are subject to higher rates of melting and refreezing undergo a faster rate of densification, owing to meltwater percolating into pore spaces and refreezing [156]. Thus the process of firn densification is dependent on environmental factors including accumulation rates, overburden pressure, temperature and local strain rates [157]. For instance, the Seward Glacier, Yukon, Canada fully consolidates at a depth of 13 m, in contrast to sites at the Greenland ice sheet where transitions from firn to glacial ice occur at depths of approximately 66 m [151]. Data from surrounding borehole samples should therefore be considered when assessing whether to include the effects of firn layer properties.

The fracture analysis used in the following sections also assumes that over short timescales ice behaves as an elastic compressive material ($\nu = 0.35$), with crevasses propagating rapidly in a brittle manner. However in reality, ice behaves like an incompressible fluid over longer timescales, with viscous deformation being described using Glen's flow law [123]. The effects of time dependent deformation can be included in an *ad hoc* manner by taking the stress from Stokes based formulations and using LEFM to propagate crevasses in a staggered manner [53]. Furthermore, owing to the small tensile strength of ice, the size of the fracture process zone is defined by the length scale $\ell_c \approx K_{IC}^2(1-\nu^2)/\sigma_c^2$, where K_{IC} is the mode I fracture toughness of ice and σ_c is the cohesive tensile strength of ice [72].

For the values typically used for ice in the literature $\ell_c \approx 2.3$ m, which may not be sufficiently small for LEFM to be strictly valid in all cases. To account for the nonlinear fracture mechanics and to avoid *ad hoc* coupling between ice flow and fracture modeling, it is beneficial to utilize a phase field fracture model [132] or a cohesive zone model [83] or a nonlocal creep damage model [73, 74]. However, these nonlinear models are computationally expensive and not so straightforward to implement within numerical ice sheet models, hence analytical LEFM models are desirable.

5.2 Results for grounded glaciers

Currently, the numerical results for the grounded glacier case are presented for each material property distribution and are compared with the homogeneous solutions. Figure 5.2 shows the analytical solutions of the far field longitudinal stress σ_{xx} in a land terminating grounded glacier ($h_w = 0$ m) of height $H = 125$ m. Each subfigure includes the longitudinal stress versus depth profiles for depth-dependent properties (derived in the previous section) and are compared to the homogeneous case. In addition to the analytical solutions, numerical results from the finite element solver COMSOL Multiphysics are plotted for verification of the analytical expressions. The analytical solutions derived are identical to the numerical results, confirming the correctness of the presented expressions along with appropriateness of the membrane strain assumption.

Using these stress solutions, crevasse depths based on an analytical LEFM model are predicted, based on the formulation described in Appendices C and D. For grounded glaciers with free tangential slip at the base, the 'double edge crack' weight functions are used (refer to Appendix C), since this was shown to provide

stress intensity factors that are consistent with those calculated using the displacement correlation method [142]. Specifically, the evolution of an isolated surface crevasse within a grounded glacier of height $H = 125$ m is considered, assuming damage to initialise beneath a pre-specified surface crack of depth $d_{\mathrm{s}} = 10$ m.

The proceeding subsections discuss the impact of including depth-dependent material properties on the longitudinal stress distribution and the stabilised crevasse depth, compared to the homogeneous case.

5.2.1 Influence of Depth-Dependent Density

If the material properties of ice are assumed to be depth-independent, then the longitudinal stress σ_{xx} varies linearly with depth, according to Eq. (5.1). In the case of a land terminating glacier ($h_{\mathrm{w}} = 0$) with free tangential slip at the base, the σ_{xx} profile is symmetric about the centre line ($z = H/2$). This stress is tensile in the regions above the centre line with a maximum value of $\sigma_{xx} \approx 300$ kPa at the top surface for ice thickness $H = 125$ m (blue line in Figure 5.2). If a depth-dependent density is incorporated (green line in Figure 5.2a), the maximum value of σ_{xx} is reduced to ≈ 235 kPa, with a nonlinear distribution in the upper region. Approximately 50 m below the top surface, σ_{xx} tends towards a linear distribution, with the compressive stress nearer the base slightly less than that compared to the homogeneous case due to the reduced weight of the ice. Parametric studies are now discussed to explore the effect of depth-dependent properties on crevasse propagation.

The first parametric study considers a dry (air filled) crevasse, with different values of ocean water height h_{w}. The normalized crevasse depths (d_{s}/H) obtained using LEFM for this case are presented in Figure 5.3a. For land terminating

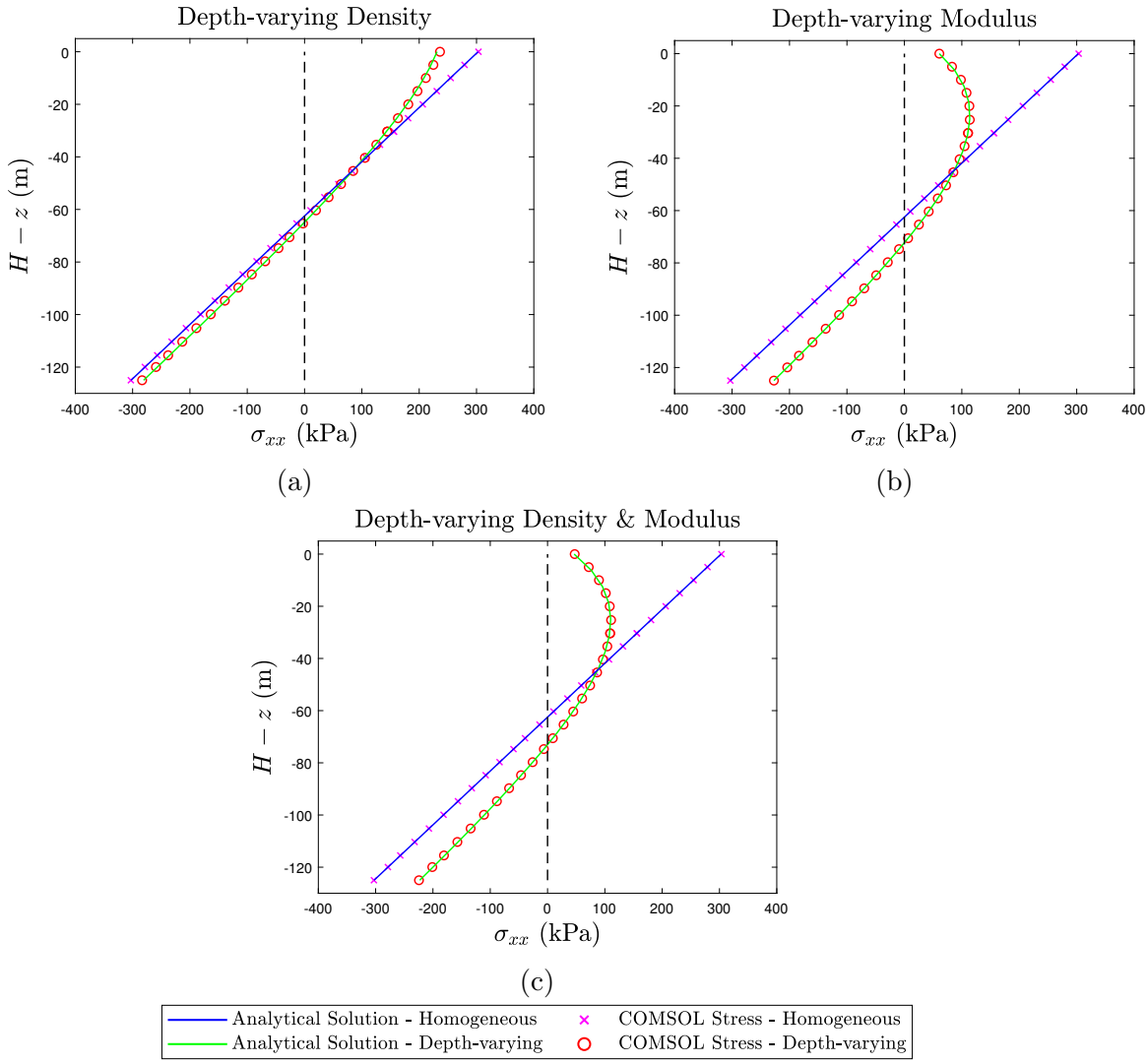

Figure 5.2: Far field longitudinal stress σ_{xx} throughout the depth of a land terminating glacier ($h_{\mathrm{w}} = 0$), showing the effects of (a) variations in density, (b) variations in Young's modulus, and (c) variations in both density and Young's modulus. Numerical reference values are obtained via the COMSOL Multiphysics model for constant (crosses) and depth-dependent properties (circles). The analytical solution for depth-dependent properties are found in Eq. (5.14), (5.20), and (5.23) respectively, and represented by the green lines. The horizontal dashed line indicates the zero stress level.

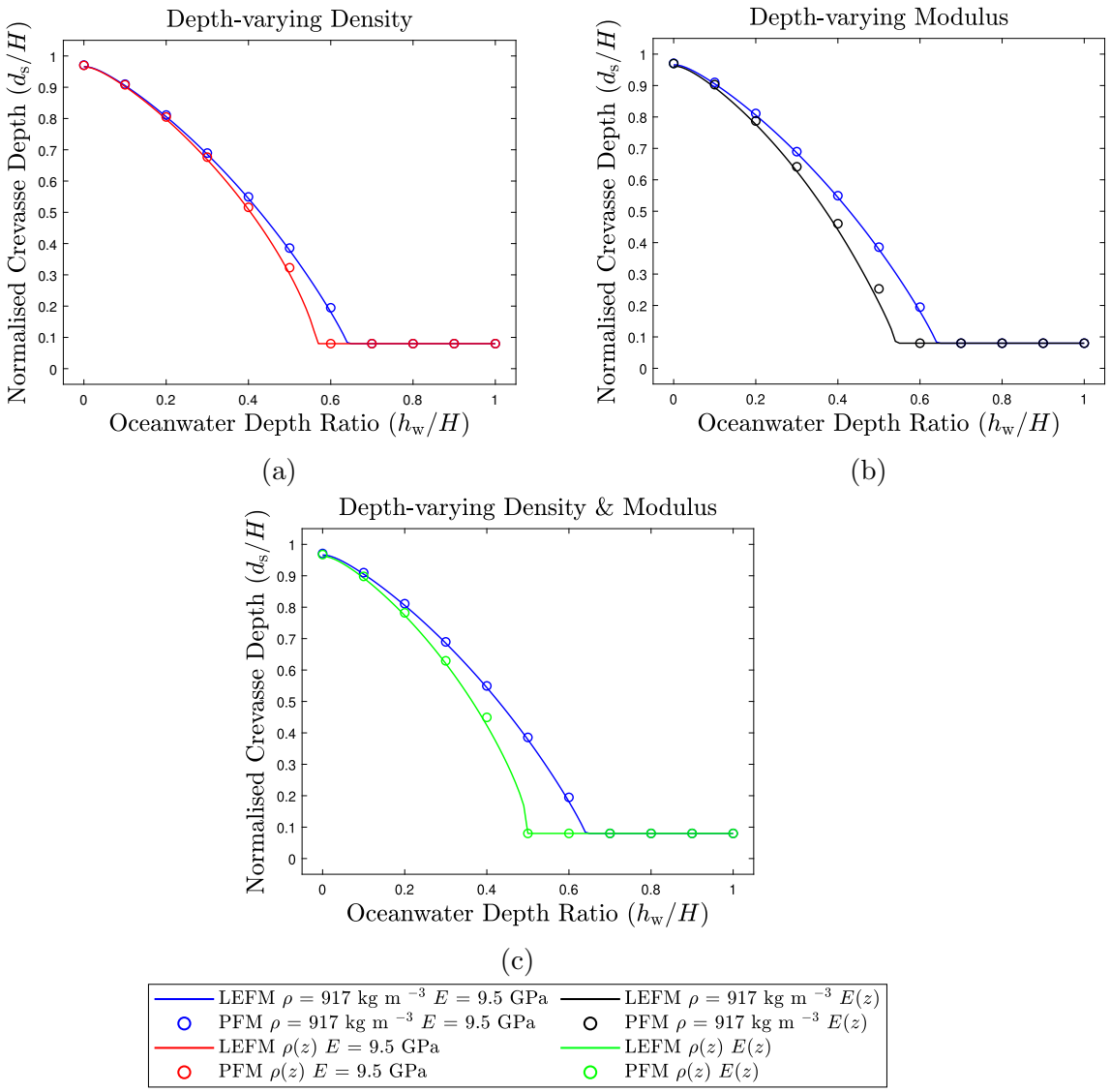

Figure 5.3: Normalised crevasse depth predictions versus oceanwater height ratio for a single isolated dry crevasse in a linear elastic ice sheet, considering homogeneous and depth-dependent mechanical properties.

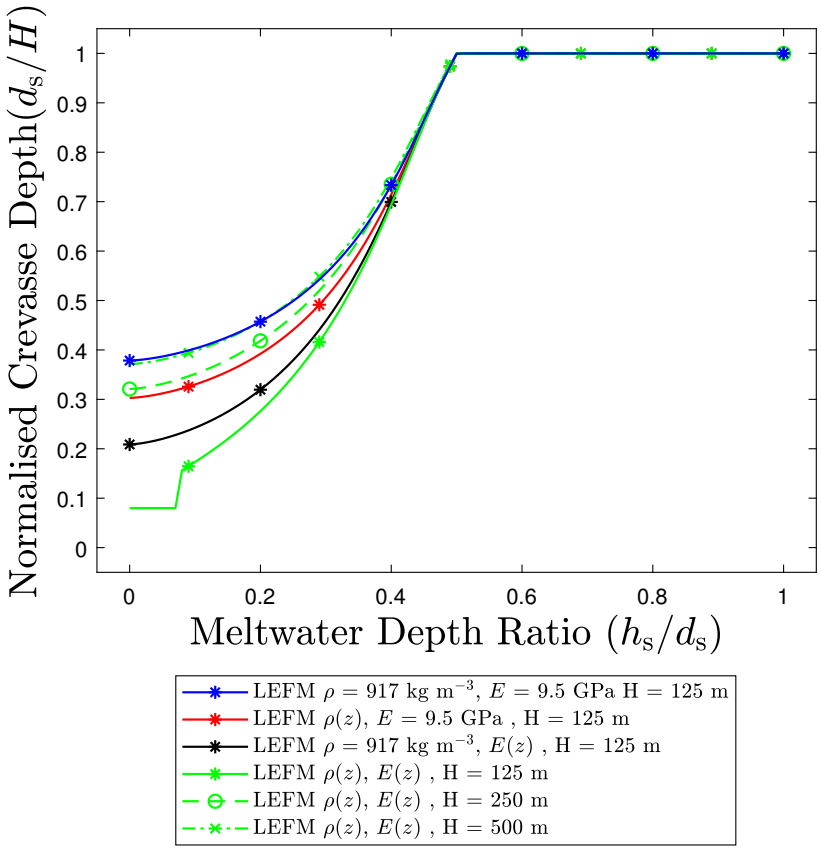

Figure 5.4: Normalised crevasse depth predictions versus meltwater depth ratio for a single isolated crevasse in a linear elastic ice sheet, considering homogeneous and depth-dependent mechanical properties, for an oceanwater height $h_w = 0.5H$.

glaciers ($h_w = 0$ m), the crevasse propagates to the full thickness of the glacier for both the homogeneous and depth-dependent cases, because there is no compressive ocean water pressure to arrest crevasse growth. However, as ocean water height is increased, the stabilised crevasse depth reduces and the inclusion of the depth-dependent density comes into effect and further reduces the stabilised crevasse depth. With ocean water heights of $h_w > 0.7H$, the longitudinal stress is sufficiently compressive such that the crevasse does not grow beyond the initial specified depth of 10 m. To verify the accuracy of the LEFM model (solid line) results presented, the results obtained from the phase field fracture model (markers) are also shown in Figure 5.3 [132].

In Figure 5.4, the relation between the crevasse depth ratio (d_s/H) and the meltwater depth ratio (h_s/d_s) for the thinner glacier ($H = 125$ m). The ocean water height is fixed at $h_w = 0.5H$ for both the homogeneous (blue line) and depth--dependent density (red line) scenarios. The largest reduction of 20% in the stabilised crevasse depth is observed for a dry crack ($h_s = 0$) when considering the effect of depth-dependent density. The additional tensile stress provided by the presence of meltwater allows the surface crevasse to penetrate deeper into the strata, with full fracture occurring for meltwater depth ratios greater than 0.5 in both scenarios.

As shown in Figure 5.2a, the inclusion of the firn layer reduces the longitudinal stress in the upper regions of the glacier, and tends towards the homogeneous stress profile in the consolidated strata. The effect of this stress variation can be understood from Figure 5.4. As the meltwater depth ratio is increased, the crevasse penetrates deeper into the glacier and the influence of the firn layer on the stress state disappears; hence the crevasse depth for depth-dependent case agrees with the homogeneous case for all $h_s/d_s > 0.4$. It is found that the normalized crevasse depth ratio is insensitive to the glacier thickness H in

the homogeneous case, because the thickness only controls the magnitude of the longitudinal stress but not the depth at which the stress becomes compressive. However, in the depth-dependent case, the normalized crevasse depth ratio is sensitive to the glacier thickness, but converges with the homogeneous case for thicker glaciers. For example, the maximum percentage difference in crevasse depth ratio between the depth-dependent and homogeneous cases is 20%, 4.5% and 1% for $H = 125$ m, $H = 250$ m and $H = 500$ m, respectively.

5.2.2 Influence of Depth-Dependent Young's Modulus

The influence of a variable Young's modulus on the far field longitudinal stress is shown in Figure 5.2b. It can be observed that there is a greater deviation from the homogeneous case, relative to the depth-dependent density case. In the upper regions σ_{xx} is further reduced to approximately 60 kPa and the stress profile is highly nonlinear. However, at lower depths where the firn fully consolidates to ice, the stress profile becomes linear. The maximum compressive stress at the glacier base is less due to the reduction in overburden pressure in the upper strata. Notably, the depth at which the stress becomes zero increases from 62.5 m in the homogeneous case to 72.3 m in the variable Young's modulus case. However, the stress intensity factor at the crevasse tip decreases due to a reduction in the magnitude of longitudinal stress; the firn layer thus causes a reduction in crevasse penetration depth.

The propagation of isolated dry crevasses are now considered for the depth--dependent Young's modulus scenario, using the LEFM model and the longitudinal stress relation derived in Eq. (5.20). The results for the parametric study evaluating the normalized crevasse depths for various ocean water heights h_{w} are presented in Figure 5.3b. Similar to the results in Figure 5.3a, the dry crevasse

propagates to the same depth in the depth-dependent and homogeneous cases for low ocean water heights. Since the crevasse propagates deeper into the fully consolidated ice regions, the properties of firn layer have little impact on crevasse depth. As the ocean water height increases, the compressive stress resisting crevasse propagation increases, the crevasse growth is thus arrested at a shallower depth. The influence of the variable Young's modulus can be observed in these intermediate ocean water heights where $h_{\mathrm{w}}/H = [0.2 - 0.6]$, as the crevasse depth reduces when accounting for the firn layers. The maximum difference in crevasse depth is approximately $0.2H$, at an ocean water height of $h_{\mathrm{w}} = 0.55H$. For ocean water heights greater than $h_{\mathrm{w}} = 0.55H$, the crevasse does not propagate beyond the initial specified depth of 10 m.

In Figure 5.4, the normalized crevasse depth ratio versus meltwater depth ratio considering depth-dependent Young's modulus is also reported (black line). The largest reductions in crevasse depth are observed for the thinner glacier ($H = 125$ m) with a dry crevasse, where d_{s}/H is reduced from 0.378 in the homogeneous case to 0.209 in the depth-dependent case. The difference in normalized crevasse depth reduces as the meltwater depth ratio increases because the crevasse penetrates deeper into the fully consolidated strata, thus reducing the influence of firn properties. For thicker glaciers, the difference between the homogeneous and depth-dependent Young's modulus cases is smaller, which is attributed to the increase in magnitude of far field longitudinal stress based on the stress analysis. The maximum percentage difference in crevasse depths for $H = 125$ m is 44.9%, $H = 250$ m is 16.5% and 6.0% for $H = 500$ m.

5.2.3 Influence of Depth-Dependent Young's Modulus and Density

The next set of results entails the propagation of an isolated surface crevasse driven by the longitudinal stress considering both depth-dependent Young's modulus and density shown in Eq. (5.23). The stabilised crevasse depths for a dry crevasse in a grounded glacier of height $H = 125$ m, calculated using LEFM and the phase field method, for various ocean water heights h_{w} are presented in Figure 5.3c.

As expected, for lower ocean water heights the crevasse depths are in agreement with the homogeneous case, owing to the crevasse penetrating deeper into the compressive regions of the glacier. The largest reductions in crevasse depths are observed for intermediate values of ocean water height $h_{\mathrm{w}}/H = [0.2{-}0.4]$; whereas the crevasse does not propagate beyond the initially specified depth for ocean water heights greater than $h_{\mathrm{w}} = 0.4H$ in this case (green line in Figure 5.3c).

The relationship between stabilised crevasse depth ratios and meltwater depth ratios is presented in Figure 5.4 for three different glacier thicknesses (green lines). For the thinnest glacier ($H = 125$ m) the longitudinal stress is significantly reduced in the upper regions due to the smaller stiffness and density of the firn layer, which prevents the dry crevasse from propagating beyond the initially specified depth of $0.08H$, compared to a crevasse depth ratio of $0.378H$ for the homogeneous case. The difference in crevasse depth ratios reduces with increasing meltwater depth ratios because the crevasse propagates deeper into the consolidated ice strata. Full depth propagation is achieved for meltwater depth ratios $h_{\mathrm{s}}/d_{\mathrm{s}} \geq 0.5$. The percentage difference in penetration depth for the dry crevasse is 18.0% for $H = 250$ m and 6.21% for $H = 500$ m. Overall, it is found that the influence of depth-dependent firn material properties is lesser in thicker glaciers,

but the effect is more prominent if the variation in both Young's modulus and density with depth is considered.

5.2.4 Influence of Depth-Dependent Poisson Ratio

For the crevasse propagation studies previously presented, a depth invariant Poisson ratio of $\nu = 0.35$ was assumed. However, it has been suggested that the Poisson ratio also exhibits a linear dependency on ice density and therefore leads to a depth-dependent profile [158]. Furthermore, Schlegel et al. [159] and King and Jarvis [160] provide a depth-dependent Poisson ratio profile based on seismic velocity measurements on ice cores. To study the effect of this depth-dependent Poisson ratio, a linear elastic fracture mechanics study is performed. It is assumed that Poisson's ratio follows an exponential distribution with depth, similar to the density and Young's modulus distributions:

$$\nu(z) = \nu_{\mathrm{i}} - (\nu_{\mathrm{i}} - \nu_{\mathrm{f}})e^{-(H-z)/D} \tag{5.24}$$

where $\nu_{\mathrm{f}} = 0.07$ is the Poisson ratio of firn in the upper surface, $\nu_{\mathrm{i}} = 0.35$ is the Poisson ratio of fully consolidated ice and $D = 32.5$ m is the tuned constant. This profile approximates the observations from Schlegel et al. [159], where the length parameter D is scaled to match the current density and Young's modulus profiles as this profile was obtained at a different location (with significantly different ice sheet and firn thickness). Since it is not possible to derive a fully analytical expression for the stress profiles with this depth-dependent Poisson ratio, the longitudinal stress profiles are obtained numerically through the finite element method. Once obtained, the stresses are used to drive the propagation of the surface crevasse in the linear elastic fracture mechanics study. A dry (air filled) crevasse is considered, with different values of oceanwater height h_{w} and

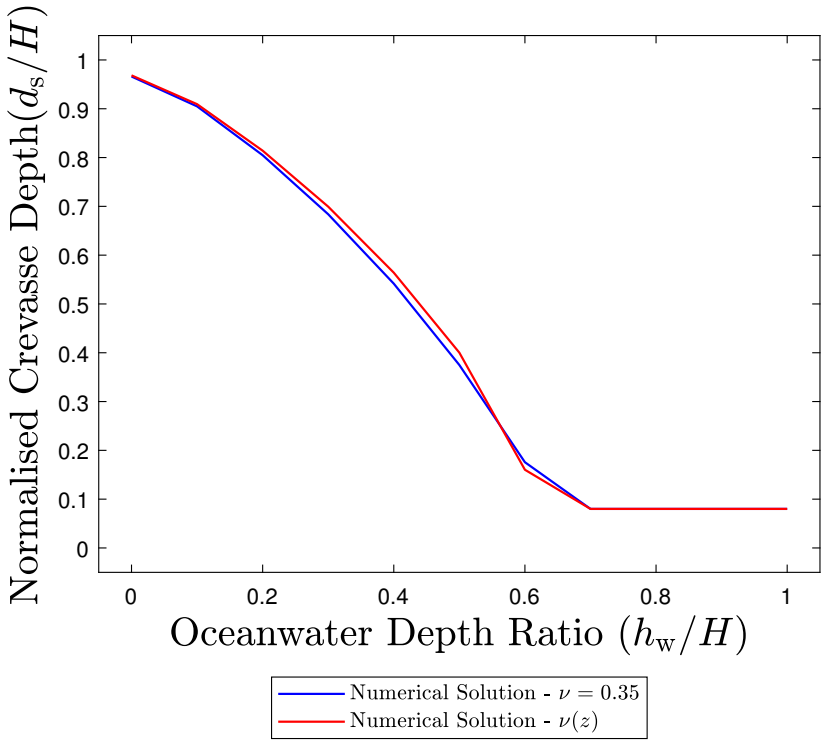

Figure 5.5: Normalised crevasse depth predictions versus oceanwater height ratio for a single isolated dry crevasse in a linear elastic ice sheet, considering homogeneous and depth-dependent Poisson Ratio.

the normalised crevasse penetration depth versus oceanwater height h_{w} is plotted in Figure 5.5. This figure shows that the effect of including variations in Poisson ratio have a more limited effect compared to density and Young's modulus variations. The largest percentage difference in crevasse depth was observed for intermediate oceanwater levels, with an increase of 6% in crevasse depth with respect to the homogeneous case when considering a depth-dependent Poisson ratio, for an oceanwater height of $h_{\mathrm{w}} = 0.5H$. This is in contrast to the inclusion of firn density and Young's modulus, which predict a reduction in stabilised crevasse depth for surface crevasses in grounded glaciers. The effect of including a depth-dependent Poisson ratio is less influential compared to density and Young's modulus, as depth-dependent density resulted in a reduction of 20% of the crevasse depth and depth-dependent Young's modulus resulted in a reduction of 45% of the crevasse depth. It is therefore concluded that the inclusion of variations in Poisson ratio does not play a significant role in crevasse propagation.

5.3 Results for floating ice shelves

The final set of results entail the propagation of surface crevasses in floating ice shelves. An idealised rectangular ice shelf geometry is considered, of variable height H and length $L = 5000$ m. Three types of external loads act on the ice shelf: gravitational self-weight causing a body force, ocean water pressure at the base and terminus of the ice shelf and meltwater pressure in the crevasse causing surface forces. A Robin-type boundary condition is applied at the base of the ice shelf, because the buoyancy pressure is a function of the vertical displacement u_z, as given by $\rho_{\mathrm{s}} g \left(h_{\mathrm{w}} - u_z\right)$. The far left terminus is constrained to prevent free body motion, the top surface is considered to be traction free, and Neumann boundary condition is applied on the right edge to account for the ocean water pressure,

similarly to the grounded glacier case. A schematic diagram representing the applied boundary conditions is shown in Figure 4.10.

The floatation heights for the buoyancy pressure are found by assuming local hydrostatic equilibrium. For the homogeneous ice case, this simplifies to the ratio of ice density to ocean water density, that is $h_{\mathrm{w}}/H = \rho_{\mathrm{i}}/\rho_{\mathrm{s}} \approx 0.9$. However, the inclusion of the depth-dependent density profile leads to a reduction in the applied gravitational body force, causing a decrease in the floatation height. The reduction in floatation heights is evaluated for each ice shelf thickness by integrating the depth-dependent density profile over the entire ice shelf thickness and dividing by the thickness and ocean water density. Thus, h_{w}/H is equal to 0.7560 for $H = 125$ m, 0.8268 for $H = 250$ m, 0.8629 for $H = 500$ m and 0.8809 for $H = 1000$ m. For deeper ice shelves, the material properties of firn layers become less significant as the firn layer thickness is small relative to ice shelf thickness; therefore, the floatation depth tends towards the homogeneous case for thicker ice shelves.

Because of the buoyancy condition at the base and the dependence on ice shelf deflection, the analytical solutions for longitudinal stress derived in Sections 5.1.1, 5.1.2 and 5.1.3 are not appropriate in the regions closer to the terminus. In Clayton et al [132], it is shown that far away from the terminus the longitudinal stress in the ice shelf agrees well with analytical solutions for grounded glaciers. Therefore, a finite element analysis is used to extract the longitudinal stress data as a function of vertical coordinate z at the horizontal position $x = 4750$ m (i.e., 250 m from the ice shelf terminus). The data is fitted to a sixth order polynomial equation, with coefficients presented in Table D.1, which defines the stress function $\sigma_{xx}(z)$. Surface crevasses in the far field region are ignored because the longitudinal stress is significantly compressive, preventing their propagation, regardless of whether the crevasses were filled with meltwater or not. The propaga-

H	$\rho = 917$ kg m^{-3}, $E = 9.5$ GPa	$\rho = 917$ kg m^{-3}, $E(z)$	$\rho(z)$, $E = 9.5$ GPa	$\rho(z)$, $E(z)$
125 m	0.099	0.080 (-19.5%)	0.250 (+151.8%)	0.194 (+95.0%)
250 m	0.127	0.080 (-36.9%)	0.203 (+59.8%)	0.174 (+37.4%)
500 m	0.129	0.108 (-16.2%)	0.167 (+28.8%)	0.156 (+20.3%)
1000 m	0.121	0.114 (-5.8%)	0.138 (+14.0%)	0.134 (+10.7%)

Table 5.1: Normalised crevasse depths for a dry ($h_s/d_s = 0.0$) isolated surface crevasse within a floating ice shelf close to the front ($x = 4750$ m), calculated using the LEFM method in [141]. Bracketed values represent the difference in crevasse depth between the variational and homogeneous cases normalised by the crevasse depth for homogeneous ice.

H	$\rho = 917$ kg m^{-3}, $E = 9.5$ GPa	$\rho = 917$ kg m^{-3}, $E(z)$	$\rho(z)$, $E = 9.5$ GPa	$\rho(z)$, $E(z)$
125 m	0.317	0.294 (-7.2%)	0.911 (+187.1%)	0.914 (+187.9%)
250 m	0.362	0.359 (-1.0%)	0.649 (+79.2%)	0.651 (+79.8%)
500 m	0.370	0.370 (0.0%)	0.512 (+38.4%)	0.513 (+38.6%)
1000 m	0.375	0.374 (-0.3%)	0.447 (+19.2%)	0.445 (+18.7%)

Table 5.2: Normalised crevasse depths for an isolated surface crevasse with a meltwater depth ratio of $h_s/d_s = 0.75$ within a floating ice shelf close to the front ($x = 4750$ m), calculated using the LEFM method in [141]. Bracketed values represent the difference in crevasse depth between the variational and homogeneous cases normalised by the crevasse depth for homogeneous ice.

tion of surface crevasses close to the terminus (ice-ocean front) is investigated by estimating the final/stabilized crevasse depth using LEFM. The LEFM model used in Krug et al [141] (see Appendix D) is appropriate for floating ice shelves, as this was shown to match numerically calculated stress intensity factors using the displacement correlation method [142].

Crevasse penetration depths versus meltwater depth ratio h_s/d_s from the LEFM model are presented in Figure 5.6. Penetration depths for the dry crevasse ($h_s/d_s = 0$) and for $h_s/d_s = 0.75$ are also reported in Table 5.1 and Table 5.2 respectively, for ease of comparing data points.

For the homogeneous ice case, there is minimal influence in normalised crevasse

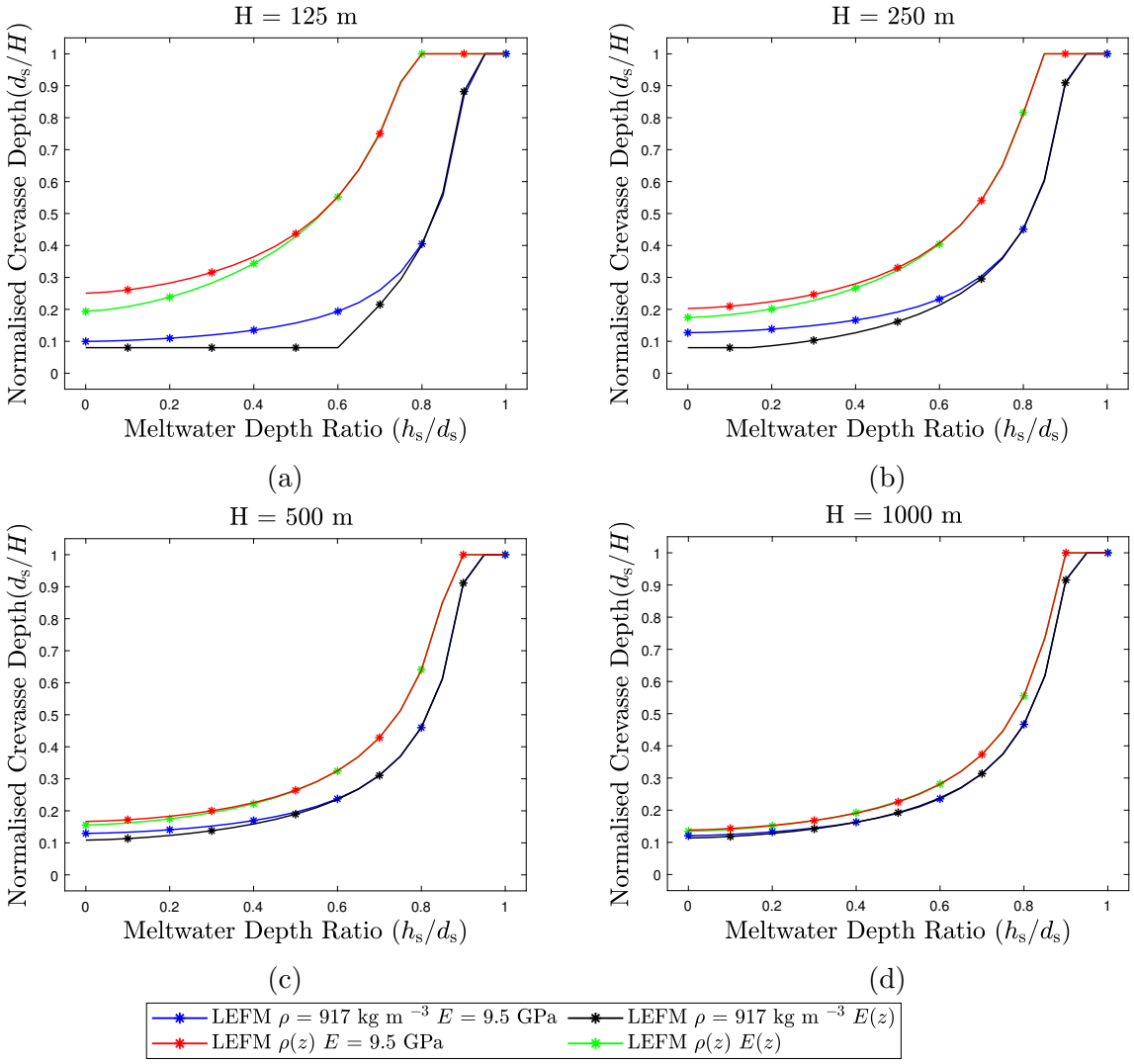

Figure 5.6: Normalised crevasse depth predictions versus meltwater depth ratio for an isolated surface crevasse in a floating ice shelf close to the front $x = 4750$ m.

depth from increasing glacier thickness (blue lines); for example the maximum difference in penetration depth for the dry crevasse is $0.022H$ when increasing ice shelf thickness. Surface crevasses with low levels of meltwater only penetrate a few metres below the surface, owing to the longitudinal stress profile being predominantly compressive due to the high ocean water pressure. For $h_{\mathrm{s}}/d_{\mathrm{s}} < 0.6$, an incremental increase in meltwater does not result in significant crevasse growth. Full fracture propagation is only observed when crevasses are almost fully filled with meltwater ($h_{\mathrm{s}}/d_{\mathrm{s}} > 0.9$), where the meltwater pressure is sufficient to overcome the compressive longitudinal stress.

Considering depth-dependent Young's modulus leads to a minor reduction in stabilised crevasse depth (black lines), with no growth occurring beyond the initial notch for meltwater depth ratios of $h_{\mathrm{s}}/d_{\mathrm{s}} < 0.6$ for $H = 125$ m. Penetration depths match with the homogeneous case for meltwater depth ratios of $h_s/d_s \geq 0.8$ as the crevasse penetrates deeper into the ice strata. The influence of depth-dependent Young's modulus reduces with increasing ice shelf thickness. This is the most noticeable for the crevasse depths reported in Table 5.2, as the percentage difference between the depth-dependent modulus and the homogeneous cases reduces to 1% for $H = 250$ m.

Considering depth-dependent density in the fracture analysis results in surface crevasses propagating to deeper into the ice strata (red lines), with a dry crevasse propagating to a depth of $0.250H$ compared to $0.099H$ for homogeneous ice within an ice shelf of thickness $H = 125$ m. This is in contrast to the grounded glacier case (where crevasse depth decreased) and can be attributed to the reduction in overburden pressure and the reduced buoyancy height, specific to ice shelves. The inclusion of meltwater within the crevasse results in an increased penetration depth, and full thickness fracture is achieved for meltwater depth ratios of $h_{\mathrm{s}}/d_{\mathrm{s}} \geq 0.8$. The largest differences in penetration depth for the depth-

dependent density, compared to the homogeneous case are observed in Table 5.2. For thin ice shelves ($H = 125$ m), and a meltwater depth ratio of $h_s/d_s = 0.75$, the crevasse propagates approximately 3 times deeper when accounting for the depth-dependent density. Similarly to the grounded glacier case, the influence of the depth-dependent density is reduced when the ice shelf thickness increases, owing to a larger proportion of ice being fully consolidated. However, there are still some differences in penetration depth compared to the homogeneous case for thick ice shelves ($H = 1000$ m), with a percentage difference of 14.0% for the dry crevasse, and 19.2% for $h_s/d_s = 0.75$.

Including the effects of both depth-dependent density and depth-dependent modulus highlights that density is the more prominent property influencing surface crevasse propagation in ice shelves. It is observed in Figure 5.6 that the majority of results for depth-dependent density and modulus (green lines) overlap the depth-dependent density results (red lines). The exception to this is for dry crevasses in thin ice shelves, where the stabilised penetration depth is $0.194H$ compared to $0.250H$ when considering solely depth-dependent density.

The current study suggests as the ice shelves become thinner due to increased basal melting in warmer oceans, the effects of the firn layer can make them more vulnerable by allowing deeper crevasse propagation. However, without the presence of any meltwater, full depth penetration of surface crevasses in ice shelves may not be possible. Therefore, an important aspect to explore in a future study is the effect of the firn layer on basal crevasse propagation in ice shelves, which likely controls rift formation and iceberg calving.

5.4 Nonlinear Viscous Incompressible Rheology

The above analysis has considered ice to behave as a linear elastic compressible solid, with a Poisson ratio of $\nu = 0.35$. This is a common assumption if crevasse propagation occurs in a rapid and brittle manner, such that the cracking occurs on a timescale well below the Maxwell time (for glacial ice this is in the order of hours to days). If the slow development of crevasses is to be considered, with crevasses stabilising over a span of weeks, then ice should be considered as an incompressible solid. This can be achieved by setting the Poisson ratio to $\nu \approx 0.5$ (using $\nu = 0.49$ in the studies to prevent numerical issues). In addition, a finite element simulation is conducted for a grounded glacier, including the viscous contributions of ice flow, modelled through Glen's flow law and extracted numerical values of the longitudinal stress. To illustrate the influence of ice rheology, the longitudinal stress profile for a land terminating ($h_{\mathrm{w}} = 0$) grounded glacier is plotted, considering linear elastic compressibility ($\nu = 0.35$), linear elastic incompressibility ($\nu \approx 0.5$) and a nonlinear viscous rheology in Figure 5.7. Firstly, it is noted that when ice is considered as linear elastic incompressible ($\nu \approx 0.5$), a stress solution is obtained which matches the steady state creep stress state derived by Weertman 1957 [153] for a depth-independent density, and matches stress profiles obtained through simulations using a viscoelastic rheology. This is owing to elastic and viscous stress components being equal in a Maxwell model and strain components being additive. It is observed that stresses are more extensional in the upper surface and more compressive at the base when considering incompressibility and that stress is independent of ice rheology (Glen's law creep coefficients). For the homogeneous case, the longitudinal stress varies linearly with depth and is symmetrical about the centre line $z = H/2$. Similar to the linear elastic compressible case, the inclusion of depth-dependent density results in a reduction in both the lithostatic stress contribution σ_{zz} and the resisitive

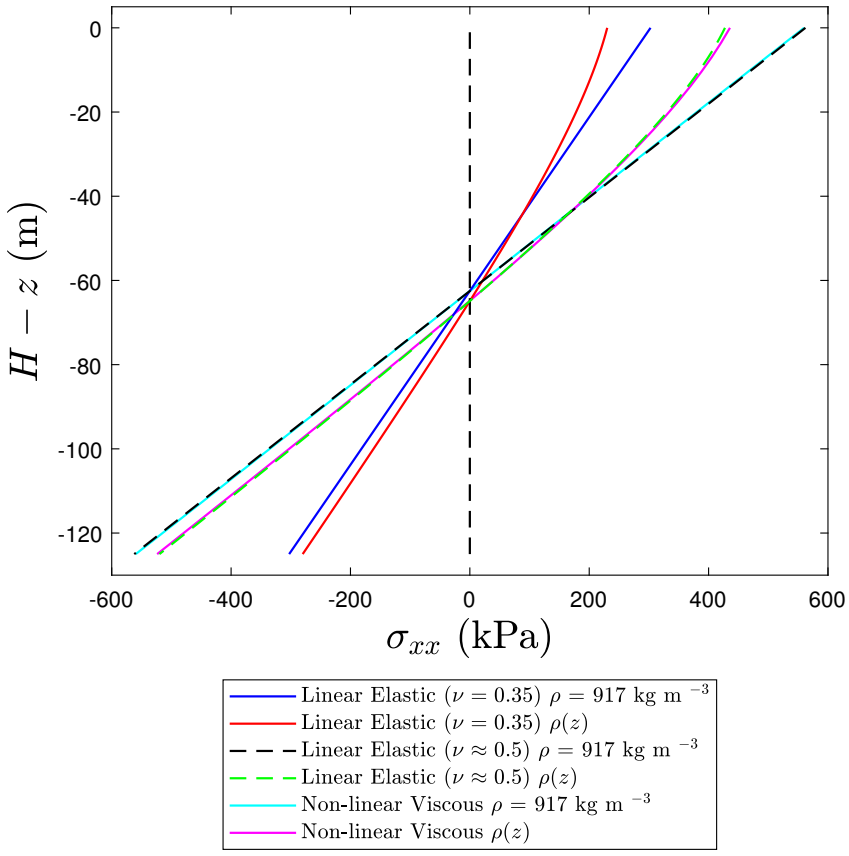

Figure 5.7: Far field longitudinal stress σ_{xx} throughout the depth of a land terminating glacier ($h_{\mathrm{w}} = 0$), showing the effects of depth-dependent density $\rho(z)$; considering linear elastic compressibility ($\nu = 0.35$), linear elastic incompressibility ($\nu \approx 0.5$) and a nonlinear viscous rheology.

stress R_{xx}, for both material rheologies, a point that was neglected by van der Veen 1998 [50] who considered R_{xx} to be independent of depth-dependent density. The longitudinal stress profiles presented in Figure 5.7 are used to drive crevasse

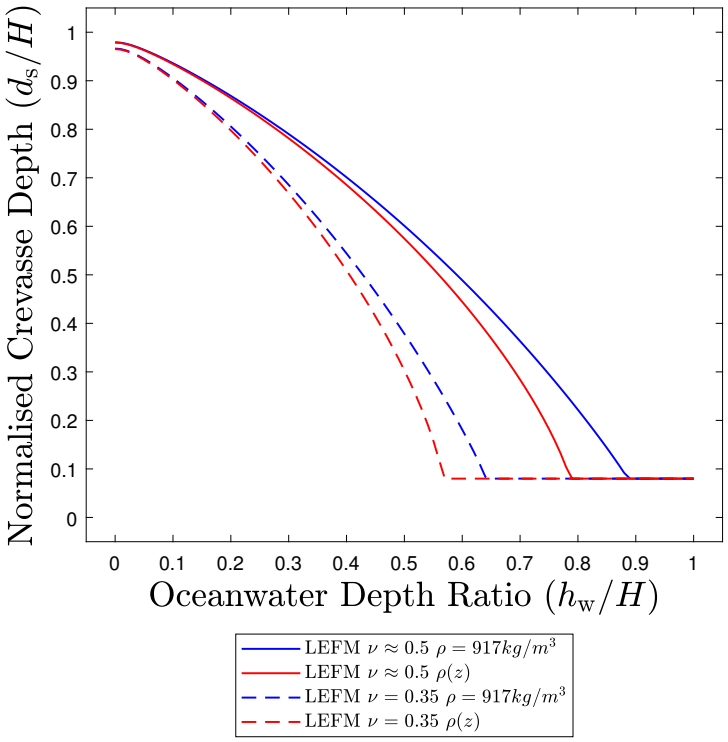

Figure 5.8: Normalised crevasse depth predictions versus oceanwater height ratio for a single isolated dry crevasse in a grounded glacier, considering compressible ($\nu = 0.35$) and incompressible ($\nu \approx 0.5$) ice homogeneous and depth-dependent mechanical properties.

propagation in the linear elastic fracture mechanics study. Values of crevasse penetration depth for an isolated dry crevasse in a grounded glacier, subject to different values of oceanwater height h_w are presented in Figure 5.8. The solid line curves consider incompressible ice, whilst the dashed lines represent compressible ice of Poisson ratio $\nu = 0.35$. Considering ice as an incompressible solid leads to deeper crevasse penetration depths compared to linear elastic compressibility, but these crevasses follow a similar trend as observed for the compressible case: for surface crevasses in glaciers subject to low levels of oceanwater, the penetration

depth is unaffected by firn density due to crevasses stabilising in fully consolidated strata. However, as the oceanwater height increases, crevasses become shallower, and as a result, the inclusion of firn density becomes more prevalent. Comparing the effects of assuming an incompressible/viscous rheology, the percentage difference in penetration depth when considering depth-dependent density, for a dry crevasse of oceanwater height $h_{\mathrm{w}} = 0.5H$ reduces to 4%, compared to 20% for linear elastic compressibility. The oceanwater height required to prevent any development of dry crevasses differs, with values of $h_{\mathrm{w}} = 0.55H$ being sufficient for compressible depth-dependent density cases, whereas oceanwater levels of $h_{\mathrm{w}} = 0.8H$ are required for the incompressible case. Comparing this to the cases in which no density variations are considered still shows a similar trend with higher oceanwater needed to stabilise crevasses when density variations are not considered.

Finally, water-filled surface crevasses are considered in floating ice shelves of height $H = 125$ m and length $L = 5000$ m, using a nonlinear viscous ice rheology. Similar to the linear elastic compressible case, surface crevasses at the horizontal position $x = 4750$ m (250 m from the ice shelf terminus) are considered and the longitudinal stress profiles are extracted from the finite element analysis. The stabilised crevasse depth versus meltwater depth ratio are plotted for the nonlinear viscous (NLV) rheology in Figure 5.9b along with the results for linear elastic (LE) compressibility ($\nu = 0.35$) and incompressibility ($\nu = 0.49$). When comparing the stabilised crevasse depths close to the front, it is noted that the penetration depth is independent of ice rheology, which is in contrast to the grounded glacier case. For the homogeneous density, minimal crevasse propagation is observed for meltwater depth ratios below $h_{\mathrm{s}}/d_{\mathrm{s}} < 0.6$, with full thickness propagation only occurring when fractures are close to saturation. The inclusion of the depth-dependent density results in deeper crevasse penetration

depths, with minimal differences in penetration depth between the linear elastic cases and nonlinear viscous rheology. This likely indicates that for crevasses close to the front, fracture is driven by the floatation height and the bending stresses due to the floating condition. For depth-dependent density, the reduction in floatation height leads to an increase in tensile stress in the upper surface, due to increases in R_{xx} and increased bending stress. In addition, the lithostatic component of longitudinal stress is reduced, leading to deeper crevasse propagation when including firn density. The propagation of an isolated surface crevasse is

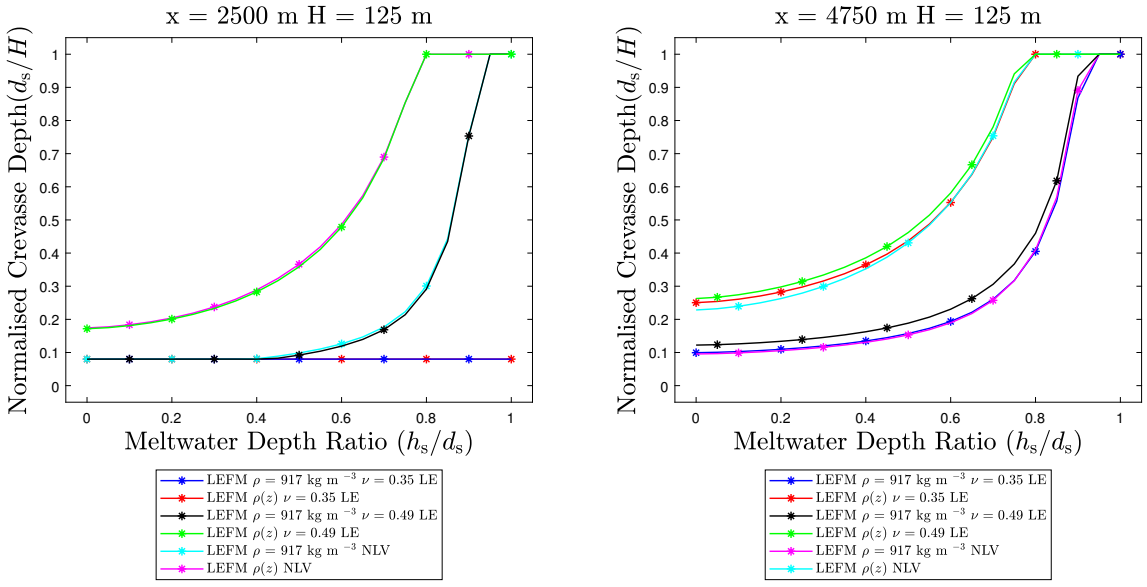

(a) (b)

Figure 5.9: Normalised crevasse depth predictions versus meltwater depth ratio for a single isolated surface crevasse located in the far field region ($x = 2500$ m) considering a linear elastic (LE) and nonlinear viscous (NLV) rheology for (a) the far field region ($x = 2500$ m) and (b) close to the front ($x = 4750$ m).

also considered, located in the far field region ($x = 2500$ m) of a floating ice shelf, with results presented in Figure 5.9a. As shown previously, for the linear elastic compressible rheology the stress state is fully compressive for both the homogeneous and the depth-dependent density case, thus no crevasse propagation is observed regardless of meltwater depth ratio. By contrast, when considering the nonlinear viscous rheology of ice, surface crevasses may propagate in the far

field region if there is sufficient meltwater pressure present. Large increases in crevasse penetration depth are observed for meltwater depth ratios greater than $h_s/d_s = 0.50$, with full thickness propagation being observed close to crevasse saturation at $h_s/d_s = 0.95$. Similar to crevasses near the front, the inclusion of depth-dependent density results in increased crevasse penetration depths compared to the homogeneous density scenario. Thus, similar conclusions can be drawn for both elastic and viscous rheologies.

5.5 Discussion

The analytical (closed form) and numerical (polynomial-fitted) solutions developed in this paper provide a more realistic description of the longitudinal stress in glaciers and ice shelves. The effect of depth-dependent firn/ice properties could be accounted for in the shallow shelf approximation (SSA) and coupled with LEFM models to enable the prediction of potential rift propagation. Krug et al. [141] proposed a simple method for estimating crevasse depths in an ice shelf, wherein the longitudinal stress calculated from the full Stokes model was used to evaluate the stress intensity factors based on a LEFM model. A similar approach can be developed to estimate crevasse depths from shallow shelf models or remote sensing data. In Appendix E, it is discussed how the 2D stress fields obtained from a shallow ice shelf model can be augmented to include depth-dependent density and Young's modulus. This stress can then be used within an analytical LEFM model to predict crevasse depth and calving.

It is acknowledged there are a few limitations to the current study. Firstly, it is assumed that the glacier/ice shelf geometry is a 2D rectangle with the free slip condition at the base, which is highly idealised and does not consider any contri-

butions from frictional sliding at the base for the grounded case, or buttressing stresses for floating ice shelves [161, 162]. Another limitation of the current model is that the rate of firn consolidation is assumed to be uniform with horizontal position and unaffected by glacier thickness H. However, firn densification is dependent on environmental factors including accumulation rates, overburden pressure, temperature and local strain rates [163, 164]. Firn densification near terminus regions or in thinner glaciers potentially results in a thinner firn layer and thus a reduced value of the parameter D, indicating a shorter length scale for the transition between firn and dense ice properties. However, while the findings presented currently are based on the density profiles from the Ronne ice shelf [4], the analytical models allow for a straightforward way to evaluate the impact for specific firn heights. This makes it possible to estimate the impact of including firn properties on the crevasse depth for specific locations.

One final limitation of the analytical models is related to water-filled crevasses. While the inclusion of firn density and Young's modulus are investigated, both these effects are (partially) driven by the porosity of the firn. However, when water-filled crevasses are considered, no model is included to account for water leaking from the crevasse into the surrounding firn. For colder ice sheets and deeper crevasses, such that the full water contents is surrounded by ice of sub-zero temperatures, this assumption is reasonable: any water that seeps into the surrounding ice/firn will freeze, creating an impermeable ice layer surrounding the crevasse which will prevent water from permeating further into the firn [165, 163]. Since these ice layers are typically very thin, they do not alter the mechanical properties of the ice. However, if more temperate glaciers are considered, or conditions where water-filled crevasses do not penetrate to considerable depth, the firn/ice surrounding the crevasse might not be sufficiently cold to cause this ice layer to form. In such circumstances, the presented model would overestimate

the crevasse depths obtained, since the saturated firn would reduce the effects of the water pressure within the crevasse by redistributing this pressure over a larger region surrounding the crevasse.

5.6 Concluding Remarks

In the current chapter, analytical equations are derived for the far field longitudinal stress including the effects of surface firn layers, described by depth--dependent density and Young's modulus profiles based on field data. These analytical expressions were used to conduct fracture propagation studies on isolated air/water filled surface crevasses in grounded glaciers and ice shelves for the homogeneous (assuming fully consolidated glacial ice) and depth-dependent ice cases. The following conclusions may be drawn from the presented work:

- The derived analytical equations for the far field longitudinal stress in grounded glaciers are in good agreement with the stress profiles obtained through finite element analysis.
- For shallow surface crevasses in grounded glaciers, the inclusion of depth-dependent density and Young's modulus results in a reduction of crevasse penetration depth compared to the homogeneous case.
- By assuming ice to be a linear elastic compressible material, it is found that considering depth-dependent Young's modulus has a greater influence on crevasse depths than density in thinner glaciers.
- The largest reductions in crevasse depths are observed in thinner glaciers (depths of approximately 100–150 m), where the stabilizing effects of the firn layers appear to be more prominent.

- For thicker glaciers or for large meltwater depth ratios, the crevasse propagates into the fully consolidated strata, resulting in minimal changes in crevasse penetration depth compared to the homogeneous case.

- Accounting for depth-dependent density in the floating ice shelf case increases the penetration depth of surface crevasses close to the ice-ocean front, with this increase caused by reductions in buoyancy height and lithostatic compressive stresses.

- The effect of depth-dependent density is dominant in thinner ice shelves, but it can still impact the surface crevasse propagation process in ice shelves as thick as $H = 1000$ m, although to a lesser extent.

- Considering depth-dependent Young's modulus in the floating ice shelf case slightly reduces surface crevasse depth for low meltwater depths, and the effect becomes less significant in thicker ice shelves.

Chapter 6

Numerical investigation of ice cliff stability using a shear stress-based phase field model

Glacial mass losses from the Greenland and Antarctic ice sheets has become the leading contributor to sea level rise in recent years, with the main processes of mass loss being iceberg calving events and ocean-induced melting at the underside of ice shelves [26, 8]. The processes of mass ablation have accelerated in recent years due to climate forcing and have exceeded ice accumulation rates via snowfall, leading to net mass loss from the Greenland and Antarctic ice sheets [15]. However, quantifying these losses due to fracture/iceberg calving is complex, requiring accurate models for the nucleation and propagation of crevasses under mixed mode loading, and accounting for the effects of meltwater on this propagation.

In addition to meltwater induced crevasses, ice shelves are vulnerable to thinning at the underside due to warm eddy currents inducing basal melt. The thinning of

ice shelves has led to a reduction in lateral drag forces at the margins and local pinning points, leading to increased ice flux into the ocean. This is of particular concern to the regions of Western Antarctica, such as Pine Island Glacier and Thwaites Glacier, where ice is grounded well below sea level and the glacier sits on a retrograde bed slope, where the bed deepens upstream. As a result, if ice sheet regression occurs beyond a critical "tipping point", irreversible rapid grounding line retreat is likely to occur [166]: as the ice progressively gets thicker inland, and ice flux is a function of ice thickness, the rate of ice loss increases as the grounding line retreats [167]; this process is known as the marine ice sheet instability (MISI).

The removal of floating ice shelves has the potential to expose ice cliffs at the grounding line which, if sufficiently tall, are prone to structural failure. Similar to MISI, if the ice sheet is located on a retrograde bed slope, progressively thicker cliff faces will become exposed, leading to a potential rapid grounding line retreat; a theory known as the marine ice cliff instability (MICI). However, both MICI and MISI remain controversial, as they are based on theoretical principles and are yet to be observed directly [168, 169].

The majority of analytical and numerical fracture analyses (including the previous analyses in the present thesis) in glacial ice has considered mode I fracture to be purely tensile, with crevasses propagating vertically downward as a result of the far field longitudinal stress state. Existing models have assumed that iceberg calving events would take place if a combination of surface and basal crevasses penetrate the full thickness of the grounded glacier or ice shelf [38].

However, a mode of failure that has been largely unexplored is that of brittle shear and compression through a combination of wing and comb cracks, leading to shear faulting [170, 171]. Since this shear failure is the mode of failure upon

which MICI is based, it becomes relevant to extend traditional (tensile only) fracture models to capture shear cracks in addition.

Bassis and Walker considered the combination of shear and tensile failures to determine a semi-empirical upper and lower bound for maximum cliff height, depending on the presence of crevasses [147]. For a dry land terminating cliff, the maximum cliff height was calculated as $H_{\max} = 220$ m for a depth averaged yield strength of 1 MPa [147]. These empirical calving laws have been coupled with ice sheet models and found that MICI has the potential to accelerate the collapse of the Western Antarctic Ice Sheet to a timescale of decades, resulting in a global sea level rise of 17 m within a few thousand years [148, 172].

Ma et al and Benn et al solved the 2D full Stokes equations using the finite element method, finding that glaciers subject to free slip are dominated by tensile failure and no slip glaciers are subject to shear failure [173, 6]. In addition, calving laws have recently been suggested based on the maximum shear stress in no slip glaciers, to determine the maximum freeboard at which ice cliffs may be sustained [174].

In recent years, discrete element methods (DEM) have been used to simulate the breakup of ice cliffs via shear failure [146, 175]. These methods consider solids as a mass of discrete particles, with forces being transmitted through the particles via elastic bonding [176]. Particle bonding may be represented through elastic beams and failure occurs when bonds break under the Mohr-Coulomb failure criterion [177]. DEM has been used to capture the complex fracture patterns occurring during ice cliff collapse events, capturing both the alternating surface and basal cracking on which MICI is based [178]. However, DEMs are computationally expensive and linking the particle interactions to physical parameters is complex, such that the method does not typically include the nonlinear viscous

creep deformation of ice.

An alternative to using DEM, which is able to overcome its limitations, is the phase field method. Phase field fracture is an emerging computational non-local continuum damage mechanics method which has recently been used to study the propagation of crevasses in glaciers and ice shelves [131, 132, 179]. The phase field method is advantageous since it can capture complex fracture phenomena such as crack bifurcation, coalescence and initiation from arbitrary sites. Initially developed for brittle fracture in elastic media [87], phase field methods may be coupled with other physical processes to solve complex multi-physics problems including hydraulic fracture [96, 98], corrosion damage [102, 104] and hydrogen embrittlement [100, 101] among others.

In this chapter, the use of the non-local phase field fracture method is proposed to capture ice cliff instabilities, and this method is extended by introducing a stress-based driving force based on the Mohr-Coulomb failure criterion. This driving force allows for shear, tensile, and mixed mode fractures to be captured, thereby allowing for the mechanisms assumed to drive ice cliff instabilities. Finite element simulations are then conducted to assess the structural failure of ice cliffs at the terminus of grounded glaciers. Variations in basal slip boundary conditions, glacier thickness H, oceanwater height h_{w} and ice strength parameters are considered to determine the criteria in which ice cliffs become stable. Finally, these results are compared to observational measurements and empirical relations derived in the literature, in the hope of informing ice sheet modellers the type of conditions that are required to trigger ice cliff failure.

6.1 Shear Stress Based Crack Driving Force

While Eq. (3.23) is a commonly used crack driving force, it is only able to capture mode I (tensile) cracks. An alternative crack driving force is now proposed, based on a Mohr-Coulomb failure criterion, to describe brittle compressive failure in response to shear stresses, inspired by the work of Schlemm & Leverman [174]. In the general form, shear stresses τ are resisted by a combination of the material's cohesive strength τ_{c} and internal friction μ acting based on the normal stress P, such that the fracture criterion is given as:

$$f_{\mathrm{c}} = \tau - \mu P - \tau_{\mathrm{c}} \tag{6.1}$$

with fracture occurring when $f_{\mathrm{c}} > 0$. The Mohr-Coulomb failure criterion may be rewritten in terms of maximum shear stress $\tau_{\max}$ [170, 180]:

$$f_{\mathrm{c}} = \sqrt{\mu^2 + 1}\, \tau_{\max} - \mu P - \tau_{\mathrm{c}} \tag{6.2}$$

For a 2D plane strain case, the maximum shear stress $\tau_{\max}$ is given by

$$\tau_{\max} = \sqrt{\left(\frac{\sigma_{xx} - \sigma_{zz}}{2}\right)^2 + \sigma_{xz}^2} \tag{6.3}$$

and is the equivalent to the radius of the Mohr circle. This operates at 45° to the maximum principal stress σ_1

$$\sigma_1 = \frac{\sigma_{xx} + \sigma_{zz}}{2} + \sqrt{\left(\frac{\sigma_{xx} - \sigma_{zz}}{2}\right)^2 + \sigma_{xz}^2}\,. \tag{6.4}$$

The isotropic pressure P is given as

$$P = -\frac{\sigma_{xx} + \sigma_{yy} + \sigma_{zz}}{3}\,. \tag{6.5}$$

The Mohr-Coulomb failure criterion outlined above may be normalised with respect to the cohesive strength. Similar to the stress based crack driving force criterion in Eq. (3.23), this gives a crack driving force for pressure dependent fractures:

$$D_{\mathrm{d}} = \left(\frac{\sqrt{\mu^2 + 1}\, \tau_{\max} - \mu P}{\tau_{\mathrm{c}}} \right)^2 . \tag{6.6}$$

The absence of the -1 term is noted, acting as a damage threshold in Eq. (6.6) when comparing the crack driving force found in [121], thus the Mohr-Coulomb approach follows an AT2 formulation. As a result, the obtained phase field solutions have a smooth transition between the damaged and non-damaged areas, in contrast with the more direct transition present for AT1 models (e.g. when using a -1 in the driving force term, or using ϕ instead of ϕ^2 in the fracture distribution function γ). Furthermore, this choice will result in the failure exhibiting a more progressive softening (i.e. a shallower gradient of phase field distribution with distance from the sharp crack interface - see Figure 3.2), spreading the failure over several time increments and thereby assisting with numerical convergence.

The yield surface for the crack driving force based on principal stresses in Eq. (3.23) is plotted in Figure 6.1 for $\zeta = 1$. The presence of the Macaulay brackets in Eq. (3.23) results in a Rankine type failure in regions where only either σ_{xx} or σ_{zz} is tensile, with yielding occurring above the fracture stress σ_{c}. When both σ_{xx} and σ_{zz} are tensile, the failure surface is bounded by a quadratic barrier function, the size of which is dependent on σ_{c}, and the post failure slope being dependent on ζ.

The yield surfaces for the Mohr-Coulomb based crack driving forces described in Eq. (6.6) are presented in Figure 6.1 considering $\mu = [0.0,\ 0.3,\ 0.8]$. For the no friction case ($\mu = 0.0$), a Tresca-type yield surface is produced. In the 3D space, this gives a hexagonal prism of infinite length centred around the line $\sigma_{xx} = \sigma_{yy} =$

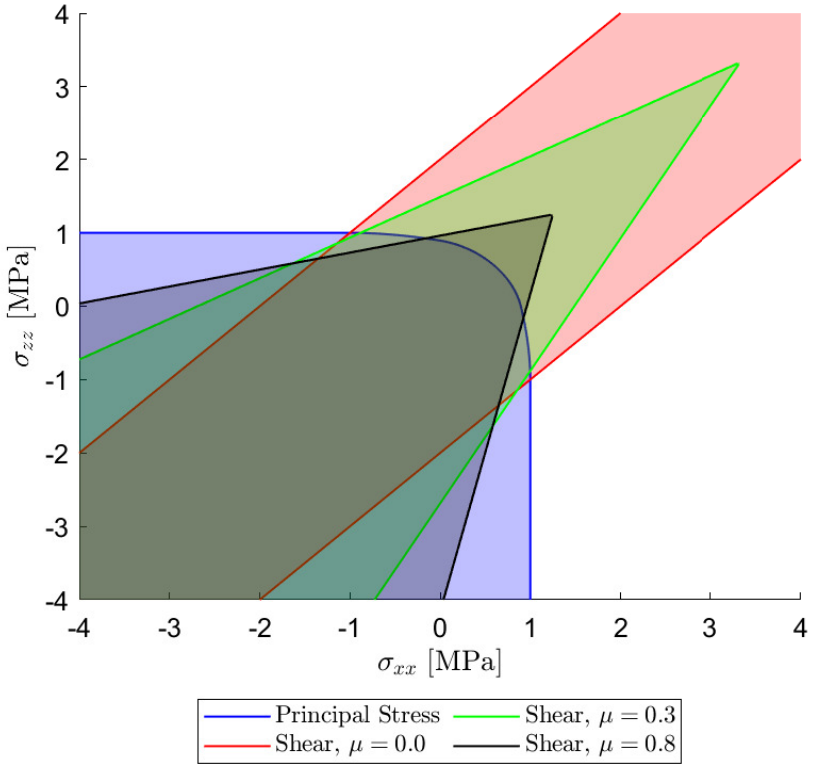

Figure 6.1: Diagram showing yield surfaces for the principal stress criterion (blue surface) and Mohr-Coulomb failure criterion for internal friction $\mu = 0.0$ (red surface), $\mu = 0.3$ (green surface), $\mu = 0.8$ (black surface). Shaded regions indicate combinations of stress σ_{xx} and σ_{zz} where the material does not undergo yielding (i.e. $D_{\mathrm{d}} = 0$).

σ_{zz} and the material is stable in regions where normal stresses are approximately equivalent (i.e. $\tau_{\max}$ in Eq. (6.3) tends to zero for $\sigma_{xx} \approx \sigma_{zz}$). The yield surface expressed in Figure 6.1 shows two parallel lines of infinite length, representative of the longitudinal section of the 3D hexagonal prism, where failure is independent of isotropic pressure. As a result, cracks can only nucleate when deviatoric (shear) stresses are present, whereas even when the ice undergoes uniform tension, it does not fracture. These deviatoric stresses also drive the plastic deformations through Glen's law (Eq. (3.27)), which in turn dissipates these deviatoric stresses. As a result, when using $\mu = 0$, fracture only occurs when a sudden change in the stress state occurs.

As the value of internal friction increases, failure becomes dependent on volumetric pressure, tending towards a Mohr-Coulomb failure surface. In the 3D space, this is represented by a hexagonal based pyramid, with the apex located on the $\sigma_{xx} = \sigma_{yy} = \sigma_{zz}$ line. Within this region of the yield surface, failure is purely pressure based and the critical applied stress σ_{a} is equal to τ_{c}/μ, thus for $\mu = 0$, $\sigma_{\mathrm{a}} = \infty$ leading to the parallel lines in Figure 6.1. This surface allows for ice to fail under both tensile and shear stress states, with ice being less likely to crack if uniform tension is applied compared to the principal stress-based criterion, and allowing fracture before the tensile strength is reached when under compression. As a result, this model allows fracture to occur in compressive regions based on deviatoric stresses, which is not captured by the principal stress phase field formulation. For freely floating ice shelves and glaciers undergoing free slip, the horizontal deviatoric stress is equal to the maximum shear stress which is $\rho_{\mathrm{i}} g H (1 - \rho_{\mathrm{i}}/\rho_{\mathrm{w}})$ [181, 153].

The interaction between values of cohesion τ_{c} and internal friction μ should also be acknowledged. If the Mohr-Coulomb failure envelope is plotted in 2D, considering the normal stress P against the shear stress τ, then a linear relationship

is predicted with a y-intercept value of cohesion τ_c. If cohesion is kept constant and the angle of internal friction is increased, then the tensile area, bounded by the y-axis and the negative x-axis decreases, shown in Figure 6.2 below. If the stress regime is located within this tensile area on the stability region, then it may incorrectly imply that an increase in angle of shearing resistance may lead to a reduction in the material's stability.

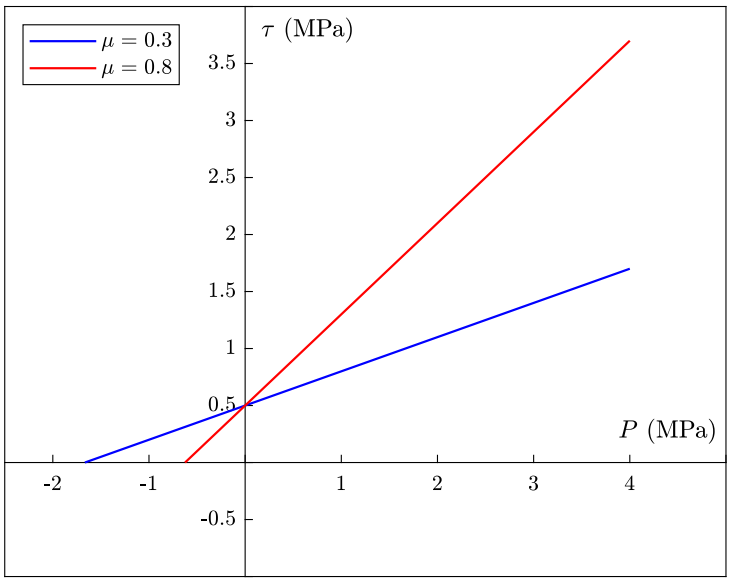

Figure 6.2: Graph showing the 2D yield surface for internal friction values $\mu = 0.3$ and $\mu = 0.8$ for applied shear stress τ versus normal stress P. If the stress regime is beneath the yield line, then the material will not fail.

6.2 Boundary Conditions

For the interactions between the glacier and the bedrock, a variety of boundary conditions are considered to test for cliff failure, as illustrated in Figure 6.3. In every case, displacement in the vertical direction is restrained, preventing the glacier from passing through the basal rock. However, the degree of motion in the horizontal direction is varied. For most cases, a Weertman type sliding law

Material Parameter	Value
Young's Modulus, E [MPa]	9500
Poisson's Ratio, ν [-]	0.35
Density of Glacial ice, ρ_{i} [kg m^{-3}]	917
Density of Ocean water, ρ_{s} [kg m^{-3}]	1020
Creep exponent, n [-]	3
Creep coefficient, A [MPa$^{-\mathrm{n}}$s^{-1}]	7.156 $\times 10^{-7}$
Internal Friction, μ [-]	0.8
Shear Strength, τ_{c} [MPa]	1
Reference Traction, τ_0 [MPa]	0.75
Basal Sliding Exponent, m [-]	3
Phase Field Viscosity, η [s]	33.8
Phase Field Length Scale, ℓ_{c} [m]	10

Table 6.1: Characteristic material properties for glacial ice assumed in this work (unless otherwise stated).

is considered which applies a basal shear traction τ_{b} to oppose motion [40]:

$$\tau_{\mathrm{b}} = -\left[\frac{1}{C\left|\dot{\mathbf{u}}_{\mathrm{t}}\right|^{1/m-1}} + \frac{\left|\dot{\mathbf{u}}_{\mathrm{t}}\right|}{\tau_0}\right]^{-1} \dot{\mathbf{u}}_{\mathrm{t}} \tag{6.7}$$

this friction is dependent on the basal friction coefficient C, the basal sliding exponent m and the tangential sliding velocity $\dot{\mathbf{u}}_{\mathrm{t}}$. Values of the basal friction coefficient vary throughout Antarctica and are inferred through inversions of observed velocities [182, 183], thus a range of values for the basal friction coefficient are considered $C = [10^5 - 10^9]$ Pa m$^{-1/m}$s$^{1/m}$. The extreme cases of no friction and a fully frozen boundary are also considered. For the free slip basal boundary condition (Figure 6.3a), horizontal displacement at the base is unrestrained. For the no slip condition (Figure 6.3c), horizontal displacement at the base is fully restrained ($u_x = 0$), representing a glacier with a frozen base.

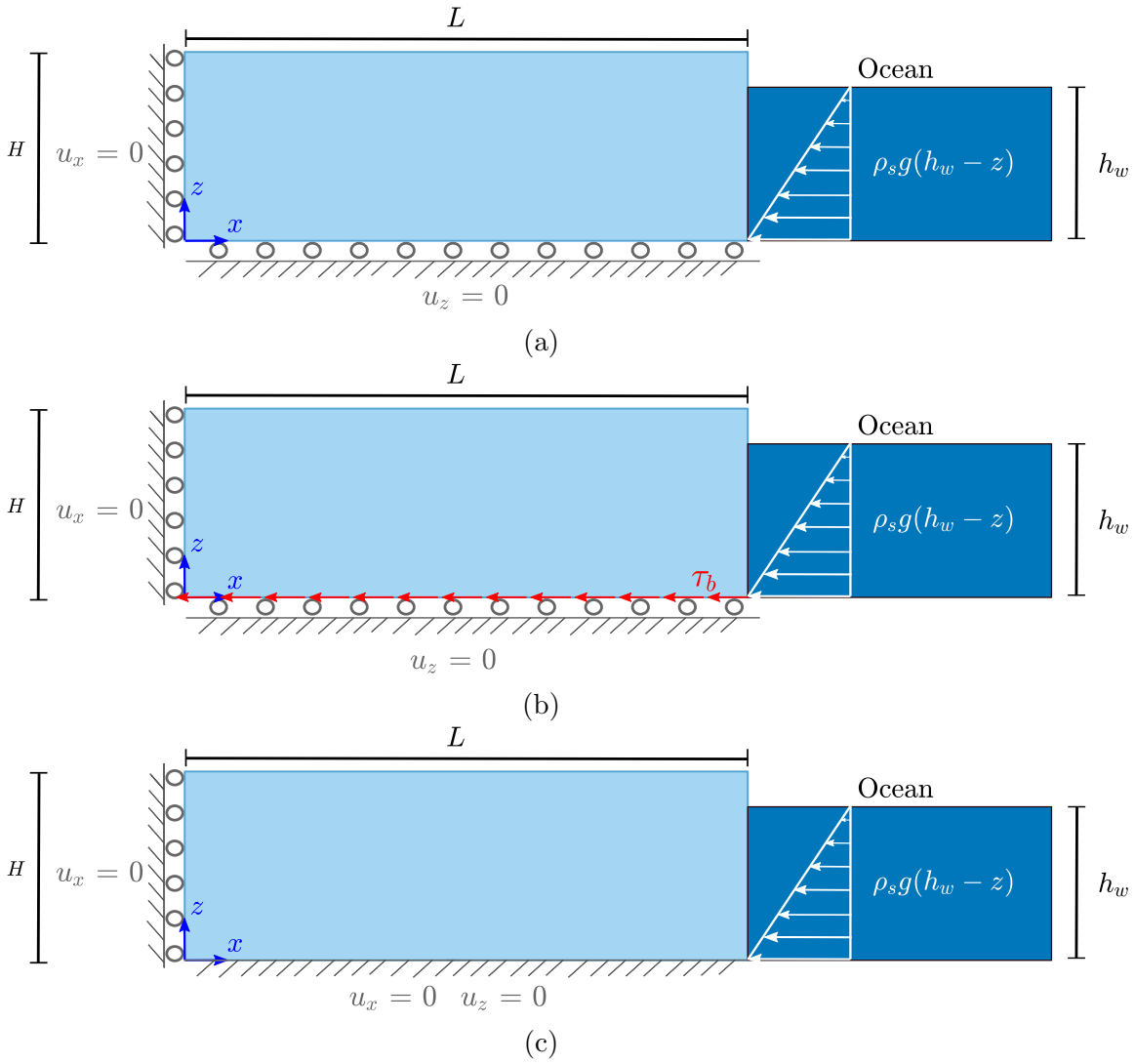

Figure 6.3: Schematic diagram showing boundary conditions for a grounded glacier subject to the following basal conditions (a) free slip, (b) basal sliding and (c) frozen base.

6.3 Land Terminating Glaciers

In the numerical analysis, an idealised rectangular grounded glacier is considered sitting on bedrock. This glacier has thickness H and length L, adopting a length-to-thickness ratio of $L/H = 6$ such that when the ice thickness is increased longer glaciers are considered to capture both the near terminus and far field stress states. The model uses the plane strain assumption, since the out-of-plane dimension is typically larger than the in-plane length, allowing the three-dimensional geometry to be reduced to a two-dimensional geometry of flow-line x and vertical coordinate z. A Neumann-type boundary condition is applied to the far right terminus, applying a pressure to represent the hydrostatic oceanwater with this pressure varying linearly with depth, $p = -\rho_{\mathrm{s}} g \langle h_{\mathrm{w}} - z \rangle$. The presence of the Macaulay brackets denotes that oceanwater pressure above the ocean surface h_{w} is zero. Gravitational self-weight is applied as a body force throughout the entire domain in the vertical z-direction, with a value of $\rho_{\mathrm{i}} g$. The upper surface representing the air-ice interface is considered as a free surface and the displacement normal to the far left terminus is restrained to prevent rigid body motion in the horizontal direction. The material properties for glacial ice used within this study are reported in Table 6.1 unless stated otherwise.

6.3.1 Stress Distributions

Prior to conducting phase field damage simulations, the stress states in the pristine grounded glacier are considered. These stress states are obtained through a time dependent creep simulation without fractures (no phase field damage), obtaining a steady state creep stress profile in the domain after simulating 7 days. Contour maps for the maximum shear stress $\tau_{\max}$ and maximum principal stress

σ_1 are plotted in Figure 6.4 calculated using Eq. (6.3) and Eq. (6.4) respectively. For this case, the free slip and frozen base cases for a land terminating glacier of thickness $H = 200$ m are considered.

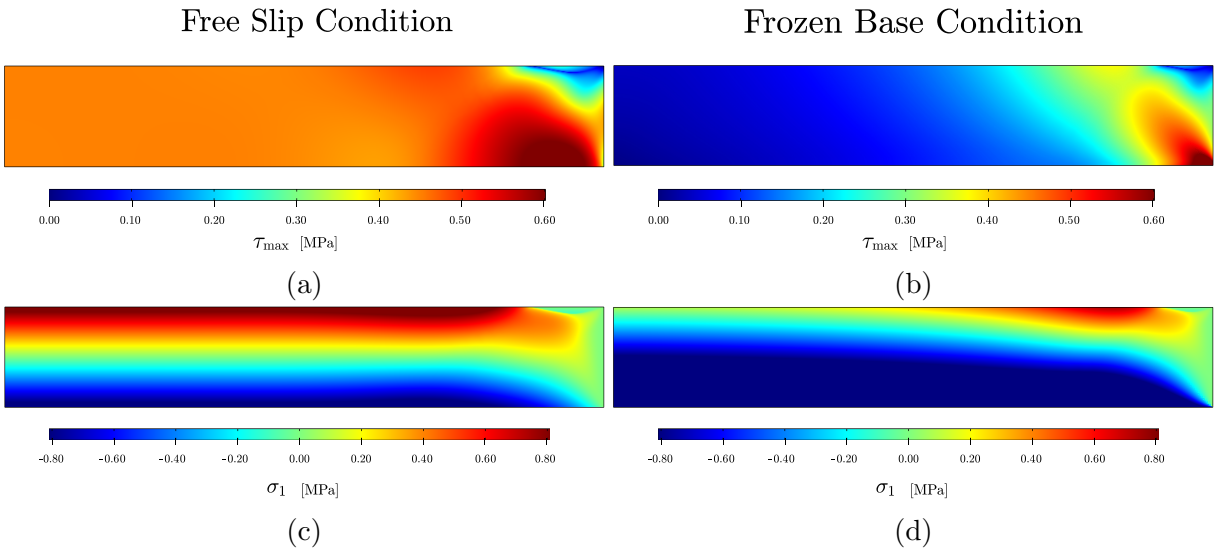

Figure 6.4: Steady state creep stress states showing maximum shear stress and first principal stress for a grounded glacier of height $H = 200$ m undergoing free slip (a) and (c) and no slip (b) and (d).

For the free slip condition, the maximum shear stress is plotted in Figure 6.4a. It is observed that the maximum shear stress is non-zero throughout the entire domain, and in the far field region is invariant with depth, having an approximate value of $\frac{1}{4}\rho_i g H$. An elevation in maximum shear stress is observed at the base of the glacier close to the front, with a peak value of 1.4 times the maximum shear stress in the far field region. The stress distribution for the maximum principal stress in the free slip glacier is plotted in Figure 6.4c. The upper surface layers in the far field region are subject to tensile stress, with a maximum value of $\frac{1}{2}\rho_i g H$ being observed, in the absence of oceanwater pressure. Maximum principal stresses vary linearly with depth and become compressive at the base, with the distribution being symmetrical about the centre line $z = H/2$. An edge effect is observed close to the front due to the traction free condition. Based on these stress profiles, it is expected that densely spaced crevasses will develop in the far

field, while near the terminus the surface is unlikely to develop any crevasses. If cracks were to propagate based on tensile principal stresses, no cracks would develop at the base due to the compressive stress state, even near the terminus. In contrast, using a shear-based criterion allows for basal cracks to develop near the terminus due to the increase in shear stress near the base.

The maximum shear stress for the frozen base glacier is presented in Figure 6.4b. Values of maximum shear stress away from the glacier front are negligible, however, a concentration in shear stress is observed at the base of the glacier near the terminus, with a maximum value of 1.35 MPa being recorded. Finally, the maximum principal stress for the frozen base is plotted in Figure 6.4d. In contrast to the free slip condition, the stress state is predominantly compressive in the far field region, with linear variation with depth and upper surface layers exhibiting low levels of tensile stress (approximately 0.1 MPa). Maximum values of principal stress are observed at a distance of a thickness H from the glacier terminus at the upper surface. As a result of this stress state, surface crevasses will be prevented in the far field, whereas mode I (tensile) cracks are likely to develop near the terminus at the surface, and mode II (shear) cracks at the base.

It is also observed that the magnitude of the principal stress and shear stress states are scaled by the glacier thickness H due to load contributions being gravitational body forces. This is the case regardless of basal boundary condition.

6.3.2 Cliff Failure: Influence of Basal Boundary Condition

Time dependent phase field damage simulation studies are now conducted to determine the requirements for ice cliff failure. The steady state creep stress

states reported in Section 6.3.1 are used to initialise the cliff failure simulations, in order to study the propagation of damage based on the incompressible stress state.

Phase field contour plots for the grounded glacier undergoing free slip are presented in Figure 6.5. It is observed that uniform damage initiates in the upper surface regions in the far field region and stabilises at a thickness of approximately $0.5H$, a depth that is consistent with the Nye zero stress prediction for a land terminating glacier. A concentration in damage is located close to the front and propagates vertically downward to a normalised depth of $0.76H$. This difference in crevasse depth is a result of the shielding effect, with the rightmost crevasse propagating to a depth comparable to that predicted for a single crevasse in isolation (e.g. following LEFM), whereas the remainder of the crevasses behave as densely spaced, thus follow the zero stress depth estimates. The damage accumulated in the free slip glacier is driven by the longitudinal stress and as a result can be categorised as mode I tensile failure. It is acknowledged that the damage presented in Figure 6.5 is not localised to produce sharp crevasses, instead producing a uniform damage region in the upper surface. To overcome this, a crack driving force threshold and rectangular notches may be introduced to calibrate damage to propagate directly beneath pre-existing cracks, as sharp mode I fractures. For this approach, see Chapter 4. However, since this requires inserting notches beforehand to cause the surface crevasses to localise properly, it removes the ability to study where and if these crevasses nucleate. As such, the method used presently produces smeared damage regions to indicate the presence of crevasse fields, while it does capture the nucleation of these crevasse fields starting from a pristine ice sheet.

By contrast, the phase field contour plots for the frozen base glacier are reported in Figure 6.6. In this instance, damage is localised at the base of the glacier at the

terminus and in the upper surface regions approximately one thickness away from the front. Damage at the upper surface initially propagates downwards, however at greater depths, the fracture path begins to curve towards the glacier front. Damage initiates at the base near the terminus, as a result of the concentration in maximum shear stress $\tau_{\max}$ reported in Fig 6.4b. This basal fracture propagates upwards in a mixed mode manner and cliff failure is observed once the basal fracture approaches the surface fracture and makes contact with the terminus. Fracture coalescence occurs in a rapid and brittle manner, and once cliff failure is achieved, a stable cliff surface is observed. No glacier retreat is observed for this example because the bed is flat, thus the exposed surface is shallower than the initial upright cliff surface.

Damage accumulation graphs versus time are also plotted in Figure 6.7, normalised with respect to the in-plane glacier area ($H \times L$). This does not indicate the area of ice lost due to crevasses, since the presence of the surface does not result in iceberg calving, e.g. Figure 6.5. Instead, it gives an indication of the crevassing process, with jumps indicating that areas of the ice sheet become detached, such as is observed for the frozen base case between 150-250 s in Figure 6.6c-d. Here, the frozen and free slip cases are considered, as well as the glacier subject to basal shear, with a variety of basal friction coefficient values C. For basal friction coefficients $C < 1 \times 10^5$, the basal shear stress is sufficiently low such that damage accumulation tends towards the free slip glacier case. Damage accumulation occurs in a rapid and brittle manner, with damage accumulation areas stabilising at approximately $t = 50$ s.

As the basal friction coefficient increases, basal shear resists glacial flow and the total damage accumulation decreases due to the longitudinal stress profile becoming more compressive. For high values of C, far field damage is no longer present and damage only accumulates close to the glacier front. Cliff failure

is observed for basal friction coefficients greater than $C > 1 \times 10^9$, with this behaviour tending towards the frozen base case.

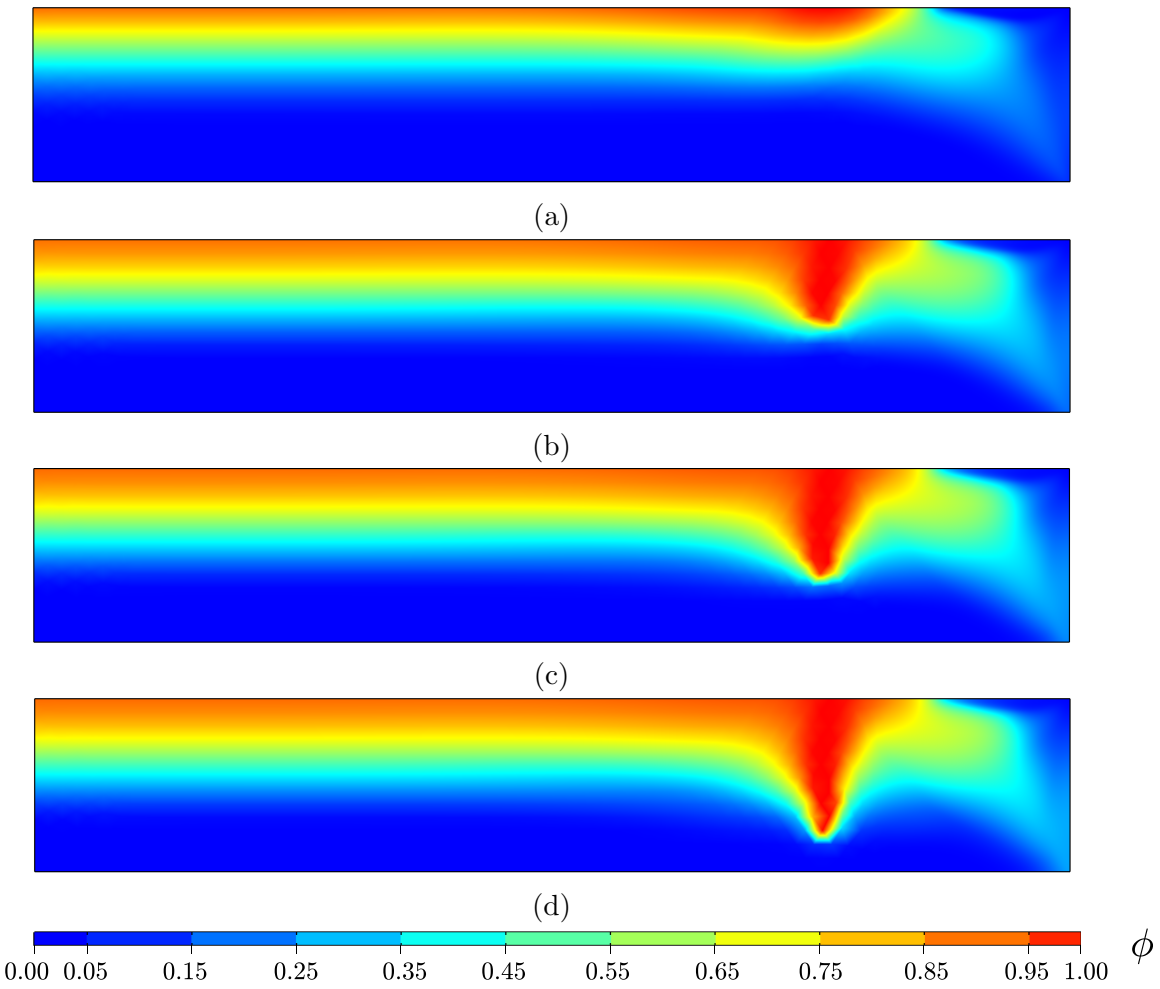

Figure 6.5: Phase field damage evolution over time for a land terminating grounded glacier undergoing free slip at the base with internal friction $\mu = 0.8$ and cohesion $\tau_c = 1$ MPa at time (a) $t = 15$s, (b) $t = 50$ s, (c) $t = 75$ s and (d) $t = 200$ s.

6.3.3 Cliff Failure: Influence of Internal Friction

In the current section the influence of internal friction parameter μ on the mode of fracture is explored, since there is a wide range of reported values in the literature. Kennedy [184] found that internal friction decreases with sliding velocity and ice temperature. Beeman [185] conducted frictional sliding experiments on cold ice

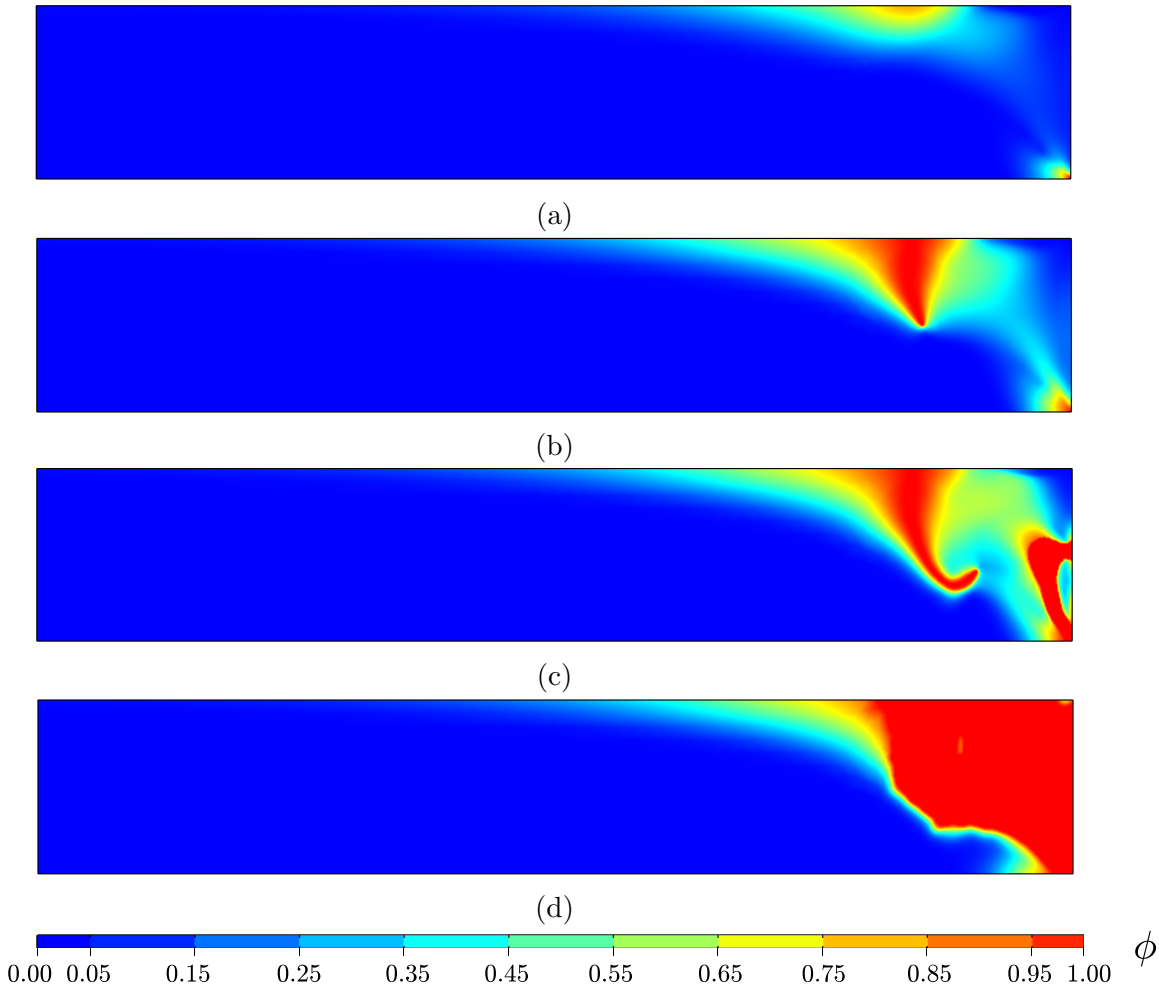

Figure 6.6: Phase field damage evolution over time for a land terminating grounded glacier subject to a frozen base with internal friction $\mu = 0.8$ and cohesion $\tau_c = 1$ MPa at time (a) $t = 15$ s, (b) $t = 60$ s, (c) $t = 150$ s and (d) $t = 250$ s.

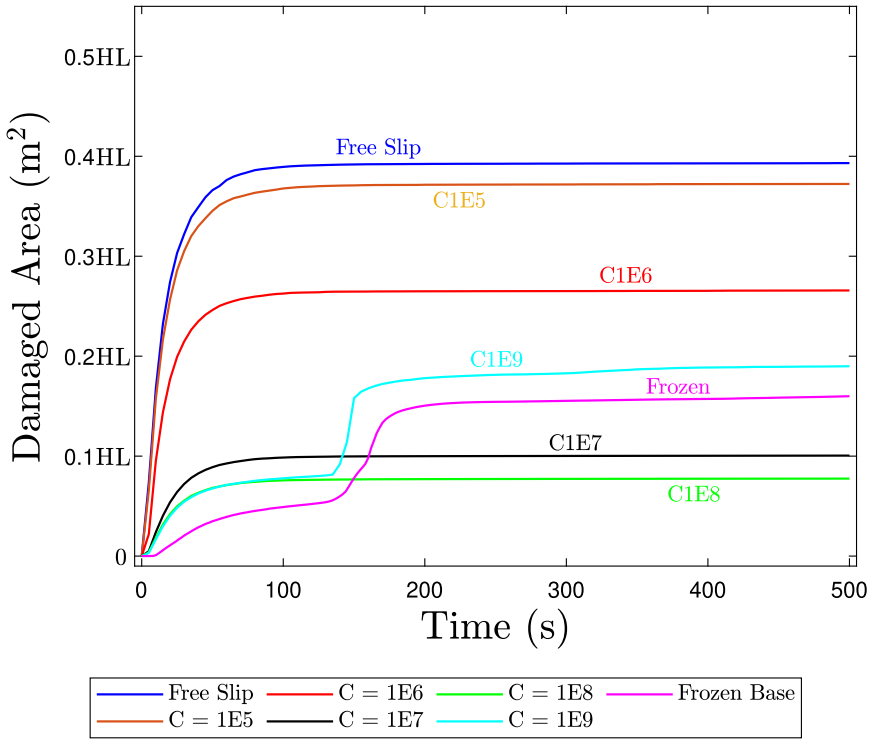

Figure 6.7: Graph showing damage accumulation area normalised with respect to in-plane glacier area ($H \times L$) versus time for a land terminating graph of height $H = 200$ m for different basal boundary conditions.

and fitted a failure envelope with a friction coefficient of $\mu = 0.55$-0.65. Weiss and Schulson carried out biaxial testing on columnar ice and determined friction coefficient to be scale independent with an approximate value of $\mu = 0.8$ [186].

By contrast, Bassis and Walker carried out cliff failure analysis by considering $\mu = 0$, reverting to a Tresca yield criterion [147]. Phase field fracture simulations are conducted for the frozen base no-slip, land terminating grounded glacier case of height $H = 200$ m and consider the extreme values of $\mu = 0$ and $\mu = 0.8$ reported in the literature. Results for $\mu = 0.8$ have been presented in Figure 6.6 and discussed previously.

The phase field contour plots for the no-friction case are presented in Figure 6.8. The absence of the isotropic pressure P in the crack driving force, results in

damage initiating solely as a result of the maximum shear stress $\tau_{\max}$. This occurs at the base of the glacier in close proximity of the front. Fracture propagates from the base upwards and penetrates the full thickness of the glacier. Damage begins to spread laterally until the entire front is fully damaged. Once this occurs a second basal fracture is initiated and propagates through the entire glacier thickness.

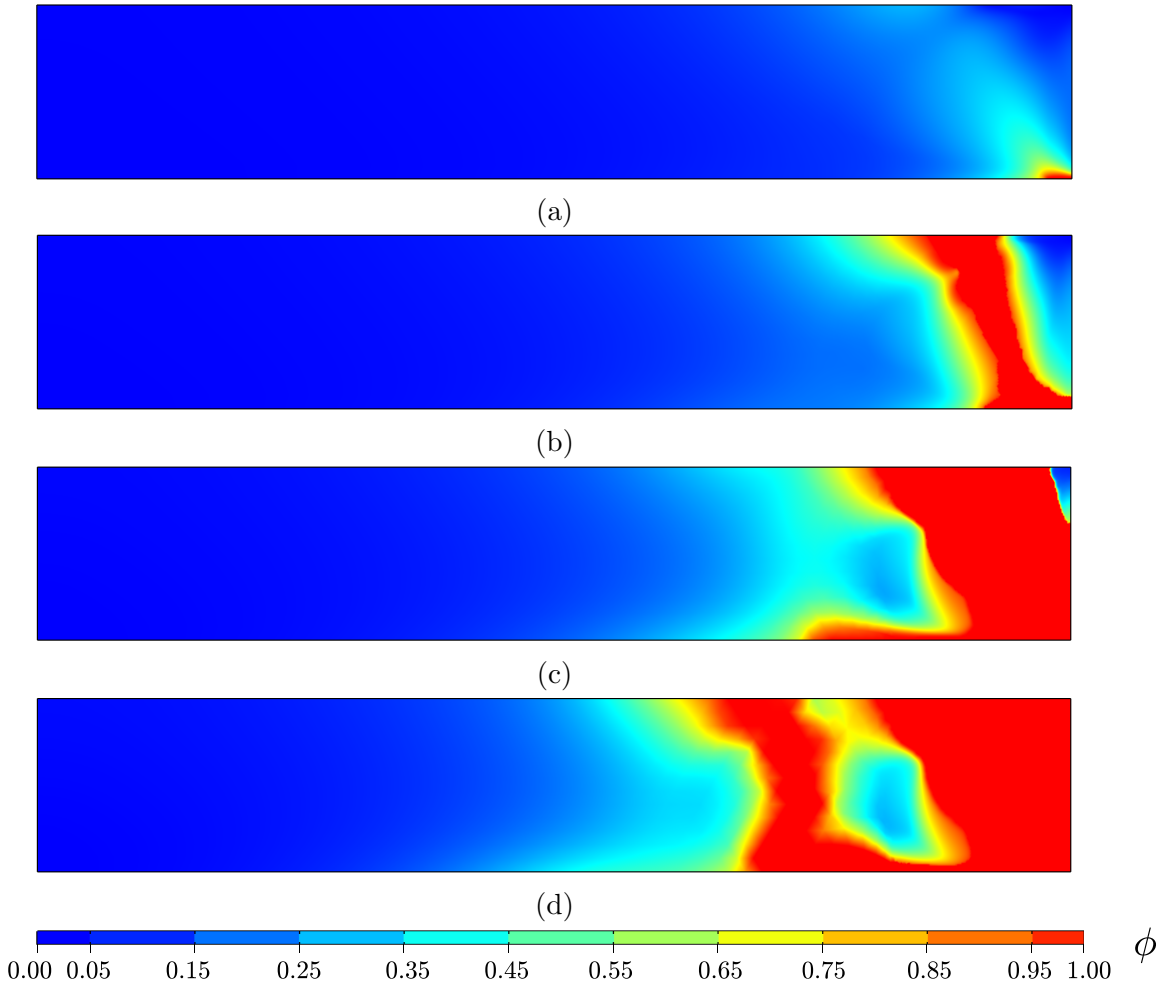

Figure 6.8: Phase field damage evolution over time for a land terminating grounded glacier subject to a frozen base with internal friction $\mu = 0.0$ and cohesion $\tau_c = 1$ MPa at time (a) $t = 17$ s, (b) $t = 35$ s, (c) $t = 70$ s and (d) $t = 93$ s.

In addition to the difference in mode of failure, it is observed that there is a reduction of approximately 40 m in maximum sustainable glacier thickness height for the land terminating no-slip condition when considering $\mu = 0.0$.

6.3.4 Cliff Failure: Influence of Shear Strength

There is also large variation in reported values of cohesion τ_c in the literature. Firstly, Beeman reports a cohesion value of $\tau_c = 1$ MPa under low confining pressures for cold ice [185]. This value of cohesion has been used in several numerical studies such as by Bassis & Walker [147] and by Schlemm & Leverman [174]. However, observational data suggests lower values of cohesion closer to $\tau_c = 0.5$ MPa [187]. Frederking et al reported similar values of cohesion, with an average value of $\tau_c = 0.6$ MPa being obtained from laboratory testing [188]. By contrast, triaxial tests conducted by Rist et al [189] and Gagnon & Gammon [190] have been shown to result in values of shear strength of up to 5 MPa.

Phase field damage studies are therefore conducted for cohesion $\tau_c = \{0.25, 0.5, 0.75, 1\}$ MPa for the frozen base case at different glacier thicknesses, to determine the minimum height at which cliff failure is observed, assuming internal friction of $\mu = 0.0$ and $\mu = 0.8$. Based on the crack driving force D_d in Eq. (6.6), an alteration in cohesion scales the magnitude of crack diving force. This does not alter the mode of failure observed, but cohesion influences the minimum height at which cliff failure occurs.

For $\tau_c = 1$ MPa, land terminating glaciers of height $H \geq 200$ m are subject to cliff failure, with this result being consistent with the findings of Bassis & Walker [147]. As the cohesion decreases, the height at which cliff failure occurs reduces, lowering to $H \geq 85$ m when considering $\tau_c = 0.25$ MPa, as shown in Figure 6.9. These results are obtained by performing simulations for a range of ice thicknesses, determining the minimum thickness required for failure with an accuracy of 5 m. Notably, for the range of cohesion values considered, the relation between cohesion and stable cliff height is close to linear. However, it is expected that as the cohesion approaches zero, the stable cliff height would also

approximate zero thickness. Since stable cliff heights observed are typically in the range of 100–150 m, it may be concluded that for land terminating glaciers realistic values for the cohesion are in the range of $\tau_c = 0.3$–0.6 MPa.

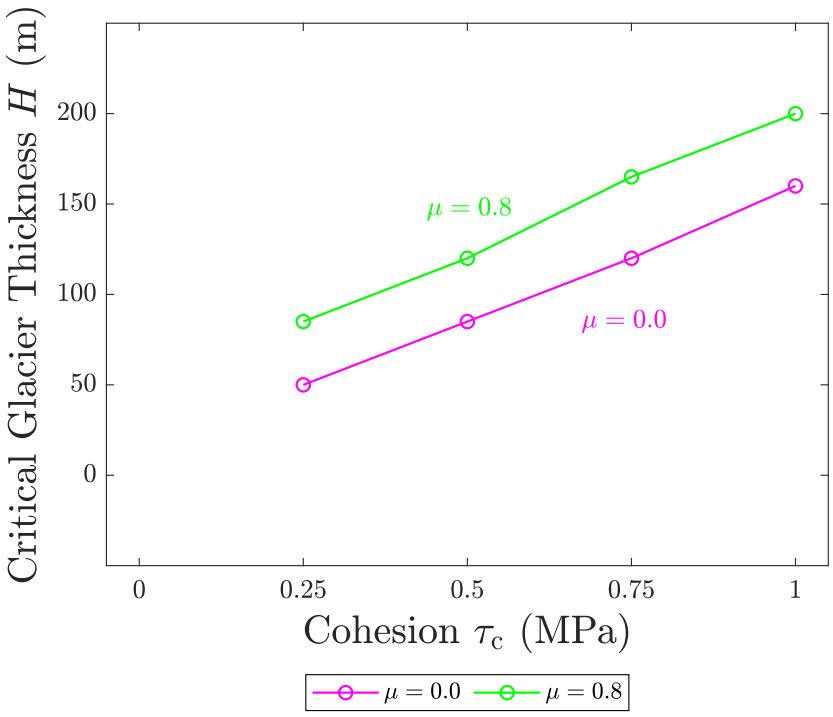

Figure 6.9: Graph showing minimum glacier thickness required to trigger cliff failure versus cohesion τ_c.

6.4 Ocean Terminating Glaciers

The possibility of cliff failure in thicker glaciers that terminate at the ocean is now considered. A depth-dependent hydrostatic oceanwater pressure p_w is applied at the far right terminus of the glacier with a magnitude of $p_w = \rho_w g \langle h_w - z \rangle$, where h_w represents the oceanwater height. The inclusion of this oceanwater pressure provides a compressive stress that resists glacier motion, and allows for thicker glaciers to stabilise. Since the cliff failure was most pronounced for frozen

base conditions, these will be used presently. Additionally, floatation/uplift is neglected throughout the current work, instead solely considering ice sheets with sufficient free-board to remain grounded.

The phase field contours for an ocean terminating glacier of height $H = 800$ m and oceanwater height $h_{\mathrm{w}} = 585$ m are presented in Figure 6.10 for a value of $\tau_{\mathrm{c}} = 0.5$ MPa. Damage is localised in the upper surface close to the calving front and slumping is observed in the ice above the waterfront until a subaerial calving event is achieved. By contrast with the land terminating case, full thickness failure is not achieved. Instead, a stable ice thickness at the calving front is sustained, equal to the oceanwater height h_{w}. Retreat of the glacier as a result of subsequent buoyant calving is not observed in this model due to neglecting buoyant forces and melt undercutting once the glacier foot is exposed.

Cliff failure in ocean terminating glaciers is therefore dependent upon the exposed free-board above the oceanwater surface (i.e. $H - h_{\mathrm{w}}$), as an increase in oceanwater height results in a reduction in tensile stress at the calving front. This behaviour pattern is consistent with the results of Parizek et al [191] and also supports empirical calving laws, based on the height above buoyancy [192]. For this instance, the minimum glacier free-board to cause cliff failure is 215 m, which is larger than the critical glacier thickness for the land terminating case ($H = 125$ m). This increase in critical glacier free-board is likely observed due to the absence of damage at the base, which is stabilised by the oceanwater pressure p_{w}. Values of glacier free-board would reduce if the presence of meltwater pressure in damaged regions in the upper surface is considered.

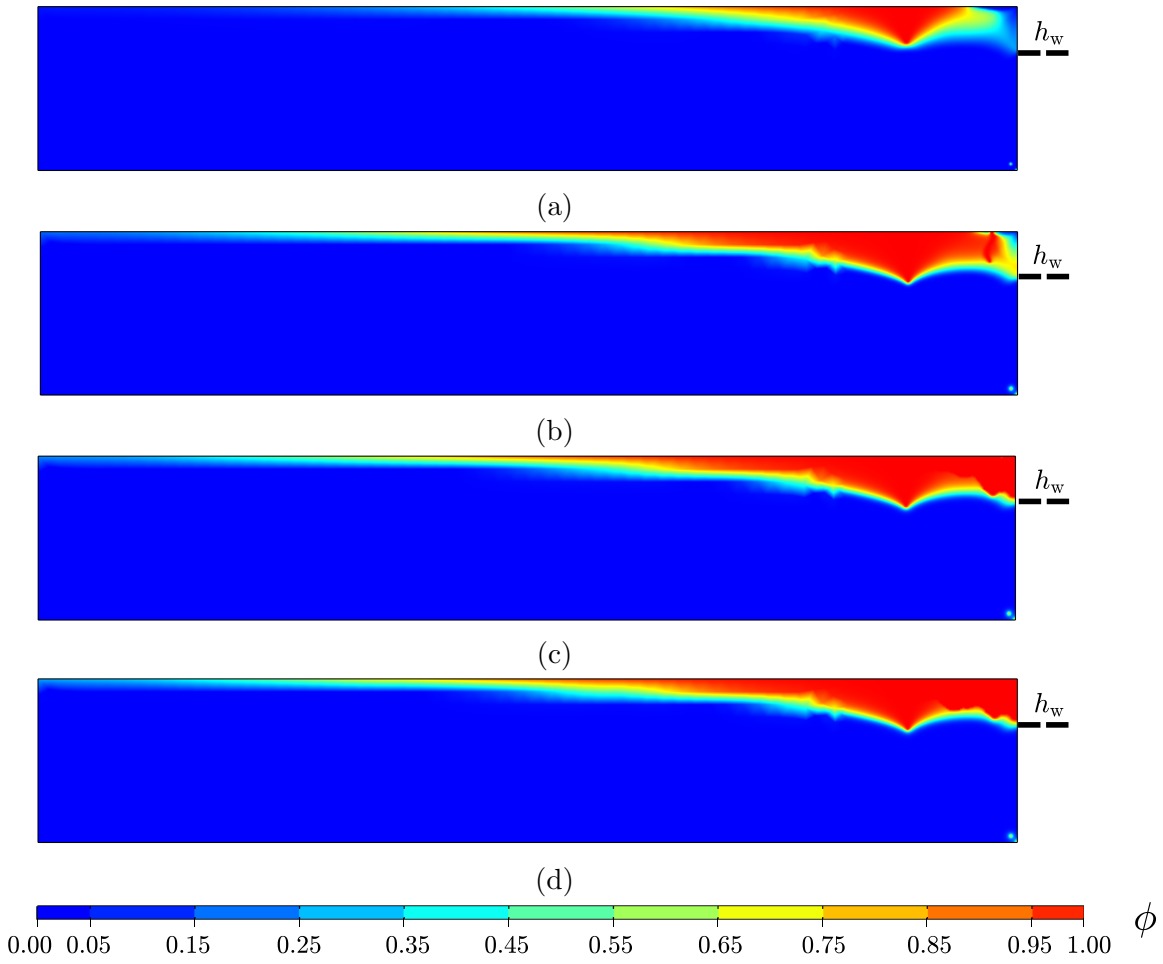

Figure 6.10: Phase field damage evolution over time for a grounded glacier subject to a frozen base, of height $H = 800$ m and oceanwater height of $h_w = 585$ m with internal friction $\mu = 0.8$ and cohesion $\tau_c = 0.5$ MPa at time (a) $t = 5$ s, (b) $t = 40$ s, (c) $t = 100$ s and (d) $t = 250$ s.

Similar to the study into the effects of cohesion, multiple phase field fracture simulations are now conducted for a variety of glacier thicknesses and oceanwater heights, producing the stability envelope shown in Figure 6.11. This shows the critical value of oceanwater height h_{w} required to cause ice cliff failure at glacier thickness increments of 200 m. If the oceanwater exceeds this critical value, (i.e. the data point lies within the shaded region) calving will not be observed, but if the oceanwater is below the critical value (i.e. the data point lies below the stability envelope), cliff failure will occur. An upper bound for the stability region is determined by the oceanwater height required for the glacier to become buoyant (i.e. for homogeneous ice $h_{\mathrm{w}} = \rho_{\mathrm{i}}/\rho_{\mathrm{w}} H$). For floating ice tongues and ice shelves, failure by shear is unlikely to occur due to the no slip condition being replaced with a buoyancy pressure at the base. This analysis does not imply that floating ice shelves cannot form, merely that the cliff failure mechanism is no longer appropriate, once the ice sheet begins to become buoyant. Instead, failure for floating ice shelves is dictated by the tensile propagation of rifts leading to the detachment of tabular icebergs instead of cliff slump [147] a fracture mechanism which is not considered within this study. This fracture mechanism is not considered within this study but can be captured by the proposed fracture model if the pore-water pressure were to be included and if the grounded basal boundary condition were to be replaced with the floating boundary condition.

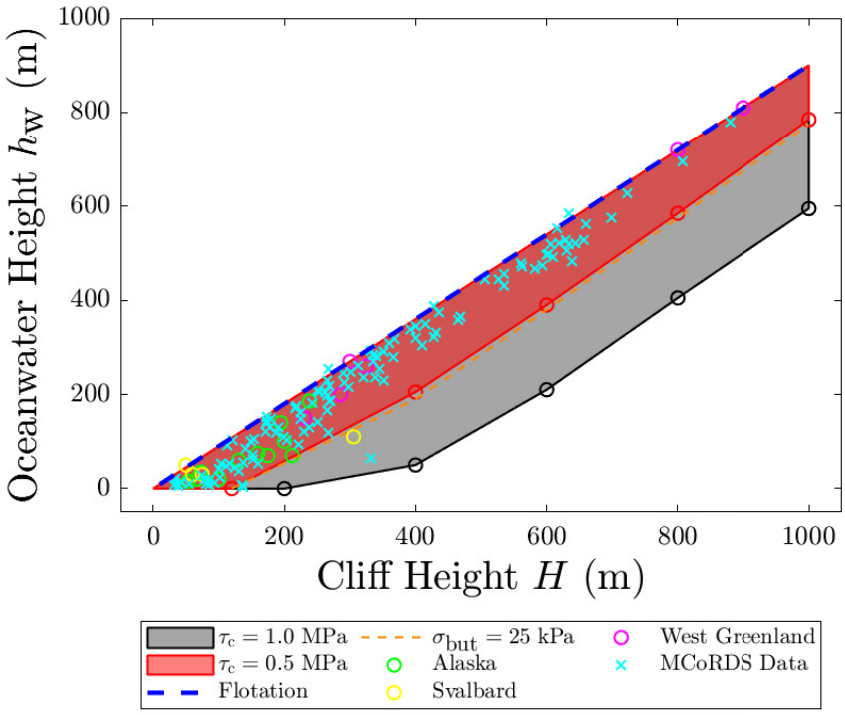

Figure 6.11: Combination of glacier thickness and oceanwater height required for stable ice cliffs to exist (shaded regions), floatation to occur (upper-left triangular region), or cliff slumping to trigger (bottom right triangle). Observational data from Alaska, Svalbard and West Greenland Glaciers from Pelto et al [5] and MCoRDS radar data for various Greenland outlet glaciers from Ma et al [6].

A mostly linear relationship between glacier thickness and critical oceanwater height is observed, meaning the critical glacier free-board ($H - h_{\mathrm{w}}$) is independent of glacier thickness. Instead, the critical glacier free-board is dependent on cohesion τ_{c}. For $\tau_{\mathrm{c}} = 0.5$ MPa, the stability region is bounded by the red zone in Figure 6.11. It is observed that a critical glacier free-board of $H - h_{\mathrm{w}} \approx 215$ m is achieved, which is in accordance with observational data (i.e. recorded measurements of existing glaciers are within the stability zone). However, increasing the cohesion to $\tau_{\mathrm{c}} = 1.0$ MPa gives a larger stability region (grey zone in Figure 6.11) and results in a critical glacial free-board of $H - h_{\mathrm{w}} \approx 405$ m. Observational measurements for glacier thickness and oceanwater height have been added to Figure 6.11. The data used was recorded by Landsat 4, reported in Pelto et al [5], with measurements taken from the Columbia glacier in Alaska, West Greenland and Svallbard Glaciers. Additional data for Greenland glaciers including the Helheim, Jakobshavn, Petermann and Hayes glaciers has been measured using Multichannel Coherent Radar Depth Sounder (MCoRDS) from Ma et al [6] (cyan datapoints in Figure 6.11). When comparing the observational data to the stability envelope produced from phase field simulations, it can be seen that the majority of observations are encompassed within the stability envelope for $\tau_{\mathrm{c}} = 0.5$ MPa, whereas $\tau = 1.0_{\mathrm{c}}$ MPa provides an overly conservative approximation. The majority of glacier observations show thicknesses of less than 400 m, whilst thicker glaciers tend towards buoyancy.

The current analysis also implies an upper limit on glacial ice thickness H_{crit}, which will be achieved when the critical oceanwater height for cliff failure exceeds the oceanwater height for the glacier to become buoyant. This is indicated by the failure envelope (red line) and the line indicating floatation (blue line) not being parallel. This means that glaciers thicker than this limit will have to form a floating ice tongue for $(H - h_{\mathrm{w}}^{\mathrm{crit}}) \leq (1 - \rho_{\mathrm{i}}/\rho_{\mathrm{sw}})\, H$. If the numerical results

for critical oceanwater height are extrapolated for deep glacier thicknesses, the thickness at which the critical oceanwater height for cliff failure is equal to the oceanwater height for floatation (i.e. where the blue and red lines intersect) is approximately equal to $H_{\text{crit}} = 2200\text{m}$. Thus for glaciers of thickness $H_{\text{crit}} > 2200\text{m}$ it is not possible to have a stable cliff height and for the glacier to remain grounded. Ice shelves of this thickness would also thin due melting at the underside of the shelf.

6.4.1 Inclusion of Buttressing Stresses

The current analysis of cliff failure in marine terminating glaciers has neglected any buttressing stresses that may be applied at the glacier front due to the formation of ice mélange from calving events. Various simulations have shown that the presence of ice mélange has led to reductions in iceberg calving [193, 194]. This may contribute to seasonal variations in calving rates (as well as increased production in meltwater), where mélange is present in winter periods and absent in the summer.

To investigate the influence of buttressing stress on calving, a horizontal traction is applied at the far right terminus of the glacier, with a magnitude of 25 kPa and a contact area extended 25 m above the waterline h_{w} and 55 m beneath the waterline as per Bassis et al [175].

For this configuration of buttressing stress, it is observed that an increase of 10 m in the critical glacier free-board for glaciers thicker than $H \geq 600$ m, whilst for thinner glaciers, a 15 m increase in critical glacier free-board is observed. This result is expected, since the difference in oceanwater pressure can be approximately equated to the buttressing stress and thus the change in oceanwater height

is $\Delta h_{\mathrm{w}} \approx \sqrt{2\sigma_{\mathrm{but}} w/(\rho_{\mathrm{w}} g)}$.

Whilst this increase in free-board is relatively trivial, a greater understanding of magnitude and application of buttressing stress is required to achieve more representative results. The modified stability envelope for $\tau_{\mathrm{c}} = 0.5$ MPa is represented by the orange dashed line in Figure 6.11, showing the limited increase in stable heights obtained through buttressing stress.

6.5 Discussion

It is acknowledged that there are a few limitations to the assessment presented in the present chapter. Firstly, the ice sheet geometry used is a highly idealised rectangular slab with a horizontal grounding line, and no pre-existing crevasses are included. These pre-existing crevasses, originating from extensional strains or previous fracture events, could act to localise the crevasses or increase stresses beyond what is expected for a pristine ice sheet. As a result, crevasses are likely to develop sooner, and the ice sheet might calve at greater ocean heights. The influence of a prograde or retrograde bed slope is also not explored within the present chapter, which may lead to progressive failure and rapid grounding retreat. While these progressive failures were observed for some of the $\mu = 0$ cases, prograde slopes would enhance the stability of the ice cliff, whereas retrograde slopes would expose taller ice cliffs as subsequent crevassing occurs. While not considered presently, the current model could be applied to study these events, as no *a priori* information is required for the expected location of crevasses, and intersecting crevasses are automatically resolved.

In addition, it is found that in order for cliff failure to occur for ground terminating glaciers, ice sheets must be undergoing high basal friction or are subject to no-slip

frozen base conditions. This assumption is valid if basal ice is sufficiently cold, and friction coefficients approaching this no slip condition have been observed [195]. However, temperate ice in close vicinity to the ocean may undergo melting, leading to ingress of oceanwater and therefore basal lubrication and increased sliding. This increase in sliding may favour the propagation of crevasses in far field regions as opposed to cliff failure near the glacier terminus.

In addition, the model also neglects the effects of melt undercutting and buoyancy pressures applied to the base of the glacier after a subaerial calving event, which may trigger subsequent buoyant calving and lead to rapid glacier retreat. Glacial mass losses in the form of basal undercutting may lead to altered stress states which would affect calving rates. However, it is unclear whether submarine melting prevents or enhances calving [196, 197].

Although the analysis has explored variations in cohesive strength τ_c and internal friction μ, there remains a high level of uncertainty as to what is the most realistic value for glacial ice, with differing values having a large influence on critical glacier free-board.

Finally, the above analysis has assumed that all surface fractures are dry. While the inclusion of meltwater is straightforward in the present framework, see [132, 72], no studies have been performed on its effect here, to limit the number of parameters being varied. However, if included, the inclusion of meltwater driven hydrofracture would result in increased tensile stresses in fractured regions and reduce the critical glacier free-board value to cause calving. Furthermore, as meltwater driven cracks typically are mode I (tensile) fractures, they tend to propagate vertically, causing steeper cliffs to be created compared to those predicted within this model. As such, including meltwater within this framework would allow for further study of the successive crevassing observed within the

$\mu = 0$ cases (Figure 6.8); providing insight into the role of meltwater in ice cliff stability.

The current analysis implies that the glacier fronts from observational data are encompassed within the stability region for $\tau_c = 0.5$MPa and therefore are not likely to calve, based off of the above assumptions stated. In reality, these glacier fronts may become unstable and undergo subaerial calving if meltwater was allowed to accumulate within upper surface fractures, or may undergo submarine calving if the effects of melt undercutting/buoyancy pressures are considered. Further research should therefore be conducted to include these mechanisms and to determine how this influences the stability of the calving front.

6.5.1 Implications for fracture modelling

The results produced in the current chapter inform ice fracture modellers on appropriate values of cohesion and internal friction coefficients to use in future studies. As stated previously, a large amount of variation exists in the literature for experimental data for τ_c and μ. It is found that for high values of internal friction, values of cohesion in the range of $\tau_c = 0.3$-0.6 MPa provide a stability envelope for ice cliff failure which is in good agreement with observational measurements from Pelto et al [5] and Ma et al [6]. These values of cohesion are in accordance with shear tests conducted by Frederking [188], Butkovich [198] and Paige [199].

Since variations in internal friction μ alter the fracture criterion significantly, the current work has also indicated the role of extending phase field models to include the correct failure criteria for ice. This research has provided a first step in extending these methods beyond only considering tensile driven mode I crevasses.

However, further analysis is required into determining the correct failure surface for mixed mode fractures within ice. While the produced failure events match to observed cliff heights, it is yet unclear if the Mohr-Coulomb type fracture criterion used here is most appropriate. Alternatives used within literature for other materials include Drucker-Prager type models [200, 201], or models which assign unique fracture energies for mode I and mode II [202]. However, even though the exact constitutive model to use is unclear, the results obtained here indicate that standard phase field schemes that are commonly used to model crevasses through ice sheets, e.g. [179, 71], are not applicable to the near terminus region, instead requiring models such as the one presented currently that are capable of capturing mixed mode fracture processes.

6.5.2 Stability criteria for large scale ice sheet models

The results from the current study provide a sound justification for height above buoyancy models previously suggested in the literature [203, 40]. However, the stability criteria predicted from the phase field method is conservative in comparison with that of discrete element method approaches, with the phase field model predicting a height above buoyancy limit of approximately 200 m for $\tau_c = 0.5$ MPa. For example, Benn et al [178] predict a maximum cliff height of 110 m for a strength of $\tau_c = 1$ MPa. Crawford et al [146] predicts structural cliff failure of cliff heights greater than 135 m, whilst for thinner glaciers, failure is driven by buoyant calving. This result is consistent with the findings of Bassis et al [175]. For empirical relations, Deconto and Pollard [148, 172] determine a limit for subaerial cliff heights of 100 m for a strength of 1 MPa, whilst Bassis et al [147] predicts a cliff thickness of 221 m for land terminating glaciers with no friction and $\tau_c = 1$ MPa. One other finding resulting from the present model is that for land terminating glaciers, the height limitation is reduced below the height-above-buoyancy criterion, with failure observed above a height of 125 m (versus the height above buoyancy criterion indicating 200 m). This indicates that, as ice sheets retreat and become land terminating, the criterion for removing ice at the terminus within large scale ice sheet models needs to be adapted to reflect this reduced stability. As different failure mechanisms were observed depending on the basal friction coefficient, these criteria also need to account for the basal conditions: if the bed is at near melting temperatures, even steep ice cliffs of above 200 m are predicted to be stable. In contrast, if the base is frozen, cliffs with heights above 125 m collapse. Including this enhanced strength as the bed becomes warmer would act to increase the stability, counteracting some of the mass loss due to the enhanced melting.

6.6 Concluding Remarks

In the current chapter, the phase field fracture method using a Mohr-Coulomb failure criterion has been presented and used to study the critical conditions at which creeping grounded glaciers are susceptible to structural ice cliff failure. The following conclusions have been drawn from the presented work.

- For glaciers undergoing free slip and subject to low levels of basal shear stress, damage propagates as a result of tensile far field longitudinal stresses and fractures can therefore be considered as mode I tensile crevasses.
- For high values of basal friction and for glaciers frozen to the bedrock, fracture occurs as a result of shear faulting and may lead to full thickness cliff failure.
- Different values of internal friction μ and cohesion τ_c are also considered in this analysis, finding that friction influences the mode of failure, whilst cohesion influences the height at which a stable cliff height is achieved.
- For values of $\tau_c = 1$ MPa, it is found that cliff failure occurs in glaciers of height $H \geq 200$ m, a result that is consistent with the literature. This reduces to $H \geq 85$ m, when considering a cohesion of $\tau_c = 0.25$ MPa.
- For marine terminating glaciers, the application of oceanwater pressure results in a compressive stress that offsets extensional stresses from glacier motion, allowing for thicker glaciers to exist. Cliff failure in marine terminating glaciers is observed, with fracture occurring above the oceanwater surface, if the glacier free-board exceeds a critical value.
- Similar to land terminating glaciers, the value of critical free-board is highly dependent on cohesive strength τ_c, but larger values of glacier free-board

are observed compared to the land terminating case. For $\tau_c = 0.5$ MPa, a critical free-board of $H - h_w \approx 215$ m is observed, but this increases to $H - h_w \approx 425$ m for $\tau_c = 1.0$ MPa.

- For lower values of cohesive strength, the results are in accordance with field observations.

Chapter 7

Conclusions

The current work has presented a numerical framework to model diffuse fracture patterns using the phase field method, implemented using the standard finite element method. This has been applied in the context of modelling crevasse propagation subject to hydrofracture in glaciers and ice shelves, with the results being validated with analytical solutions and observational data.

In Chapter 4, the propagation of water filled surface and basal crevasses, subject to hydrofracture in grounded glaciers and floating ice shelves is studied, using the phase field fracture method. It was found that a crack driving force, driven by tensile states of maximum principal stress produce results that are insensitive to the phase field length scale ℓ_c and can capture the tensile-compressive asymmetric behaviour of ice, which traditional energy based splits cannot. For isolated crevasses, the phase field method gave excellent agreement with crevasse penetration depths predicted by linear elastic fracture mechanics (LEFM), when using crack driving force thresholds to localise damage solely beneath pre-specified notches. Whilst for densely spaced crevasses, phase field accurately captured crevasse shielding, with predictions being in good agreement with the

Nye zero stress method. The presence of meltwater in crevasses results in additional pressures being applied to the crack walls, leading to deeper stabilised penetration depths. By contrast, the presence of oceanwater pressure at the terminus provides compressive longitudinal stresses that aid in stabilising the glacier. Crevasse penetration depths are also dependent on ice rheology, with the inclusion of steady state creep leading to stresses being more extensional in the upper surface and resulting in deeper crevasses. For floating ice shelves, no surface crevasse propagation is observed in far field regions, regardless of the amount of meltwater present, owing to the longitudinal stress profile being entirely compressive. By contrast, for crevasses located close to the ice shelf front, there is potential for full thickness propagation, leading to tabular iceberg calving if the crevasse is close to full saturation. It is also demonstrated that the phase field method can capture crevasse coalescence and cracking in 3D.

In Chapter 5, novel equations for longitudinal stress are derived, considering depth-dependent material properties due to upper surface firn layers, with analytical expressions agreeing well with numerical stress solutions. LEFM and phase field studies are conducted to determine the influence of firn on crevasse penetration depth, with results compared to the fully consolidated homogeneous ice case. It was found that for surface crevasses in grounded glaciers, the inclusion of depth-dependent density and Young's modulus resulted in a maximum reduction in penetration depth of 20% and 44.9% respectively, when comparing to the homogeneous case for a linear elastic rheology. The influence of firn material properties is most prevalent for shallow crevasses in thin glaciers, and the difference in penetration depth begins to reduce when the crevasse begins to stabilise in fully consolidated strata. For floating ice shelves, crevasses in close proximity to the front propagate deeper when considering a depth dependent density due to the reduction in floatation height and lithostatic stress. However, the inclusion

of depth-dependent Young's modulus results in more stable crevasses. Unlike the grounded glacier case – where differences in crevasse penetration depths begin to become negligible at $H > 250$ m – increases in crevasse penetration depth can still be observed in thick ice shelves, up to $H = 1000$ m.

In Chapter 6, a phase field fracture method based on a Mohr-Coulomb failure criterion is implemented to determine the critical conditions required for subaerial ice cliff failure. It is found that glaciers undergoing free slip or subject to low levels of basal friction at the base are susceptible to mode I crevassing in the far field region, as a result of longitudinal tensile stresses. By contrast, for the no-slip condition or glaciers undergoing high basal friction, damage initiates at one thickness away from the terminus and ice cliff calving may occur if the glacier thickness exceeds a critical value, with the conditions to cause failure being dependent on cohesive strength τ_c and internal friction coefficient μ. For marine terminating glaciers, subaerial ice cliff calving is dependent on whether a critical glacier free-board is exceeded. For $\tau_c = 0.5$ MPa, the critical glacier free-board required for cliff failure is $H - h_w \approx 215$ m, which provides a stability envelope that well-encompasses observational data of existing stable outlet glaciers in West Greenland and Alaska. These results are slightly conservative, compared to empirical relations and discrete element models, which predict a critical glacier free-board of 100-150 m.

7.1 Future Work

The limitations presented currently has helped to outline potential future work. Firstly, the phase field fracture model presented assumes ice to be an isothermal solid and neglects any thermal effects, including melting/refreezing or frictional

heating [84]. This assumption is valid if the thermal process is slow in comparison to the rate of fracture. The inclusion of thermal modelling may assist in the understanding of the production of basal meltwater, leading to enhanced subglacial hydrology flow and altered basal conditions.

In addition, the use of poro-damage mechanics methods to prescribe set meltwater depth ratios is an effective way to parametrise the effect of melt accumulation rates on crevasse propagation. Instead, phase field methods could be coupled with fluid transport models, where pressure is solved through the fluid mass balance equation [204, 205]. Meltwater can therefore be prescribed using inlet volume fluxes which may be linked to meltwater production rates and the drainage of supraglacial lakes.

Finally, owing to the insensitivity of length scale for stress based phase field methods and their ability to capture damage initiation from arbitrary sites, there is potential to incorporate these into large scale ice sheet models to capture the propagation of historic ice shelf rifts, to facilitate a better understanding of previous iceberg calving events.

Bibliography

[1] C. Miehe, M. Hofacker, F. Welschinger, A phase field model for rate-independent crack propagation: Robust algorithmic implementation based on operator splits, Computer Methods in Applied Mechanics and Engineering 199 (45-48) (2010) 2765–2778.

[2] J. F. Nye, Comments on Dr. Loewe's letter and notes on crevasses, Journal of Glaciology 2 (17) (1955) 512–514.

[3] F. M. Nick, A. Vieli, I. M. Howat, I. Joughin, Large-scale changes in Greenland outlet glacier dynamics triggered at the terminus, Nature Geoscience 2 (2) (2009) 110–114.

[4] M. A. Rist, P. R. Sammonds, H. Oerter, C. S. M. Doake, Fracture of Antarctic shelf ice, Journal of Geophysical Research: Solid Earth 107 (B1) (2002) 1–13.

[5] M. Pelto, C. Warren, Relationship between tidewater glacier calving velocity and water depth at the calving front, Annals of Glaciology 15 (1991) 115–118.

[6] Y. Ma, C. S. Tripathy, J. Bassis, Bounds on the calving cliff height of marine terminating glaciers, Geophysical Research Letters 44 (2017) 1369–1375.

[7] M. Siegert, Ice Sheets and Late Quaternary environmental change, John Wiley & Sons, Inc., 2001.

[8] M. Siegert, R. B. Alley, E. Rignot, J. Englander, R. Corell, Twenty-first century sea-level rise could exceed IPCC projections for strong-warming futures, One Earth 3 (6) (2020) 691–703.

[9] R. Williams, J. Ferrigno, Satellite image atlas of glaciers of the world, US Geological Survey Professional Paper 1386 (A) (2002).

[10] J. J. Furst, G. Durand, F. Gillet-Chaulet, L. Tavard, M. Rankl, M. Braun, O. Gagliardini, The safety band of antarctic ice shelves (2016).

[11] R. Reese, G. Gudmundsson, A. Levermann, R. Winkelmann, The far reach of ice-shelf thinning in antarctica (2017).

[12] C. Y. Lai, J. Kingslake, M. G. Wearing, P. H. C. Chen, P. Gentine, H. Li, J. J. Spergel, J. M. van Wessem, Vulnerability of Antarctica's ice shelves to meltwater-driven fracture, Nature 584 (7822) (2020) 574–578.

[13] C. Gerli, S. Rosier, G. H. Gudmundsson, S. Sun, Weak relationship between remotely detected crevasses and inferred ice rheological parameters on antarctic ice shelves, The Cryosphere 18 (2023) 2677–2689.

[14] M. J. Siegert, 164: Role of glaciers and ice sheets in climate, in: M. G. Anderson (Ed.), Encyclopedia of Hydrological Sciences, John Wiley & Sons, 2005, pp. 1–16.

[15] D. I. Benn, D. J. Evans, Glaciers & glaciation, 2nd Edition, Taylor & Francis Group, 2010.

[16] J. H. Mercer, West Antarctic ice sheet and CO2 greenhouse effect: A threat of disaster, Nature 271 (5643) (1978) 321–325.

[17] H. Rott, P. Skvarca, T. Nagler, Rapid collapse of northern Larsen Ice Shelf, Antarctica, Science 271 (5250) (1996) 788–792.

[18] E. Domack, D. Duran, A. Leventer, S. Ishman, S. Doane, S. McCallum, D. Amblas, J. Ring, R. Gilbert, M. Prentice, Stability of the Larsen B ice shelf on the Antarctic Peninsula during the Holocene epoch, Nature 436 (7051) (2005) 681–685.

[19] T. Mitcham, G. H. Gudmundsson, J. L. Bamber, G. Centre, The instantaneous impact of calving and thinning on the Larsen C Ice Shelf, The Cryosphere 16 (2022) 883–901.

[20] S. Lhermitte, S. Sun, C. Shuman, B. Wouters, F. Pattyn, J. Wuite, E. Berthier, T. Nagler, Damage accelerates ice shelf instability and mass loss in Amundsen Sea Embayment, Proceedings of the National Academy of Sciences of the United States of America 117 (40) (2020) 24735–24741.

[21] C. Walker, J. Millstein, B. Miles, S. Cook, A. Fraser, A. Colliander, S. Misra, L. Trusel, S. Adusumilli, H. Fricker, The multi-decadal collapse of east antarctica's conger-glenzer ice shelf [Submitted], Nature Portfolio (2024).

[22] M. A. Depoorter, J. L. Bamaber, J. A. Griggs, J. T. M. Leneaerts, S. R. M. Ligtenberg, M. R. van den Broeke, G. Moholdt, Calving fluxes and basal melt rates of antarctic ice shelves, nature 502 (2013) 89–92.

[23] K. A. Naughten, K. J. Meissner, B. K. Galton-Fenzi, M. H. England, R. Timmermann, H. H. Hellmer, Future projections of antarctic ice shelf melting based on cmip5 scenarios 31 (2018) 5243–5261.

[24] F. Paolo, H. Fricker, L. Padman, Volume loss from antarctic ice shelves is accelerating, Science 348 (2015) 327–331.

[25] E. Rignot, G. Casassa, P. Gogineni, W. Krabill, A. Rivera, R. Thomas, Accelerated ice discharge from the antarctic peninsula following thecollapse of larsen b ice shelf, Geophysical Research Letters 31 (2004).

[26] T. Frederikse, F. Landerer, L. Caron, S. Adhikari, D. Parkes, V. W. Humphrey, S. Dangendorf, P. Hogarth, L. Zanna, L. Cheng, Y. H. Wu, The causes of sea-level rise since 1900, Nature 584 (7821) (2020) 393–397.

[27] IPCC, Summary for policymakers. In IPCC Special Report on the Ocean and Cryosphere in a Changing Climate, 2019.

[28] E. M. Schulson, The structure and mechanical behavior of ice, The Journal of The Minerals, Metals & Materials Society 51 (1999) 21–27.

[29] J. J. Petrovic, Mechanical properties of ice and snow, Journal of Materials Science 38 (2003) 1–6.

[30] W. Colgan, H. Rajaram, W. Abdalati, C. McCutchan, R. Mottran, M. Moussavi, S. Grigsby, Glacier crevasses: Observations, models, and mass balance implications, Review of Geophysics 54 (2016) 119–161.

[31] E. M. Enderlin, T. C. Bartholomaus, Sharp contrasts in observed and modeled crevasse patterns at Greenland's marine terminating glaciers, Cryosphere 14 (11) (2020) 4121–4133.

[32] N. Selmes, T. Murray, D. James, Fast draining lakes on the greenland ice sheet, Geophysical Research Letters 38 (2011).

[33] R. Alley, T. K. Dupont, B. Parizek, S. Anandakrishnan, Access of surface meltwater to beds of sub-freezing glaciers: preliminary insights, Annals of Glaciology 40 (2005) 8–14.

[34] D. Lampkin, N. Amador, B. Parizek, K. Farness, K. Jezek, Drainage from water-filled crevasses along the margins of jakobshavn isbræ: A potential

catalyst for catchment expansion, Journal of Geophysical Research: Earth Surface 118 (2013) 795–813.

[35] P. Tuckett, J. Ely, A. Sole, S. Livingstone, B. Davison, M. van Wessem, J. Howard, Rapid accelerations of antarctic peninsula outlet glaciers driven by surface melt, Nature Communications (2019) 1–8.

[36] K. Poinar, I. Joughin, D. Lilien, L. Brucker, L. Kehrl, S. Nowicki, Drainage of southeast greenland firn aquifer water through crevasses to the bed, Frontiers in Earth Science 5 (2017).

[37] T. A. Scambos, J. A. Bohlander, C. A. Shuman, P. Skvarca, Glacier acceleration and thinning after ice shelf collapse in the Larsen B embayment, Antarctica, Geophysical Research Letters 31 (18) (2004) 2001–2004.

[38] T. Scambos, H. A. Fricker, C. C. Liu, J. Bohlander, J. Fastook, A. Sargent, R. Massom, A. M. Wu, Ice shelf disintegration by plate bending and hydro-fracture: Satellite observations and model results of the 2008 Wilkins ice shelf break-ups, Earth and Planetary Science Letters 280 (1-4) (2009) 51–60.

[39] J. F. Nye, The distribution of stress and velocity in glaciers and ice-sheets, Proceedings of the Royal Society of London. Series A. Mathematical and Physical Sciences 239 (1216) (1957) 113–133.

[40] D. I. Benn, C. R. Warren, R. H. Mottram, Calving processes and the dynamics of calving glaciers, Earth-Science Reviews 82 (3-4) (2007) 143–179.

[41] F. M. Nick, C. J. van der Veen, A. Vieli, D. I. Benn, A physically based calving model applied to marine outlet glaciers and implications for the glacier dynamics, Journal of Glaciology 56 (199) (2010) 781–794.

[42] S. Sun, S. L. Cornford, J. C. Moore, R. Gladstone, L. Zhao, Ice shelf fracture parameterization in an ice sheet model, Cryosphere 11 (6) (2017) 2543–2554.

[43] J. Weertman, Theory of water-filled crevasses in glaciers applied to vertical magma transport beneath oceanic ridge, Journal of Geophysical Research 76 (1971) 1171–1183.

[44] J. Weertman, Can a water-filled crevasse reach the bottom surface of a glacier?, IAHS 95 (1973) 139–145.

[45] G. Irwin, Analysis of stresses and strains near the end of a crack traversing a plate, Journal of Applied Mechanics 24 (1957) 361–364.

[46] S. DeFranco, J. Dempsey, Fracture process zone analysis in saline ice, ASME Applied Mechanics Division Publications - AMD 163 (1993).

[47] W. F. Hu, X. Z., Fracture energy and fracture process zone, Materials and Structures 25 (1992) 319–326.

[48] R. Smith, The application of fracture mechanics to the problem of crevasse penetration, Journal of Glaciology 17 (1976) 223–228.

[49] C. J. van der Veen, Fracture mechanics approach to penetration of surface crevasses on glaciers, Cold Regions Science and Technology 27 (1) (1998) 31–47.

[50] C. J. van der Veen, Fracture mechanics approach to penetration of bottom crevasses on glaciers, Cold Regions Science and Technology 27 (3) (1998) 213–223.

[51] J. R. Rice, A path independent integral and the approximate analysis of strain concentration by notches and cracks, Journal of Applied Mechanics 35 (1968) 379–386.

[52] R. H. Mottram, D. I. Benn, Testing crevasse-depth models: A field study at breidõamerkurjö kull, iceland, Journal of Glaciology 55 (192) (2009) 746–752.

[53] H. Yu, E. Rignot, M. Morlinghem, H. Seroussi, Iceberg calving of thwaites glacier, west antarctica: full-stokes modeling combined with linear elastic fracture mechanics, The Cryosphere 11 (2017) 1283–1296.

[54] M. Zarrinderakht, C. Schoof, A. Peirce, An analysis of the interaction between surface and basal crevasses in ice shelves, The Cryosphere 18 (2024) 3841–3856.

[55] M. Zarrinderakht, C. Schoof, A. Peirce, The effect of hydrology and crevasse wall contact on calving, Cryosphere 16 (10) (2022) 4491–4512.

[56] S. S. Thompson, S. Cook, B. Kulessa, J. P. Winberry, A. D. Fraser, B. K. Galton-Fenzi, Comparing satellite and helicopter-based methods for observing crevasses, application in east antarctica, Cold Regions Science and Technology 178 (2020).

[57] N. Glasser, T. Scamnbos, A structural glaciological analysis of the 2002 larsen b ice shelf collapse, Journal of Glaciology 54 (2008) 3–16.

[58] D. MacAyeal, T. Scambos, C. Hulbe, M. Fahnestock, Catastrophic ice shelf breakup by an ice shelf fragment capsize mechanism, Journal of Glaciology 49 (2003) 22–36.

[59] M. van den Broeke, Strong surface melting preceded collapse of antarctic peninsula ice shelf, Geophysical Research Letters 32 (2005).

[60] E. Rignot, J. Mouginot, B. Scheuchl, Ice flow of the antarctic ice sheet, Science 333 (2011) 1427–1430.

[61] A. Kovacs, G. Abele, Crevasse detection using an impulse radar system, Antarctic Journal 9 (1974).

[62] A. Taurisano, S. Tronstad, O. Brandt, J. Kohler, On the use of ground penetrating radar for detecting and reducing crevasse-hazard in dronning maud land, antarctica, Cold Regions of Science and Technology 45 (2006) 166–177.

[63] D. Karr, K. Choi, A three-dimensional constitutive damage model for polycrystalline ice, Mechanics of Materials 8 (1989) 55–66.

[64] M. Mellor, D. Cole, Deformation and failure of ice under constant stress or constant strain-rate, Cold Regions Science and Technology 5 (1982) 201–219.

[65] A. Pralong, M. Funk, Dynamic damage model of crevasse opening and application to glacier calving, Journal of Geophysical Research: Solid Earth 110 (1) (2005) 1–12.

[66] A. Pralong, M. Funk, M. Luthi, A description of crevasse formation using continuum damage mechanics, Annals of Glaciology 37 (2003) 77–82.

[67] R. Duddu, H. Waisman, A temperature dependent creep damage model for polycrystalline ice, Mechanics of Materials 46 (2012) 23–41.

[68] R. Duddu, H. Waisman, A nonlocal continuum damage mechanics approach to simulation of creep fracture in ice sheets, Computational Mechanics 51 (6) (2013) 961–974.

[69] S. Jiménez, R. Duddu, J. Bassis, An updated-lagrangian damage mechanics formulation for modeling the creeping flow and fracture of ice sheets, Computer Methods in Applied Mechanics and Engineering 313 (2017) 406–432.

[70] S. Jimenez, Damage mechanics approaches for sharp and diffuse fracture propagation: Application to ice sheet fracture and composite delamination, Ph.D. thesis, Vanderbilt University (2017).

[71] M. E. Mobasher, R. Duddu, J. N. Bassis, H. Waisman, Modeling hydraulic fracture of glaciers using continuum damage mechanics, Journal of Glaciology 62 (234) (2016) 794–804.

[72] R. Duddu, S. Jiménez, J. Bassis, A non-local continuum poro-damage mechanics model for hydrofracturing of surface crevasses in grounded glaciers, Journal of Glaciology 66 (257) (2020) 415–429.

[73] A. Huth, R. Duddu, B. Smith, A generalized interpolation material point method for shallow ice shelves. 2: Anisotropic nonlocal damage mechanics and rift propagation, Journal of Advances in Modeling Earth Systems (2021).

[74] A. Huth, R. Duddu, B. Smith, O. Sergienko, Simulating the processes controlling ice-shelf rift paths using damage mechanics, Journal of Glaciology (2023) 1–14.

[75] A. Huth, R. Duddu, B. Smith, A generalized interpolation material point method for shallow ice shelves. 1: Shallow shelf approximation and ice thickness evolution, Journal of Advances in Modeling Earth Systems 13 (2021).

[76] G. I. Barenblatt, The mathematical theory of equilibrium cracks in brittle fracture, Advances in Applied Mechanics 7 (1962) 55–129.

[77] D. S. Dugdale, Yielding of steel sheets containing slits, Journal of the Mechanics and Physics of Solids 8 (1960) 100–104.

[78] G. Alfano, M. A. Crisfield, Finite element interface models for the delamination analysis of laminated composites: Mechanical and computational issues, International Journal for Numerical Methods in Engineering 50 (2001) 1701–1736.

[79] X. Liu, R. Duddu, H. Waisman, Discrete damage zone model for fracture initiation and propagation, Engineering Fracture Mechanics 92 (2012) 1–18.

[80] K. Park, G. H. Paulino, J. R. Roesler, A unified potential-based cohesive model of mixed-mode fracture, Journal of Mechanics and Physics in Solids 57 (2009) 891–908.

[81] J. C. J. Schellekens, R. De Borst, A non-linear finite element approach for the analysis of mode-i free edge delamination in composites, International Journal of Solid Structures 30 (1993) 1239–1253.

[82] S. Jimenez, R. Duddu, J. Bassis, On the parametric sensitivity of cohesive zone models for high-cycle fatigue delamination of composites, International Journal of Solids and Structures 82 (2016) 111–124.

[83] Y. Gao, G. Ghosh, S. Jiménez, R. Duddu, A finite-element-based cohesive zone model of water-filled surface crevasse propagation in floating ice tongues, Computing in Science & Engineering (2023).

[84] T. Hageman, J. Z. Mejia, R. Duddu, E. Martínez-Pañeda, Ice viscosity governs hydraulic fracture causing rapid drainage of supraglacial lakes, The Cryosphere 18 (2024) 3991–4009.

[85] B. Bourdin, G. Francfort, J. J. Marigo, The variational approach to fracture, Journal of Elasticity 91 (2008) 5–148.

[86] G. A. Francfort, J.-J. Marigo, Revisiting brittle fracture as an energy minimization problem, Journal of the Mechanics and Physics of Solids 46 (8) (1998) 1319–1342.

[87] C. Miehe, M. Hofacker, F. Welschinger, A phase field model for rate-independent crack propagation: Robust algorithmic implementation based on operator splits, Computer Methods in Applied Mechanics and Engineering 199 (45-48) (2010) 2765–2778.

[88] M. J. Borden, T. J. Hughes, C. M. Landis, C. V. Verhoosel, A higher-order phase-field model for brittle fracture: Formulation and analysis within the isogeometric analysis framework, Computer Methods in Applied Mechanics and Engineering 273 (2014) 100–118.

[89] T. K. Mandal, V. P. Nguyen, J. Y. Wu, Evaluation of variational phase-field models for dynamic brittle fracture, Engineering Fracture Mechanics 235 (2020) 107169.

[90] Hirshikesh, S. Natarajan, R. K. Annabattula, E. Martínez-Pañeda, Phase field modelling of crack propagation in functionally graded materials, Composites Part B: Engineering 169 (2019) 239–248.

[91] W. Tan, E. Martínez-Pañeda, Phase field predictions of microscopic fracture and r-curve behaviour of fibre-reinforced composites, Composites Science and Technology 202 (2021) 108539.

[92] J. Reinoso, A. Arteiro, M. Paggi, P. Camanho, Strength prediction of notched thin ply laminates using finite fracture mechanics and the phase field approach, Composites Science and Technology 150 (2017) 205–216.

[93] A. Mitrou, A. Arteiro, J. Reinoso, P. Camanho, Modeling fracture of multidirectional thin-ply laminates using an anisotropic phase field formula-

tion at the macro-scale, International Journal of Solids and Structures 273 (2023) 112221.

[94] M. Hasan, M. Zhang, T. Baxevanis, A finite-strain phase-field description of thermomechanically induced fracture in shape memory alloys, Shape Memory and Superelasticity 8 (2022) 356–372.

[95] M. Simoes, E. Martínez-Pañeda, Phase field modelling of fracture and fatigue in shape memory alloys, Computer Methods in Applied Mechanics and Engineering 373 (2021) 113504.

[96] S. Zhou, X. Zhuang, H. Zhu, T. Rabczuk, Phase field modelling of crack propagation, branching and coalescence in rocks, Theoretical and Applied Fracture Mechanics 96 (2018) 174–192.

[97] S. Zhou, X. Zhuang, T. Rabczuk, A phase-field modeling approach of fracture propagation in poroelastic media, Engineering Geology 240 (May) (2018) 189–203.

[98] S. Zhou, X. Zhuang, T. Rabczuk, Phase-field modeling of fluid-driven dynamic cracking in porous media, Computer Methods in Applied Mechanics and Engineering 350 (2019) 169–198.

[99] S. Zhou, X. Zhuang, Phase field modeling of hydraulic fracture propagation in transversely isotropic poroelastic media, Acta Geotechnica 15 (9) (2020) 2599–2618.

[100] A. Golahmar, P. Kristensen, C. Niordson, E. Martínez-Pañeda, A phase field model for hydrogen-assisted fatigue, International Journal of Fatigue 154 (2022) 106521.

[101] C. Huang, X. Gao, Phase field modeling of hydrogen embrittlement, International Journal of Hydrogen Energy 45 (2020) 20053–20068.

[102] T. T. Nguyen, J. Bolivar, J. Réthoré, M. C. Baietto, M. Fregonese, A phase field method for modeling stress corrosion crack propagation in a nickel base alloy, International Journal of Solids and Structures 112 (2017) 65–82.

[103] E. Korec, M. Jirasek, H. Wong, E. Martínez-Pañeda, A phase-field chemo-mechanical model for corrosion-induced cracking in reinforced concrete, Construction and Building Materials 393 (2023) 131964.

[104] S. Kovacevic, W. Ali, E. Martínez-Pañeda, J. LLorca, Phase-field modeling of pitting and mechanically-assisted corrosion of mg alloys for biomedical applications, Acta Biomaterialia 164 (2023) 641–658.

[105] Z. Khalil, A. Elghazouli, E. Martínez-Pañeda, A generalised phase field model for fatigue crack growth in elastic–plastic solids with an efficient monolithic solver, Computer Methods in Applied Mechanics and Engineering 388 (2022) 114286.

[106] P. Carrara, M. Ambati, R. Alessi, L. De Lorenzis, A framework to model the fatigue behavior of brittle materials based on a variational phase-field approach, Computer Methods in Applied Mechanics and Engineering 361 (2020) 112731.

[107] A. Boyce, E. Martínez-Pañeda, A. Wade, Y. Zhang, J. Bailey, T. Heenan, D. Brett, P. Shearing, Cracking predictions of lithium-ion battery electrodes by x-ray computed tomography and modelling, Journal of Power Sources 526 (2022).

[108] R. Xue, X. Li, H. Zhao, Z. Chen, Phase field model coupling with strain gradient plasticity for fracture in lithium-ion battery electrodes, Engineering Fracture Mechanics 269 (2022) 108518.

[109] Y. Zhao, R. Wang, E. Martínez-Pañeda, A phase field electro-chemo-mechanical formulation for predicting void evolution at the li–electrolyte

interface in all-solid-state batteries, Journal of the Mechanics and Physics of Solids 167 (2022) 104999.

[110] M. Hofacker, C. Miehe, A phase field model of dynamic fracture: Robust field updates for the analysis of complex crack patterns, International Journal for Numerical Methods in Engineering 93 (2013) 276–301.

[111] A. A. Griffiths, The phenomena of rupture and flow in solids, Royal Society 221 (582-593) (1920) 163–198.

[112] B. Bourdin, G. A. Francfort, J. J. Marigo, Numerical experiments in revisited brittle fracture, Journal of the Mechanics and Physics of Solids 48 (4) (2000) 797–826.

[113] T. L. Anderson, Fracture Mechanics. Fundamentals and Applications, 3rd Edition, CRC Press, Taylor & Francis, Boca Raton, 2005.

[114] L. Ambrosio, V. M. Tortorelli, Approximation of functional depending on jumps by elliptic functional via t-convergence, Communications on Pure and Applied Mathematics 43 (8) (1990) 999–1036.

[115] D. Mumford, J. Shah, Optimal approximations by piecewise smooth functions and associated variational problems, Communications on Pure and Applied Mathematics 42 (5) (1989) 577–685.

[116] G. Bellettini, A. Coscia, Discrete approximation of a free discontinuity problem, Numerical Functional Analysis and Optimization 15 (3-4) (1994) 201–224.

[117] A. Chambolle, An approximation result for special functions with bounded deformation, Journal des Mathematiques Pures et Appliquees 83 (7) (2004) 929–954.

[118] P. K. Kristensen, E. Martínez-Pañeda, Phase field fracture modelling using quasi-Newton methods and a new adaptive step scheme, Theoretical and Applied Fracture Mechanics 107 (2020) 102446.

[119] P. Li, W. Li, B. Li, S. Yang, Y. Shen, Q. Wang, K. Zhou, A review on phase field models for fracture and fatigue, Engineering Fracture Mechanics 289 (2023) 109419.

[120] H. Amor, J.-J. Marigo, C. Maurini, Regularized formulation of the variational brittle fracture with unilateral contact: Numerical experiments, Journal of the Mechanics and Physics of Solids 57 (2009) 1209–1229.

[121] C. Miehe, L. M. Schänzel, H. Ulmer, Phase field modeling of fracture in multi-physics problems. Part I. Balance of crack surface and failure criteria for brittle crack propagation in thermo-elastic solids, Computer Methods in Applied Mechanics and Engineering 294 (2015) 449–485.

[122] K. Pham, H. Amor, J. J. Marigo, C. Maurini, Gradient damage models and their use to approximate brittle fracture, International Journal of Damage Mechanics 20 (2011) 618–652.

[123] J. W. Glen, The creep of polycrystalline ice, in: Proceedings of the Royal Society of London. Series A, Mathematical and Physical Sciences, 1955, pp. 519–538.

[124] G. Jellinek, H. H, R. Brill, Viscoelastic properties of ice, Journal of Applied Physics 27 (1956) 1198–1209.

[125] L. Ultee, C. Meyer, B. Minchew, Tensile strength of glacial ice deduced from observations of the 2015 eastern skaftá cauldron collapse, vatnajökull ice cap, iceland, Journal of Glaciology 66 (2020) 1024–1033.

[126] E. C. Pettit, E. D. Waddington, Ice flow at low deviatoric stress (2003).

[127] N. Reeh, E. L. Christensen, C. Mayer, O. B. Olesen, Tidal bending of glaciers: A linear viscoelastic approach, Annals of Glaciology 37 (2003) 83–89.

[128] J. M. Thompson, The short-timescale behavior of glacial ice, Ph.D. thesis, California Institute of Technology (2013).

[129] K. Terzaghi, Die berechnung der durchlassigkeitsziffer des tones aus dem verlauf der hydrodynamischen spannungsercheinungen, Akademie der Wissenschaften, Wien Mathematiesch-Naturwissenschaftliche Klasse, Abteilung 132 (1923) 105–124.

[130] M. A. Biot, General theory of three-dimensional consolidation, Journal of Applied Physics 12 (2) (1941) 155–164.

[131] X. Sun, R. Duddu, Hirshikesh, A poro-damage phase field model for hydrofracturing of glacier crevasses, Extreme Mechanics Letters 45 (2021) 101277.

[132] T. Clayton, R. Duddu, M. Siegert, E. Martínez-Pañeda, A stress-based poro-damage phase field model for hydrofracturing of creeping glaciers and ice shelves, Engineering Fracture Mechanics 272 (2022) 108693.

[133] D. G. Karr, K. Choi, A three-dimensional constitutive damage model for polycrystalline ice, Mechanics of Materials 8 (1) (1989) 55–66.

[134] S. Jiménez, R. Duddu, On the evaluation of the stress intensity factor in calving models using linear elastic fracture mechanics, Journal of Glaciology 64 (247) (2018) 759–770.

[135] M. P. Fischer, R. B. Alley, T. Engelder, Fracture toughness of ice and firn determined from the modified ring test, Journal of Glaciology 41 (138) (1995) 383–394.

[136] J. Krug, J. Weiss, O. Gagliardini, G. Durand, Combining damage and fracture mechanics to model calving, Cryosphere 8 (6) (2014) 2101–2117.

[137] C. J. van der Veen, Fundamentals of Glacier Dynamics, CRC Press, 2013.

[138] A. Hillerborg, M. Modeer, P. E. Petersson, Analysis of crack formation and crack growth in concrete by means of fracture mechanics and finite elements, American Concrete Institute, ACI Special Publication SP-249 (2008) 225–237.

[139] C. Plate, R. Muller, A. Humbert, D. Gross, Evaluation of the criticality of cracks in ice shelves using finite element simulations, The Cryosphere 6 973–984.

[140] M. A. Rist, P. R. Sammonds, S. A. F. Murrell, P. G. Meredith, C. S. M. Doake, H. Oerter, K. Matsuki, Experimental and theoretical fracture mechanics applied to Antarctic ice fracture and surface crevassing, Journal of Geophysical Research: Solid Earth 104 (B2) (1999) 2973–2987.

[141] J. Krug, J. Weiss, O. Gagliardini, G. Durand, Combining damage and fracture mechanics to model calving, Cryosphere 8 (6) (2014) 2101–2117.

[142] S. Jiménez, R. Duddu, On the evaluation of the stress intensity factor in calving models using linear elastic fracture mechanics, Journal of Glaciology 64 (247) (2018) 759–770.

[143] M. B. Nooru-Mohamed, Mixed-mode fracture of concrete: An experimental approach, Ph.D. thesis, TU Delft (1993).

[144] V. Acocella, A. Gudmundsson, R. Funiciello, Interaction and linkage of extension fractures and normal faults: examples from the rift zone of Iceland, Journal of Structural Geolog 22 (2000) 1–14.

[145] G. Wesley Patterson, J. W. Head, Segmented lineaments on Europa: Implications for the formation of ridge complexes and bright bands, Icarus 205 (2) (2010) 528–539.

[146] A. Crawford, D. Benn, J. Todd, J. Astrom, J. Bassis, T. Zwinger, Marine ice-cliff instability modeling shows mixed-mode ice-cliff failure and yields calving rate parameterization, Nature Communications 2701 (2021).

[147] J. N. Bassis, C. C. Walker, Upper and lower limits on the stability of calving glaciers from the yield strength envelope of ice, Proceedings of the Royal Society A: Mathematical, Physical and Engineering Sciences 468 (2140) (2012) 913–931.

[148] D. Pollard, R. M. DeConto, R. B. Alley, Potential Antarctic Ice Sheet retreat driven by hydrofracturing and ice cliff failure, Earth and Planetary Science Letters 412 (2015) 112–121.

[149] S. Veldhuijsen, W. van de Berg, M. Brils, P. Munneke, M. can den Broeke, Characteristics of the contemporary antarctic firn layer simulated with imau-fdm v1.2a (1979-2020), The Cryosphere 17 (2022) 1675–1696.

[150] M. A. Rist, P. R. Sammonds, S. A. Murrell, P. G. Meredith, H. Oerter, C. S. Doake, Experimental fracture and mechanical properties of Antarctic ice: Preliminary results, Annals of Glaciology 23 (1996) 284–292.

[151] W. Paterson, The physics of glaciers, 3rd Edition, Elsevier, Oxford, 1994.

[152] T. Clayton, R. Duddu, T. Hageman, E. Martínez-Pañeda, The influence of firn-layer material properties on surface crevasse propagation in glaciers and ice shelves [Submitted], The Cryosphere (2024).

[153] J. Weertman, Deformation of Floating Ice Shelves , Journal of Glaciology 3 (21) (1957) 38–42.

[154] M. Ashby, A. Evans, N. Fleck, L. Gibson, J. Hutchinson, H. Wadley, Chapter 4 - properties of metal foams, in: Metal Foams, Butterworth-Heinemann, Burlington, 2000, pp. 40–54.

[155] S. Timoshenko, S. Woinowsky-Krieger, Theory of plates and shells, 2nd Edition, McGraw Hill, 1959.

[156] G. Wakahama, D. Kuroiwa, T. Hasemi, Field observations and experimental and theoretical studies on the superimposed ice of McCall Glacier, Alaska, Journal of Glaciology 16 (74) (1976) 135–149.

[157] F. Oraschewski, A. Grinsted, Modeling enhanced firn densification due to strain softening, The Cryosphere 16 (2022) 2683–2700.

[158] J. L. Smith, The elastic constants, strength and density of greenland snow as determined from measurements of sonic wave velocity, Tech. rep., US Army Cold Regions Research & Engineering Laboratory (1965).

[159] R. Schlegel, A. Diez, A. Lowe, H. Mayer, C. Lambrecht, A. Freitag, H. Miller, C. Hofstede, O. Eisen, Comparison of elastic moduli from seismic diving-wave and ice-core microstructure analysis in antarctic polar firn, Annals of Glaciology 60 (2019) 220–230.

[160] E. C. King, E. P. Jarvis, Use of shear waves to measure poisson's ratio in polar firn, Journal of Environmental and Engineering Geophysics 12 (2007) 15–21.

[161] W. R. Buck, The role of fresh water in driving ice shelf crevassing, rifting and calving, Earth and Planetary Science Letters 624 (2023) 118444.

[162] W. R. Buck, C.-Y. Lai, Flexural control of basal crevasse opening under ice shelves, Geophysical Research Letters (2021).

[163] C. Amory, C. Buizert, S. Buzzard, E. Case, N. Clerx, R. Culberg, R. T. Datta, R. Dey, R. Drews, D. Dunmire, C. Eayrs, N. Hansen, A. Humbert, A. Kaitheri, K. Keegan, P. Kuipers Munneke, J. T. M. Lenaerts, S. Lhermitte, D. Mair, I. McDowell, J. Mejia, C. R. Meyer, E. Morris, D. Moser, F. M. Oraschewski, E. Pearce, S. de Roda Husman, N.-J. Schlegel, T. Schultz, S. B. Simonsen, C. M. Stevens, E. R. Thomas, M. Thompson-Munson, N. Wever, B. Wouters, The Firn Symposium team, Firn on ice sheets, Nature Reviews Earth & Environment 5 (2) (2024) 79–99.

[164] M. van den Broeke, Depth and Density of the Antarctic Firn Layer, Arctic, Antarctic, and Alpine Research 40 (2) (2008) 432–438.

[165] S. C. Buzzard, D. L. Feltham, D. Flocco, A Mathematical Model of Melt Lake Development on an Ice Shelf, Journal of Advances in Modeling Earth Systems 10 (2) (2018) 262–283.

[166] E. Hill, B. Urruty, R. Reese, J. Garbe, O. Gagliardini, G. Durand, F. Gilet-Chaulet, H. Gudmundsson, R. Winklemann, M. Chekki, D. Chandler, P. Langebroek, The stability of present-day antarctic grounding lines – part 1: No indication of marine ice sheet instability in the current geometry, The Cryosphere 17 (2023) 3739–3759.

[167] C. Schoof, Ice sheet grounding line dynamics: steady states, stability, and hysteresis, Journal of Geophysical Research 112 (2007).

[168] M. Wise, J. Dowdeswell, M. Jakobsson, R. Larter, Evidence of marine ice-cliff instability in pine island bay from iceberg-keel plough marks, Nature Letters 550 (2017) 506–510.

[169] T. Edwards, M. Brandon, G. Durand, N. Edwards, N. Golledge, P. Holden, I. Nias, A. Payne, C. Ritz, A. Wernecke, Revisiting antarctic ice loss due to marine ice-cliff instability, Nature 566 (2019) 58–64.

[170] E. M. Schulson, Brittle failure of ice, Engineering Fracture Mechanics 68 (2001) 1839–1887.

[171] E. M. Schulson, D. Iliescu, C. Renshaw, On the initiation of shear faults during brittle compressive failure: A new mechanism, Journal of Geophysical Research 104 (1999) 697–705.

[172] R. M. DeConto, D. Pollard, Contribution of Antarctica to past and future sea-level rise, Nature 531 (7596) (2016) 591–597.

[173] D. Benn, J. Astrom, T. Zwinger, J. Todd, F. M. Nick, S. Cook, N. Hulton, A. Luckman, Melt-under-cutting and buoyancy-driven calving from tidewater glaciers: new insights from discrete element and continuum model simulations, Journal of Glaciology 63 (2017) 691–702.

[174] T. Schlemm, A. Levermann, A simple stress-based cliff-calving law, The Cryosphere 13 (2019) 2475–2488.

[175] J. N. Bassis, B. Berg, A. J. Crawford, D. I. Benn, Transition to marine ice cliff instability controlled by ice thickness gradients and velocity, Science 372 (6548) (2021) 1342–1344.

[176] Y. Wang, S. Abe, S. Latham, P. Mora, Implementation of particle-scale rotation in the 3-d lattice solid model, Pure and Applied Geophysics 163 (2006) 1769–1785.

[177] J. A. Åström, T. I. Riikilä, T. Tallinen, T. Zwinger, D. Benn, J. C. Moore, J. Timonen, A particle based simulation model for glacier dynamics, The Cryosphere 7 (2013) 1591–1602.

[178] D. I. Benn, J. A. Åström, Calving glaciers and ice shelves, Advances in Physics: X 3 (1) (2018) 1513819.

[179] R. Sondershaus, A. Humbert, R. Muller, A phase field model for fractures in ice shelves, Proceedings in Applied Mathematics & Mechanics (2022).

[180] J. C. Jaeger, N. G. W. Cook, R. Zimmerman, Fundamentals of Rock Mechanics, 4th Edition, Blackwell Publishing, 2007.

[181] B. P. Lipovsky, Ice shelf rift propagation: stability, three-dimensional effects, and the role of marginal weakening, The Cryosphere 14 (2020) 1673–1683.

[182] D. MacAyeal, A tutorial on the use of control methods in ice-sheet modeling, Journal of Glaciology 1993 (1993) 91–98.

[183] J. Barnes, H. Gudmundsson, The predictive power of ice sheet models and the regional sensitivity of ice loss to basal sliding parameterisations: a case study of pine island and thwaites glaciers, west antarctica, The Cryosphere 16 (2022) 4291–4304.

[184] F. e. Kennedy, E. M. Schulson, D. E. Jones, The fricton of ice on ice at low sliding velocities, Philosophical Magazine 80 (2000) 1093–1110.

[185] M. Beeman, W. B. Durham, S. Kirby, Friction of ice, Journal of Geophysical Research 93 (1988).

[186] J. Weiss, E. Schulson, Coulombic faulting from the grain scale to the geophysical scale: lessons from ice, Journal of Physics D: Applied Physics 42 (2009) 214017.

[187] D. Vaughan, Relating the occurrence of crevasses to surface strain rates, Journal of Glaciology 39 (1993) 255–266.

[188] R. M. W. Frederking, O. J. Svec, G. W. Timco, On measuring the shear strength of ice, Proceedings of the 9th International Symposium on Ice (1988).

[189] M. A. Rist, S. A. F. Murrell, Ice triaxial deformation and fracture, Journal of Glaciology 40 (1994) 305–318.

[190] R. E. Gagnon, P. H. Gammon, Triaxial experiments on iceberg and glacier ice, Journal of Glaciology 41 (1995) 528–540.

[191] B. R. Parizek, K. Christianson, R. B. Alley, D. Voytenko, I. Vaňková, T. H. Dixon, R. T. Walker, D. M. Holland, Ice-cliff failure via retrogressive slumping, Geology 47 (5) (2019) 449–452.

[192] C. J. van der Veen, Tidewater calving, Journal of Glaciology 42 (141) (1996) 375–385.

[193] J. Krug, G. Durand, O. Gagliardini, J. Weiss, Modelling the impact of submarine frontal melting and ice mélange on glacier dynamics, The Cryosphere 9 (2015) 989–1003.

[194] A. Robel, Thinning sea ice weakens buttressing force of iceberg mélange and promotes calving, Nature Communications (2017).

[195] D. Pollard, R. M. DeConto, A simple inverse method for the distribution of basal sliding coefficients under ice sheets, applied to Antarctica, The Cryosphere 6 (5) (2012) 953–971.

[196] Y. Ma, J. Bassis, The effect of submarine melting on calving frommarine terminating glaciers, Journal of Geophysical Research 124 (2019) 334–346.

[197] M. O'Leary, P. Christoffersen, Calving on tidewater glaciers amplified by submarine frontal melting, The Cryosphere 7 (2013) 119–128.

[198] T. C. Butkovich, Strength of sea ice, Tech. rep., Snow, Ice and Permafrost Research Establishment (1956).

[199] R. A. Paige, C. W. Lee, Preliminary studies on sea ice in mcmurdo sound, antarctica, Journal of Glaciology 7 (1967) 515–528.

[200] Y. Navidtehrani, C. Betegón, E. Martínez-Pañeda, A general framework for decomposing the phase field fracture driving force, particularised to a Drucker–Prager failure surface, Theoretical and Applied Fracture Mechanics 121 (2022) 103555.

[201] L. D. Lorenzis, C. Maurini, Nucleation under multi-axial loading in variational phase-field models of brittle fracture, International Journal of Fracture (2021) 1–21.

[202] Y. Feng, J. Li, A unified regularized variational cohesive fracture theory with directional energy decomposition, International Journal of Engineering Science 182 (2023) 103773.

[203] W. G. Sikonia, Finite element glacier dynamics model applied to columbia glacier, alaska, United States Geological Survey Professional Paper (1982).

[204] V. C. Tsai, J. R. Rice, A model for turbulent hydraulic fracture and application to crack propagation at glacier beds, Journal of Geophysical Research: Earth Surface 115 (2010).

[205] V. C. Tsai, J. R. Rice, Modeling turbulent hydraulic fracture near a free surface, Journal of Applied Mechanics 79 (2012).

[206] A. Hillerborg, M. Modeer, P. E. Petersson, Analysis of crack formation and crack growth in concrete by means of fracture mechanics and finite elements, American Concrete Institute, ACI Special Publication SP-249 (2008) 225–237.

[207] P. K. Kristensen, C. F. Niordson, E. Martínez-Pañeda, An assessment of phase field fracture: crack initiation and growth, Philosophical transactions of the royal society 379 (2021).

[208] M. Ambati, T. Gerasimov, L. De Lorenzis, A review on phase-field models of brittle fracture and a new fast hybrid formulation, Computational Mechanics 55 (2015) 383–405.

[209] H. Tada, P. C. Paris, G. R. Irwin, The stress analysis of cracks handbook, 1973, Del Research Corporation (1985).

[210] H. Blatter, Velocity and stress-fields in grounded glaciers: A simplealgorithm for including deviatoric stress gradients, Journal of Glaciology 41 (1995) 333–344.

[211] F. Pattyn, A new three-dimensional higher-order thermomechanicalice sheet model: Basic sensitivity, ice stream development, and ice flowacross subglacial lakes, Journal of Geophysical Research 108 (2003).

[212] C. van der Veen, I. Whillans, Force budget: I. theory and numerical methods, Journal of Glaciology 35 (1989).

[213] D. MacAyeal, Large-scale ice flow over a viscous basal sediment:theory and application to ice stream-b, antarctica, Journal of Geophysical Research (1989).

Appendix A

Comparison of Phase Field Fracture Models - Single Edge Notched Specimen

In this Appendix, a phase field fracture model is implemented into the finite element software COMSOL Multiphysics and the model is validated with a benchmark example widely used within the literature. A thin square plate of dimensions 1 mm with a horizontal notch is considered, running from the left hand edge to the centre of the specimen. At the base of the plate, the vertical displacement is restrained and horizontal displacement is restrained at the lower right vertex, to prevent rigid body motion, any out-of-plane stresses are neglected through the plane stress assumption.

A.1 Uniaxial Tension Test

A uniaxial tension test is first considered by applying displacement u normal to the upper surface. A quasi-static displacement controlled simulation is conducted to determine the crack evolution, where a displacement u is applied at the upper surface, and monotonically increased in increments of $\Delta u = 2.5 \times 10^{-6}$ mm until full thickness fracture is achieved at the critical displacement value u_{crit}.

The material behaviour is assumed to be a brittle elastic solid and material parameters for steel are used as reported in [1] (presented in Table A.1). The numerical analysis is performed using both a strain energy based crack driving force, considering a volumetric-deviatoric Amor split, and a principal stress based crack driving force. The results are then compared with the literature and validated with analytical solutions. The critical fracture stress σ_{c} used in the stress based approach – reported in Table A.1 – is found by exploiting the Hillerborg relationship [206] thus:

$$\sigma_{\text{c}} = \sqrt{\frac{EG_{\text{c}}}{\ell_{\text{c}}}} \tag{A.1}$$

Diagrams showing the specimen geometry and finite element mesh for the tension test are found in Figure A.1a and Figure A.1b respectively. The model is meshed using linear quadratic elements, with the mesh being refined locally in the region in which the crack is expected to extend. It is good practice to have an element size h_{c} that is 6 times smaller than the length scale parameter ℓ_{c}, within the refined region in order to achieve mesh-independent results [118], thus a mesh size of $h_{\text{c}} = 0.004$ mm is adopted ahead of the crack and a maximum element size of 0.115 mm is used elsewhere.

The results of the present study are in the form of phase field contour maps, as shown in Figure A.2. For the strain energy density based approach, it can be

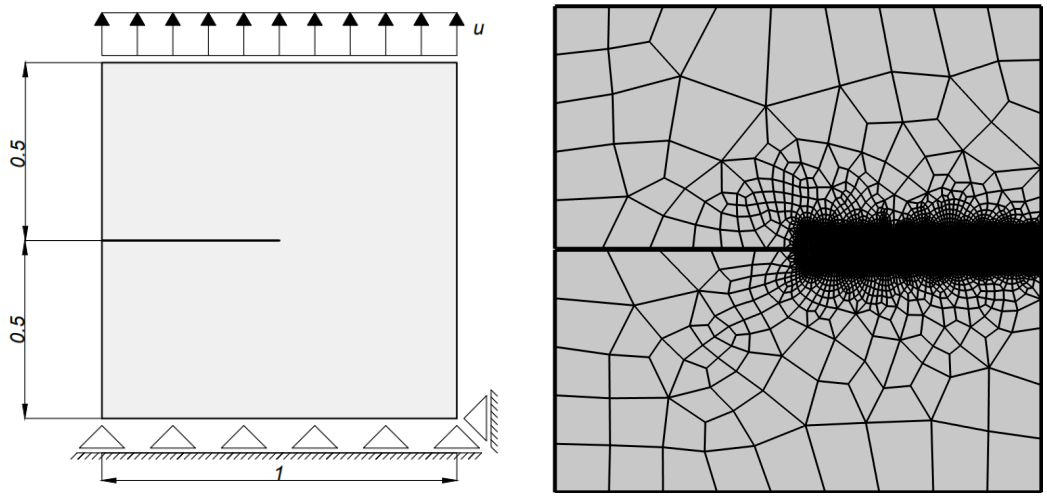

(a) (b)

Figure A.1: (a) Schematic diagram of the cracked plate in tension (dimensions in mm) (b) finite element mesh used for the analysis

Material parameter	Magnitude
Young's modulus, E [MPa]	210000
Poisson's ratio, ν [-]	0.3
Density, ρ [kg/m^3]	7850
Fracture Toughness, G_c [kg/m^3]	2700
Phase Field Length Scale, ℓ_c [mm]	0.024
Refined Mesh Size, h_c [mm]	0.04
Critical fracture stress, σ_c [MPa]	4860

Table A.1: Characteristic material properties for steel assumed to model the square cracked plate in tension, taken from [1].

seen that no damage is observed beyond the initial crack for displacements below a displacement of $u = 5.74 \times 10^{-3}$ mm (Figure A.2a). Damage begins to initiate at this point, and a purely mode I crack begins to develop, with full propagation being achieved at the critical displacement value of $u_{\text{crit}} = 6.07 \times 10^{-3}$ mm (Figure A.2c). A similar distribution in damage is observed for the principal stress based approach. Damage begins to extend beyond the initial notch at the applied displacement $u = 5.40 \times 10^{-3}$ mm (Figure A.2d). Propagation is rapid and brittle, occuring at a much faster rate than the strain energy based approach, with a full thickness crack developing at a critical displacement of $u_{\text{crit}} = 5.50 \times 10^{-3}$ mm (Figure A.2f).

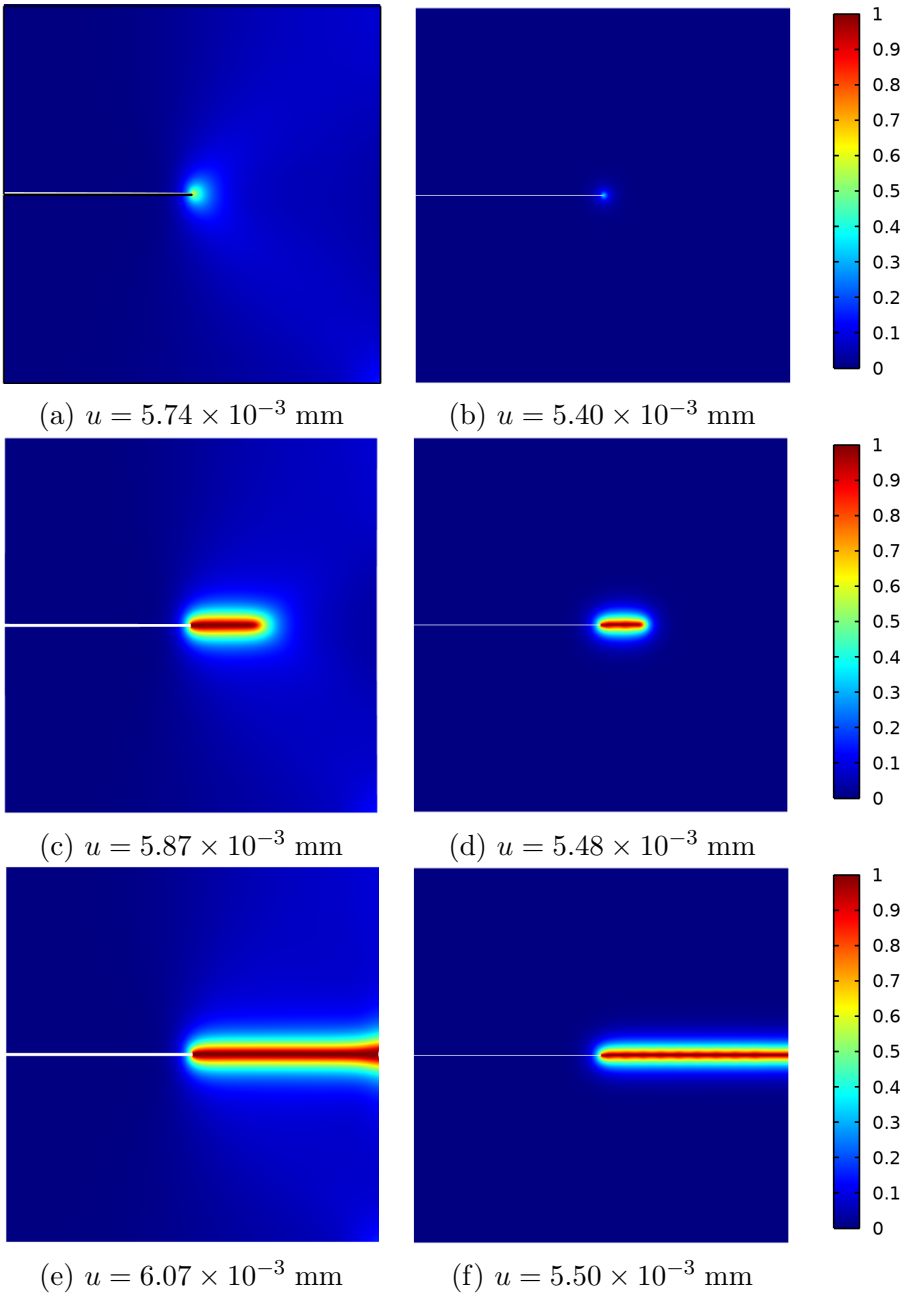

(a) $u = 5.74 \times 10^{-3}$ mm (b) $u = 5.40 \times 10^{-3}$ mm

(c) $u = 5.87 \times 10^{-3}$ mm (d) $u = 5.48 \times 10^{-3}$ mm

(e) $u = 6.07 \times 10^{-3}$ mm (f) $u = 5.50 \times 10^{-3}$ mm

Figure A.2: Evolution of the phase field parameter for the uniaxial tension test, from (a) an intact specimen to (c) an intermediate crack and (e) to a fully fractured specimen for the strain energy density approach. Phase field plots for the principal stress based approach are shown in (b), (d) and (f) respectively.

The evidence of brittle failure is further illustrated in the reaction force versus applied displacement curves shown in Figure A.3. Here, the axial force begins to grow in a linear fashion for both approaches, with respect to applied displacement, prior to damage initiation. The rate of growth for low values of displacement are equal for both approaches, but for displacements above $u = 3.50 \times 10^{-3}$ mm the gradient begins to decrease for the strain energy based approach. The linear load-displacement response prior to damage is expected for the stress based approach, owing to it being based on the phase field AT1 model. However, the strain energy approach used is based on the AT2 model which does not contain a threshold for damage, thus an earlier deviation from the linear response is expected [207].

A maximum value of axial force is achieved prior to damage initiation. However, as the crack begins to propagate, the axial force reduces rapidly and tends towards zero, once full thickness propagation has occurred. This occurs due to the applied load no longer be transmitted to the support at the base and the material above the crack becoming an unrestrained free body.

Hooke's Law can be used to calculate the theoretical value of the maximum reaction force F using Eq. (A.2)

$$F = \frac{EAu}{L} = \frac{(210 \times 10^3) \times (0.5 \times 1) \times (5.74 \times 10^{-3})}{1} = 616.35 \text{ N} \qquad \text{(A.2)}$$

for a peak applied displacement prior to damage $u = 5.74 \times 10^{-3}$ mm. This gives a value of 616.35 N. By comparison, the reaction force prior to damage initiation for the numerical analysis is 604.92 N for the strain energy density approach and 659.11 N at a displacement of $u = 5.47 \times 10^{-3}$ mm for the stress based approach, yielding a percentage difference of 1.85% and 6.94% between the theoretical value respectively. The results from this study are consistent with the

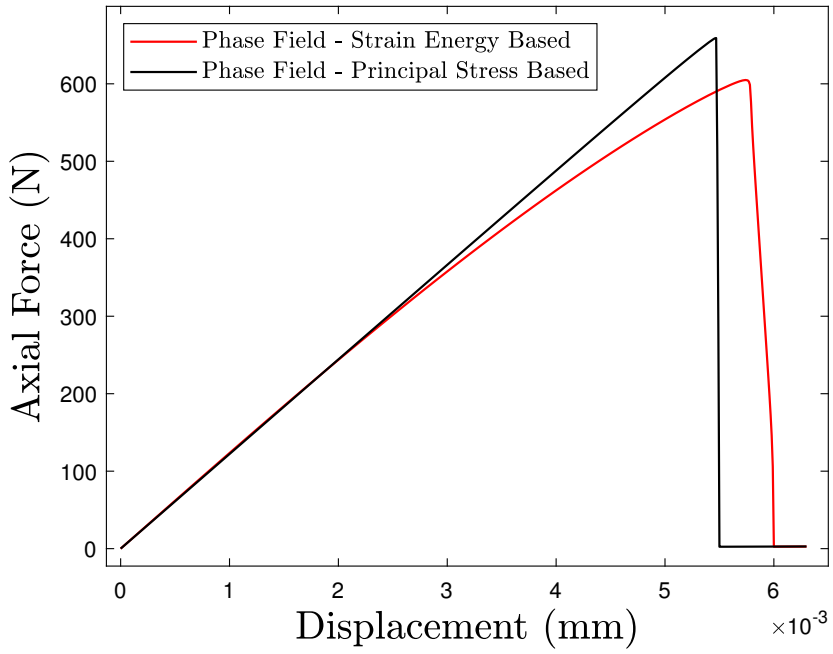

Figure A.3: Uniaxial force versus applied displacement at the base of the single notched edge plate for the phase field strain energy based scheme and principal stress based scheme.

results reported in [1] and [118]; thus, confirming the correct implementation of phase field damage in COMSOL Multiphysics.

A.2 Remote Shear Test

The second numerical example considered is a specimen undergoing remote shear loading. The specimen geometry and material parameters used are the same as the values used in the uniaxial tension test. However the displacement u is applied parallel to the upper surface, represented in Figure A.4a. Vertical displacement is restrained at the upper plate surface and the base is fully fixed. Similar to the previous example, the mesh is refined in regions where damage is expected to propagate - i.e. the lower right quadrant. The study is displacement controlled, with monotonic displacement increments of $\Delta u = 1.0 \times 10^{-5}$ mm being applied

until failure is achieved. Qualitative results are presented in Figure A.5 in the

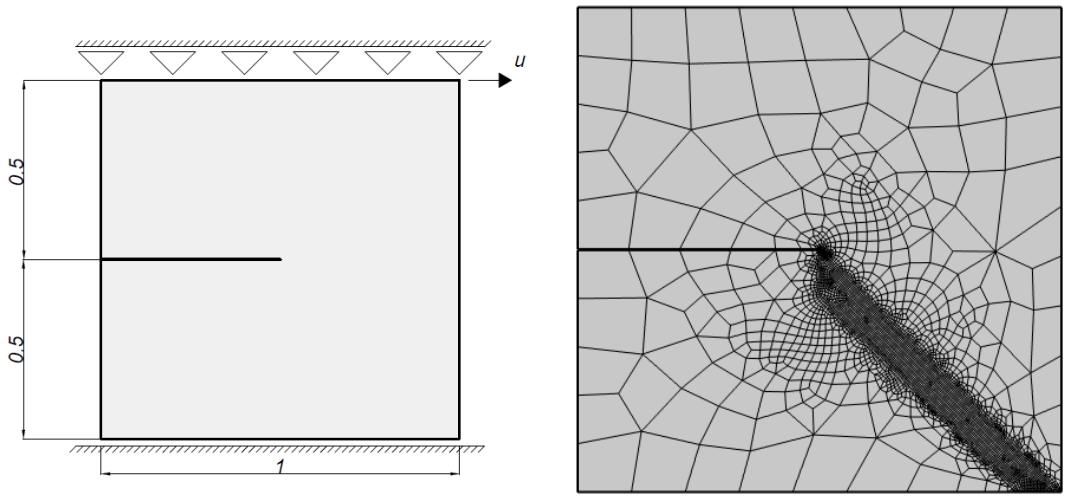

(a) (b)

Figure A.4: (a) Schematic diagram of the cracked plate undergoing shear (dimensions in mm) (b) finite element mesh used for the analysis

form of phase field parameter plots. For both crack driving force methods, damage propagation occurs over a larger number of applied displacement increments compared to the uniaxial tension test - with the crack path being deflected towards the lower right corner of the plate. Full fracture is achieved at critical applied displacements of $u_{\text{crit}} = 14.5 \times 10^{-3}$ mm and $u_{\text{crit}} = 19.5 \times 10^{-3}$ mm for the energy and stress based formulations respectively. The crack pattern is also in agreement with the supporting literature [208].

The load-displacement curves for the pure shear test are presented in Figure A.3 considering both driving force approaches. As expected, the load-displacement response curves behave in a linear elastic manner, prior to damage initiation. The peak shear load sustained is higher for the stress based approach, owing to damage initiation occurring at a higher applied displacement value ($u_{\text{initiation}} = 9.6 \times 10^{-3}$ mm for the stress based approach compared to $u_{\text{initiation}} = 8.0 \times 10^{-3}$ mm for the strain energy approach). Once the crack begins to propagate, the material's load carrying capacity reduces and the sustained shear load decreases.

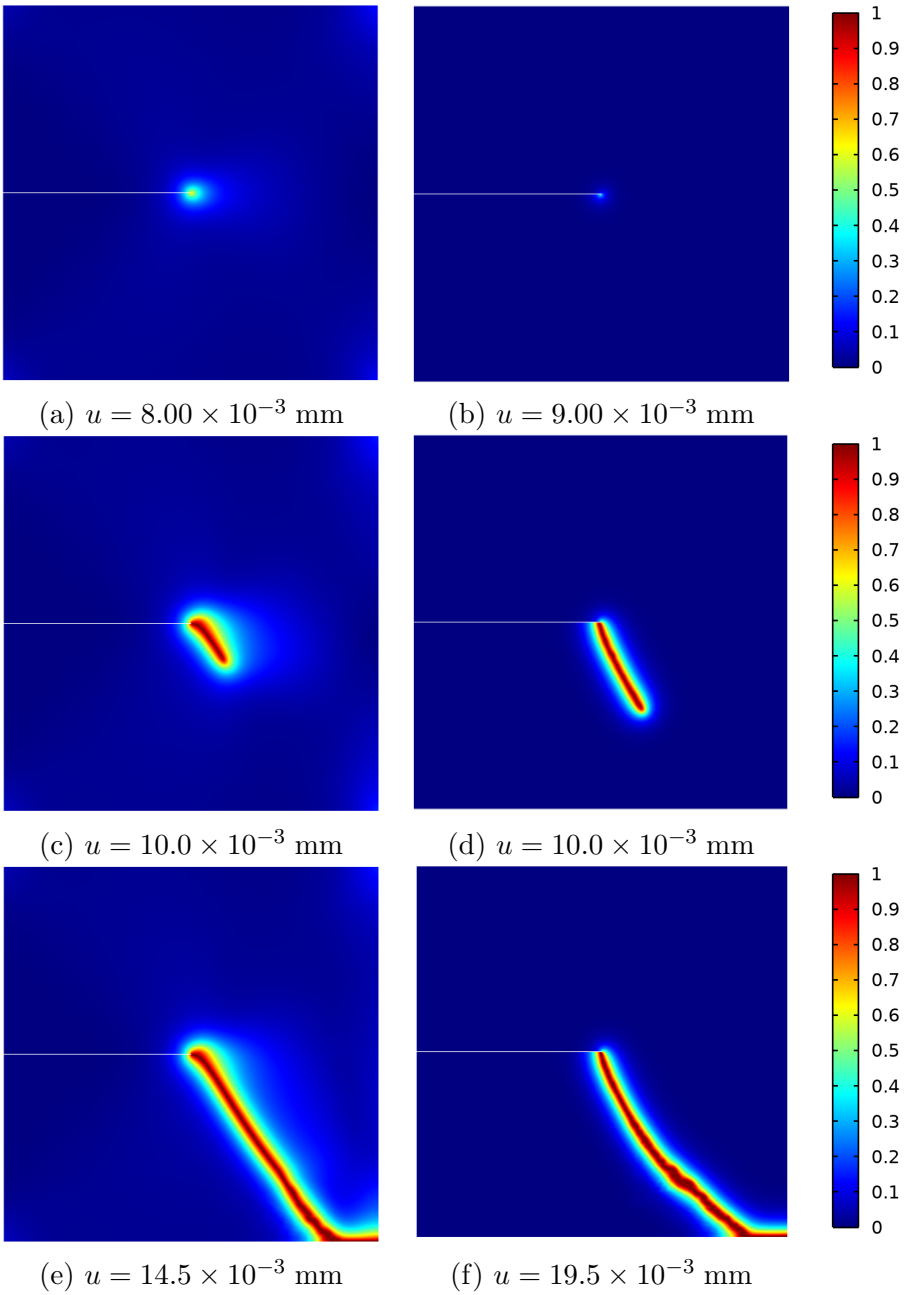

(a) $u = 8.00 \times 10^{-3}$ mm (b) $u = 9.00 \times 10^{-3}$ mm

(c) $u = 10.0 \times 10^{-3}$ mm (d) $u = 10.0 \times 10^{-3}$ mm

(e) $u = 14.5 \times 10^{-3}$ mm (f) $u = 19.5 \times 10^{-3}$ mm

Figure A.5: Evolution of the phase field parameter for the shear test, from (a) an intact specimen to (c) an intermediate crack and (e) to a fully fractured specimen for the strain energy density approach. Phase field plots for the principal stress based approach are shown in (b), (d) and (f) respectively.

For the strain energy based approach, damage propagates at an angle from the initial notch at a continuous rate, until $u = 12.6 \times 10^{-3}$ mm where a secondary crack develops at the lower right corner, leading to a rapid drop in the sustained shear force. These two damage regions continue to grow, and fully coalesce at a critical applied displacement of $u = 14.5 \times 10^{-3}$ mm, resulting in the plate no longer being able to sustain the applied shear load. The load-displacement curve for the stress based approach shows an alternate post-failure response. Here, the crack propagates in a series of successive brittle failures, with each crack growth event being represented by the sudden decrease in the sustained shear load. Between these events, the crack stabilises and an increase in applied displacement results in a linear increase in the sustained shear force, until the crack length begins to increase again. The crack reaches the base of the plate at a critical applied displacement of $u = 19.5 \times 10^{-3}$ mm, resulting in the sustained shear load reducing to zero.

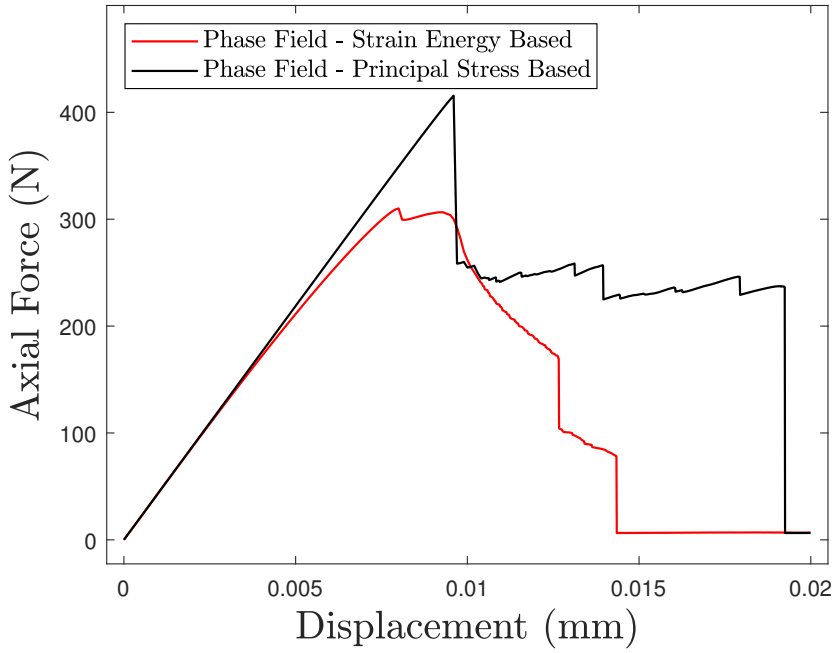

Figure A.6: Force versus applied displacement graph for the remote shear test considering the phase field strain energy based scheme and principal stress based scheme.

Appendix B

Derivation of Longitudinal Stress in Grounded Glaciers for Isotropic Homogeneous Glacial Ice

In this appendix, the derivation of the far field longitudinal stress in a grounded rectangular ice sheet is conducted, assuming linear elastic compressibility and glacial ice to be fully consolidated and isotropic. An ice sheet of height H and length L is considered, which terminates at an ocean with a surface level h_{w} above a datum point – for a visual representation refer to Figure 4.1a. Ice sheet fracture is predominately driven by mode I loading, with basal or surface crevasses growing as a result of the horizontal normal stress σ_{xx}. It is therefore important to understand the stress state within the ice sheet to evaluate fracture.

The forces acting on the ice sheet consist of the lithostatic force which varies linearly with depth, the hydrostatic force acting on the far edge of the ice sheet due

to the ocean water and the tensile forces due to meltwater in the crevasses. The normal stress σ_{xx} can therefore be derived using the equilibrium equations and Hooke's law for three dimensional linear elasticity. The equations of equilibrium are as follows:

$$\frac{\partial \sigma_{xx}}{\partial x} + \frac{\partial \sigma_{xy}}{\partial y} + \frac{\partial \sigma_{xz}}{\partial z} = 0 \tag{B.1}$$

$$\frac{\partial \sigma_{xy}}{\partial x} + \frac{\partial \sigma_{yy}}{\partial y} + \frac{\partial \sigma_{yz}}{\partial z} = 0 \tag{B.2}$$

$$\frac{\partial \sigma_{xz}}{\partial x} + \frac{\partial \sigma_{yz}}{\partial y} + \frac{\partial \sigma_{zz}}{\partial z} + \rho_{\mathrm{i}} g = 0 \tag{B.3}$$

It is assumed that the ice sheet undergoes plane strain deformation, owing to the through thickness dimension being several orders of magnitude larger than the height and the length dimensions. In addition, the stresses are invariant with the x-coordinate and that the out-of-plane stress derivatives are zero. This simplifies the stress equilibrium equations to:

$$\frac{\partial \sigma_{xy}}{\partial y} = 0 \tag{B.4}$$

$$\frac{\partial \sigma_{yy}}{\partial y} = 0 \tag{B.5}$$

$$\frac{\partial \sigma_{zz}}{\partial z} + \rho_{\mathrm{i}} g = 0 \tag{B.6}$$

Rearranging Eq. (B.6) and integrating with respect to the vertical direction z provides the vertical normal stress σ_{zz} due to lithostatic forces only:

$$\sigma_{zz} = \int -\rho_{\mathrm{i}} g \, dz \tag{B.7}$$

$$\sigma_{zz} = -\rho_{\mathrm{i}} g H \quad \text{when} \quad z = 0 \tag{B.8}$$

$$\sigma_{zz} = 0 \quad \text{when} \quad z = H \tag{B.9}$$

$$\sigma_{zz} = -\rho_{\mathrm{i}} g (H - z) \tag{B.10}$$

The equations of linear elasticity are as follows:

$$\varepsilon_{xx} = \frac{1}{E}[\sigma_{xx} - \nu(\sigma_{yy} + \sigma_{zz})] \tag{B.11}$$

$$\varepsilon_{yy} = \frac{1}{E}[\sigma_{yy} - \nu(\sigma_{xx} + \sigma_{zz})] \tag{B.12}$$

$$\varepsilon_{zz} = \frac{1}{E}[\sigma_{xx} - \nu(\sigma_{xx} + \sigma_{yy})] \tag{B.13}$$

And using the plane strain assumption (i.e. $\varepsilon_{yy} = 0$) the out-of-plane normal stress σ_{yy} can be found in relation to the in-plane normal stresses σ_{xx} and σ_{zz}:

$$\sigma_{yy} = \nu(\sigma_{xx} + \sigma_{zz}) \tag{B.14}$$

This is then substituted into the longitudinal strain equation Eq. (B.11) giving:

$$\varepsilon_{xx} = \frac{1}{E}\left[(1-\nu^2)\sigma_{xx} - \nu(1+\nu)\sigma_{zz}\right] \tag{B.15}$$

The membrane strain assumption is assumed due to the thickness H being an order of magnitude smaller than the length L. As a result, the horizontal displacement is vertically invariant with depth

$$\sigma_{xx} = -\frac{\nu}{1-\nu}\rho_{\mathrm{i}} g + C \tag{B.16}$$

Where C is the constant of indefinite integration, which can be determined by considering the force equilibrium in the longitudinal direction for the lithostatic force of ice and the hydrostatic force of the ocean water $F_{\mathrm{w}} = \frac{1}{2}\rho_{\mathrm{s}} g h_{\mathrm{w}}^2$.

$$\sum F_x = \int_0^H \sigma_{xx}\, \mathrm{d}z + F_{\mathrm{w}} = 0 \tag{B.17}$$

Evaluating the definite integral in Eq. (B.17) allows for the constant C to be

determined, thus.

$$\left[-\frac{\nu}{1-\nu}\frac{\rho_{\mathrm{i}}gz^2}{2}+Cz\right]_0^H=-\frac{\nu}{1-\nu}\frac{\rho_{\mathrm{i}}gH^2}{2}+CH \tag{B.18}$$

$$-\frac{\nu}{1-\nu}\frac{\rho_{\mathrm{i}}gH^2}{2}+CH=-\rho_{\mathrm{s}}g\frac{h_{\mathrm{w}}^2}{2} \tag{B.19}$$

$$C=\frac{\nu}{2(1-\nu)}\rho_{\mathrm{i}}gH-\frac{1}{2}\rho_{\mathrm{s}}g\frac{h_{\mathrm{w}}^2}{H} \tag{B.20}$$

The stress in the horizontal direction σ_{xx} is therefore:

$$\sigma_{xx}=\frac{\nu}{1-\nu}\left[\rho_{\mathrm{i}}g\left(z-\frac{H}{2}\right)\right]-\frac{1}{2}\rho_{\mathrm{s}}g\frac{h_{\mathrm{w}}^2}{H} \tag{B.21}$$

It can be seen that the longitudinal stress σ_{xx} is tensile at the surface and compressive at the grounding line, with linear variation with depth. If the ice sheet is land terminating, (i.e $h_{\mathrm{w}}=0$) then the longitudinal stress is symmetric about the centre line ($\sigma_{xx}=0$ at $H/2$) and the magnitude of the maximum stresses at the extreme fibres are equal and opposite ($\sigma_{xx}^{\max}=\frac{\nu}{2(1-\nu)}\rho_{\mathrm{i}}gH$). The presence of the ocean water introduces a constant compressive stress, reducing the tensile zone and therefore decreasing the likelihood of fracture. A representative plot of the stress state can be found in Figure B.1.

The current analysis however, does not consider the effects of a meltwater pressure acting within surface crevasses which will introduce an additional unfavourable tensile stress. The meltwater pressure

$$p_{\mathrm{w}}=\rho_{\mathrm{w}}g\left\langle h_{\mathrm{s}}-(z-z_{\mathrm{s}})\right\rangle \tag{B.22}$$

is added to σ_{xx} to produce the net stress. Where h_{s} is the meltwater level above the base of the crevasse, ρ_{w} is the density of meltwater, z is the vertical distance from the base of the ice sheet and z_s is the vertical distance from the base of the

ice sheet to the base of the crevasse. The presence of the Macaulay brackets in Eq. (B.22) prevent a negative pressure above the meltwater surface.

$$\sigma_{net}(z) = \sigma_{xx}(z) + p_{\mathrm{w}}(z) \tag{B.23}$$

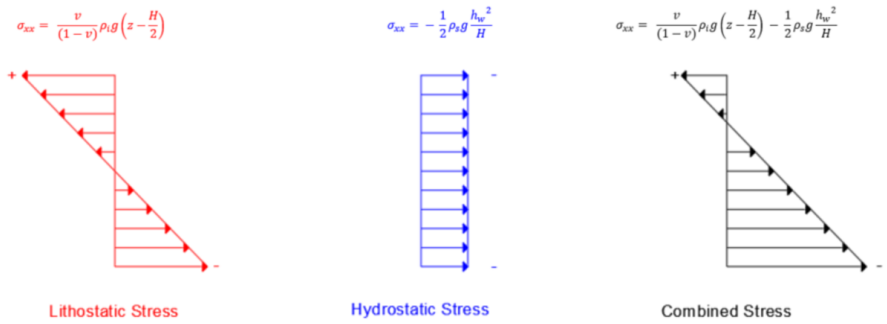

Figure B.1: Plot of the lithostatic, hydrostatic and combined stress states with depth for a grounded ice sheet

It is noted that the terms lithostatic stress and hydrostatic stress in Figure B.1 refer to the contributions of these to the longitudinal stress, as indicated by the derivation above and are not actual plots of the lithostatic stress ($\rho_{\mathrm{i}} g(H - z)$) or hydrostatic pressure ($\rho_{\mathrm{w}} g \langle h_{\mathrm{w}} - z \rangle$). The derivation of net longitudinal stress in this section considers glacial ice to be a homogeneous material and has been predominantly used for analytical comparisons in Section 4.3.1 and Section 4.4. This is elaborated upon within Chapter 5 by considering the contributions of firn in the upper surface layers and the effects this has on crevasse propagations.

Appendix C

Linear Elastic Fracture Mechanics for a Grounded Glacier

In this appendix, the linear elastic fracture mechanics method is presented for a grounded glacier; LEFM considers local stress concentrations around the crevasse by evaluating the net stress intensity factor $K_{\mathrm{I}}^{\mathrm{net}}$. LEFM exploits the principle of superposition and individually considers contributions from the normal tensile stress, lithostatic compressive stress and meltwater pressure. An initial crevasse depth d is suggested and the net stress intensity factor is found by integrating over the crevasse depth, owing to the varying stress field with depth. Unlike the Nye zero stress model, LEFM assumes that there is some tensile resistance to crack propagation by comparing the stress intensity factor to the fracture toughness K_{IC}, which for glacial ice is taken as $K_{\mathrm{IC}} = 0.1$ MPa $\mathrm{m}^{1/2}$, found from experimental data [135]. If $K_{\mathrm{I}}^{\mathrm{net}} > K_{\mathrm{IC}}$ then the crack is considered unstable and will continue to propagate. The LEFM problem is solved using an iterative

code in MATLAB by gradually increasing the trial crevasse depth d. Since $K_{\mathrm{I}}^{\mathrm{net}}$ is proportional to the net longitudinal stress σ_{net}, the stress intensity factor will begin to reduce once the crevasse penetrates into the compressive region of the ice sheet. Crevasse propagation arrests once the condition $K_{\mathrm{I}}^{\mathrm{net}} = K_{\mathrm{IC}}$ is met. The net longitudinal stress σ_{net} derived in Eq. (B.23) is used to propagate the crevasse, to consider the contributions of the normal tensile stress, lithostatic compressive stress and meltwater pressure.

The stress intensity factor is calculated using the following equation:

$$K_{\mathrm{I}}^{\mathrm{net}} = \int_0^d M_{\mathrm{D}}\left(\chi, H, d\right) \sigma_{\mathrm{net}}\left(\chi\right)\ \mathrm{d}\chi. \tag{C.1}$$

Here, M_{D} is a weight function dependent on the applied boundary conditions and domain geometry, the selection of which has been debated in various literature sources [49, 136]. For surface crevasses located in the far field region of a grounded glacier undergoing free slip, the 'double edge cracks' formulation is followed since this gives good agreement with stress intensity factors calculated using the displacement correlation method with FEM [134]. The weight function is taken from [209] and takes the form:

$$M_{\mathrm{D}} = \frac{2}{\sqrt{2H}}\left[1 + f_1\left(\frac{\chi}{d}\right) f_2\left(\frac{d}{H}\right)\right] \phi\left(\frac{d}{H}, \frac{\chi}{H}\right) \tag{C.2}$$

where $\chi = H - z$, d is the trial crevasse depth, and the functions f_1, f_2 and θ are defined as:

$$f_1 = 0.3\left[1 - \left(\frac{\chi}{d}\right)^{\frac{5}{4}}\right] \tag{C.3}$$

$$f_2 = \frac{1}{2}\left[1 - \sin\left(\frac{\pi d}{2H}\right)\right]\left[2 + \sin\left(\frac{\pi d}{2H}\right)\right] \tag{C.4}$$

$$\phi = \frac{\sqrt{\tan(\frac{\pi d}{2H})}}{\sqrt{1 - \left[\frac{\cos(\frac{\pi d}{2H})}{\cos(\frac{\pi X}{2H})}\right]^2}} \tag{C.5}$$

The stabilised crevasse depths plotted in Figure 4.3b and Figure 4.5b are found by calculating the mode I stress intensity factor $K_{\mathrm{I}}^{\mathrm{net}}$ in Eq. (C.1), using the weight function M_D presented in Eq. (C.2). The crevasse depth d is incrementally increased until the stress intensity factor is equal to the fracture toughness and the crevasse stabilises.

Appendix D

Linear Elastic Fracture Mechanics for a Floating Ice Shelf

In this Appendix, the linear elastic fracture mechanics formulation is presented for the propagation of surface crevasses in floating ice shelves. As stated previously, the weighting function used in LEFM studies is dependent on the specimen geometry and applied boundary conditions. As a result, the removal of the free slip condition at the base and application of the buoyancy pressure means the 'double edge crack' formulation is no longer appropriate for floating ice shelves. It was found that the stress intensity factors calculated using the weight function presented in Krug et al. [136] gave better agreement with stress intesity factors using the displacement correlation method [134] for surface crevasses in a floating ice shelf.

$$K_{\mathrm{I}}^{\mathrm{net}} = \int_0^d \beta\left(z, H, d\right) \sigma_{net}\left(\chi\right) \, \mathrm{d}\chi \tag{D.1}$$

where $\beta(z, H, d)$ is the appropriate weight function for the floating ice shelf:

$$\beta(z, H, d) = \frac{2}{\sqrt{2\pi(d-z)}}\left[1 + M_1\left(1 - \frac{z}{d}\right)^{0.5} + M_2\left(1 - \frac{z}{d}\right) + M_3\left(1 - \frac{z}{d}\right)^{1.5}\right], \tag{D.2}$$

$$\begin{aligned} M_1 = {} & 0.0719768 - 1.513476\lambda - 61.1001\lambda^2 + 1554.95\lambda^3 \\ & - 14583.8\lambda^4 + 71590.7\lambda^5 - 205384\lambda^6 + 356469\lambda^7 \\ & - 368270\lambda^8 + 208233\lambda^9 - 49544\lambda^{10}, \end{aligned} \tag{D.3}$$

$$\begin{aligned} M_2 = {} & 0.246984 + 6.47583\lambda + 176.456\lambda^2 - 4058.76\lambda^3 \\ & + 37303.8\lambda^4 - 181755\lambda^5 + 520551\lambda^6 - 904370\lambda^7 \\ & + 936863\lambda^8 - 531940\lambda^9 + 12729\lambda^{10}, \end{aligned} \tag{D.4}$$

$$\begin{aligned} M_3 = {} & 0.529659 - 22.3235\lambda + 532.074\lambda^2 - 5479.53\lambda^3 \\ & + 28592.2\lambda^4 - 81388.6\lambda^5 + 128746\lambda^6 - 106246\lambda^7 \\ & + 35780.7\lambda^8, \end{aligned} \tag{D.5}$$

and $\lambda = d/H$.

Similarly to the grounded glacier case, the crevasse penetration depths are calculated using an iterative code in MATLAB, where the trial crevasse depth d is gradually increased until $K_{\mathrm{I}}^{\mathrm{net}} = K_{\mathrm{IC}}$. The stabilised crevasse depths plotted in Figure 4.12, Figure 5.6 and Figure 5.9 are calculated using the above formulation.

The longitudinal stress in the ice shelf close to the front cannot be determined analytically due to the bending stress contribution from the floatation pressure at the base. The stress profiles at the front are obtained numerically (normalised with respect to $\rho_{\mathrm{i}} g H$) and are fitted to a sixth order polynomial equation, taking

the general form below:

$$\begin{aligned}\frac{\sigma_{xx}}{\rho_{\mathrm{i}} g H} = & A\left(\frac{\chi}{H}\right)^6 + B\left(\frac{\chi}{H}\right)^5 + C\left(\frac{\chi}{H}\right)^4 \\ & + D\left(\frac{\chi}{H}\right)^3 + E\left(\frac{\chi}{H}\right)^2 + F\left(\frac{\chi}{H}\right) + G\end{aligned} \tag{D.6}$$

Where A, B, C, D, E, F, G are non-dimensionalised stress coefficients that are presented in Table D.1. These stress profiles are used to obtain the crevasse propagation results in Section 4.5.1 and Section 5.3.

	A	B	C	D
$\rho = 917$ kg m^{-3}, $E = 9.5$ GPa , $H = 125$ m	0.000	0.000	0.000	-0.003
$\rho = 917$ kg m^{-3}, $E(z)$, $H = 125$ m	-0.435	1.858	-3.422	3.543
$\rho(z)$, $E = 9.5$ GPa, $H = 125$ m	-0.064	0.295	-0.611	0.761
$\rho(z)$, $E(z)$, $H = 125$ m	-0.542	2.352	-4.454	4.845
$\rho = 917$ kg m^{-3}, $E = 9.5$ GPa , $H = 250$ m	-0.012	0.034	-0.023	-0.016
$\rho = 917$ kg m^{-3}, $E(z)$, $H = 250$ m	-2.688	9.862	-14.657	11.290
$\rho(z)$, $E = 9.5$ GPa, $H = 250$ m	-0.453	1.711	-2.652	2.207
$\rho(z)$, $E(z)$, $H = 250$ m	-3.297	12.198	-18.367	14.477
$\rho = 917$ kg m^{-3}, $E = 9.5$ GPa , $H = 500$ m	0.189	-0.728	1.113	-0.819
$\rho = 917$ kg m^{-3}, $E(z)$, $H = 500$ m	-6.425	21.878	-29.374	19.695
$\rho(z)$, $E = 9.5$ GPa, $H = 500$ m	-0.804	2.694	-3.575	2.458
$\rho(z)$, $E(z)$, $H = 500$ m	-7.599	25.940	-34.968	23.630
$\rho = 917$ kg m^{-3}, $E = 9.5$ GPa , $H = 1000$ m	1.246	-3.946	4.596	-2.235
$\rho = 917$ kg m^{-3}, $E(z)$, $H = 1000$ m	-6.490	21.657	-28.390	18.540
$\rho(z)$, $E = 9.5$ GPa, $H = 1000$ m	0.506	-1.453	1.248	0.077
$\rho(z)$, $E(z)$, $H = 1000$ m	-6.858	22.931	-30.191	19.901

	E	F	G
$\rho = 917$ kg m^{-3}, $E = 9.5$ GPa , $H = 125$ m	-0.005	-1.05	0.073
$\rho = 917$ kg m^{-3}, $E(z)$, $H = 125$ m	-2.178	-0.372	0.013
$\rho(z)$, $E = 9.5$ GPa, $H = 125$ m	-0.626	-0.703	0.110
$\rho(z)$, $E(z)$, $H = 125$ m	-3.267	0.217	0.025
$\rho = 917$ kg m^{-3}, $E = 9.5$ GPa , $H = 250$ m	0.022	1.075	0.083
$\rho = 917$ kg m^{-3}, $E(z)$, $H = 250$ m	-4.749	-0.074	0.017
$\rho(z)$, $E = 9.5$ GPa, $H = 250$ m	-1.083	-0.725	0.100
$\rho(z)$, $E(z)$, $H = 250$ m	-6.361	0.418	0.022
$\rho = 917$ kg m^{-3}, $E = 9.5$ GPa , $H = 500$ m	0.254	-1.086	0.082
$\rho = 917$ kg m^{-3}, $E(z)$, $H = 500$ m	-6.876	0.075	0.024
$\rho(z)$, $E = 9.5$ GPa, $H = 500$ m	-1.007	-0.805	0.088
$\rho(z)$, $E(z)$, $H = 500$ m	-8.396	0.406	0.027
$\rho = 917$ kg m^{-3}, $E = 9.5$ GPa , $H = 1000$ m	0.216	-0.945	0.067
$\rho = 917$ kg m^{-3}, $E(z)$, $H = 1000$ m	-6.324	-0.028	0.030
$\rho(z)$, $E = 9.5$ GPa, $H = 1000$ m	-0.674	-0.751	0.066
$\rho(z)$, $E(z)$, $H = 1000$ m	-6.927	0.129	0.031

Table D.1: Coefficients of normalised longitudinal stress in Eq. (D.6) for a floating ice shelf at horizontal position ($x = 4750$ m).

Appendix E

Shallow Ice/Shelf Approximations

Over the longer timescales considered in ice-sheet models, ice behaves as an incompressible viscous fluid, where the elastic deformations are negligible compared to the viscous component. As a result, instead of considering ice as a solid material within the momentum balance, the incompressible Stokes equations are used to describe ice as a liquid. Thus, the volumetric stress or pressure is constitutively indeterminate and the deviatoric stress components are defined by a nonlinear viscous (fluid-like) constitutive law:

$$\boldsymbol{\sigma}' = \boldsymbol{\sigma} - p\boldsymbol{I} = 2\eta^{\mathrm{v}}(\dot{\varepsilon}_{\mathrm{eq}})\dot{\boldsymbol{\varepsilon}}, \tag{E.1}$$

where $\dot{\boldsymbol{\varepsilon}}$ is the strain rate tensor given by the symmetric part of the velocity gradient tensor, $\boldsymbol{I}$ is the second-order identity tensor, and the viscosity η^{v} is determined using a Bingham - Norton - Maxwell type relation [123] that accounts for shear thinning behaviour.

While it is possible to simulate ice sheets using a full Stokes flow model, due to the large scale dimensions this is computationally expensive. Simplified models have been suggested, such as the Blatter and Pattyn models [210, 211] that consider horizontal gradients of vertical velocities to be negligible and that bridging effects are insignificant [212]. This allows for the momentum balance in the horizontal direction to be decoupled from the vertical velocity w. Shallow ice/shelf models further simplify this by considering vertical shear to equal zero [213], leading to the following governing equations in the horizontal x and y directions:

$$\begin{aligned}
\frac{\partial}{\partial x}\left(4\overline{\eta^{\mathrm{v}}}\frac{\partial u}{\partial x}+2\overline{\eta^{\mathrm{v}}}\frac{\partial v}{\partial y}\right)+\frac{\partial}{\partial y}\left(\overline{\eta^{\mathrm{v}}}\frac{\partial u}{\partial y}+\overline{\eta^{\mathrm{v}}}\frac{\partial v}{\partial x}\right)&=\rho g H\frac{\partial s}{\partial x},\\
\frac{\partial}{\partial y}\left(4\overline{\eta^{\mathrm{v}}}\frac{\partial v}{\partial y}+2\overline{\eta^{\mathrm{v}}}\frac{\partial u}{\partial x}\right)+\frac{\partial}{\partial x}\left(\overline{\eta^{\mathrm{v}}}\frac{\partial v}{\partial x}+\overline{\eta^{\mathrm{v}}}\frac{\partial u}{\partial y}\right)&=\rho g H\frac{\partial s}{\partial y},
\end{aligned} \tag{E.2}$$

where $\overline{\eta^{\mathrm{v}}}=\int_0^H \eta^{\mathrm{v}}\,\mathrm{d}z$ is the depth-integrated viscosity and s is the upper surface elevation. Together with appropriate boundary conditions (e.g. velocity and terminus ocean water pressure), solving this equation provides an excellent approximation of the flow of ice sheets.